7

# Evolution of Tollmien-Schlichting Waves Over a Compliant Panel

Chris Davies

B.Sc., P.G.C.E., M.Sc.

submitted for the degree of Ph.D. at

The University of Warwick

Department of Engineering

January 1995

## Abstract

The adaptation of Tollmien-Schlichting waves as they propagate over the leading and trailing edges of finite-length compliant panels is investigated by means of numerical simulation. The behaviour so determined is pertinent to the application of compliant walls for transition delay. We consider a model problem where the compliant panels form a section in the walls bounding a plane channel fluid flow. The results obtained are encouraging. They indicate that compliant panels with lengths comparable to the Tollmien-Schlichting wavelength can have a significant stabilising effect. In some instances, the passage of a Tollmien-Schlichting wave over the edges of a compliant panel leads to the excitation of stable flow-induced surface waves. The presence of such additional waves does not appear to be associated with any adverse effect upon the stability of the Tollmien-Schlichting wave.

The numerical scheme used for the simulations derives from a mixed finite-difference/spectral discretisation of the linearised two-dimensional Navier-Stokes equations, which were taken in a vorticity-velocity formulation. Numerical stability problems were overcome by treating the inertia of the compliant wall and the fluid together when imposing the boundary conditions. This allowed the interactively coupled fluid and the wall motion to be computed without any prior restriction on the form taken by the disturbances.

An investigation was also carried out into the linear stability of plane channel flow bounded by compliant walls throughout. In the case of the Tollmien-Schlichting mode this relied, for the most part, on the determination of numerical solutions to the Orr-Sommerfeld equation. Flow-induced surface waves could be studied more readily using an approximate analytic theory. Good agreement was achieved between the predictions of the analytic theory and numerical results obtained directly from the Orr-Sommerfeld equation, particularly for travelling wave flutter. The linear stability results for the wholly compliant-walled channel were used to analyse the behaviour displayed by Tollmien-Schlichting waves in the numerical simulations that were conducted with finite-length compliant panels.

# Contents


**1 Introduction** 1

**2 Instabilities in a plane channel with compliant walls** 9

2.1 Earlier work . . . . . 9

2.2 Orr-Sommerfeld equation for a channel with compliant walls . . . . . 15

2.2.1 General formulation . . . . . 15

2.2.2 Wall model and boundary conditions . . . . . 19

2.2.3 Discretisation of the Orr-Sommerfeld equation . . . . . 22

2.2.4 Numerical results for Tollmien-Schlichting waves . . . . . 28

2.3 Flow-induced surface instabilities . . . . . 36

2.3.1 Potential theory . . . . . 38

2.3.2 Inviscid theory . . . . . 46

2.3.3 Travelling wave flutter . . . . . 51

2.3.4 Viscous wall layer corrections . . . . . 60

2.3.5 Numerical results for travelling wave flutter . . . . . 66

2.3.6 Modal coalescence and the onset of divergence instability . . . 74

**3 Methods for simulating the coupled fluid and wall motion** 96

3.1 Numerical Simulation of Transition . . . . . 97

3.2 Problem Formulation . . . . . 102

3.2.1 Mathematical model of the fluid . . . . . 102

3.2.2 Wall motion . . . . . 112
3.3 Numerical Methods . . . . . 114
3.3.1 Numerical discretisation of the fluid equations . . . . . 115
3.3.2 Discretisation of the wall motion equation . . . . . 128
3.4 Code validation . . . . . 145

**4 Simulation results for the spatial adaptation of Tollmien-Schlichting waves 154**

4.1 Selection of compliant-wall parameters . . . . . 156
4.2 Results for a selected case . . . . . 162
4.3 Energy balance . . . . . 173
4.4 Results for a partially stabilised wave . . . . . 181
4.5 Wall excitation . . . . . 183
4.5.1 Time-periodic homogeneous solutions for the wall motion . . . 186
4.5.2 Non-homogeneous solutions for the wall motion . . . . . 193
4.5.3 Comparison with numerical simulation results . . . . . 198
4.6 Results involving a superposition with flow-induced surface waves . . 202
4.6.1 Behaviour for undamped compliant walls . . . . . 204
4.6.2 Three wave fit to the simulation data . . . . . 216
4.6.3 Some additional remarks about cut-off frequencies . . . . . 225
4.6.4 Behaviour for damped compliant walls . . . . . 230

**5 Conclusions and further work 238**

**A Equivalent formulations of the fluid governing equations 247**

**B Note on the formulation of the energy balance equation 250**

# List of Figures


1.1 Maximum amplitude envelopes . . . . . 6

1.2 Tollmien-Schlichting wave propagating in a rigid/compliant-walled channel . . . . . 7

2.1 Neutral curves for the Tollmien-Schlichting instability . . . . . 31

2.2 Neutral curves showing the effect of wall damping on the Tollmien-Schlichting instability . . . . . 32

2.3 Neutral curves showing the effect of wall damping on travelling wave flutter . . . . . 33

2.4 Eigenfunction profile of a Tollmien-Schlichting wave . . . . . 34

2.5 Eigenfunction profile for travelling wave flutter . . . . . 35

2.6 Eigenvalue spectra for $\omega = 0.26$ . . . . . 37

2.7 Eigenvalue spectrum for $\omega = 1$ . . . . . 37

2.8 Onset of flutter instability from potential theory . . . . . 43

2.9 Neutrally stable waves from potential theory . . . . . 43

2.10 Onset of divergence instability from potential theory . . . . . 44

2.11 Onset of flutter instability from inviscid theory . . . . . 49

2.12 Onset of divergence instability from inviscid theory . . . . . 50

2.13 Onset of flutter instability from inviscid theory, with no critical layer 57

2.14 Onset of travelling wave flutter/flutter instability from inviscid theory 57

2.15 Comparison of neutral stability curves for travelling wave flutter . . . 67

2.16 Neutral stability curves showing the effect of the wall layer . . . . . 70
2.17 Neutral stability curves showing the merger of the Tollmien-Schlichting mode and travelling wave flutter . . . . . 71
2.18 Neutral stability curves from inviscid theory using the approximation $J = J_0 + i\alpha^2 \Im(J_1)$ . . . . . 73
2.19 Neutral stability curves from inviscid theory using $J = J_0 + \alpha^2 J_1$ and wall layer corrected version . . . . . 75
2.20 Neutral stability curve from the full numerical solution of the Orr-Sommerfeld equation . . . . . 75
2.21 Variation of $mc^2 + J_0(c)$ . . . . . 84
2.22 Variation of $mc^2 + J_d^r(\alpha, c)$ . . . . . 86
2.23 Real and imaginary parts of the phase velocity, as obtained from the inviscid dispersion relation . . . . . 88
2.24 Real and imaginary parts of the phase velocity, as obtained from direct numerical solution of the Orr-Sommerfeld equation . . . . . 90

3.1 Streamwise development of Tollmien-Schlichting wave propagating in a rigid-walled channel . . . . . 147
3.2 Streamwise variation of locally-defined wavenumbers and growth rates 148

4.1 Tollmien-Schlichting wave propagating in a channel with a compliant-walled section . . . . . 155
4.2 Neutral stability curves for Tollmien-Schlichting waves . . . . . 164
4.3 Streamwise development of Tollmien-Schlichting wave propagating in a channel containing a compliant-walled section . . . . . 166
4.4 Streamwise variation of wall displacement, velocity and fluid perturbation pressure . . . . . 168
4.5 $u$-component of the fluid perturbation velocity . . . . . 170
4.6 $v$-component of fluid perturbation velocity . . . . . 171

4.7 Fluid perturbation vorticity . . . . . 172
4.8 Fluid perturbation pressure . . . . . 173
4.9 Streamwise variation of the terms from the energy balance equation . 178
4.10 Streamwise development of Tollmien-Schlichting wave . . . . . 184
4.11 Streamwise variation of the terms from the energy balance equation . 185
4.12 Streamwise distribution of time-averages for the squared wall-displacements and the pressure work . . . . . 200
4.13 Neutral stability curves for Tollmien-Schlichting waves . . . . . 204
4.14 Instantaneous streamwise distribution of fluid disturbance energy and integrated square vorticity . . . . . 207
4.15 Wall motion variables and flow-field variables at the wall . . . . . 209
4.16 Time-averaged square of the wall displacement . . . . . 210
4.17 $u$-component of the fluid perturbation velocity . . . . . 211
4.18 Power spectra for the wall displacement and wall vorticity . . . . . 213
4.19 Fitted wall displacement and velocity distributions . . . . . 219
4.20 Components of the wall displacement . . . . . 221
4.21 Fitted wall perturbation fluid pressure and time-averaged squared wall displacement . . . . . 223
4.22 Components of the wall vorticity . . . . . 224
4.23 Variation with temporal frequency of spatial eigenvalues associated with flow-induced surface waves, $K = 4B$ . . . . . 227
4.24 Variation with temporal frequency of spatial eigenvalues associated with flow-induced surface waves, $K = B/4$ . . . . . 229
4.25 Instantaneous fluid disturbance energy and integrated square vorticity 232
4.26 Wall velocity and displacement, and perturbation fluid pressure and vorticity at the wall . . . . . 234
4.27 Power spectra for the wall displacement and wall vorticity . . . . . 235

4.28 Instantaneous components of the wall displacement, for non-zero wall damping . . . . . 237

5.1 Streamwise distributions of the time-averaged convected disturbance energy . . . . . 246

## Acknowledgements

This work was supported by the SERC and MTD Ltd. under grant GR/G22725.

I would like to thank to Peter Carpenter for his support and guidance.

## Declaration

This thesis was prepared by myself.

# Chapter 1

# Introduction

It is now over three decades since the first experimental studies were conducted by Kramer with the aim of establishing the drag reducing capabilities of compliant coatings [1],[2]. Kramer intended to exploit what he believed to be the secret behind the swiftness of the dolphin. Gray had argued that dolphins were able to maintain swimming speeds that were anomalously high [3]. Kramer covered solid bodies of revolution with rubber coatings that were fashioned so as to emulate dolphin skin. He then towed these bodies at high speed through sea water, achieving considerable reductions in drag. Not surprisingly, Kramer's experiments stimulated extensive theoretical investigation of the stability effects of compliant walls on boundary layer flows. The work of Benjamin and Landahl [4],[5] provided the first vindications for Kramer's contention that the drag reduction bestowed by his compliant coatings was the consequence of a delay in the transition between laminar and turbulent flow. It was demonstrated that the introduction of a flexible wall as the boundary to a fluid flow could yield a beneficial influence on the linear stability of Tollmien-Schlichting disturbance waves. (The exponentional amplification of such waves represents the most spatially extended stage in boundary layer transition.) However, the same theoretical studies also indicated that there would be additional modes of instability, which could only exist because the wall was no longer rigid. The presence of what

have since been called flow-induced surface instabilities, might be expected to limit, if not completely destroy, any advantages that would accrue from the stabilisation of Tollmien-Schlichting waves. It also turned out that, in a key respect, Kramer's intuition about the mechanism by which his coatings could bring about a stabilisation of Tollmien-Schlichting waves was in error. It was shown, again using linear stability theory, that the inclusion of damping in the compliant wall model would generate a destabilising effect on Tollmien-Schlichting waves. This was in direct opposition to the behaviour that had been presumed by Kramer. His coatings contained internal cavities, within which he enclosed a highly viscous fluid, with the intent of damping out 'boundary layer' waves (presumably, a reference to Tollmien-Schlichting waves).

The history of subsequent experimental attempts to verify the favourable stability effect of wall compliance on boundary layer flows is somewhat chequered. Kramer's original investigations have, at various times, been thrown into doubt. However, as was argued in detail by Carpenter & Garrad [6], none of the experiments which appeared to undermine Kramer's work were carried out in a manner that could provide any conclusive refutation. Partly as a result of the supporting theoretical studies that were conducted by the same two authors [6],[7], Kramer's claims can now be treated with less reservation. By making use of an improved theoretical model of Kramer's compliant coatings, Carpenter & Garrad were able to conclude that substantial transition delays, and hence drag reductions, could have been achieved in practice. Moreover, they argued that some of the coatings constructed by Kramer would, for the specific flow speeds that were realised in his experiments, have given a performance that was close to being optimal. Although Kramer had employed a form of wall motion damping that was expected to reduce the stabilisation of Tollmien-Schlichting waves, this detrimental influence could be more than made up for by the strongly stabilising effect that would be exerted upon flow-induced surface waves. In particular, the effect of wall damping in postponing the onset of the flow-induced mode of instability that is now termed as travelling-wave flutter, may have allowed

the use of softer compliant wall materials than would otherwise have proved possible.

Following on from the investigations of Carpenter & Garrad, a series of detailed experiments in water were conducted by Gaster and his co-workers [8],[9]. These established, in an unequivocal manner for the first time, that substantial reductions in the growth rates of Tollmien-Schlichting waves could be obtained along a fluid boundary layer adjacent to a compliant wall. Furthermore, there was good quantitative agreement between the experimental results and predictions that were obtained by Willis from a numerical linear stability analysis [10]. Because of the above mentioned experimental success, and the supporting evidence that has now been provided by numerous theoretical studies (for some recent examples, see the work of Sen & Arora [11], Yeo [12],[13], and Carpenter and his co-workers [14],[15]), we will take it for granted that compliant coatings can, in fact, be used to obtain significant delays in the transition from laminar to turbulent boundary layer flow. Consequently, we will not attempt to give an exhaustive survey of all the previous work on the subject. Such a task has, in any case, been undertaken in a recent review completed by Carpenter [16]. There is also a survey, with a greater emphasis on experimental work, by Riley *et al* [17]. Rather than replicating the content of these two reviews we will prefer to make references to earlier investigations only as and when the need arises. (As an exception to this general policy, there will be an overview of the studies that have been conducted for the specific case of a compliant-walled channel.)

Starting from a position where it is presumed that compliant surfaces can be employed to postpone transition, our main concern in the present work will be to resolve an issue that is pertinent to the development of *practical* devices for use in marine applications. Before formulating any of the particular questions to be addressed, we will provide a brief description of the problem situation in which they arise. As has already been remarked, the effectiveness of a compliant wall in delaying the transition to turbulence in a fluid flow over a solid body is limited by the occurrence of flow-induced instabilities that are based in the wall itself. Although increasing wall

flexibility suppresses the growth of Tollmien-Schlichting waves, this benefit may only be achieved at the expense of making the flow/wall system vulnerable to additional modes of instability that are only possible because the wall is no longer rigid. Such instabilities may themselves take over the role of initiating transition in the flow, defeating the objective of delaying the onset of turbulence [18],[19]. Any favourable change in the drag will then be lost or even reversed. Thus the design of practical compliant surfaces involves the delicate balancing of wall properties so as to ensure maximal stabilisation of Tollmien-Schlichting waves, subject to the constraint that no other instabilities are triggered [20],[21],[22],[23].

For the case of Blasius flow over a flat plate, the optimum wall properties are highly Reynolds number dependent; the properties most appropriate for transition delay vary with the distance from the leading edge of the plate. The situation is illustrated in Figure 1.1, which plots maximum amplification envelopes for the Tollmien-Schlichting instability as a function of the Reynolds number. Each of the separate envelopes corresponds to a different set of compliant wall properties. All the sets were chosen so as to make the walls as flexible as possible without introducing any flow-induced surface instabilities (for a fixed free-stream flow speed). For the particular type of compliant wall model adopted, the wall properties could then be characterised using a single parameter $\bar{\alpha}_d$. It can be seen that the stability effect that is achieved is strongest at different Reynolds numbers for different choices of the wall parameter. This behaviour can be anticipated on very general grounds. We might only expect to find a significant stability effect on Tollmien-Schlichting waves when, at a given streamwise location, the lengthscale that can be taken to define such waves, for example the boundary layer displacement thickness, is comparable to a characteristic lengthscale that can be associated with the wall motion. The latter lengthscale could be derived by considering the minimisation of some effective measure of the wall stiffness, for wavelike forms of disturbance, when the disturbance wavenumber is varied. For a compliant wall with unchanging material properties and geometry, any

such lengthscale will, by definition, be constant and independent of the nature of the fluid flow. This means that it will not be possible to preserve any match between the lengthscale that is intrinsic to the wall and the varying lengthscale that characterises Tollmien-Schlichting waves at different streamwise locations. Consequently, the stability effect of the compliant wall on Tollmien-Schlichting waves can be expected to be highly Reynolds number dependent, just as is illustrated in the figure. Moreover, if the compliant wall properties are altered so as to increase the lengthscale associated with the wall motion, then we can anticipate that the maximum stability effect will be shifted to larger Reynolds numbers. This is also exhibited in the figure. The parameter $\bar{\alpha}_d$ denotes a non-dimensional critical wavenumber that characterises the compliant wall. Decreasing values of $\bar{\alpha}_d$ thus correspond to an increasing lengthscale.

The above observations suggest that for technological applications a series of compliant panels, each with locally optimised properties, would give the best performance in delaying transition [24],[25]. This leads to the question: How short can a compliant panel be whilst remaining effective in stabilising Tollmien-Schlichting waves? Or put differently: How long does it take for a Tollmien-Schlichting wave to adapt to the presence of a compliant wall? The present work is mainly concerned with numerical simulations that were undertaken in order to answer such questions.

Numerical studies were conducted, initially, for the situation that is depicted in Figure 1.2, *i.e.* a Tollmien-Schlichting wave travelling down a plane channel bounded first by rigid walls and then by compliant walls. As should be clear from the foregoing discussion, the corresponding problem for Blasius flow has more obvious technological significance. However, it might be expected that much of the essential physics would be retained for the simpler case of plane channel flow. Although the consideration of boundary layer growth is fundamental in providing a motivation for the current investigations, it would not appear to be strictly necessary to take such growth into account when assessing the actual adaptation of Tollmien-Schlichting waves. It turns out that, at least in the case of plane channel flow, Tollmien-Schlichting waves can

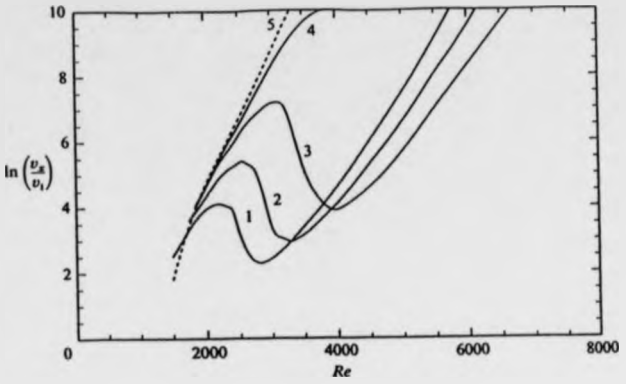


Figure 1.1: Maximum amplitude envelopes as functions of the displacement thickness Reynolds number for various compliant walls with optimal properties. Curves 1 to 4 correspond to compliant walls that are parameterised by a decreasing non-dimensional critical wavenumber $\bar{\alpha}_d$. Curve 5 is for the rigid-walled case. (The selected values of $\bar{\alpha}_d$ are given, approximately, as follows. Curve 1, $\bar{\alpha}_d = 6 \times 10^{-5}$, Curve 2, $\bar{\alpha}_d = 5 \times 10^{-5}$, Curve 3, $\bar{\alpha}_d = 4 \times 10^{-5}$, Curve 4, $\bar{\alpha}_d = 3 \times 10^{-5}$.) Reproduced from reference [14].

adapt to the presence of wall compliance over a relatively small distance that is comparable to the wavelength. Assuming that such short range adaptation carries over to the case of Blasius flow, it can be anticipated that the growth in the boundary layer would be of rather limited significance; on the basis of the channel flow results that will be reported later, it may be conjectured that Tollmien-Schlichting waves propagating in a Blasius flow above a rigid/compliant wall join will only be subject to adjustment over a streamwise distance for which the boundary layer thickness can be treated as effectively constant. Turning this around, it can be seen that limiting the simulations to the case of plane channel flow is not so restrictive as might first

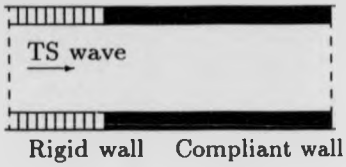


Figure 1.2: Tollmien-Schlichting wave propagating in a rigid/compliant-walled channel. The mean flow $U = 1 - y^2$ is from left to right. (The $y$-direction is normal to the channel walls and the channel centre-line is located at $y = 0$.)

have been thought.

Because the numerical simulations conducted for the situation shown in Figure 1.2 indicated that the adaptation of Tollmien-Schlichting waves could occur on a short lengthscale, it proved possible to tackle a more ambitious problem, without generating excessive computational expense. Instead of just resolving the behaviour of a Tollmien-Schlichting wave in the vicinity of a rigid/compliant wall join, the behaviour of the wave as it propagated over both ends of a finite-length compliant panel could be examined, though again only in the context of a plane channel flow. This enabled the contrasting effects of rigid/compliant and compliant/rigid wall joins to be investigated. It also allowed a more direct approach to the question of how short a compliant panel could be made without losing its capability to stabilise Tollmien-Schlichting waves.

Before embarking upon a report of the numerical simulations, and the particular numerical methods that were developed in order to conduct them, we will provide a general analysis of the instabilities that can arise for the case of an entirely compliant-walled plane channel flow. Such an analysis is necessary in order to make sensible choices of compliant wall parameters for use in the simulations. It is also of considerable interest in its own right. Somewhat surprisingly, there have been very few studies of the effect of wall compliance on the hydrodynamic stability of plane channel flow,

in contrast to the extensive investigations that have been completed for Blasius flow. It will be seen that the relatively simple form of the analysis for the channel flow facilitates the identification of some interesting features that may turn out to have wider implications.

# Chapter 2

# Instabilities in a plane channel with compliant walls

## 2.1 Earlier work

This section gives a review of previous studies of the hydrodynamic stability of plane channel flow between flexible walls. The comprehensive investigations that have been made for the case of Blasius flow over a compliant wall have not been repeated to any great extent for plane channel flow. That plane channel flow has received less attention is not in itself surprising, since there is no well-known situation in which the transition-delaying characteristics of a compliant-walled channel would be of practical concern. A number of studies have been conducted for the idealised case of plug flow, *i.e.* constant velocity flow, between flexible channel walls [26], [27], [28]. These studies aimed to model physical behaviour, such as that displayed by flows in human lung airways, occurring in circumstances somewhat different from those of present interest. Both linear and non-linear stability investigations were undertaken, with some emphasis on the latter. Such work has recently been described in a review by Grotberg [29], to which reference should be made for further details. However, in all of the studies referred to by Grotberg, the absence of shear in the

specified mean flow precludes any account being given of the Tollmien-Schlichting instability. This instability provides the central interest for the present investigation. We are concerned with plane channel flow between flexible walls only to the extent that it provides a simple model problem involving a boundary layer that can be subject to laminar-turbulent transition via the amplification of Tollmien-Schlichting waves. Consistent with this outlook, we will not attempt to give any direct account of applications in fields of interest other than drag reduction and transition delay.

The first studies of the effects of wall compliance on the stability of plane channel flow were conducted by Hains & Price [30] over thirty years ago. These followed the pioneering theoretical studies made by Benjamin [4] for the case of Blasius flow. Hains & Price numerically integrated the Orr-Sommerfeld equation for disturbances in a plane channel with flexible walls. They thus provided a means of checking, albeit for a simpler flow, the predictions made by Benjamin using an approximate analytic theory. The channel walls were modelled simply as tensioned membranes, with damping accounted for via the introduction of a single damping coefficient. The numerical results obtained showed the behaviour expected from Benjamin's work. Increasing wall flexibility tended to stabilise Tollmien-Schlichting waves. In fact, for the case of a membrane with negligible inertia and zero wall damping, Hains & Price concluded that the Tollmien-Schlichting instability could be completely eliminated if the walls were made sufficiently compliant. Furthermore, they found that small levels of damping in the wall had a destabilising effect on the Tollmien-Schlichting waves, in accord with Benjamin's counter-intuitive conclusion. (Hains [31] went on to conduct a numerical investigation of the additional modes of instability that are introduced when the walls are made flexible. The possibility of such modes had been addressed by Benjamin. In general, they become unstable with increased wall flexibility, and so tend to undermine the beneficial effect of wall compliance on the Tollmien-Schlichting waves. Unfortunately, Hains' work contains an elementary error in the interpretation of eigenvalues; he appears to confuse stability with instability. Consequently he found

that increasing tension in the walls destabilised the modes he investigated, which is the opposite of what would be expected on physical grounds.)

Korotkin [32] provided an approximate analytic theory for Tollmien-Schlichting waves in a compliant channel. The response of the wall to the fluid stresses was described by assuming a constant proportionality between the amplitudes of the wall motion and the fluid forcing, together with a constant difference between their respective phases. The results obtained by modelling the effect of wall flexibility in such a fashion suggested that the critical Reynolds number for the onset of Tollmien-Schlichting instability could either be increased or decreased with increasing wall flexibility, depending on the phase relationship imposed between the wall pressure and wall motion. Despite its apparent generality in approach, Korotkin's work is flawed by an incorrect formulation of the boundary conditions on the fluid at the walls. In matching the velocities of the fluid and the walls in the direction of the mean flow, no account was taken of the fact that at the perturbed location of the walls, the mean flow is non-zero. Later studies have shown that the neglect of the associated term in the boundary conditions makes a significant difference to the results that are obtained. For instance, Tsvelodub [33] found that the stabilising effect of wall compliance on Tollmien-Schlichting waves may be replaced by destabilisation if the boundary conditions are improperly implemented.

Korotkin's work cannot be compared directly with the earlier results of Hains & Price, owing to differences in the way the wall properties are non-dimensionalised. Hains [31] examined the various possibilities for non-dimensionalisation and argued that the most physically interesting case was the one in which the dimensional, as well as the non-dimensional, wall parameters could be held constant whilst varying the Reynolds number via changes in the centre-line velocity of the mean flow. In an experimental realisation, this corresponds to a channel with a non-adjustable separation between compliant walls which have specified inertia and stiffness properties. Results for different Reynolds numbers would be obtained by performing experiments

with the same channel and fluid, but at different flow speeds. In contrast, Korotkin's neutral stability curves display results in which the variation of the Reynolds number must be interpreted as being due to changes in the fluid viscosity alone; otherwise the points at different Reynolds numbers correspond to physically distinct walls.

The studies made by Green & Ellen [34] of the linear stability of plane channel flow between flexible walls appear to be motivated mainly by the need to assess the effectiveness of a general numerical solution procedure. The solution of the Orr-Sommerfeld equation, subject to compliant-wall boundary conditions, is treated as a model problem from a broad class of boundary value problems. Nevertheless, the results obtained are some of the most extensive published to date for the compliant channel problem. In addition to results for Tollmien-Schlichting waves which improve on the numerical accuracy of the results obtained by Hains & Price, the work of Green & Ellen includes neutral curves in which the presence of other instabilities can be discerned. For sufficiently compliant walls, they found that the neutral stability curve for the Tollmien-Schlichting mode could deform to include a further region of instability at higher wavenumbers. Furthermore, they observed that the critical Reynolds number for the onset of Tollmien-Schlichting instability could be significantly reduced from its rigid-wall value for channels with relatively high levels of wall damping.

Green & Ellen derived analytic results for the onset of two distinct flow-induced instabilities, which can be identified with the divergence and flutter instabilities that occur in the case of Blasius flow [7]. However, it would appear that they overlooked a further mode of instability, namely what is now known as travelling wave flutter. Benjamin [4] had discussed this instability in his earliest studies. Because of their failure to identify travelling wave flutter, Green & Ellen were unable to give a full explanation of their numerical results. Further details are given later, when comparisons are made with results from the present work.

Tsvelodub [33] investigated the stability of plane channel flow between walls mod-

elled as unsupported elastic plates. Consequently, he found that a flow-induced instability could occur at all Reynolds numbers. No physical interpretation of the instability was given, though its connection with the Tollmien-Schlichting instability was explored numerically. The inclusion or exclusion of the normal viscous stress in the fluid forces driving the wall motion was shown to make a qualitative difference to the form of the neutral stability curves. This suggests that the instability involved may have been rather weak, at least for the large values of the Reynolds number that are relevant to studies concerned with laminar-turbulent transition. In any case, the physical significance of Tsvelodub's work is unclear; the existence of instability for arbitrarily small Reynolds numbers could be viewed as pathological behaviour arising from the use of an oversimplified wall model. Besides this, the interpretation of the numerical results is hampered by the fact that the wall properties were non-dimensionalised in such a way that variations in the Reynolds number must be attributed to changes in the fluid viscosity, as in the work of Korotkin.

The studies mentioned thus far were all restricted to two-dimensional disturbances of the mean fluid flow. Ganiev *et al* [35] investigated a three-dimensional generalisation of the compliant channels considered by Tsvelodub. Only the Tollmien-Schlichting mode was considered. With variations in the Reynolds number again interpreted as being due to alterations in the fluid viscosity, the results obtained by Ganiev imply that there are ranges of wall parameters for which the onset of Tollmien-Schlichting instability is determined by three-dimensional disturbances. However, in order to interpret his numerical results, Ganiev makes use of a Squire transformation [36], which includes a scaling of the non-dimensional wall properties. It can be shown that if the Reynolds number is viewed as varying due to changes in the centre-line velocity of the mean flow, then the scaling of the non-dimensional wall properties noted by Ganiev is precisely what is needed to ensure that the dimensional wall properties are kept constant. From this it follows that a generalisation of Squire's theorem, *i.e.* that two-dimensional disturbances determine the critical

Reynolds number in wall bounded shear flows, can be made for compliant channels. Thus by a change of interpretation, it is possible to avoid Ganiev's conclusion that three-dimensional disturbances may determine the onset of instability. The validity of Squire's theorem has since been demonstrated by Rotenberry & Saffmann [37] for the wider class of compliant-walled channels which have walls that may be modelled as spring-backed plates. Further details are given in Section 2.2.2.

Pierucci & Morales [38] conducted a study of the effect of a finite thickness flexible boundary upon the stability of plane channel flow. The behaviour of the walls was modelled via the Navier equations, instead of using a simplified surface-based wall model as in previous studies. (The distinction between surface-based and volume-based wall models, such as that given by the Navier equations, is discussed by Carpenter in [16].) Unfortunately, it appears that in implementing the boundary conditions, Pierucci & Morales reproduced the error found in the work of Korotkin which had been completed twenty five years earlier. The non-vanishing of the mean flow at the perturbed wall location was not taken into consideration. In any case, the significance of the results obtained is rather limited, since disturbances with only one arbitrarily selected wavenumber are considered.

Most recent studies of the stability of plane channel flow between flexible walls have been concerned with non-linear aspects of the problem. In particular, interest has focussed on the question of whether wall properties can be selected so that the nature of the instability changes from subcritical to supercritical. Rotenbery & Saffman [37] derived a Ginzburg-Landau equation for finite amplitude disturbances, which they used to show that, in principle, the subcritical instability found in rigid-walled channels could be replaced by supercritical instability for sufficiently compliant walls. Subsequent study by Rotenberry [39] suggested that the extent of this effect was so limited that it would not be expected to give rise to any significant qualitative difference between the process of transition in compliant-walled channels and what is found in a rigid-walled channel. Rossi [40] also derived a Ginzburg-Landau equation

for the non-linear evolution of disturbances in a channel, but for a case with broken symmetry; only one of the channel walls was taken to be compliant, the other being kept rigid. Finally, Pierce [41] used plane channel flow between flexible walls as a model problem to illustrate a general method for deriving the Ginzburg-Landau equation in situations involving interfacial instability. A more sophisticated model for the walls was taken than in the other studies mentioned directly above. For the particular wall parameters selected, the critical Reynolds number was found to be below the rigid-wall value and the nature of the instability remained subcritical.

With the exception of the work of Pierce, none of the non-linear studies to date have explicitly considered the possibility of instability modes other than the Tollmien-Schlichting mode found in the rigid-walled problem. For example, Rotenberry studied non-linear effects at Reynolds numbers which, for the parameters he selects in his wall model, are considerably greater than the Reynolds numbers at which other instabilities can be shown to have set in. It is arguable that there is little merit in examining the non-linear intricacies of the onset of the Tollmien-Schlichting instability if the role of this instability in initiating transition to turbulence has been usurped by a flow-induced surface instability [18]. One possible application of the study of such surface instabilities, that is presented below, would be in making a choice of appropriate wall properties to be used in non-linear investigations.

## 2.2 Orr-Sommerfeld equation for a channel with compliant walls

### 2.2.1 General formulation

This section outlines the mathematical formulation of the linear stability problem for plane channel flow. We consider channels which have infinite streamwise extent. The wall properties are constant throughout the channel; the walls are either entirely

rigid or else compliant with unvarying stiffness and inertia parameters.

For a rigid-walled channel, linear stability studies are usually restricted to two-dimensional disturbances from the mean flow. This stems from Squire's theorem; the critical Reynolds number for a two-dimensional parallel flow (over a rigid wall) is lowest for two-dimensional disturbances. For a compliant-walled channel, an extension of Squire's theorem can be made, provided the wall properties are non-dimensionalised in a particular fashion [37]. Thus we confine attention to two-dimensional disturbances. Introducing a streamfunction $\psi$, the disturbances are further assumed to take the form of normal modes,

$$\psi(x,y,t) = \phi(y)e^{i(\alpha x - \omega t)}\,, \tag{2.1}$$

where $x$ is the streamwise direction, $y$ is normal to the walls, $\phi$ the disturbance profile, and $\alpha$,$\omega$ are the spatial wavenumber and temporal frequency respectively. In general, both $\alpha$ and $\omega$ could be complex valued. The two special cases, $\alpha$ real, $\omega$ complex and $\alpha$ complex, $\omega$ real correspond to temporally and spatially growing waves. For the convective Tollmien-Schlichting instabilities found in flows over rigid walls, spatial growth is of most physical interest [42]. In addition, for compliant walls, the travelling wave flutter instability, which is related to the free-waves that propagate in the wall in the absence of the fluid, can also be modelled as spatially growing. Consequently, we shall restrict attention to the case of spatially growing normal modes. It should be noted, though, that such an approach is not sufficient for studying all of the instabilities that can occur for flows over compliant walls. In particular, it will not be adequate for describing the divergence absolute instability arising when each wall is made so compliant that it can no longer withstand the hydrodynamic pressure forces.

Substitution of the normal mode form (2.1) into the linearised vorticity transport equation for the fluid gives the Orr-Sommerfeld equation for the disturbance profile,

$$(U-c)(D^2-\alpha^2)\phi - U''\phi = \frac{1}{i\alpha R}(D^2-\alpha^2)^2\phi\,, \tag{2.2}$$

where $U$ is the mean velocity profile, $R$ is the Reynolds number and $D = d/dy$. For plane channel flow, the Reynolds number is defined using the dimensional channel half-width and the centre-line velocity. The non-dimensionalised mean velocity profile then takes the form $U = 1 - y^2$. The mean flow is driven by a constant pressure gradient $dP/dx = -2/R$. It is assumed that in the case of a compliant-walled channel, the effect of this pressure gradient on the walls can either be ignored, or balanced by prescribed body forces in each wall. Such an assumption is needed to ensure that there is a solution to the coupled fluid/wall equations with the walls statically located at $y = \pm 1$ when the mean flow is unperturbed[1].

For a rigid-walled channel, the Orr-Sommerfeld equation is solved subject to the homogeneous boundary conditions,

$$\phi = D\phi = 0 \quad , \text{at } y = \pm 1 \quad . \tag{2.3}$$

In view of the reflective symmetry of the mean profile $U = 1 - y^2$ about the channel centre-line, the problem can be split into two decoupled problems for symmetric and antisymmetric disturbances; we can either take $\phi(y) = \phi(-y)$ or $\phi(y) = -\phi(-y)$. For the case of a compliant-walled channel, the boundary conditions can be formulated as

$$\alpha U'\phi + \omega D\phi = \alpha\phi \mp iY(\alpha,\omega)\, p = 0 \quad , \text{at } y = \pm 1 \, , \tag{2.4}$$

where $Y$ is an admittance coefficient determined by the wall properties and $p$ is the amplitude of the fluid perturbation pressure. The choice of sign in the pressure term arises because the fluid lies above the lower wall, but below the upper wall. It can be shown that $p(\pm 1)$ are linear functionals of the streamfunction profile $\phi$. Specific forms for both $Y$ and $p(\pm 1)$ are discussed in the next section. For present purposes, the important thing to note is that the homogeneous form of the boundary conditions

[1]There are also mean flow shear stresses $\sigma_{12} = \mp 2/R$ which act at the walls. These have no effect on the wall motion for the types of compliant wall considered below, where the wall model excludes tangential motion.

found for the rigid walls can be retained for the case of compliant walls. Furthermore, $Y$ vanishes as the wall is made more and more rigid; thus it can be seen that the rigid-wall boundary conditions (2.3) can be recovered from (2.4) for sufficiently stiff compliant walls.

Symmetric and antisymmetric disturbances can still be considered separately for compliant-walled channels. The introduction of the same wall compliance at both the upper and lower walls preserves the reflective symmetry of the problem. For the rigid-walled case, the stability characteristics are determined by the symmetric $\phi(y) = \phi(-y)$ disturbances alone [36]. Since the primary interest of introducing wall compliance stems from its stabilising effect on the Tollmien-Schlichting waves found in flows over rigid walls, it would seem plausible to study only symmetric disturbances when the walls are made compliant. However, as will be discussed in detail later, the presence of wall compliance may make the flow vulnerable to instabilities additional to the Tollmien-Schlichting waves. These other instabilities will also be separable into symmetric and antisymmetric modes, but without further study it is not clear which symmetry mode will be the least stable. Thus, restricting attention to symmetric solutions of the Orr-Sommerfeld equation, whilst useful for investigating the stabilisation of Tollmien-Schlichting waves, may be unjustifiable from a more general viewpoint.

The Orr-Sommerfeld equation, together with the homogeneous boundary conditions (2.3) or (2.4) for either rigid or compliant walls, gives an eigenvalue problem. This yields, in principle, a dispersion relation of the form

$$\mathcal{F}(\alpha, \omega, R) = 0\,. \tag{2.5}$$

Neutral stability curves are obtained by finding solutions of (2.5) for which both $\alpha$ and $\omega$ are real. Formally, we can think of the introduction of wall compliance as a means of modifying the dispersion relation. This can lead to shifts in the neutral curves found for the rigid wall, and hence the possibility of improved stability properties for

Tollmien-Schlichting waves. However, the modified dispersion relation also admits solutions which are unrelated to those found for the rigid wall. If these additional waves can themselves become unstable, the benefits accrued from any stabilisation of Tollmien-Schlichting waves may be lost.

The numerical formulation of (2.5), and its solution for a simple model of the compliant walls, is the subject of Section 2.2.3. The physical classification of the additional solutions introduced when the walls are allowed to be compliant is taken up in Section 2.3. It turns out that for these compliance-induced solutions, the dispersion relation can be approximated analytically in a relatively straightforward manner. But before proceeding any further we first need to consider the formulation of the boundary conditions at the wall. So far, these have been stated, but not justified. In addition, we need to introduce a specific model for the compliant walls.

### 2.2.2 Wall model and boundary conditions

In this section we derive the detailed form of the fluid boundary conditions needed for the solution of the Orr-Sommerfeld equation. The compliant walls of the channel are modelled as spring-backed plates and are constrained to move only in the vertical direction. Letting asterisks denote dimensional quantities and taking $\eta^*$ as the vertical displacement of the upper wall from its equilibrium position, the equation of motion of the upper wall can be written as

$$\left(m^* \frac{\partial^2}{\partial t^{*2}} + d^* \frac{\partial}{\partial t^*} + B^* \frac{\partial^4}{\partial x^{*4}} - T^* \frac{\partial^2}{\partial x^{*2}} + K^*\right) \eta^* = p^*(h) \,. \tag{2.6}$$

The wall parameters are: $m^*$ the plate mass per unit area, $d^*$ the wall damping coefficient, $B^*$ the flexural rigidity of the plate, $T^*$ the longitudinal tension per unit width, and $K^*$ the spring stiffness. The hydrodynamic forcing of the wall is given by the perturbation fluid pressure $p^*$ at the mean wall location $y^* = h$, where $h$ is the dimensional half-width of the channel. The contribution of the normal viscous stress may be ignored since it is negligible for the large values of the Reynolds number that

are of current interest. The equation for the lower wall at $y^* = -h$ is identical in form, except that the sign of the pressure is reversed.

Various choices are possible for non-dimensionalising the wall equations using the dimensional channel half-width $h$, centre-line mean fluid velocity $U_m$, fluid density $\rho$, and viscosity $\nu$ . The choice depends on how the Reynolds number $R$ is varied whilst keeping the dimensional wall properties fixed; we want to be able to interpret results for different $R$ as pertaining to the same physical walls. Holding the half-width $h$, density $\rho$, and viscosity $\nu$ fixed, so that $R = U_m h/\nu$ is varied only through changes in the centre-line velocity $U_m$, we obtain the following non-dimensionalisation of the wall properties:

$$m = \frac{m^*}{\rho h} \, , \; d = \frac{d^* h}{\rho \nu} \, , \; B = \frac{B^*}{h \rho \nu^2} \, , \; T = \frac{T^* h}{\rho \nu^2} \, , \; K = \frac{K^* h^3}{\rho \nu^2} \, . \tag{2.7}$$

The wall equation can then be written as

$$\left( m \frac{\partial^2}{\partial t^2} + \frac{d}{R} \frac{\partial}{\partial t} + \frac{1}{R^2} (B \frac{\partial^4}{\partial x^4} - T \frac{\partial^2}{\partial x^2} + K) \right) \tilde{\eta} = \tilde{p}(1) \, , \tag{2.8}$$

where $x = x^*/h$, $t = t^* U_m/h$, $\tilde{\eta} = \eta^*/h$, and $\tilde{p} = p^*/\rho U_m^2$. With this particular scheme of non-dimensionalisation, the previously mentioned extension of Squire's theorem holds; restricting attention to two-dimensional disturbances in the fluid can be justified. (To obtain this result, we first need to generalise the wall equation to include three-dimensional disturbances by making the replacements $\partial^2/\partial x^2 \rightarrow \nabla^2$, $\partial^4/\partial x^4 \rightarrow \nabla^4$ in equation (2.8), where $\nabla^2 = \partial^2/\partial x^2 + \partial^2/\partial z^2$ , with $z$ the spanwise direction in the channel.)

Assuming a normal mode form for the wall displacement, $\tilde{\eta} = \eta \, e^{i(\alpha x - \omega t)}$ , the linearised fluid boundary conditions at the upper wall are

$$D\phi(1) + U'(1)\eta = \alpha\phi(1) - \omega\eta = 0 \, . \tag{2.9}$$

These correspond to matching the horizontal and vertical velocities of the fluid to those of the wall. The $U'(1)\eta$ term in the first condition was erroneously omitted

in some earlier studies. It takes account of the mean flow velocity at the perturbed location of the wall. Eliminating $\eta$ between the two conditions gives

$$\alpha U'(1)\phi(1) + \omega D\phi(1) = 0\,. \tag{2.10}$$

Writing the perturbation fluid pressure as $\bar{p} = p\, e^{i(\alpha x - \omega t)}$ , the wall equation (2.8) gives

$$\left(-(m\omega^2 + i\frac{1}{R}\omega d) + \frac{1}{R^2}(B\alpha^4 + T\alpha^2 + K)\right)\eta = p(1)\,. \tag{2.11}$$

On eliminating $\eta$, using the second condition stated in (2.9), we obtain

$$\alpha\phi(1) - iY(\alpha,\omega)\,p(1) = 0\,, \tag{2.12}$$

where the wall admittance

$$Y(\alpha,\omega) = i\omega\left(m\omega^2 + \frac{1}{R}id\omega - \frac{1}{R^2}(B\alpha^4 + T\alpha^2 + K)\right)^{-1} \tag{2.13}$$

is the ratio of the wall velocity to the perturbation fluid pressure at the wall. Equations (2.10) and (2.12) restate the conditions (2.4) for the case $y = 1$; we have derived, for the upper wall, the fluid boundary conditions given in the previous section. The conditions at the lower wall are obtained in the same manner. Notably, there is no explicit reference to the wall displacement in these boundary conditions; the possibility of wall motion is incorporated indirectly through the use of a non-vanishing wall admittance. Equation (2.13) gives the specific form for the admittance when the wall is modelled as a spring-backed plate.

It remains now to specify the determination of the fluid pressure at the walls. The $x$-momentum equation for the fluid can be used, in conjunction with the first set of boundary conditions given in (2.4), to obtain the expressions

$$p = \frac{1}{i\alpha R}(D^2 - \alpha^2)\,D\phi \quad \text{, at } y = \pm 1\ . \tag{2.14}$$

Substitution into the second set of boundary conditions stated in (2.4) then gives constraints written entirely in terms of the disturbance amplitude $\phi$. (As mentioned

previously, we can think of the wall pressures as just linear functionals of $\phi$.) Using the $y$-momentum equation for the fluid, we obtain an alternative method for determining the wall pressures. When the disturbance profile is symmetric, the pressure profile $p$ is anti-symmetric, and so the $y$-momentum equation can be integrated across the channel to give

$$p(1) = -\alpha \int_0^1 \left( (\alpha U - \omega)\phi - \frac{i\alpha^2}{R}\phi \right) dy - \frac{i\alpha}{R} D\phi(1) \,. \tag{2.15}$$

The magnitude of the final term in the above expression is half that of the normal viscous stress acting at the walls. Consistent with the previously made assumption that the fluid stresses driving the wall motion can be approximated using the pressure alone, this term could be neglected. In fact, it follows directly from the first of the boundary conditions given in (2.9) that the normal stress is only of magnitude $O(\eta/R)$. Similarly, the other term in (2.15) that involves the factor $1/R$ may be dispensed with. Thus we can choose to calculate the pressure using the approximate expression

$$p(1) = -\alpha \int_0^1 (\alpha U - \omega)\, \phi dy \,. \tag{2.16}$$

If attention is restricted to disturbances for which $\phi$ is symmetric, then calculating the wall pressure via (2.15) or (2.16) has advantages over using (2.14), so far as the numerical solution of the Orr-Sommerfeld equation is concerned. This is explained in the next section.

### 2.2.3 Discretisation of the Orr-Sommerfeld equation

The Orr-Sommerfeld equation is solved numerically using a Chebyshev tau-method [43]. This section is mainly concerned with the discretisation process and the modifications required to consider compliant-walled channels, rather than the rigid-walled problems which have been tackled in previous studies. Once the discretisation has been obtained, the numerical methods then needed are the same for both rigid and compliant walls.

We restrict attention to the case of symmetric disturbances for which $\phi(y) = \phi(-y)$. (The numerical formulation is similar for anti-symmetric disturbances, except that the boundary conditions on $\phi$ would have to be implemented using (2.14) to determine the wall pressures. For symmetric disturbances we can choose the most convenient of either (2.14) or (2.15) in the corresponding pressure calculation.) The disturbance profile is approximated as a finite series of even Chebyshev polynomials,

$$\phi(y) = \frac{c_1}{2} + \sum_{k=2}^{N} c_k \, T_{2(k-1)}(y) \, . \tag{2.17}$$

This ensures that $\phi$ is symmetric about the channel centre-line. The symmetry incorporates two of the four boundary conditions to be imposed on $\phi$ ; if the conditions (2.3) or (2.4) hold at the upper wall then they will automatically hold at the lower wall as well. Before discretisation, the Orr-Sommerfeld equation is integrated indefinitely four times to give, (for symmetric $\phi$),

$$\begin{aligned} \omega \iint \phi - \alpha \iint U\phi + 2\alpha \iiint U'\phi - \alpha^2\omega \iiiint \phi + \alpha^3 \iiiint U\phi \\ + \frac{1}{iR}\left(\phi - 2\alpha^2 \iint \phi + \alpha^4 \iiiint \phi\right) + b_1 + b_2 y^2 = 0 \, , \end{aligned} \tag{2.18}$$

where $\iint \phi$ is shorthand for $\int_0^y \int_0^{y'} \phi(y'')\, dy''\, dy'$ etc., and $b_1$, $b_2$ are integration constants. This procedure is adopted because the integral operators take a more convenient form than the corresponding differential operators, when they are applied to the Chebyshev expansion for $\phi$. For instance, the second integral operator

$$\phi \;\rightarrow\; \iint \phi$$

becomes

$$c_k \;\rightarrow\; \frac{1}{8}\left(\frac{c_{k-1}}{(k-1)(2k-3)} - \frac{4c_k}{(2k-3)(2k-1)} + \frac{c_{k+1}}{(k-1)(2k-1)}\right)$$

for $k \geq 2$, when it is viewed as a matrix acting on the Chebyshev coefficients. The matrix forms of the other operators appearing in (2.18) are specified in the appendix of Bridges & Morris [44].

Substituting the Chebyshev expansion for $\phi$ into the left-hand side of the integrated Orr-Sommerfeld equation gives a series of the form

$$\sum_{j=1}^{N+3}\left(\sum_{k=1}^{N} M_{jk}c_k\right) T_{2(j-1)}(y) + \frac{3}{2}b_1 T_0(y) + \frac{1}{2}b_2 T_2(y) \tag{2.19}$$

(Note that $T_0(y) = 1$ and $T_2(y) = 2y^2 - 1$.) The matrix $\boldsymbol{M} = (M_{jk})$ collects together all the operators that appear in (2.18). It may be seen that the action of these operators generates a Chebyshev series which is of higher order than the series used to approximate $\phi$. We introduce the notation

$$\tau_i = \sum_{k=1}^{N} M_{(N+i)k}\, c_k \ , \ i = 1, 2, 3 \ , \tag{2.20}$$

for the coefficients of the three highest order terms. They can be interpreted as measuring the 'overspill' of the operators acting on $\phi$ into Chebyshev polynomials of higher order than those retained in the expansion for $\phi$.

Substitution of the expansion for $\phi$ into the boundary conditions at $y = 1$ yields conditions of the general form

$$\sum_{k=1}^{N} p_k c_k = \sum_{k=1}^{N} q_k c_k = 0. \tag{2.21}$$

The derivation of the specific forms taken by $p_k$, $q_k$ for the cases of both rigid and compliant-walled channels is postponed until later. For the present, all that need be noted is that the boundary conditions give two linear constraints on the Chebyshev coefficients $c_k$.

If we required that (2.19) vanished identically, we would obtain $N + 3$ conditions to be satisfied, since the coefficient of each Chebyshev polynomial would need to be set equal to zero. If the constraints derived from the boundary conditions were also imposed, this would give a total of $N + 5$ constraints on the $N + 2$ unknowns $b_1, b_2, c_1, \ldots, c_N$. The problem would be over-determined. To overcome this difficulty, the tau-method is applied. Relaxing the conditions on the coefficients $\tau_i$ of the three highest order Chebyshev polynomials, we obtain a soluble system. (The non-zero values of these tau-coefficients can then be determined after the reduced set of equations

has been solved. They give an indication of the extent to which the finite-order Chebyshev expansion obtained for $\phi$ fails to be an exact solution of the Orr-Sommerfeld equation. The expansion for $\phi$ is a solution to a modified version of (2.18) with the zero on the right-hand side replaced by $\tau_1 T_{2N}(y) + \tau_2 T_{2(N+1)}(y) + \tau_3 T_{2(N+2)}(y)$.) In practice, there is no need calculate the integration constants $b_1$, $b_2$, and so since they only appear in the two equations obtained by setting the coefficients of $T_0$, $T_2$ in (2.19) to zero, these equations can be neglected. Thus we arrive at a system of $N$ equations in the $N$ unknowns $c_1, \ldots, c_N$. This is comprised of the two constraints (2.21) derived from the boundary conditions, and the $N-2$ constraints obtained by setting the coefficients of $T_4, T_6, \ldots, T_{2(N-1)}$ to zero in (2.19). Formally, the system to be solved can be written as

$$\sum_{k=1}^{N} D_{jk} c_k = 0 \quad \text{for } j = 1, \ldots, N \tag{2.22}$$

where $D_{1k} = p_k$, $D_{2k} = q_k$ and $D_{jk} = M_{jk}$ for $j = 3, \ldots, N$.

The matrix $\boldsymbol{M}$ is a fourth-order matrix polynomial in $\alpha$; this follows from the manner in which $\alpha$ appears in (2.18). It will be shown below how the boundary conditions can be formulated so that the associated constraints (2.21) are at most fourth-order in $\alpha$. Thus, the matrix $\boldsymbol{D}$ can also be written as a fourth-order matrix polynomial. The system (2.22) can then be cast in the form

$$\left( \sum_{i=0}^{4} \alpha^i \boldsymbol{L}_i \right) \boldsymbol{c} = 0 \tag{2.23}$$

where $\boldsymbol{c} = (c_1, \ldots, c_N)^T$ is the vector formed by the Chebyshev coefficients of $\phi$ and the $\boldsymbol{L}_i$ are matrices independent of $\alpha$. This is seen to be a form of eigenvalue problem, from which possible values of $\alpha$ are determined. To obtain a non-trivial solution of (2.23), $\alpha$ must satisfy the condition

$$\det \left( \sum_{i=0}^{4} \alpha^i \boldsymbol{L}_i \right) = 0 \,. \tag{2.24}$$

Equation (2.24) gives a numerical approximation to the dispersion relation (2.5), obtained from the Chebyshev discretisation.

We now turn to the description of how the boundary conditions are incorporated in the constraints (2.21), via specific forms for the multipliers $p_k$ and $q_k$. For a rigid-walled channel the boundary conditions are simply $\phi(1) = D\phi(1) = 0$ . Substituting the Chebyshev expansion (2.17) into these conditions gives

$$\frac{c_1}{2} + \sum_{k=2}^{N} T_{2(k-1)}(1)\, c_k = \sum_{k=2}^{N} T'_{2(k-1)}(1)\, c_k = 0\,. \tag{2.25}$$

Using the facts that

$$T_{2k}(1) = 1\ ,\ T'_{2k}(1) = 4k^2 \tag{2.26}$$

we see that we can take

$$\begin{aligned} p_1 &= \frac{1}{2} \quad ,\quad q_1 = 0 \\ p_k &= 1 \quad ,\quad q_k = (k-1)^2\ ,\ k = 2, \ldots, N\,. \end{aligned} \tag{2.27}$$

as the multipliers in (2.21) when the walls are rigid. For a compliant-walled channel we have the boundary conditions (2.10), (2.12). Choosing to use the expression (2.16) for the wall pressure, and taking the wall admittance $Y$ to be given by (2.13), we can rewrite the second boundary condition as

$$S(\alpha,\omega)\phi(1) + \omega \int_0^1 (\alpha U - \omega)\, \phi \, dy = 0 \tag{2.28}$$

where

$$S(\alpha,\omega) = \frac{1}{R^2}(B\alpha^4 + T\alpha^2 + K) - (m\omega^2 + \frac{1}{R} i\omega d) \tag{2.29}$$

is a stiffness coefficient for the wall. Note that the expression equated to zero in the condition (2.28) is a fourth-order polynomial in $\alpha$. The other boundary condition for the compliant-walled channel is first-order in $\alpha$, whilst for the rigid-walled case both boundary conditions are independent of $\alpha$. Thus, whether we consider rigid or compliant walls, the highest order to which $\alpha$ appears in the boundary conditions is at most the same as that found in the Orr-Sommerfeld equation itself. So in either case, we can obtain the eigenvalue problem for $\alpha$ in the previously stated form (2.23). (If

instead of using (2.15) we had calculated the wall pressure using (2.14), the boundary conditions for the compliant case would become fifth-order in $\alpha$, with a consequent increase in computational difficulty.)

It is straightforward to determine the specific forms taken by the multipliers $p_k$, $q_k$ for the compliant-walled channel. The Chebyshev expansion for $\phi$ is substituted into the boundary conditions (2.10) and (2.28) to obtain conditions analogous to (2.25). The only new ingredient is that the relations

$$\begin{aligned} \int_0^1 T_{2k}(y)\,dy &= -\frac{1}{(4k^2-1)}\,, \\ \int_0^1 U(y)T_{2k}(y)\,dy &= \frac{6}{(4k^2-9)(4k^2-1)}\,, \quad (\text{ for } U = 1-y^2\,) \end{aligned} \tag{2.30}$$

are needed to evaluate the integral terms occuring in (2.28).

Having described all the components involved in the discretisation of the Orr-Sommerfeld equation, we can now turn to its solution. This amounts to solving the eigenvalue problem (2.23) to obtain the eigenvalues $\alpha$ and corresponding eigenvectors $\mathbf{c}$. The latter determine the disturbance profile $\phi$ via the Chebyshev expansion coefficients. The form of (2.23) is different from that usually found in matrix eigenvalue problems; the eigenvalue $\alpha$ appears to the fourth power rather than linearly as in the standard problem. Consequently, specialised techniques are needed for its solution. The particular numerical methods adopted are taken from the work of Bridges & Morris [44], to which reference should be made for further details. Their work presents global methods for obtaining, in a single calculation, all the eigenvalues $\alpha$ and eigenvectors $\mathbf{c}$ associated with specified values of the temporal frequency $\omega$ and Reynolds number $R$. Local methods for iteratively improving an initial estimate for a selected eigenvalue, together with techniques for determining the corresponding eigenvector, are also given.

It is, in fact, a major advantage of the chosen method of discretisation that it facilitates the simultaneous determination of all the eigenvalues associated with selected values of $\omega$ and $R$. This amounts to finding values of $\alpha$ from all branches

of the dispersion relation (2.5). Such a global determination of the eigenvalues is necessary to ensure that all possible instabilities are identified when the walls are compliant. Computationally less expensive methods, which find a single eigenvalue from an initial estimate, may fail to highlight the occurrence of instability. A good initial guess for $\alpha$ would be needed in order to get convergence to the value associated with a particular eigenmode. Such a guess would not be available if the existence of the mode was unsuspected.

### 2.2.4 Numerical results for Tollmien-Schlichting waves

This section contains some preliminary results that were obtained by solving the Orr-Sommerfeld equation using the numerical discretisation described above. It is mainly concerned with the Tollmien-Schlichting instability, though a few results are also mentioned for the additional modes of instability that can arise when the channel walls are made sufficiently compliant.

Before presenting new results, we first give some indication of how the numerical scheme can be checked against previous work. For the case of a rigid-walled channel, the numerically determined eigenvalues agree very closely with the results obtained by Bridges & Morris [44]. This is what would be expected; apart from some minor details, the same numerical methods are used in the present study. For instance, at a Reynolds number $R = 6000$ and frequency $\omega = 0.26$, the eigenvalue $\alpha = 1.00047 - i0.00086$ quoted by Bridges & Morris, which corresponds to an unstable Tollmien-Schlichting wave, is reproduced exactly. Checking the accuracy of the numerical methods for the case of a compliant-walled channel is less straightforward, since previously published studies either use a less general wall model or are known to be in error due to an incorrect formulation of the boundary conditions. Furthermore, no studies of spatially growing instabilities have been made; only the temporally growing formulation has received any attention. (This does not cause any difficulties in making comparisons

of neutral stability curves. For neutral stability, the results determined using spatial and temporal approaches should coincide.)

The largest set of results which can be directly compared with the present studies is included in the work of Green & Ellen [34]. These results are restricted to channels with the walls modelled as tensioned membranes. In a more recent study, Rotenberry [39] formulates the problem for the same wall model as is used in present work, but only gives results from the numerical solution of the Orr-Sommerfeld equation for a very limited range of wall parameters. (It should be noted that Rotenberry's interest was in non-linear rather than linear stability.) Agreement can be obtained between results determined using present methods and those given in the two studies mentioned directly above. For instance, points on the neutral stability curves given by Rotenberry can be reproduced. These curves show the stabilisation of Tollmien-Schlichting waves as the wall compliance is increased, for the simplistic situation where the wall motion is governed by a form of Hooke's law, *i.e.* the only non-zero wall parameter is the spring stiffness. The results given by Green & Ellen are arguably of greater physical interest, but can only be understood when flow-induced surface instabilities are considered. Accordingly, further discussion of Green & Ellen's results is deferred until later.

Figure 2.1 shows neutral stability curves for the Tollmien-Schlichting instability. They were computed using the local iteration scheme described by Bridges & Morris to determine eigenvalues from the discretised version of the dispersion relation (2.24). A further iteration loop was necessary to find the eigenvalues corresponding to neutral stability. The displayed results are for channels whose walls are modelled as untensioned spring-backed plates with no internal damping. Such a wall model was used by Carpenter & Garrad [6] in their investigation of the stability of Blasius flow over Kramer-type compliant surfaces. In fact, if the fluid is taken to be water and the channel half-width is 1 mm, then the curve for a non-dimensional spring stiffness of $K = 6 \times 10^7$ corresponds to a Kramer surface that has dimensional properties in

the range considered by these authors; in particular it closely matches a wall with Young's modulus $E = 0.5 \times 10^6$ N m$^{-2}$. It can be seen from Figure 2.1 that the effect of increasing wall compliance is to shrink the neutral stability curve, causing it to close into a single loop which then vanishes for sufficiently low values of the wall stiffness parameters $B$ and $K$. Unlike the situation for Blasius flow, the neutral stability loop does not appear to break into two pieces; there is no remnant of the rigid-wall curve for higher Reynolds numbers. This qualitative difference must be due to the different non-dimensionalisations of the wall properties that are used in Blasius and plane channel flow. For Blasius flow, the Reynolds number is varied through changes in the boundary layer thickness; different values of R correspond to different streamwise locations, the mean flow velocity being held constant. It follows that the effective non-dimensional spring stiffness increases with the Reynolds number, so at large enough values of R the wall behaves as if it were rigid. In contrast, for the case of channel flow, the fact that the Reynolds number is varied via changes in the mean flow velocity has the consequence that the effective wall parameters all decrease as R increases, with the exception of the wall mass which remains unchanged. (That this is the case can be seen directly from the non-dimensionalised wall equation (2.8).) Thus, the stabilising effect of the channel walls is enhanced at large Reynolds numbers and it is not surprising that the neutral curves become confined to finite values of $R$. Similar results were found by Hains & Price [30] for channels with walls modelled as tensioned membranes.

Figure 2.2 shows the effect of wall damping on the Tollmien-Schlichting mode. In agreement with earlier studies, it can be seen to be weakly destabilising. Anticipating the results of the analysis of flow-induced surface instabilities given later, Figure 2.3 displays neutral curves for travelling wave flutter. The wall parameters are the same as those taken in Figure 2.2, except that for the damped wall the level of damping has been reduced by a factor of a hundred. For the travelling wave flutter mode of instability the effect of the wall damping is reversed; it acts in the conventional

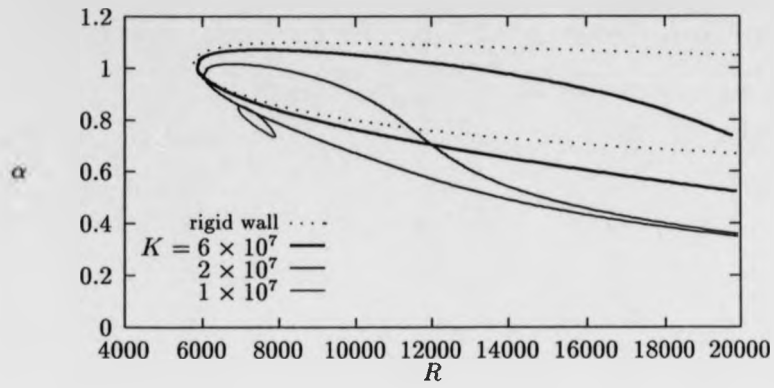


Figure 2.1: Neutral curves for the Tollmien-Schlichting instability. In all the compliant-walled cases $B = 4K$, $m = 2$, $T = d = 0$.

stabilising fashion. Furthermore, the effect is far stronger than that found for the Tollmien-Schlichting waves. Even for the low level of damping considered [2], the onset of travelling wave flutter is postponed to an appreciably higher Reynolds number.

Figure 2.4 shows the typical form that is found for the streamfunction profile of a stabilised Tollmien-Schlichting wave. For comparison, the profile of a wave identified as travelling wave flutter is displayed in Figure 2.5. Both profiles were computed by determining the Chebyshev eigenvector $\mathbf{c}$ associated with a selected eigenvalue found from the discretised dispersion relation (2.24). Further details of the numerical procedure involved are given by Bridges & Morris. It can be seen that the disturbance amplitude for the travelling wave flutter mode is largest in the vicinity of the wall. In contrast, the amplitude for the Tollmien-Schlichting wave is greatest at the channel centre. (Both profiles are normalised to unity at the channel centre $y = 0$.) It may also be noted that the phase velocity $c_r = \omega/\alpha_r$ is several times larger for

[2] Recall that the effective level of damping is determined by $d/R$.

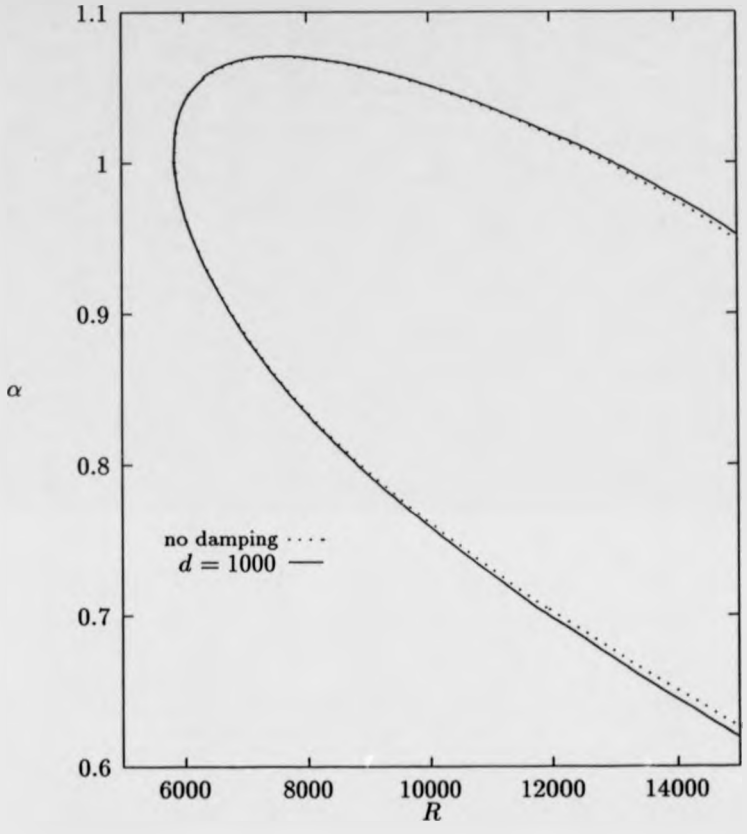


Figure 2.2: Neutral curves showing the effect of wall damping on the Tollmien-Schlichting instability. The other wall parameters are $K = 6 \times 10^7$, $B = 4K$, $m = 2$, $T = 0$.

the travelling wave flutter than for the Tollmien-Schlichting wave. This means that the critical layer, *i.e.* the point $y_c$ in the channel where $c_r = U(y_c)$, is closer to the channel centre for travelling wave flutter. Such differences help to distinguish other modes of instability from the Tollmien-Schlichting mode. However, it may be

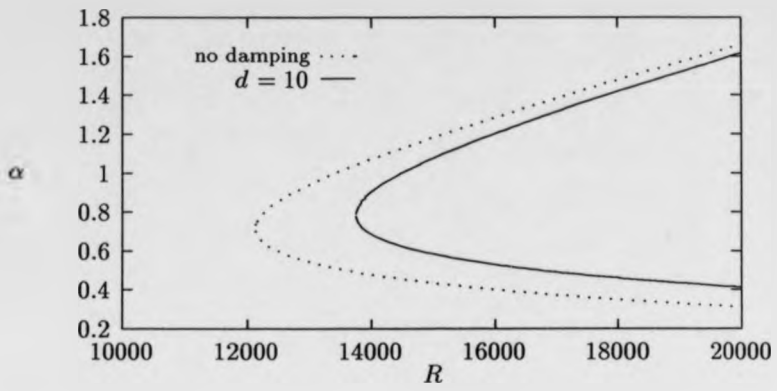


Figure 2.3: Neutral curves showing the effect of wall damping on travelling wave flutter. The other wall parameters are the same as in the previous figure.

difficult to isolate the various possible instabilities in the first place, without some prior knowledge of their characteristics. In particular, eigenvalues corresponding to travelling wave flutter are very hard to determine using local iteration schemes which refine an initial guess for the eigenvalue. It happens that many of the stable higher-order Tollmien-Schlichting modes present for both rigid and compliant-walled channels have phase velocities close to those of travelling wave flutter. Consequently, to obtain convergence to an eigenvalue associated with travelling wave flutter, rather than a nearby eigenvalue corresponding to a high-order Tollmien-Schlichting mode, a very accurate first estimate for the eigenvalue would be required. Such an estimate can be supplied by the approximate analytic theory presented in the next section for flow-induced surface instabilities. Alternatively, the difficulties with local iteration schemes can be circumvented by using a global scheme to obtain a simultaneous determination of all the eigenvalues associated with selected values of the disturbance frequency and Reynolds number. This section concludes with a brief look at some

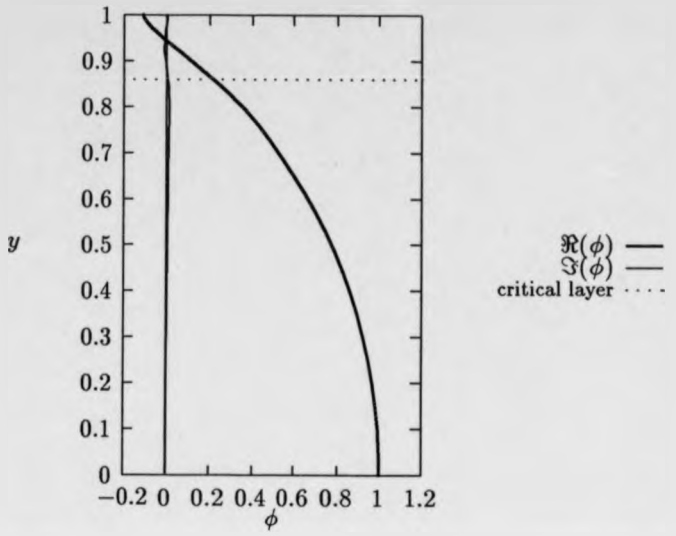


Figure 2.4: Eigenfunction profile of a Tollmien-Schlichting wave at $R = 10000$ for $\omega = 0.26$. The associated spatial eigenvalue is $\alpha = 0.99 + 0.014i$. The wall parameters are $K = 2 \times 10^7$, $B = 4K$, $m = 2$, $T = d = 0$.

examples of such eigenvalue spectra. The interpretation of the eigenvalues relies on the theory for flow-induced surface instabilities which is set out in the section that follows. In the absence of such a theory it would be difficult to make much sense of the numerical results.

Figure 2.6 displays eigenvalue spectra for both a compliant-walled channel and a rigid-walled channel, at the same values of $R$ and $\omega$. They were found by applying the companion matrix method described by Bridges & Morris to the eigenvalue problem (2.24). For the rigid-walled channel there is a single eigenvalue with negative imaginary part. This corresponds to an unstable Tollmien-Schlichting wave. The other rigid-wall eigenvalues are associated with higher-order Tollmien-Schlichting

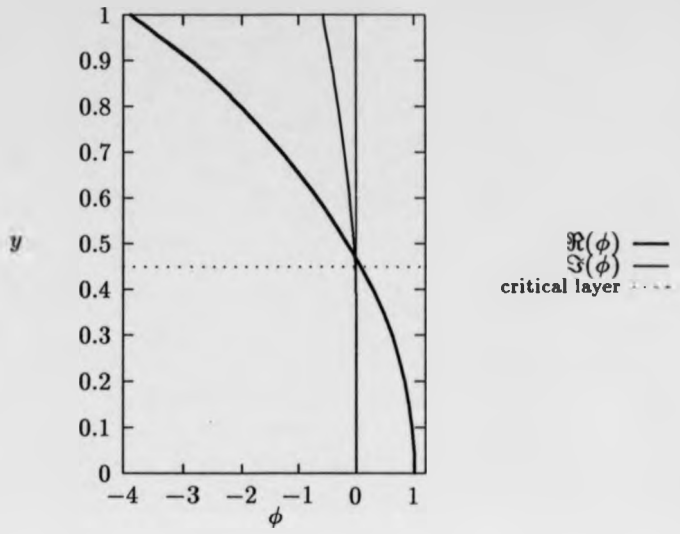


Figure 2.5: Eigenfunction profile for travelling wave flutter. The parameters are the same as for the previous figure except that $\omega = 0.26$ and $\alpha = 1.25 - 0.0003i$.

modes. These are all stable. For case of the compliant-walled channel, the previously unstable Tollmien-Schlichting wave can be seen to have been stabilised. The real part of its wavenumber is also changed. In contrast, wall compliance has very little effect on the higher-order modes. For the compliant-walled channel two additional eigenvalues have been introduced. These are labelled (A), (B) in Figure 2.6. The eigenvalue (A) corresponds to an upstream travelling wave. It can be shown to be related to the free waves that may propagate in either direction along the compliant walls in the absence of the fluid. The fact that both the real and imaginary parts of the eigenvalue (A) are negative suggests that such a wave would decay in its direction of propagation. Thus it may be classified as stable. (More precisely, it can be considered convectively stable if its group velocity rather than its phase velocity is known

to be negative.) The wave corresponding to the eigenvalue (B) is also related to the free waves that can be sustained in the channel walls. The real part of (B) is positive but relatively small, so the associated wave would travel with a large phase velocity in the downstream direction. From the imaginary part of (B), it can be seen that the wave is very nearly neutrally stable. In fact, it has a small positive imaginary part, which indicates stability.

Figure 2.7 shows the eigenvalue spectrum for a compliant-walled channel with the same wall properties as in the previous figure, but the selected frequency $\omega$ is higher. Again, there is a stable upstream-travelling wave, labelled (C). The eigenvalue labelled as (TWF) can be identified as travelling wave flutter. The corresponding wave profile has already been shown in Figure 2.5. The wave is unstable, though for the particular case shown the growth rate is quite small. At other parameter values, travelling wave flutter may be strongly unstable.

## 2.3 Flow-induced surface instabilities

This section is concerned with the development of an approximate analytic theory for the description of the flow-induced surface instabilities that may occur when the channel walls are made sufficiently compliant. The approach taken mirrors that used in previous work for the case of Blasius flow. In many respects the theory is more straightforward for the channel, owing to the relative simplicity of the mean flow profile $U = 1 - y^2$ as compared with that of Blasius flow. In particular, the evaluation of various integrals that arise in the calculation of the perturbation fluid pressure at the channel walls is less complicated.

In Section 2.2 the governing equation describing the wall motion was used to provide boundary conditions to be imposed on the fluid. In this way an eigenvalue problem arises in which the wall motion equation only appears implicitly. The equation of motion for the fluid, *i.e.* the Orr-Sommerfeld equation, plays the primary

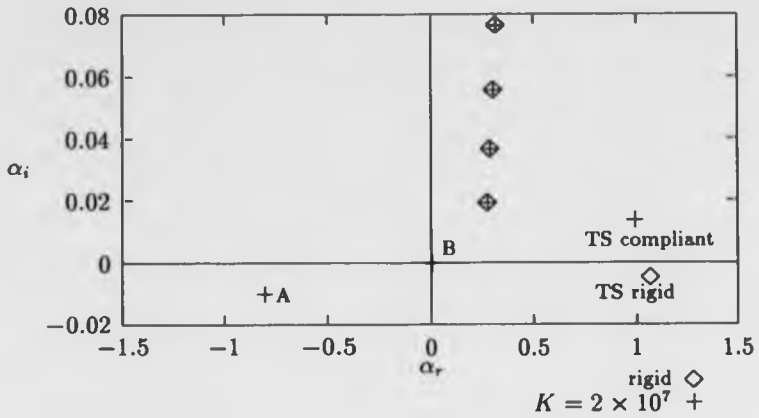


Figure 2.6: Eigenvalue spectra at $R = 10000$ for $\omega = 0.26$. In the compliant-walled case $B = 4K$, $m = 2$, $T = d = 0$.

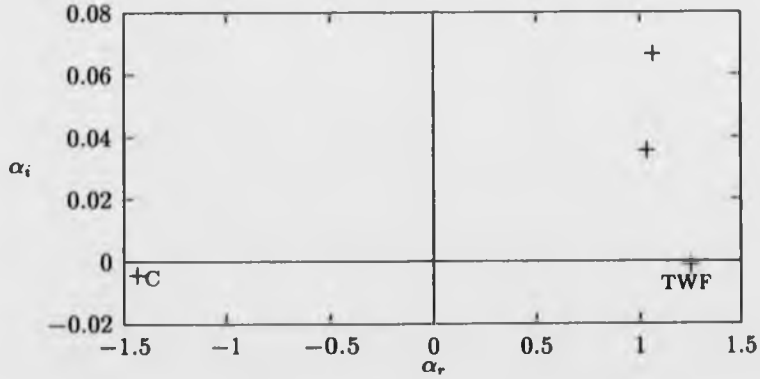


Figure 2.7: Eigenvalue spectrum at $R = 10000$ for $\omega = 1$. The wall parameters are the same as for the compliant-walled case shown in the previous figure.

role. For flow-induced surface instabilities the roles of the wall equations and the fluid equations can be reversed. Approximate expressions for the fluid pressure at the wall are first derived. These are then substituted into the wall motion equation to give a dispersion relation from which eigenvalues can be obtained directly. The computational requirements for determining eigenvalues in such a fashion are trivial compared with what is involved in solving the Orr-Sommerfeld equation using the numerical methods described previously.

Comparisons will be made between results determined via the approximate analytic theory and the corresponding results obtained from direct numerical solution of the Orr-Sommerfeld equation. For the travelling wave flutter instability there is particularly good quantitative agreement, which evidences the validity of the analytic approach. Aside from this, it could be argued that the most important achievement of the analytic theory lies in the insight it provides into the physical mechanisms that give rise to instability. As might be expected, the instabilities found for the channel flow display many of characteristics that have previously been identified in studies of Blasius flow. However, the relative simplicity of the analytic theory for the channel facilitates the examination of behaviour which is difficult to discern in the Blasius case. In particular, the results obtained for the onset of divergence have some interesting implications.

### 2.3.1 Potential theory

The divergence instability found in Blasius flow over a flexible wall can be successfully modelled using potential theory to describe the mean flow. Neither viscosity nor the presence of a boundary shear layer are necessary for understanding the instability mechanism. Potential theory is also a useful starting point for the description of travelling wave flutter. The shear layer just provides a means of perturbing, in a destabilising fashion, the neutrally stable waves which are found in a potential flow.

However, for plane channel flow there is no clear sense in which the mean flow can be split into regions of potential flow and thin boundary layers. The parabolic profile of the flow may need to be accounted for even in a first approximation. Nevertheless, in order to highlight differences between the cases of Blasius flow and plane channel flow, we begin the study of the flow-induced surface instabilities with an account of the results that can be derived assuming a potential mean flow.

For potential flow we have a constant (dimensional) velocity $U_p$ across the whole of the channel. Assuming a normal mode form for the disturbances, it is straightforward to show that the fluid perturbation pressure at the upper wall is given by

$$p(1) = \alpha \tanh \alpha \, (1 - c)^2 \eta \tag{2.31}$$

where $p$, $\eta$ are defined as previously, except that $U_p$ rather than the centre-line velocity is used in their non-dimensionalisation, and $c = \omega/\alpha$ is the phase velocity of the waves. As previously, we only consider disturbances which are symmetric across the channel, *i.e.* disturbances for which $v(y) = v(-y)$, where $v$ is the profile of the normal component of the fluid perturbation velocity. (The anti-symmetric case is similar; we would just need to replace $\tanh \alpha$ by $\coth \alpha$ in (2.31).)

In order to facilitate comparisons with the results obtained in the next section using inviscid theory, we write (2.31) as

$$p(1) = \alpha^2 \, (1 - c)^2 \eta + O(\alpha^4) \tag{2.32}$$

and retain only the lowest order term in $\alpha$. This can be justified if we restrict attention to disturbances that have sufficiently long wavelength, but it is not strictly necessary to resort to such an approximation. Grotberg & Reiss [27] undertook an analysis which retained, implicitly, an expression for the wall pressure that is fully equivalent to that given in equation (2.31). They also considered the case of anti-symmetric disturbances. However, the compliant channel walls were modelled in a slightly different manner, since there was no linear tension term included in their wall

motion governing equation. Of greater significance, from the present point of view, is the fact that Grotberg & Reiss were unable to proceed to consider a parabolic mean flow profile. Their study was limited to the case of potential mean flow, apart from the crude account of fluid viscosity that they gave by incorporating a linear Darcy friction factor. Inevitably, there is some overlap between the potential theory results reported in the present section and those that were presented by Grotberg & Reiss. Our excuse for risking some replication of the earlier published work is that it is convenient to obtain potential flow results on the basis of the same long wavelength approximation that will later be utilised in developing an inviscid shear layer theory. Differences between the potential and shear layer theory results can then be discussed in a more succinct fashion. It should be noted, though, that since the results derived from the shear layer theory take direct account of the parabolic profile of plane channel flow, they can viewed as correcting, if not superseding, any results obtained entirely on the basis of potential theory.

Substitution of the approximate expression (2.32) for the wall pressure into the wall equation (2.6) yields

$$m\left(c^2 - c_0^2\right) + (1-c)^2 + i\,(c/\alpha)\,\bar{d} = 0 \tag{2.33}$$

where

$$c_0 = \left[\frac{1}{mU_p^2}\left(\bar{B}\alpha^2 + \bar{T} + \frac{\bar{K}}{\alpha^2}\right)\right]^{\frac{1}{2}} \tag{2.34}$$

is the free wave speed for the wall at a given wavenumber $\alpha$, *i.e.* the speed at which waves would propagate along the wall in the absence of the fluid (and wall damping). The wall mass $m$ is non-dimensionalised as in (2.7), but the other wall parameters are treated in a different fashion, since viscosity is no longer inherent in the problem. Thus we define

$$\bar{d} = \frac{d^*}{\rho U_p}\,,\quad \bar{B} = \frac{B^*}{\rho h^3}\,,\quad \bar{T} = \frac{T^*}{\rho h}\,,\quad \bar{K} = \frac{K^* h}{\rho}\,. \tag{2.35}$$

The damping parameter $\bar{d}$ is non-dimensional, but all the other quantities have the dimensions of a squared velocity. This is convenient for obtaining expressions for the

critical velocities that determine the onset of instability.

Equation (2.33) is a dispersion relation, which can be analysed to obtain stability boundaries. The analysis is simpler for the case of temporal instabilities, for which $c$ is allowed to be complex-valued whilst $\alpha$ is kept real. (For relatively weak instabilities, conversions between temporal and spatial growth rates may be made using the results of Gaster [45].) When there is no wall damping, (2.33) is a quadratic in $c$ with real coefficients. Its two solutions are

$$c = \frac{1}{m+1}(1 \pm r) \tag{2.36}$$

where

$$r = (m(m+1))^{\frac{1}{2}} \left(c_0^2 - \frac{1}{m+1}\right)^{\frac{1}{2}} .$$

Thus we get instabilities if

$$c_0^2 \leq \frac{1}{m+1} \tag{2.37}$$

which using (2.34) gives the condition

$$U_p^2 \geq \left(1 + \frac{1}{m}\right)\left(\bar{B}\alpha^2 + \bar{T} + \frac{\bar{K}}{\alpha^2}\right) . \tag{2.38}$$

So there is instability provided $U_p \geq U_f$ , where

$$U_f^2 = \min_{\alpha}\left[\left(1 + \frac{1}{m}\right)\left(\bar{B}\alpha^2 + \bar{T} + \frac{\bar{K}}{\alpha^2}\right)\right] . \tag{2.39}$$

The subscript $f$ denotes the identification of this instability as flutter instability. It has also been described as a Kelvin-Helmholtz instability by Benjamin [4] and Landahl [5], owing to its resemblance to the well-known shear-flow instability. For flows with $U_p < U_f$ the two solutions given in (2.36) always correspond to neutrally stable waves; one propagates in the downstream direction and the other either propagates upstream or more slowly downstream. These waves are just modified versions of the free waves which can travel in either direction in the wall when the fluid is absent. For flow velocities greater than $U_f$, there is a range of wavenumbers for which the fluid pressure exerted on the wall cannot be balanced by the effective wall stiffness,

unless the wave velocity is allowed to be complex. This is illustrated in Figure 2.8, which plots the variation of the wave velocities with the wavenumber. The imaginary parts of the wave velocities are not displayed where they are zero. For comparison, Figure 2.9 shows the neutrally stable waves found for all wavenumbers when the flow speed is less than $U_f$. The question of the physical realisability of the flutter instability is addressed later.

If wall damping is introduced, then for small values of $\bar{d}$ we obtain the solutions

$$c = \frac{1}{m+1}\left(1 \pm r - \frac{i\bar{d}}{2\alpha}\left(1 \pm \frac{1}{r}\right)\right) . \tag{2.40}$$

In this case instability sets in when $r = 1$, which implies that $c = 0$. Thus, the instability takes the form of a standing wave at its onset. From the dispersion relation (2.33), it can be seen that waves with $c = 0$ are only possible if there is a solution to

$$c_0^2 = \frac{1}{m} \tag{2.41}$$

for some value of the wavenumber $\alpha$. This yields the condition that $U_p \geq U_d$, where

$$U_d^2 = \min_{\alpha}\left[\bar{B}\alpha^2 + \bar{T} + \frac{\bar{K}}{\alpha^2}\right] . \tag{2.42}$$

The subscript $d$ indicates that the instability can be identified as divergence.

Apart from a constant multiple, the functions to be minimised in the expressions for $U_d$ and $U_f$ are the same. For convenience, we define the quantity

$$U_0 = \left(\min_{\alpha}\left[\bar{B}\alpha^2 + \bar{T} + \frac{\bar{K}}{\alpha^2}\right]\right)^{\frac{1}{2}} . \tag{2.43}$$

This is $\sqrt{m}$ times the minimum of the dimensional free wave speed. In effect, it characterises the lowest possible stiffness of the walls. It is simple to show that the minimum occurs for the non-dimensional wavenumber

$$\alpha_c = \left(\frac{\bar{K}}{\bar{B}}\right)^{\frac{1}{4}} \tag{2.44}$$

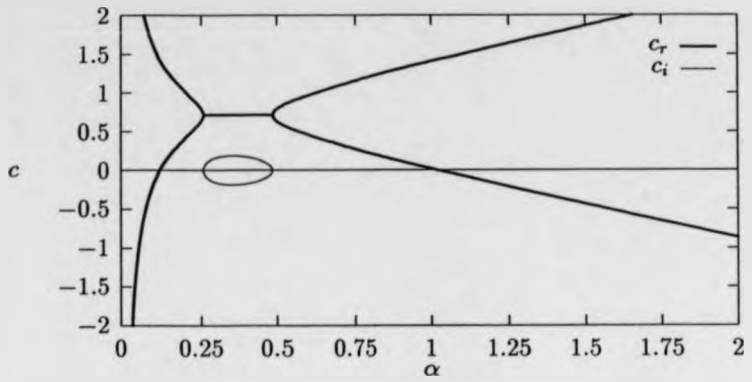


Figure 2.8: Onset of flutter instability from potential theory. The wall parameters are $\bar{B} = 4U_0^2$, $\bar{K} = U_0^2/16$, $\bar{T} = 0$, $m = 0.4$, $\bar{d} = 0$. Potential flow speed $U_p = 1.1\,U_f$.(The chosen wall parameters yield $\alpha_c^2 = 1/8$.)

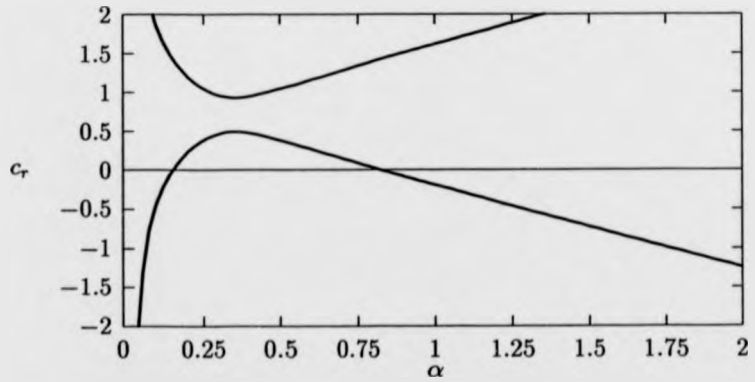


Figure 2.9: Neutrally stable waves from potential theory. The wall parameters are the same as in the previous figure. Flow speed $U_p = 0.9\,U_f$.

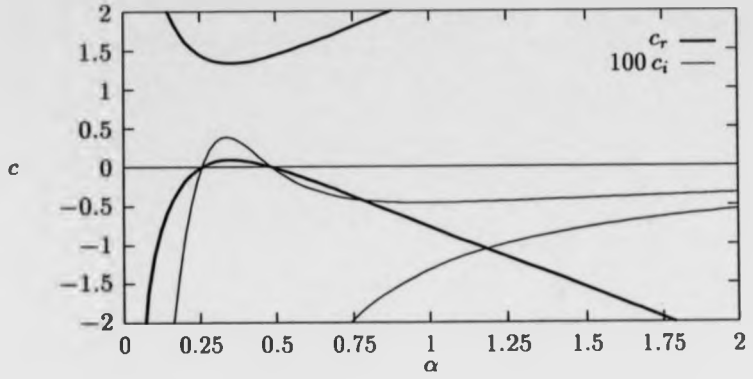


Figure 2.10: Onset of divergence instability from potential theory. The wall parameters are the same as before, except that $\bar{d} = 0.025$. Potential flow speed $U_p = 1.1\,U_d$.

and takes the value

$$U_0 = \left(2\sqrt{\bar{B}\bar{K}} + \bar{T}\right)^{\frac{1}{2}} = \left(\frac{2\sqrt{B^* K^*} + T^*}{\rho h}\right)^{\frac{1}{2}} . \tag{2.45}$$

In terms of this, the critical velocities can be written as

$$U_f = \left(\frac{1}{m} + 1\right)^{\frac{1}{2}} U_0 \ , \ \ U_d = U_0 \, . \tag{2.46}$$

It is clear that $U_d < U_f$, so divergence will always set in at a lower flow speed than the flutter instability. (Note that the dimensional velocity $U_0$ could be used to provide a non-dimensionalisation of the wall properties and mean flow speed. This is reflected in the characterisation of these quantities in the figures displayed in this section and the next.)

For flow velocities $U_p$ slightly greater than $U_d$, the divergence instability takes the form of a slowly travelling wave, which propagates in the downstream direction. This is illustrated in Figure 2.10. In the lower of the two curves that show the variation of

the phase velocity $c_r$, there is a small range of wavenumbers for which $c_r$ is positive. The corresponding curve for the growth rate $c_i$ is positive over the same range of wavenumbers.

The physical characteristics of the divergence instability, in particular its absolute nature, are discussed in [16] for the case of flow over a flat plate. (We do not repeat the details here, except to remark that modelling divergence using our present methods gives an incomplete description. When a compliant wall of finite rather than infinite streamwise extent is studied, damping no longer plays such a crucial role in creating the instability; it can be shown that the effects of the leading and trailing edges of the wall may lead to destabilisation in the absence of any wall damping [46], [47].) From the present studies, it would seem that no new ingredient is introduced when the geometry is changed from a flat plate to a channel. It will be shown in the next section that, for divergence, there is a consistency between results obtained from potential theory and those derived from a more realistic inviscid shear-flow theory. Thus it can be argued that potential theory provides the basis for understanding the instability, just as for the case of Blasius flow. Divergence arises when the flow is so fast that the internal restorative forces in the walls are overwhelmed by the perturbation pressure forces exerted by the fluid. Details concerning the mean velocity profile and any viscosity related effects are inessential to the description of the instability mechanism.

In their general form, the results obtained using potential flow in a channel are similar to those found for potential flow over a flat plate (for instance, as presented in [7]). The occurrence of upstream and downstream-travelling waves, the prediction of flutter instability, and the appearance of divergence instability when wall damping is introduced, are all common to both cases. However, as remarked at the outset of this section, it is not obvious that results from potential theory for the channel will provide good guidance to what happens when the mean flow is modelled more realistically. It will be shown in the next section that the broad features found using potential theory are retained. Nevertheless, so far as the flutter instability is

concerned, the dispersion relation (2.33) turns out to provide an inadequate approximation to the relation which holds when the parabolic profile of the flow in the channel is taken into account. This in itself would be of little consequence, since it will be shown that the flutter instability does not arise as a distinct instability when travelling wave flutter is brought into consideration. But travelling wave flutter instability cannot be described using potential theory as a starting point. Thus we now turn to the study of flow-induced instabilities using an inviscid shear-layer, rather than a potential theory, model of the mean flow.

### 2.3.2 Inviscid theory

Inviscid perturbations from the mean flow $U = 1 - y^2$ are governed by Rayleigh's equation

$$(U - c)(D^2 - \alpha^2)\phi - U''\phi = 0\,, \tag{2.47}$$

where, as before, $\phi$ is the profile of the disturbance streamfunction. There are two linearly independent solutions, which can be obtained via expansion in the wavenumber $\alpha$,

$$\phi_1 = (U-c)\left(1 + \alpha^2 \int_{y_0}^{y} \frac{1}{(U-c)^2}\,dy \int_{y_0}^{y} (U-c)^2\,dy + \cdots\right) \tag{2.48}$$

$$\begin{aligned}\phi_2 = {} & (U-c)\left(\int_{y_0}^{y} \frac{1}{(U-c)^2}\,dy\right. \\ & \left. + \alpha^2 \int_{y_0}^{y} \frac{1}{(U-c)^2}\,dy \int_{y_0}^{y} (U-c)^2\,dy \int_{y_0}^{y} \frac{1}{(U-c)^2}\,dy + \cdots\right)\,. \end{aligned} \tag{2.49}$$

These expressions were first obtained by Heisenberg [48]. The lower limit $y_0$ in the integrals is arbitrary. The path of integration needs to be specified when there is a critical point, *i.e.* when $0 < c_r < 1$, where $c_r$ is the phase speed of a near-neutral wave. Further details are given in the next section. If we choose to take $y_0 = 0$, then the two solutions $\phi_1$, $\phi_2$ correspond to symmetric and antisymmetric disturbances

respectively. Continuing to concentrate on the symmetric case, we take

$$\phi = A\,(U-c)\left(1+\alpha^2\int_0^y \frac{1}{(U-c)^2}\,dy\int_0^y (U-c)^2\,dy+\cdots\right). \tag{2.50}$$

where $A$ is some constant. For inviscid disturbances there is only a single boundary condition on the fluid at each wall. At the upper wall this takes the form

$$\phi(1) = c\,\eta\,. \tag{2.51}$$

The constant $A$ can thus be determined as

$$A = \frac{-\eta}{1+\alpha^2\int_0^1 1/(U-c)^2\,dy\int_0^y (U-c)^2\,dy+\cdots}\,. \tag{2.52}$$

Using the $y$-momentum equation for the inviscid disturbances, the perturbation fluid pressure at the upper wall can be calculated from

$$p(1) = -\alpha^2\left(\int_0^1 (U-c)\phi\,dy\right). \tag{2.53}$$

Hence we obtain

$$p(1) = \alpha^2 J(\alpha,c)\,\eta \tag{2.54}$$

where

$$J(\alpha,c) = \frac{\int_0^1 (U-c)^2\,dy+\alpha^2\int_0^1 (U-c)^2\,dy\int_0^y 1/(U-c)^2\,dy\int_0^y (U-c)^2\,dy+\cdots}{1+\alpha^2\int_0^1 1/(U-c)^2\,dy\int_0^y (U-c)^2\,dy+\cdots}\,. \tag{2.55}$$

For small enough values of $\alpha$, and after some manipulation of the integrals, the expression for the quantity $J$ can be expanded[3] to give

$$J(\alpha,c) = J_0(c)+\alpha^2 J_1(c)+\cdots \tag{2.56}$$

where the expansion coefficients are given by

$$J_0(c) = \int_0^1 (U-c)^2\,dy \tag{2.57}$$

$$J_1(c) = -\int_0^1 \frac{1}{(U-c)^2}\,dy\left(\int_0^y (U-c)^2\,dy\right)^2. \tag{2.58}$$

[3]Such an expansion cannot always be relied upon, as will be shown later.

Using the parabolic profile of $U$, the integral for $J_0$ is simple to evaluate, giving

$$J_0(c) = c^2 - \frac{4}{3}c + \frac{8}{15} \tag{2.59}$$

The integral defining $J_1$ is also straightforward to determine, though account needs to be made of the singularity which occurs when there is a critical point. The detailed form of the integral is given later.

Substituting the expression for the wall pressure into the wall equation (2.6) gives the dispersion relation

$$m\left(c^2 - c_0^2\right) + J(\alpha, c) + i\,(c/\alpha)\,\bar{d} = 0\,. \tag{2.60}$$

The free wave velocity $c_0$ and wall damping coefficient $\bar{d}$ are defined in the same way as in the previous section, except that $U_p$ is now replaced by $U_m$. The definitions of the other wall parameters are unchanged. For small $\alpha$ we can approximate $J$ by $J_0$ in the dispersion relation. (At this level of approximation the effects of the critical layer are neglected; they only appear when $J_1$ is included.) The stability analysis previously conducted for potential theory can then be repeated using (2.60) rather than (2.33). When there is no wall damping we obtain the solutions

$$c = \frac{1}{m+1}\left(\frac{2}{3} \pm r\right) \tag{2.61}$$

where we now have

$$r = (m(m+1))^{\frac{1}{2}}\left(c_0^2 - \frac{4}{45}\frac{6m+1}{m(m+1)}\right)^{\frac{1}{2}}\,.$$

As with the potential theory, there is instability provided $U_m \geq U_f$, where this time

$$U_f = \frac{3}{2}\left(\frac{5(m+1)}{6m+1}\right)^{\frac{1}{2}} U_0\,. \tag{2.62}$$

The quantity $U_0$ is the same as before, as is the corresponding critical wavenumber $\alpha_c$. Figure 2.11 displays solutions given by (2.61) for a flow speed greater than the critical velocity $U_f$. There is no obvious qualitative change from the results shown in Figure 2.8.

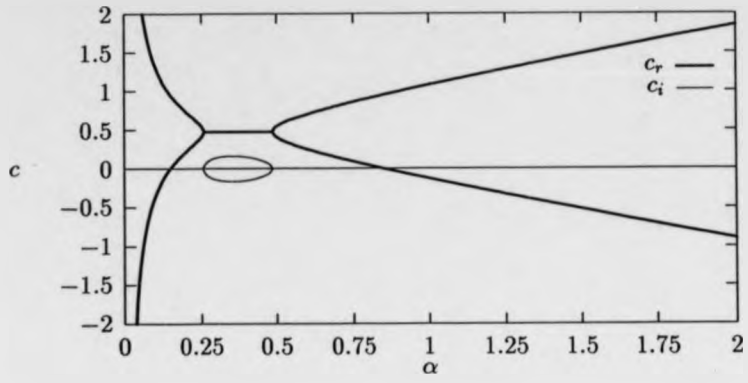


Figure 2.11: Onset of flutter instability from inviscid theory. The wall parameters are $\bar{B} = 4\,U_0^2$, $\bar{K} = U_0^2/16$, $\bar{T} = 0$, $m = 0.4$, $\bar{d} = 0$. Mean flow speed $U_m = 1.1\,U_f$.

If wall damping is introduced, the solutions (2.61) are perturbed in the same manner as found in the potential theory. For small values of the damping coefficient $\bar{d}$ we have

$$c = \frac{1}{m+1}\left(\frac{2}{3} \pm r - \frac{i\bar{d}}{2\alpha}\left(1 \pm \frac{2}{3r}\right)\right) . \tag{2.63}$$

So the divergence instability again sets in when $c = 0$. Using this, it is straightforward to show that the flow is unstable for $U_m \geq U_d$, where

$$U_d = \left(\frac{15}{8}\right)^{\frac{1}{2}} U_0 . \tag{2.64}$$

From the results (2.62) and (2.64) we have

$$U_f = \left(\frac{6(m+1)}{6m+1}\right)^{\frac{1}{2}} U_d \tag{2.65}$$

so it is clear that $U_f > U_d$ . Divergence still sets in before the flutter instability. Figure 2.12 illustrates the situation for a flow speed slightly greater than $U_d$. Just as for the onset of flutter instability, the qualitative features found from potential-theory are retained in the results of the inviscid theory. Moreover, for the branch of

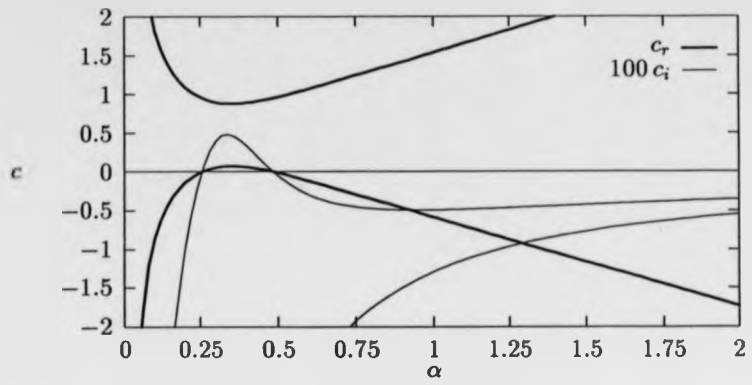


Figure 2.12: Onset of divergence instability from inviscid theory. The wall parameters are the same as in the previous figure, except that $\bar{d} = 0.025$. Mean flow speed $U_m = 1.1U_d$.

solutions associated with divergence, there is some quantitative agreement between the results shown in Figure 2.12 and their potential theory counterparts displayed in Figure 2.10. The range of unstable wavenumbers is the same in both cases. In contrast, it can be seen that the potential theory gives a poor prediction of the phase speeds on the upper branch of solutions.

For the special case of a channel with compliant walls described as unsupported tensioned membranes, *i.e.* when $K^* = B^* = 0$, $T^* \neq 0$, $m^* \neq 0$, expressions equivalent to (2.62), (2.64) were noted by Green & Ellen [34]. With such a restricted wall model, the dimensional free-wave speed takes the constant value $\sqrt{T^*/m^*}$, independent of the wavenumber. According to the inviscid theory, there is then no specific critical wavenumber at which instability sets in; both flutter and divergence become unstable for all disturbance wavelengths as soon as the respective mean flow onset velocity has been exceeded. It would appear that Green & Ellen were unable to use

their expressions for onset velocities[4] to provide a detailed analysis of the results they obtained by direct numerical solution of the Orr-Sommerfeld equation. This shortcoming stems from the fact that they did not go on to study the onset of travelling wave flutter instability. As will be discussed later, their numerical results are more readily interpreted once this further instability has been taken into account.

If we identify the constant velocity $U_p$ from potential theory with the root mean square of the real flow velocity, *i.e.* take

$$U_p^2 = \frac{1}{h}\int_0^h U^{*2}\, dy^* = \frac{8}{15} U_m^2 \tag{2.66}$$

then the results stated in (2.46) and (2.64) for the divergence onset velocities agree; in this respect the potential and inviscid theories are consistent. The same is not true for the flutter instability. As the plate mass $m$ is made smaller and smaller, it can be seen from (2.46) that the critical velocity $U_f$ found from potential theory increases without limit. (Note that $U_0$ is defined to be independent of the plate mass.) However, the result (2.62) from the inviscid theory gives a finite limit for $U_f$ as the plate mass approaches zero; the flutter instability persists. It turns out that when the effects of the critical layer in the fluid are taken into account, the onset of flutter is superseded by travelling wave flutter, but the persistence of instability for vanishingly light plates remains.

### 2.3.3 Travelling wave flutter

We now study the effect of including the critical point in the inviscid theory. For neutral disturbances with $0 < c < 1$ there are two symmetrically positioned points $y_c = \pm\sqrt{1-c}$ in the channel where $U(y_c) = c$. Each is a singular point of Rayleigh's equation. These points show up as logarithmic singularities in the integrals defining

[4] In order to facilitate comparisons with the Tollmien-Schlichting instability, they gave their results in terms of critical Reynolds numbers. Since the Reynolds number is varied only through the centre-line velocity of the mean flow, this is equivalent to giving critical flow velocities.

the solution for $\phi$ that was considered in the previous section. Although this solution will not be valid in the immediate vicinity of a critical point, it still holds elsewhere, provided the path in the integrals is suitably deformed around the critical point. By matching the solutions of the inviscid problem to solutions of the Orr-Sommerfeld equation in the limit of large Reynolds numbers, the appropriate path can be determined. Near each critical point, the integral path needs to be indented away from the real axis; below it if $U'(y_c) > 0$ and above it for $U'(y_c) < 0$. (For near-neutral disturbances the situation remains the same; the path still needs to be taken above or below the critical points – which are now placed off the real axis – in a corresponding fashion.) This procedure only gives acceptable results provided there is sufficient separation between the critical layers and the viscous layers at the walls. For small values of $c$, the critical points approach the walls and the theory breaks down.

In the calculation of the fluid perturbation pressure at the upper wall, taking account of the critical point in the manner described above introduces a non-zero imaginary part into the quantity $J(\alpha, c)$ occurring in equation (2.54). This stems from the singularity at $y_c = \sqrt{1 - c}$ in the integral for the expansion coefficient $J_1(c)$ defined in (2.58). The imaginary part of $J$ gives rise to a phase difference between the wall pressure and wall displacement, which allows the fluid to do work on the wall. Thus there is the possibility of a destabilising energy transfer to the wall. Such a mechanism was first identified for water waves by Miles in a series of papers beginning with [49]. The same mechanism was shown by Benjamin [4] to apply in the case of flow over a compliant wall. More recently, Carpenter & Garrad [7] have introduced the term travelling wave flutter to describe the associated instability.

To study the onset of travelling wave flutter instability we first solve the dispersion relation (2.60) in the same way as in the last section, *i.e.* by using the approximation $J = J_0$. If $U_m < U_f$ and there is no wall damping, this gives two neutrally stable solutions. We can then consider how these solutions are perturbed when we replace

$J_0$ by $J_0 + \alpha^2 J_1$. The solutions are shifted from $c$ to $c + \Delta c$, where

$$\Delta c = \frac{-\alpha^2 J_1}{2\left((m+1)c - \frac{2}{3}\right)}. \tag{2.67}$$

It will be shown later that if $0 < c < 1$ then the imaginary part of $J_1$ is negative. Thus we get instability provided we also have $c > 2/3(m+1)$. From the form of the solutions given in (2.61) it can be seen that this further condition holds for one of the waves but not for the other. Only the wave which travels the fastest in the downstream direction can become unstable; the other wave is stabilised if it propagates downstream and unaffected if it propagates upstream. The onset of the instability is thus determined by the condition that there is a wave with $c = 1$. (The stability boundary at $c = 2/3(m+1)$ coincides with that of the flutter instability. As will be seen below, it corresponds to a higher flow velocity than that needed to destabilise travelling wave flutter.) Substituting $c = 1$ into the dispersion relation (2.60), with $J$ replaced by $J_0$, gives the condition

$$c_0^2 = 1 + \frac{1}{5m} \tag{2.68}$$

This is only possible provided $U_m \geq U_t$, where

$$U_t = \left(\frac{1}{m + \frac{1}{5}}\right)^{\frac{1}{2}} U_0 . \tag{2.69}$$

Using the results (2.64) and (2.69) for the divergence and travelling wave flutter critical velocities, it is straightforward to show that divergence sets in at a lower flow velocity if the plate mass satisfies $m < 1/3$, whilst travelling wave flutter sets in first if $m > 1/3$. This relationship between the critical velocities is much simpler than the corresponding one for Blasius flow [7].

For vanishingly small values of the plate mass $m$, the critical velocity $U_t$ tends to a finite limit, so the travelling wave flutter instability persists. This is in apparent contrast to the situation found in Blasius flow [7], where the corresponding formula is

$$U_t^B = \left(\frac{1}{m}\right)^{\frac{1}{2}} U_0 . \tag{2.70}$$

In this case the instability sets in at indefinitely high flow speeds as $m$ decreases to zero. The difference between the two cases is connected with the assumption that potential theory provides a good first approximation for the flow over a flat plate. This assumption is not justified for the channel flow. In previous studies of Blasius flow, the critical layer has been accounted for by perturbing the expression for the wall pressure from the result given by potential theory. If we assumed that the critical layer could be treated in the same way for channel flow, *i.e.* by perturbing the expression (2.31), then the formula obtained for the critical velocity would be identical to the one given for Blasius flow. However, when the parabolic profile of the channel flow is considered, an effective mass is contributed by the fluid. This appears as the fraction 1/5 in the denominator in (2.69).

These remarks suggest that a re-examination of the situation for Blasius flow may be in order. By analogy with the result found for channel flow, it could be anticipated that the effect of explicitly considering the profile of the mean flow would be to introduce a fluid mass to be added to the wall mass in (2.70). The fact that this is actually the case is implicit in the results of Carpenter & Gajjar [50]. Restricting attention to two-dimensional disturbances, and only retaining inviscid terms, their expression [3.32] for the fluid perturbation pressure at the wall can be written as

$$p_w^B = -\left(\alpha(1-c)^2 + \alpha^2\left[1 - \frac{1}{H} - 2(1-c)\right] - \alpha^2(1-c)^2 I_\infty\right)\eta \qquad (2.71)$$

where $H$ is the boundary layer momentum thickness[5] and the term involving the quantity $I_\infty$ accounts for the phase shift due to the critical layer. The first term in (2.71) gives the pressure according to potential theory. The terms enclosed in the square brackets can be interpreted as the mean flow profile correction to the result given by potential theory. For comparison, we can split the corresponding expression for channel flow in the same way:

$$p_w = \left(\alpha^2(1-c)^2 + \alpha^2\left[\frac{1}{5} - \frac{2}{3}(1-c)\right] + \alpha^4 J_1(c)\right)\eta\,. \qquad (2.72)$$

[5] $H = 2.591$ for the Blasius velocity profile.

(The sign difference in the expressions (2.71) and (2.72) simply reflects the fact that we are considering the wall above the fluid for the channel, whilst for the Blasius case the wall is taken to be below the fluid.) Using the fact that travelling wave flutter instability sets in when $c = 1$, it can be seen that the constant $1 - 1/H$ plays a similar role in (2.71) to the constant $1/5$ in (2.72). It follows that

$$U_t^B = \left( \frac{1}{m + 1 - \frac{1}{H}} \right)^{\frac{1}{2}} U_0 \,. \tag{2.73}$$

gives the onset velocity of travelling wave flutter for Blasius flow when the mean flow profile correction to the wall pressure is taken into consideration. Thus for Blasius flow it can also be argued that travelling wave flutter persists for vanishingly light plates. Whether this result is physically significant, and consequently whether (2.73) is a genuine improvement on (2.70), will depend on the range of relative magnitudes for $m$ and $1 - 1/H$ that can occur in practice. For the wall parameters and flow regime considered in the studies of Kramer-type compliant surfaces by Carpenter & Garrad [6], [7], the wall mass dominates over the fluid mass correction, so the onset velocity is acceptably approximated by (2.70). For lighter walls made from thinner plates, this will not necessarily be the case.

It should be noted that the physical interpretation of the expression (2.73) giving the onset velocity is less straightforward for Blasius flow than it is for the channel. For channel flow there is a natural length-scale given by the channel half-width $h$. This can be used to non-dimensionalise the wall mass in the manner indicated previously. There is no such length-scale available for Blasius flow. Instead, use must be made of the boundary layer displacement thickness $\delta^*$, which is only defined locally at each streamwise position. Writing (2.73) in explicit dimensional form gives

$$U_t^B = \left( \frac{2\sqrt{B^* K^*} + T^*}{m^* + \left(1 - \frac{1}{H}\right) \rho \delta^*} \right)^{\frac{1}{2}} . \tag{2.74}$$

Thus it can be seen that the fluid mass to be added to the wall mass depends on the streamwise location via the local boundary layer thickness. The effective fluid mass

increases downstream.

Having digressed in order to consider some implications for Blasius flow, we now return to the study of the instabilities found for the channel flow. From the expressions for the flutter and travelling wave flutter onset velocities given in (2.62) and (2.69) we have

$$U_f = \frac{3}{2}\left(1 + \frac{5m^2}{6m+1}\right)^{\frac{1}{2}} U_t \tag{2.75}$$

so the travelling wave flutter always sets in first. In fact, the travelling wave flutter instability turns out to be continuously connected with the flutter instability. This is illustrated in Figures 2.13, 2.14. The first figure shows the variation in the growth rates and phase speeds with the mean flow speed, if no account is taken of the critical layer. The wavenumber is held constant at the critical value $\alpha_c$. In the second figure, the effect of the critical layer is included[6]. It can be seen that there is no longer any abrupt change in the growth rates or phase speeds in the vicinity of the critical velocity $U_f$; the flutter and travelling wave flutter instabilities have merged[7]. This is in accord with the situation found previously for flow over a flat plate [7].

We would expect the inclusion of the critical layer to also have some effect on the onset of the divergence instability. Divergence is associated with the solution given by (2.61) with the minus sign taken. Instability sets in when the corresponding wave changes its direction of propagation from upstream to downstream. It has been noted previously that when the critical layer is accounted for, the shift $\Delta c$ produced in the velocity of this wave is such that it is stabilised if it propagates downstream. Thus, we would expect the critical layer to have a stabilising effect on divergence. This is also illustrated in Figure 2.14, where the slower of the two waves is associated with the divergence instability. The imaginary part of its wave velocity is

[6]This is achieved by using the approximation $J = J_0 + i\alpha^2 \Im(J_1)$ in the dispersion relation.

[7]For the particular wall parameters selected, and on the scale used in Figure 2.14, the positive growth rate of the travelling wave flutter can only be discerned quite close to the flutter onset velocity.

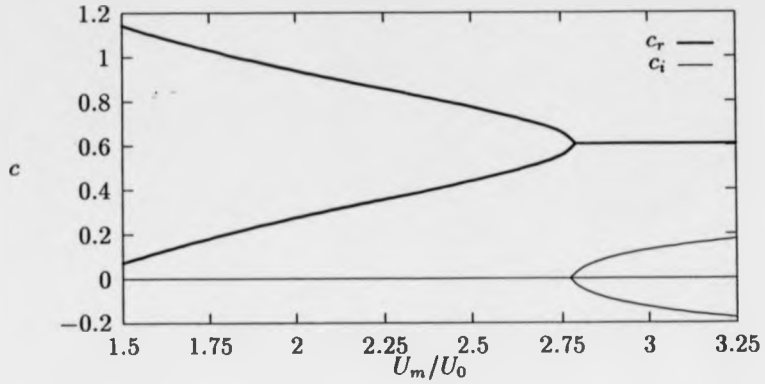


Figure 2.13: Onset of flutter instability from inviscid theory, with no account made for the critical layer. The wall parameters are specified as $\bar{B} = U_0^2$, $\bar{K} = 0.25\,U_0^2$, $\bar{T} = 0$, $m = 0.1$, $\bar{d} = 0$. The wavenumber $\alpha$ is held constant at the critical value $\alpha_c$.

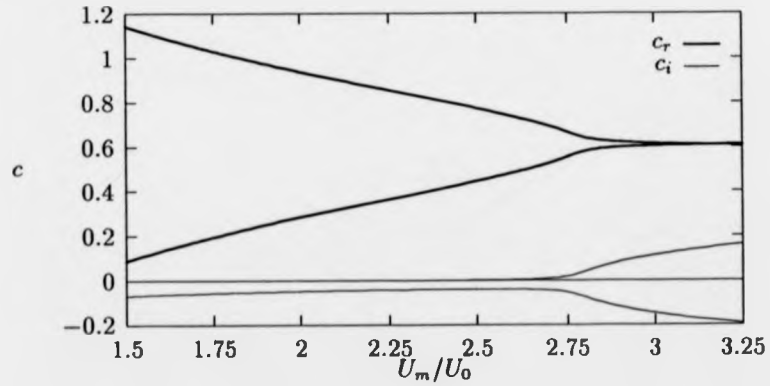


Figure 2.14: Onset of travelling wave flutter/flutter instability from inviscid theory, with the phase shift across the critical layer included. The wall parameters and wavenumber are specified in the same manner as in the previous figure.

negative for the whole range of mean flow velocities displayed[8]. However, we cannot necessarily conclude that the onset of divergence instability would be postponed to higher flow velocities. Divergence sets in when $c = 0$, which is precisely where the theory presented for the critical layer would be expected to become invalid. It is a major shortcoming of the inviscid theory presented thus far that whilst it identifies divergence as a possible mode of instability, it cannot be safely relied upon to predict its onset. In Figure 2.14 the range of mean flow velocities has been deliberately chosen to exclude points near $U_d$.

The effects on stability of including the critical layer can be described from a broader point of view using the energy analysis developed by Landahl [5] and Benjamin [51]. Waves are classed as type A, B, or C using the concept of an activation energy[9]. This classification can then be employed to understand the effects of irreversible energy transfers to and from the compliant wall. Class-A waves are stabilised/destabilised when there is a transfer of energy to/from the wall. For Class-B waves the opposite is true. Class-B behaviour is what would be anticipated in more conventional circumstances. Waves described as Class-C are relatively indifferent to the effects of irreversible energy transfer. They are destabilised by processes involving conservative energy exchanges. Thus the flutter instability can be viewed as Class-C. Travelling wave flutter is Class-B, since it is destabilised when there is a transfer of energy to the wall due to the critical layer. For divergence the same energy transfer mechanism has a stabilising effect, so divergence appears to be a Class-A instability. The utility of the energy classification can be seen when the effect of introducing wall damping is considered within the same framework. Wall damping provides a

[8]Note that the wall damping $\tilde{d}$ has been set equal to zero. For sufficiently large values of $\tilde{d}$ it might still be expected that divergence could be destabilised.

[9]The terms negative- and positive-energy waves have also been used to denote Class-A and B waves. The alternative nomenclature stems from the independent discovery of similar physical principles in the context of plasma physics [52].

means of irreversibly removing energy from the wall. Thus the fact that divergence is destabilised by wall damping is seen to be consistent with its Class-A behaviour with respect to the critical layer. Similarly, we would expect the travelling wave flutter instability to display its Class-B character by being stabilised by damping. This can be confirmed directly by inspecting (2.63). The solution given by taking the plus sign corresponds to travelling wave flutter. By considering the solution with the minus sign, it can also be seen that when there is an upstream travelling wave solution, it is stabilised by damping and so it too is Class-B. The divergence instability occurs when this initially upstream travelling wave changes its character from Class-B to Class-A as it begins to propagate downstream.

In the energy classification outlined above, there is nothing new compared with results found previously for flow over a flat plate. Because of this, we would expect the reservations expressed in [7] concerning the Class-A energy classification of divergence to also apply in the present case. When divergence is modelled realistically using a finite length compliant wall, its behaviour is more akin to that of a Class-C instability.

We now turn to the evaluation of $J_1(c)$. Using the parabolic form of the velocity profile $U$, the integral in (2.58) can be manipulated to give

$$J_1(c) = -\frac{1}{225}\left(Q(c) + 32(1-c)^4 \int_0^1 \frac{1}{U-c}\,dy\right) \tag{2.76}$$

where

$$Q(c) = \frac{9}{7} - \frac{42}{5}(1-c) + \frac{97}{3}(1-c)^2 - 64(1-c)^3 - \frac{32}{c}(1-c)^4 .$$

The $1/c$ singularity in $Q(c)$ indicates the breakdown of the present approximation for small values of $c$. When the phase velocity is such that $0 < c < 1$, the path in the remaining integral term in (2.76) needs to be indented above the critical point at $y_c = \sqrt{1-c}$. A simple calculation then gives

$$\int_0^1 \frac{1}{U-c}\,dy = \frac{1}{2y_c}\left(\log\left(\frac{1+y_c}{1-y_c}\right) + i\pi\right) . \tag{2.77}$$

We thus obtain the imaginary part of $J_1$ as

$$\Im\left(J_1(c)\right) = -\frac{16\pi}{225}(1-c)^{\frac{7}{2}} . \tag{2.78}$$

So $\Im\left(J_1\right) < 0$, as claimed earlier. If there is no critical layer, then for real values of $c$ the integral appearing in (2.76) is real and so is $J_1$.

From the expressions (2.59) and (2.76) we can specify both $J_0$ and $J_1$ in terms of known functions of the wave velocity $c$. Using the approximation $J = J_0 + \alpha^2 J_1$ in the dispersion relation (2.60), we obtain an equation written explicitly in terms of $c$ and $\alpha$. It is then a straightforward matter to solve this equation numerically in order to determine the values of the wave velocity associated with each value of the wavenumber. The computational requirements are very slight, compared with what is needed for the direct numerical solution of the Orr-Sommerfeld equation.

### 2.3.4 Viscous wall layer corrections

Results obtained by solving (2.60) in the manner outlined immediately above provide a fairly accurate basis for describing the travelling wave flutter instability. This is illustrated in the next section, when comparisons are made with numerical solutions of the Orr-Sommerfeld equation. Nevertheless, it is still informative to see if the theory can be further improved by taking account of the effects of the viscous wall layer in the fluid. For channel flow this can be achieved with little additional labour. In contrast, improving the corresponding theory for Blasius flow is quite difficult [50], partly because of the need to carefully account for the details of the mean flow profile. In fact, for the Blasius case such a theory only merits the extra work involved in its development because of its utility in studying three-dimensional instabilities and the effects of anisotropic wall compliance. The theory presented below for the channel could in principle be extended and applied in the same way, but the analysis would be expected to remain much simpler.

For large values of the Reynolds number $R$ there are two regions where viscous

effects can be considered important. (In order to simplify descriptions, only the upper half of the channel flow is explicitly considered from now onwards.) In addition to the critical layer centred on the position of the critical point, there is a viscous layer adjacent to the wall. These layers have widths of $O\{(\alpha R)^{-\frac{1}{3}}\}$ and $O\{(\alpha R)^{-\frac{1}{2}}\}$ respectively. It is assumed that they do not overlap. Violation of this assumption causes the breakdown of the inviscid theory for small enough values of $c$. We also suppose that there are approximate solutions to the Orr-Sommerfeld equation which take the form

$$\phi = A\,\Phi + a\,\phi_\nu \tag{2.79}$$

where $\Phi$ is an inviscid solution determined as before, and $\phi_\nu$ is a rapidly varying viscous solution which is insignificant outside the wall layer. The constants $A$ and $a$ are determined by the boundary conditions on the fluid at the wall. The inclusion of the viscous solution $\phi_\nu$ means that the no-slip condition on the fluid can be satisfied as well as the no-penetration condition which was previously implemented for the inviscid case. The composite solution (2.79) is invalid within the critical layer, since no direct account of viscosity is taken there. However, it will be shown that this is not important so far as the calculation of the wall pressure is concerned.

The inviscid part of the solution is specified in the same form as the solution considered previously. We take it to be defined by

$$\Phi = (U-c)\left(1 + \alpha^2 \int_0^y \frac{1}{(U-c)^2}\,dy \int_0^y (U-c)^2\,dy + \cdots\right). \tag{2.80}$$

The viscous solution is obtained by examining the Orr-Sommerfeld equation in the vicinity of the wall. Introducing the scaled normal distance from the wall $\hat{y} = (1-y)/\epsilon$, where $\epsilon = 1/\sqrt{\alpha R}$, the Orr-Sommerfeld equation can be written as

$$(\hat{D}^4 + ic\hat{D}^2)\hat{\phi} = O(\epsilon) \tag{2.81}$$

with $\hat{D} = d/d\hat{y}$ and $\hat{\phi}(\hat{y}) = \phi(y)$ . This has the general solution

$$\hat{\phi}(\hat{y}) = C_1 + C_2\hat{y} + C_3 \exp(e^{-i\frac{\pi}{4}}\sqrt{c}\,\hat{y}) + C_4 \exp(-e^{-i\frac{\pi}{4}}\sqrt{c}\,\hat{y}) + O(\epsilon)\,. \tag{2.82}$$

The first two terms correspond to the inviscid solution, whilst the third grows rapidly beyond the wall layer. The fourth term decays away from the wall and can thus be identified with the desired viscous solution $\phi_\nu$. Hence we define

$$\phi_\nu(y) = \exp\left(-e^{-i\frac{\pi}{4}}\sqrt{\alpha c R}\,(1-y)\right) . \tag{2.83}$$

This is normalised so that $\phi_\nu(1) = 1$ . Note also that its derivative at the wall is given by $D\phi_\nu(1) = e^{-i\frac{\pi}{4}}\sqrt{\alpha c R}$ which has a magnitude of $O(1/\epsilon)$.

Now that the forms taken by $\Phi$ and $\phi_\nu$ have been specified we can determine the constants appearing in the composite solution $\phi$. The boundary conditions on the fluid are

$$D\phi(1) = -U'(1)\eta \ , \ \phi(1) = c\eta \, . \tag{2.84}$$

Using these conditions, the constants $A$, $a$ can be obtained in the general form

$$A = \left(\frac{c\phi'_{\nu 1} + U'_1\phi_{\nu 1}}{\Phi_1\phi'_{\nu 1} - \phi_{\nu 1}\Phi'_1}\right)\eta \ , \ a = -\left(\frac{c\Phi'_1 + U'_1\Phi_1}{\Phi_1\phi'_{\nu 1} - \phi_{\nu 1}\Phi'_1}\right)\eta \tag{2.85}$$

where we have introduced the notation $\Phi_1 = \Phi(1)$, $\Phi'_1 = D\Phi(1)$ etc. Making use of the facts that $\phi_{\nu 1} = 1$ whilst $\phi'_{\nu 1}$ is $O(1/\epsilon)$, these expressions can expanded in terms of $\epsilon$ to give

$$A = \left(1 + \frac{1}{\phi'_{\nu 1}}\left(\frac{U'_1}{c} + \frac{\Phi'_1}{\Phi_1}\right)\right)\frac{c\eta}{\Phi_1} + O(\epsilon^2) \tag{2.86}$$

$$a = -\frac{1}{\phi'_{\nu 1}}\left(\frac{U'_1}{c} + \frac{\Phi'_1}{\Phi_1}\right)c\eta + O(\epsilon^2) \, . \tag{2.87}$$

The constant $a$ is $O(\epsilon)$. Thus it can be seen that retaining an $O(\epsilon)$ term in the definition of $\phi_\nu$ would have made no difference to the $O(\epsilon^2)$ approximation for the composite solution $\phi$.

The quantity in brackets which appears multiplied by $1/\phi'_{\nu 1}$ in the expressions for both the constants can be rewritten in terms of the previously defined quantity $J(\alpha, c)$. It is straightforward to see that the definition of $J$ given in Section 2.3.2 amounts to taking

$$J = -\frac{c}{\Phi_1}\int_0^1 (U-c)\,\Phi \, dy \, . \tag{2.88}$$

If the inviscid wall pressure associated with the profile $\Phi$ is computed using the $x$-momentum equation for inviscid disturbances, and then again using the $y$-momentum equation, the following equality can be derived

$$U_1'\Phi_1 + c\Phi_1' = -\alpha^2 \int_0^1 (U-c)\Phi \, dy \, . \tag{2.89}$$

from which it follows that

$$\frac{U_1'}{c} + \frac{\Phi_1'}{\Phi_1} = \frac{\alpha^2}{c^2} J \, . \tag{2.90}$$

(Alternatively, this can be obtained by direct manipulation of the expression defining $\Phi$.) Hence we can finally write

$$A = \left(1 + \frac{e^{i\frac{\pi}{4}}}{\sqrt{\alpha c R}} \frac{\alpha^2}{c^2} J\right) \frac{c\eta}{\Phi_1} + O(\epsilon^2) \tag{2.91}$$

$$a = -\left(\frac{e^{i\frac{\pi}{4}}}{\sqrt{\alpha c R}} \frac{\alpha^2}{c^2} J\right) c\eta + O(\epsilon^2) \tag{2.92}$$

and thus obtain

$$\phi = \left(\frac{\Phi}{\Phi_1} + \frac{e^{i\frac{\pi}{4}}}{\sqrt{\alpha c R}} \frac{\alpha^2}{c^2} J \left(\frac{\Phi}{\Phi_1} - \phi_\nu\right)\right) c\eta \tag{2.93}$$

as the composite solution to the Orr-Sommerfeld equation. This is an $O(\epsilon^2)$ approximation to the exact solution, except within the critical layer.

In order to determine the modifications to the inviscid dispersion relation (2.60) brought about by taking the viscous wall layer into account, we now need to recalculate the fluid pressure at the wall. The wall pressure corresponding to an exact solution of the Orr-Sommerfeld solution can be found using the expression (2.15). (Recall that this was obtained by integrating the $y$-momentum equation for viscous disturbances across the channel.) For convenience we restate it here as

$$p(1) = -\alpha^2 \int_0^1 (U-c)\phi \, dy - \frac{i\alpha}{R} D\phi(1) + \frac{i\alpha^3}{R} \int_0^1 \phi \, dy \, . \tag{2.94}$$

We aim to derive an $o(\epsilon)$ approximation for the wall pressure by substituting the composite solution (2.93) for $\phi$. At this level of accuracy the terms in (2.94) which involve the factor $1/R$ can be shown to be negligible. The wall derivative satisfies

$D\phi(1) = -U'(1)\eta$ , and consequently has a magnitude of $O(1)$. Thus the term involving this derivative gives an $O(\epsilon^2)$ contribution to the pressure. (Note that this term is in fact just an $O(1)$ multiple of the normal viscous stress acting at the wall. We ought to be able to neglect it in order to maintain consistency with the previous assumption that the forcing of the wall is given by the fluid pressure alone.) The integral multiplied by $1/R$ would be expected to have a similar magnitude to the integral appearing in the first term. Thus by comparison it can be omitted as giving rise to only an $O(\epsilon^2)$ quantity.

Having neglected the terms in (2.94) containing factors of $1/R$, we are left with a single integral which determines the wall pressure. Its evaluation can be simplified as follows. Since the constant $a$ is $O(\epsilon)$ and the viscous solution $\phi_\nu$ is negligible outside the wall layer, which itself has width $O(\epsilon)$, it can be seen that the contribution of the viscous part of the composite solution to the integral is $O(\epsilon^2)$. Hence the integral, and consequently the wall pressure, can be determined using the inviscid part of the solution alone. At this point it could be objected that no account has been made of the fact that the composite solution does not hold in the critical layer. This might invalidate the approximation procedure just described. However, it can be argued that even if an $O(1)$ viscous correction needed to be made to the solution within the critical layer, it would not affect the calculation of the wall pressure to the order of accuracy considered. The quantity $(U-c)$ vanishes at a point $y_c$ in the critical layer, so near this point we have $(U-c) \simeq U_c'(y-y_c)$. Because $(y-y_c)$ is $O(\epsilon^{\frac{2}{3}})$ in the critical layer, the same must be true of $(U-c)$. Integrating an $O(1)$ multiple of $(U-c)$ across the critical layer thus gives a correction to the wall pressure which is only $O(\epsilon^{\frac{4}{3}})$.

Putting together the arguments given above, we arrive at the following approximation for the wall pressure

$$p(1) = -\alpha^2 A \int_0^1 (U-c)\,\Phi\,dy + o(\epsilon)\,. \tag{2.95}$$

On using the expression (2.91) for $A$, and applying the definition of $J$ in the form given in (2.88), this yields

$$p(1) = \alpha^2 \left(1 + \frac{e^{i\frac{\pi}{4}}}{\sqrt{\alpha c R}} \frac{\alpha^2}{c^2} J\right) J\eta + o(\epsilon) \tag{2.96}$$

This should be compared with the corresponding expression (2.54) obtained from inviscid theory. It can then be seen that the effect of accounting for the viscous wall layer is to replace $J$ by $J_\nu$ where

$$J_\nu(\alpha, c) = \left(1 + \frac{e^{i\frac{\pi}{4}}}{\sqrt{\alpha c R}} \frac{\alpha^2}{c^2} J(\alpha, c)\right) J(\alpha, c)\,. \tag{2.97}$$

The modification required in the inviscid dispersion relation (2.60) is obtained by making the same replacement.

The stability effects of bringing the viscous wall layer into consideration can now be found in a manner analogous to that used previously in studying the critical layer. In Section 2.3.3 the effect of the critical layer was investigated by examining the perturbation $\Delta c$ in the wave velocities which occurs when the approximation $J = J_0$ in the inviscid dispersion relation is replaced by $J = J_0 + \alpha^2 J_1$. In likewise fashion we can look at the shift in wave velocities introduced between successive approximations for $J_\nu$. As with the inviscid case, we begin by solving the dispersion relation using the first approximation $J_\nu = J_0$. Then taking the $o(\alpha^2)$ approximation

$$J_\nu(\alpha, c) = J_0(c) + \alpha^2 \left(J_1(c) + \frac{e^{i\frac{\pi}{4}}}{c^2\sqrt{\alpha c R}} J_0^2(c)\right) \tag{2.98}$$

the shift in the wave velocities can be found in the same way as before. The expression for $\Delta c$ corresponding to the inviscid result (2.67) is readily seen to be

$$\Delta c = \frac{-\alpha^2}{2\left((m+1)c - \frac{2}{3}\right)} \left(J_1 + \frac{e^{i\frac{\pi}{4}}}{c^2\sqrt{\alpha c R}} J_0^2\right)\,. \tag{2.99}$$

In the inviscid theory, it was shown that the destabilisation of travelling wave flutter is associated with the introduction of a negative imaginary part in $J_1$ when there is a critical layer. In physical terms, a phase difference is set up between the wall pressure

and wall displacement, allowing an irreversible transfer of energy by the fluid to the wall. When the viscous wall layer is accounted for, there is a further shift in phase between the pressure and displacement. Using the result (2.78) for $\Im(J_1)$ we obtain

$$\Im(\Delta c) = \frac{-\alpha^2}{2\left((m+1)c - \frac{2}{3}\right)} \left( -\frac{16\pi}{225}(1-c)^{\frac{7}{2}} + \frac{1}{c^2\sqrt{2\alpha c R}} J_0^2 \right) . \qquad (2.100)$$

(If there is no critical layer then the first term in the large brackets should be dropped.) From this it can be seen that the effect of the wall layer is to stabilise travelling wave flutter, in direct opposition to the effect of the critical layer. On the basis of the energy classification discussed in the previous section, it would then be expected that the effect of the wall layer on divergence would be destabilising. This can be confirmed directly from (2.100); the solution corresponding to divergence has $c < 2/3(m+1)$.

The dispersion relation obtained when the viscous wall layer is included can be solved using a slight modification of the method outlined at the end of the previous section. We just need to replace $J$ by $J_\nu$. The next section considers results determined in this way, and compares them with results found from the direct numerical solution of the Orr-Sommerfeld equation.

### 2.3.5 Numerical results for travelling wave flutter

The validity of the approximate analytic theory developed for the travelling wave flutter instability is now tested by comparing its predictions with results obtained via the direct numerical solution of the Orr-Sommerfeld equation. Figure 2.15 shows computed neutral stability curves for travelling wave flutter. The sets of compliant wall parameters are the same as those chosen for the Tollmien-Schlichting neutral stability curves previously plotted in Section 2.2.3. It can be seen that the agreement between results obtained from the analytic theory and the numerical solution of the Orr-Sommerfeld equation is extremely good. In fact the curves lie directly on top of each other, except at some larger values of the wavenumber $\alpha$ where there is a slight discrepancy. (The analytic theory would not be expected to hold for such values of $\alpha$

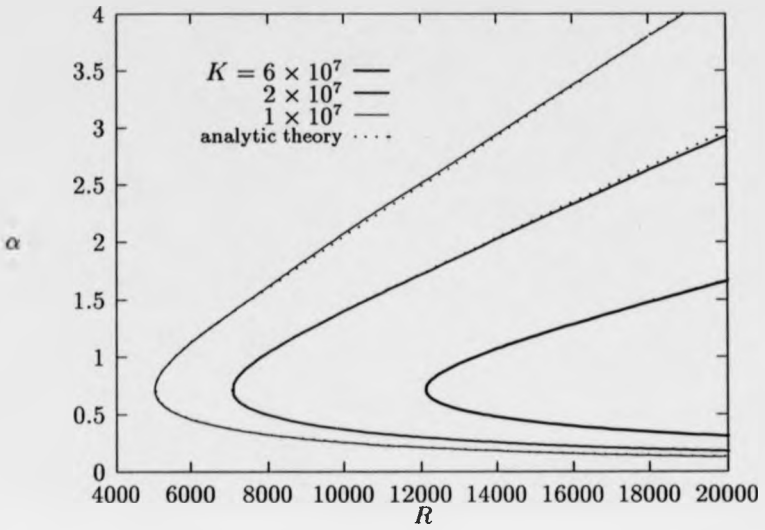


Figure 2.15: Comparison of neutral stability curves for travelling wave flutter computed via direct numerical solution of the Orr-Sommerfeld equation with results obtained from the analytic theory. The other wall parameters are $B = 4K$, $m = 2$, $T = d = 0$.

since it relies on a low wavenumber expansion.) A comparison of the curves shown for the travelling wave flutter in Figure 2.15 with the corresponding results for Tollmien-Schlichting waves displayed in Figure 2.1 makes clear the opposing effects of wall compliance on the two instabilities. The stabilisation of Tollmien-Schlichting waves gained from increasing wall compliance is achieved at the expense of greater instability for travelling wave flutter. For sufficiently compliant channel walls, travelling wave flutter can become unstable at lower Reynolds numbers than the critical value $R \simeq 5772$ for the onset of Tollmien-Schlichting instability in a rigid-walled channel.

It should be noted that the analytic theory used to obtain the curves in Figure 2.15 contains the viscous wall layer correction described in the previous section. When the

effect of viscosity is thus included, the results given by the inviscid theory, in particular the instability onset velocities, need to be interpreted in terms of Reynolds numbers. Such an interpretation is also necessary in order to facilitate comparisons with results obtained from the direct numerical solution of the Orr-Sommerfeld equation. This presents no difficulties. When the Reynolds number is only varied through changes in the centre-line velocity of the mean flow, the expressions derived previously for critical velocities can be simply converted to give corresponding expressions for critical Reynolds numbers. If we fix the dimensional channel half-width $h$ and kinematic viscosity $\nu$, then we can define

$$R_d = U_d h/\nu \ , \ R_f = U_f h/\nu \ , \ R_t = U_t h/\nu \tag{2.101}$$

as the critical Reynolds numbers for the onset of divergence, flutter and travelling wave flutter respectively. To obtain a consistent description, we also need to non-dimensionalise the compliant wall properties in the fashion described earlier in Section 2.2. This amounts to writing

$$mc_0^2 = (B\alpha^2 + T + K/\alpha^2)/R^2 \ , \ \bar{d} = d/R \tag{2.102}$$

for the free-wave speed and damping terms that occur in the inviscid dispersion relation (2.60) and the wall layer corrected version of this.

Figure 2.16 compares neutral stability curves computed from the approximate analytic theory with and without any wall layer correction. It can be seen that there is a significant discrepancy between the two curves. Although the critical wavenumber is unchanged, the Reynolds number for the onset of instability is poorly predicted when the wall layer is not included. This stems from the fact that the growth rates determined from the inviscid theory with no wall layer correction are quite weak near the expected onset. Thus the instability can be readily held in check by the stabilising effect of the wall layer. It is straightforward to estimate the extent to which the onset of travelling wave flutter is delayed, using the result (2.100) which

gives the net change in the temporal growth rate due to the effects of the critical and wall layers. When the wall layer is included, the phase velocity of the wave which first becomes unstable is no longer given by $c = 1$, but is instead displaced to a lower value by an amount

$$\Delta c_t = -\left(\frac{9}{16\pi}\right)^{\frac{2}{7}} \frac{1}{(2\alpha_c R_t)^{\frac{1}{7}}} . \tag{2.103}$$

The corresponding shift in the Reynolds number can then be estimated from the inviscid dispersion relation, employing the expression given in (2.102) for the free-wave speed. Denoting by $\Delta R_t$ the increase in the critical Reynolds number for the onset of travelling wave flutter from the value $R_t$ obtained when the effect of the wall layer is neglected, it is simple to show that

$$\frac{\Delta R_t}{R_t} = -\left(\frac{m+\frac{1}{3}}{m+\frac{1}{5}}\right)\Delta c_t = \left(\frac{m+\frac{1}{3}}{m+\frac{1}{5}}\right)\left(\frac{9}{16\pi}\right)^{\frac{2}{7}} \frac{1}{(2\alpha_c R_t)^{\frac{1}{7}}} . \tag{2.104}$$

Thus $\Delta R_t/R_t$ is $O(1/R^{\frac{1}{7}})$, and so is appreciable even for the relatively large values of $R$ that are of current interest. For the sets of compliant wall properties used in obtaining Figure 2.15, the fractional increases in the critical Reynolds number estimated from (2.104) lie in the range 15-20%. These estimates give good first approximations to the values that can be accurately determined from either the exact solution of the wall layer corrected inviscid dispersion relation or the direct numerical solution of the Orr-Sommerfeld equation. For waves corresponding to points within the unstable regions shown in Figure 2.15, results from the inviscid theory with and without the wall layer correction are in closer agreement with each other; the relative effect of the wall layer is diminished for larger growth rates.

The stabilising effect of small levels of wall damping on travelling wave flutter has previously been mentioned in Section 2.2.3, where the contrast with the destabilisation of Tollmien-Schlichting waves was noted. For the case of Blasius flow, Carpenter & Garrad [7] found that the inclusion of a viscous fluid substrate in their wall model - which in broad terms can be thought of as a means of introducing a kind of wall damping - could lead to the merger of the Tollmien-Schlichting mode of instability with

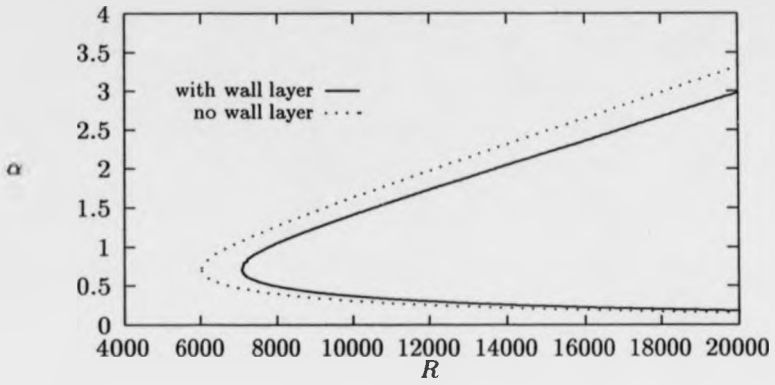


Figure 2.16: Neutral stability curves showing the effect of including/excluding the wall layer in the analytic theory. The wall parameters are $K = 2 \times 10^7$, $B = 4K$, $m = 2$, $T = d = 0$.

travelling wave flutter. Figure 2.17 shows that a similar effect can be found for the present case for sufficiently large values of the conventional wall damping parameter $d$. It can be seen that the extensive region of instability associated with travelling wave flutter in the absence of wall damping is pushed back to higher Reynolds numbers when damping is introduced. Correspondingly, the region of Tollmien-Schlichting instability is enlarged. When there is no wall damping the two regions of instability overlap each other but appear to be distinct. The inclusion of high enough levels of damping leads to their coalescence. The value of the wavenumber at which the neutral curves for travelling wave flutter and Tollmien-Schlichting instability merge is given very closely by the expression (2.44) for the critical wavenumber $\alpha_c$ that was derived in the inviscid theory. Furthermore, the corresponding value of $R$ is comparable to the flutter onset Reynolds number $R_f$ that is also given by the inviscid theory. Thus it can be conjectured that the merger of Tollmien-Schlichting instability with travelling wave flutter has replaced the interaction between divergence and travelling

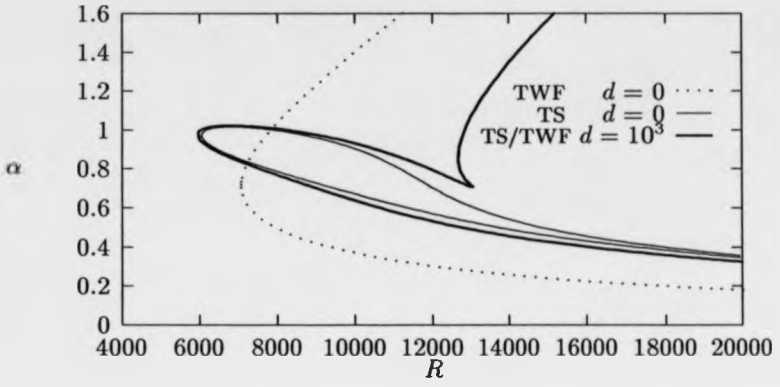


Figure 2.17: Neutral stability curves showing the merger of the Tollmien-Schlichting mode and travelling wave flutter. (The curves were determined by direct numerical solution of the Orr-Sommerfeld equation.) The other wall parameters are $K = 2 \times 10^7$, $B = 4K$, $m = 2$, $T = 0$.

wave flutter that was discussed in Section 2.3.3. Before exploring this possibility any further we first turn to a simpler case.

The same kind of qualitative behaviour in the presence of wall damping was noted by Green & Ellen [34] in their numerical studies for the case of compliant channels with walls modelled as tensioned membranes. Although these authors discussed the existence of the flow-induced surface instabilities described here as divergence and flutter, they did not appear to have been aware of the possibility of travelling wave flutter as a further mode of instability. This is despite the fact that Benjamin [4] had much earlier investigated the mechanism of its destabilisation for Blasius flow. Thus Green & Ellen were unable to analyse some key aspects of their numerical results. We now examine the relevant part of their work in the light of the theory developed for flow-induced surface instabilities.

For walls modelled as tensioned membranes, the free wave speed is independent of

the wavenumber. The inviscid theory (without wall layer corrections) then predicts that the stability boundaries in the $\alpha$-$R$ plane for the various flow-induced instabilities are just lines of constant $R$. Waves at all wavenumbers simultaneously become unstable as the flow velocity is increased beyond a critical value. The inclusion of wall damping displaces these boundaries in the manner shown in Figure 2.18. This figure was obtained by using the approximation $J = J_0 + i\alpha^2 \Im(J_1)$ in the inviscid dispersion relation, *i.e.* by taking the lowest order approximation for the wall pressure and then perturbing it by including the phase shift due the critical layer. The dispersion relation was then solved for points of neutral stability by matching the imaginary part of the wave velocity contributed by the critical layer to the part due to the wall damping. The selected wall parameters are the same as those used by Green & Ellen[10] in their Figure 2(i). The upper branch of the neutral stability curve is associated with travelling wave flutter, whilst the lower branch corresponds to divergence. The lower branch meets the $R$ axis at the divergence onset Reynolds number $R_d$, whilst the upper branch—were it to remain valid for large values of the wavenumber $\alpha$—would asymptote to the critical Reynolds number $R_t$ for travelling wave flutter. Both branches join at the Reynolds number $R_f$ that marks the onset of flutter. Figure 2.19 shows the stability boundaries computed from the inviscid theory using the improved approximation $J = J_0 + \alpha^2 J_1$, *i.e.* including the real part of $J_1$, together with the boundaries determined when the wall layer is also taken into account. It can be seen that the point where the two branches of the neutral curve join has moved to a lower Reynolds number than $R_f$ in each of the plots. Moreover, in both cases the branch of the neutral curve identified in the previous figure as bounding the region of divergence instability now lies at higher values of $\alpha$ and extends to lower values of the Reynolds number. In fact, for the plot in which the wall layer is taken into account, this instability region includes increasing values of

[10]The wall parameter that these authors denote by $c_w$ is just the free wave speed $\sqrt{T/m}$.

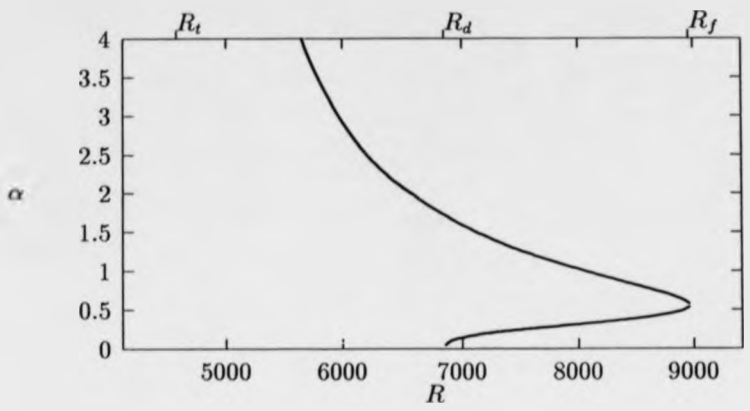


Figure 2.18: Neutral stability curves from inviscid theory using the approximation $J = J_0 + i\alpha^2 \Im(J_1)$. The wall parameters are $T = 2.5 \times 10^7$, $m = 1$, $B = K = 0$, $d = 250$. The values of $R$ labelled as $R_d$, $R_f$ and $R_t$ indicate respectively the critical values for the onset of divergence, flutter and travelling wave flutter that are predicted from inviscid theory in the absence of wall damping

$\alpha$ as $R$ is decreased. Figure 2.20 shows the neutral stability curve computed from the direct numerical solution of the Orr-Sommerfeld equation. (It also contains a repeat of the second plot that was included in Figure 2.19.) It is clear that the inviscid theory is quite effective in locating the merger of travelling wave flutter and Tollmien-Schlichting instability. The lower branch of the stability boundary determined from the wall layer corrected inviscid theory appears to be giving an approximation to the upper branch of the Tollmien-Schlichting neutral curve, rather than delimiting the region where divergence occurs. That this may happen is perhaps not too surprising. For the upper branch of the Tollmien-Schlichting neutral curve, composite solutions of the form used in Section 2.3.4 give valid—if somewhat coarse—approximations for Tollmien-Schlichting waves. In particular, the assumption that the wall layers and

critical layers are well separated can be justified in this case. (For the lower branch of Tollmien-Schlichting neutral curve this is not true, so the failure of the inviscid theory to indicate the presence of the lower branch is only to be expected.)

In the next section it will be seen that the replacement of divergence by the Tollmien-Schlichting instability in determining stability boundaries is not an exceptional occurrence. Furthermore, it would seem that the merger of the Tollmien-Schlichting and travelling wave flutter modes of instability is quite general. Before addressing these matters in more detail, we first note that there is in fact an instability region in Figure 2.20 which can be associated with divergence. This appears for low values of the wavenumber $\alpha$. (In the corresponding diagram presented by Green & Ellen, there is no such region, presumably because the computations conducted by these authors were not continued down to sufficiently small wavenumbers.) The point of onset of the instability can be predicted exactly from the version of the inviscid theory used to obtain the results shown in Figure 2.18, *i.e.* by taking an approximation which *only* accounts for the phase shift across the critical layer. Near to the onset, the group velocity vanishes, which is indicative of an absolute instability. At larger values of the Reynolds number, the instability appears to merge with the Tollmien-Schlichting mode of instability. The merger occurs at a value of $R$ somewhat lower than that at which the travelling wave flutter and Tollmien-Schlichting modes coalesce.

### 2.3.6 Modal coalescence and the onset of divergence instability

In the preceding section it was seen that, under certain circumstances, the travelling wave flutter and Tollmien-Schlichting modes of instability could coalesce. Such behaviour is consistent with the energy classification developed by Landahl and Benjamin [5], [51]. (An outline of this classification was given in Section 2.3.3.) Tollmien-

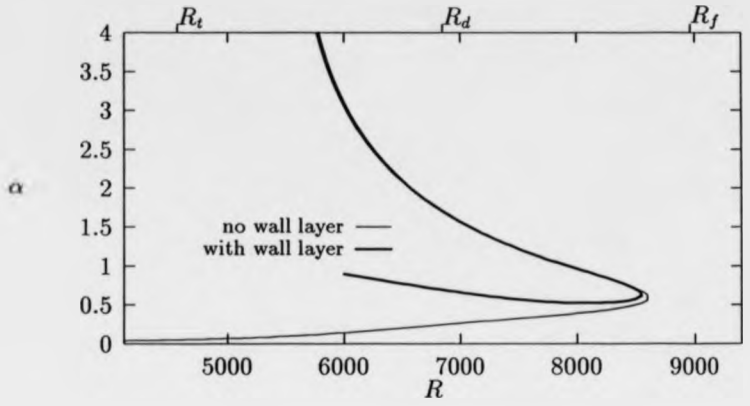


Figure 2.19: Neutral stability curves from inviscid theory using $J = J_0 + \alpha^2 J_1$ and the wall layer corrected version of this. The wall parameters are the same as in the previous figure.

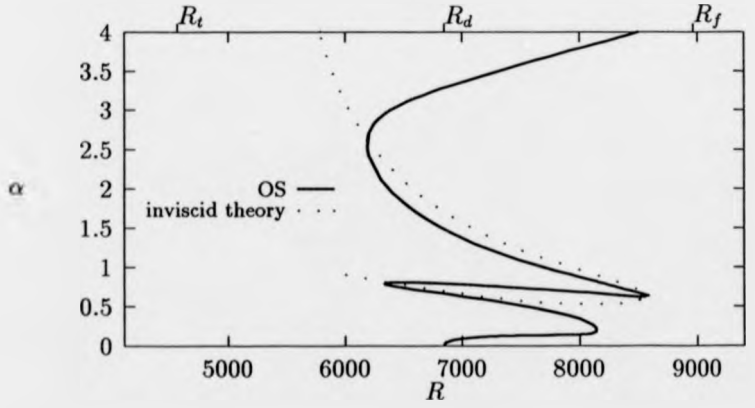


Figure 2.20: Neutral stability curve from the full numerical solution of the Orr-Sommerfeld equation, together with a re-plot of the curve obtained from the inviscid theory with wall layer correction. The wall parameters are the same as in the previous two figures.

Schlichting waves can be categorised as being of Class A, in view of the fact that, as noted earlier, wall damping has a destabilising effect. By contrast, travelling wave flutter is expected to be of Class B. Thus, there is the theoretical possibility that the Tollmien-Schlichting and travelling wave flutter modes could merge to form a Class C instability. The situation is analogous that which was described in Section 2.3.3, for the appearance of flutter instability. It was predicted that for sufficiently high mean-flow velocities (or, with the appropriate non-dimensionalisation, Reynolds numbers), the Class A divergence instability would coalesce with the Class B travelling wave flutter, generating the more powerful Class C instability designated as flutter.

Reapplying the same form of energy classification, it becomes difficult to comprehend the merger of the divergence and Tollmien-Schlichting modes of instability, which was also reported in the previous section. Both divergence and the Tollmien-Schlichting mode are usually expected to be of Class A, so their apparent coalescence is somewhat puzzling. In the present study, we will not pursue this matter any further. There are some other interesting features of the divergence branch of solutions which, arguably, require prior attention. In particular, for cases where the wall parameters are chosen so as to model Kramer-type compliant surfaces[11], it has not as yet proved possible to obtain numerical solutions of the Orr-Sommerfeld equation which locate neutral stability curves that can be attributed to divergence. From the analysis that follows, it will be seen that the difficulty in locating divergence instability is connected with the fact that the predicted merger between travelling wave flutter and divergence is superseded by the merger of travelling wave flutter with the Tollmien-Schlichting mode of instability.

It may be recalled that in Section 2.3.2 inviscid shear layer theory was used to derive a dispersion relation which described the dependency between the phase velocity $c$ and the wavenumber $\alpha$ for normal mode forms of disturbance. For convenience, we

[11]For such surfaces the bending stiffness and spring stiffness are non-vanishing, in contrast to the case for a tensioned membrane.

restate the relation here as

$$m\left(c^2 - c_0^2\right) + J(\alpha, c) = 0 \tag{2.105}$$

where the free wave speed $c_0$ is determined as

$$c_0 = \frac{1}{U_m}\left[\frac{1}{m}\left(\bar{B}\alpha^2 + \bar{T} + \frac{\bar{K}}{\alpha^2}\right)\right]^{\frac{1}{2}}$$

and the quantity $J$ represents the forcing provided by the fluid. All the quantities appearing in (2.105) take a non-dimensional form. (However, the stiffness parameters $\bar{B}, \bar{T}$ and $\bar{K}$ all have the dimensions of a squared velocity. They are defined so as to be independent of the dimensional centre-line mean-flow velocity $U_m$. Hence the factor $1/U_m$ that is retained in the expression for the non-dimensional free-wave speed.) For simplicity, it has been assumed that there is no wall damping. If $p_w$ is the perturbation fluid pressure at the upper channel wall and $\eta$ is the wall displacement, then $J$ can be defined by setting

$$p_w = \alpha^2 J(\alpha, c)\,\eta\,. \tag{2.106}$$

The application of the inviscid shear layer theory lies in the derivation of an explicit functional form for $J$.

Expressions defining the critical mean-flow velocities for the onset of the divergence, travelling wave flutter and flutter instabilities were obtained by utilising an expansion of the form $J = J_0 + \alpha^2 J_1 + \cdots$. Both divergence and flutter were dealt with by applying the first order approximation $J = J_0$. The onset of travelling wave flutter was treated in essentially the same way, except that it was first necessary to note that $J_1$ could contribute a non-vanishing imaginary part when there was critical layer, *i.e.* when the phase velocity $c$ lay in the range $0 < c < 1$. In effect, the destabilising influence of the critical layer was accounted for by considering the consequences of subjecting the approximation $J = J_0$ to an imaginary-valued perturbation.

To obtain the accurate neutral stability curves for travelling wave flutter that were presented in Section 2.3.5, the higher-order approximation $J = J_0 + \alpha^2 J_1$ was

applied before solving the inviscid dispersion relation (2.105). Additionally, a correction representing the effect of the viscous wall layer was included, in the manner described in Section 2.3.4. Improving the accuracy of the predictions for the branch of upstream travelling wave solutions associated with divergence has proved to be less straightforward. Both $J_1$ and the term that defines the viscous wall layer correction have a singularity at $c = 0$. (The same form of singular behaviour was documented by Carpenter & Garrad [50], for the case of Blasius flow.) The occurrence of this singularity is perhaps not too surprising. We might expect that any approach which relies, even implicitly, on the possibility of distinguishing separate viscous wall and critical layers would become invalid when the two layers begin to overlap. Such an overlap arises when the phase velocity $c$ takes on sufficiently small positive values. This is rather unfortunate, since according to the lowest-order inviscid approximation, divergence should be destabilised in precisely the limit where there is a wave with zero phase velocity. (Admittedly, the limit needs to be taken from below, *i.e* through negative values of $c$ representing upstream travelling waves. Within the context of the inviscid theory, it then becomes more difficult to interpret the singular behaviour. There is no longer any critical layer to be considered.) However, it turns out that the identification of a singularity at $c = 0$ may be somewhat premature.

From a comparison with eigenvalues obtained by solving the Orr-Sommerfeld equation directly, it became apparent that the dispersion relation derived from the inviscid theory was yielding poor predictions for the branch of upstream travelling wave solutions that was expected to give rise to the divergence instability. Disagreement was found even when the phase velocities were well removed from the supposed singularity at $c = 0$, and whichever of the successive approximations $J = J_0$, $J = J_0 + \alpha^2 J_1$ was applied. The inclusion of a viscous wall layer correction gave no significant improvement. At first, the failure of the inviscid theory (or its wall-layer corrected version) to determine accurate eigenvalues was a cause of consternation, particularly in view of the fact that successful predictions could be made for the

branch of solutions representing travelling wave flutter. In order to trace the source of the difficulty, it proved necessary to take account of the Tollmien-Schlichting mode of disturbance.

If we return to the definition given by equation (2.106), then it may be seen that, essentially, the quantity $J$ is the ratio of the perturbation fluid pressure at the wall to the wall displacement. In Section 2.3.2 a detailed expression for this ratio was derived by considering inviscid disturbances to the inviscid shear flow $U = 1 - y^2$. In other words, by determining solutions to Rayleigh's equation. Subsequently, in Section 2.3.4, a correction accounting for the effect of the viscous wall layer was obtained. Formally, this led to the replacement of $J$ by another quantity $J_\nu$. The latter quantity can still be interpreted as defining the ratio of the wall pressure to the wall displacement. When approximations for $J$ and $J_\nu$ were developed, no consideration was taken of the possibility that we might have $\eta = 0$. It is clear that such a possibility can be realised in the case of solutions to the Orr-Sommerfeld equation. Both the wall displacement and the wall velocity can vanish for solutions that represent Tollmien-Schlichting waves. Thus, we might expect to find singularities in $J_\nu$ at values of $\alpha$ and $c$ which correspond to Tollmien-Schlichting waves in a *rigid*-walled channel. (In general, there is no reason to anticipate that the wall pressure would also vanish, and hence eliminate the singular behaviour.) Interestingly, such singularities should occur when the phase velocity lies between the values $c = 0$ and $c = 1$ that define the stability boundaries for divergence and travelling wave flutter. As a consequence, there is likely to be some disruption of the simple relationship between the divergence and travelling wave flutter modes of instability that was described in Section 2.3.3.

Turning to the case where the viscous wall layer is neglected, it may be seen that singularities in $J$ will only occur if there are solutions of Rayleigh's equation that meet the no-penetration condition for rigid walls, which in current parlance takes the form[12] $c\eta = 0$. Such inviscid solutions could only exist, if at all, for real values of the

[12]It may be recalled that matching the vertical wall and fluid motion leads to the condition

phase velocity $c$. When $c$ is taken to be complex, with a non-vanishing imaginary part $c_i$, Rayleigh's inflexion-point theorem [36] can be applied to rule out any possibility of a singularity. Since there is no point of inflexion in the parabolic mean profile $U = 1 - y^2$, there cannot be any solution, with a non-zero value of $c_i$, which satisfies the rigid wall no-penetration condition[13].

Notwithstanding the limitation just mentioned, the behaviour of the quantity $J$ might still be expected to retain some vestige of the singularities, attributable to Tollmien-Schlichting waves, that would be found if viscosity was fully accounted for. We can address this issue directly by examining the original expression for $J$ that was given in Section 2.3.2. The expression took the form of a ratio (compare equation (2.55))

$$J(\alpha, c) = \frac{I_0(c) + \alpha^2 I_2(c) + \alpha^4 I_4 + \cdots}{1 + \alpha^2 I_1(c) + \alpha^4 I_3 + \cdots} \tag{2.107}$$

where

$$\begin{aligned} I_0(c) &= \int_0^1 (U-c)^2 \, dy \\ I_1(c) &= \int_0^1 \frac{1}{(U-c)^2} \, dy \int_0^y (U-c)^2 \, dy \\ I_2(c) &= \int_0^1 (U-c)^2 \, dy \int_0^y \frac{1}{(U-c)^2} \, dy \int_0^y (U-c)^2 \, dy \, . \end{aligned}$$

The terms $I_{2k-1}(c)$, $I_{2k}(c)$ for $k > 1$ may be defined using similar integrals in a recursive manner. As has recently been noted, results concerning the onset of the various flow-induced surface instabilities were derived by expanding $J$ as a power series in $\alpha^2$

$$\begin{aligned} J(\alpha, c) &= I_0(c) + \alpha^2 \left[ I_2(c) - I_0(c) I_1(c) \right] + \cdots \\ &= J_0(c) + \alpha^2 J_1(c) + \cdots \, . \end{aligned} \tag{2.108}$$

---

$\phi(\pm 1) = c\eta$ for the case of symmetric disturbances, where $\phi(y)$ is the streamfunction profile that appears in Rayleigh's equation.

[13] In its usual interpretation, the inflexion-point theorem is restricted to the case of instability, *i.e.* $c_i > 0$. However, it may also be applied, formally, to the stable case where $c_i < 0$.

Clearly, if there are values of $\alpha$ and $c$ for which the denominator in (2.107) becomes equal to zero, then in the vicinity of such values the stated expansion will no longer be valid. Referring back to the derivation given in Section 2.3.2, it is straightforward to verify that the denominator can only vanish if there are solutions of Rayleigh's equation that satisfy the no-penetration boundary condition for rigid walls[14]. Even if such inviscid solutions cannot be found in practice, it is still conceivable that, by using an expansion which disguises the fact that $J$ is defined by a ratio, some essential ingredient may be left out. More simply, the expansion (2.108) might become invalid without $J$ displaying any obvious singular behaviour. Bearing this possibility in mind, we will now examine the form taken by the quantity $I_1$, which appears as the coefficient of the second term in the denominator for $J$.

After substituting the parabolic profile mean-flow profile $U = 1 - y^2$, the integrals that define $I_1$ can be manipulated to yield

$$I_1(c) = \frac{1}{15}\left(\frac{3}{2} - \frac{4}{c}(1-c) + 4(1-c)\int_0^1 \frac{y}{U-c}\,dy\right) . \tag{2.109}$$

When there is a critical point, the path taken when evaluating the remaining integral in (2.109) needs to be indented above $y_c = \sqrt{1-c}$. A simple calculation then gives

$$\int_0^1 \frac{y}{U-c}\,dy = \frac{1}{2}\left(\log\left|\frac{1-c}{c}\right| + i\pi\right) .$$

If there is no critical point, then the imaginary part can be omitted. It can be seen that $I_1$ has a $1/c$ singularity, just as was noted previously for the quantity $J_1$. All of which suggests that when $c$ is small, it will be necessary to replace the truncated expansion $J = J_0 + \alpha^2 J_1$ by the rational approximation

$$\begin{aligned} J_d(\alpha, c) &= \frac{I_0(c) + \alpha^2 I_2(c)}{1 + \alpha^2 I_1(c)} \\ &= J_0(c) + \frac{\alpha^2 J_1(c)}{1 + \alpha^2 I_1(c)} . \end{aligned} \tag{2.110}$$

[14]Strictly speaking, we need to consider $c$ times the denominator. The same consideration is relevant in the interpretation of the quantities $I_1$, $J_1$. As will be noted later, both are defined in a manner that leads them to possess $1/c$ singularities.

This no longer has any singularity at $c = 0$. In fact, it is easy to check that

$$\lim_{c \to 0} J_d(\alpha, c) = 0 \tag{2.111}$$

when $\alpha$ is non-zero[15]. (Reference should be made to the explicit expression for the function $J_1$ that was given at the end of Section 2.3.3.) Similarly, it can be shown that

$$J_d(\alpha, 1) = \frac{1}{5}\left(\frac{1 + \frac{1}{14}\alpha^2}{1 + \frac{1}{10}\alpha^2}\right) , \tag{2.112}$$

which explains why, even for $\alpha^2$ of order $O(1)$, an expansion of the form (2.108) was found to give acceptable results in connection with the onset of travelling wave flutter instability, which occurs when $c = 1$.

The consequences of using different approximations for $J$ are easier to illustrate if we first rewrite the dispersion relation (2.105) as

$$\frac{1}{U_m^2}\left(\bar{B}\alpha^2 + \bar{T} + \frac{\bar{K}}{\alpha^2}\right) = mc^2 + J(\alpha, c) . \tag{2.113}$$

Somewhat loosely, this can be interpreted as defining a balance between an effective wall stiffness and the combined inertia of the wall and fluid. The factor $1/U_m^2$ that appears on the left-hand side incorporates an explicit dependency of the stiffness upon the mean-flow speed. The effective wall stiffness reduces as the flow speed is increased. For any selected value of $U_m$, and specified wall parameters $\bar{B}$, $\bar{T}$ and $\bar{K}$, the wall stiffness can be minimised at the critical wavenumber $\alpha_c = (\bar{K}/\bar{B})^{\frac{1}{4}}$.

Figure 2.21 plots the variation, with the phase velocity, of the right-hand side of (2.113) when the approximation $J = J_0$ is applied. For any given wavenumber and mean-flow speed $U_m$, the allowed values of the phase velocity can be located from intersections between the plotted curve and a horizontal line drawn at a height which corresponds to the effective wall stiffness. If $U_m$ is fixed, then a lowest possible line can be defined so as to represent the stiffness obtained when the wavenumber is taken to be equal to the critical wavenumber. Consequently, we can investigate

[15]The behaviour for $\alpha = 0$ will be discussed later.

the sequence of behaviour that occurs as $U_m$ is increased by examining intersections with horizontal lines of decreasing height. Changes in behaviour will first be realised for $\alpha = \alpha_c$. It can be seen that, provided $U_m$ is not too large, there will be one intersection that represents an upstream wave and another that corresponds to a downstream wave. (The magnitudes of the two phase velocities will be different, owing to the fact that the mean fluid flow breaks the symmetry, between the upstream and downstream directions, that would apply in the case of free waves.) The onset of travelling wave flutter can be identified when the mean-flow speed is increased to an extent that is sufficient to allow the downstream wave to achieve the phase velocity $c = 1$. The appropriate horizontal line is labelled in the figure. Similarly, divergence instability can set in when the initially upstream travelling wave reverses its direction of propagation. Finally, the onset of flutter instability can be visualised in terms of horizontal lines that lie below the minimum of the plotted curve. In such cases, the absence of any intersections implies that there are no real-valued solutions for the phase velocity. Instead, there is a pair of complex conjugate solutions, one of which represents the flutter instability.

So far, there is nothing new to report. We have merely given a different form of presentation to results that were obtained earlier. Figure 2.22 provides a counterpart to the previous figure, for the case where the approximation $J = J_d$ is utilised. More strictly speaking, it shows the variation, with the phase velocity, of the right-hand side of equation (2.113) when $J$ is replaced by the quantity

$$J_d^r(\alpha, c) = J_0(c) + \frac{\alpha^2 \Re\{J_1(c)\}}{1 + \alpha^2 \Re\{I_1(c)\}} \,. \tag{2.114}$$

Thus, the effect of the critical layer, which is manifested in the imaginary parts of the functions $J_1$ and $I_1$, has been deliberately ignored. When $J_d^r$ rather than $J_0$ is substituted for $J$, the function that is collected on the right-hand side of the dispersion relation becomes dependent upon the wavenumber. As a consequence, our graphical analysis is now restricted to a single wavenumber. In the particular case considered,

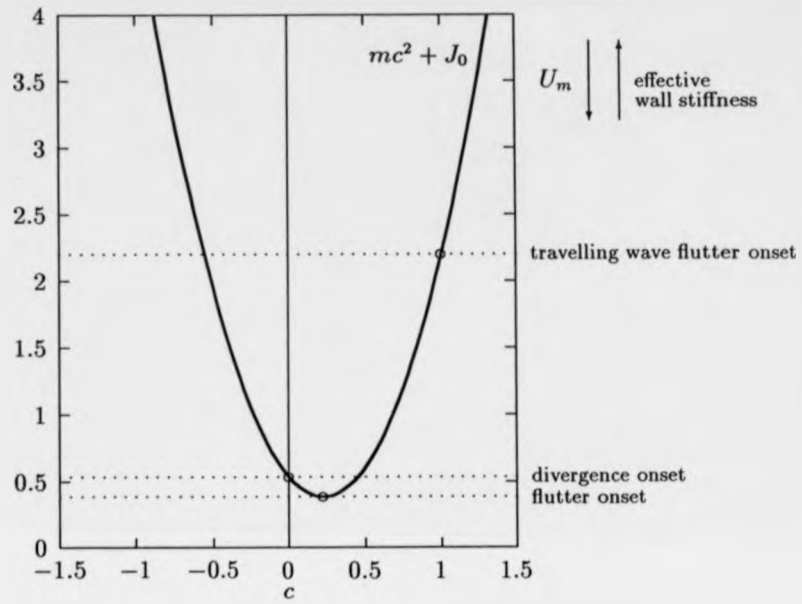


Figure 2.21: Variation of the quantity $mc^2 + J_0(c)$. The compliant wall mass is taken to be $m = 2$. Permitted values of the phase velocity $c$ can be determined from intersections between the curve and a horizontal line drawn at a height that represents the effective wall stiffness, *i.e.* the quantity appearing on the left-hand side of (2.113).

the value of the wavenumber was set by taking $\alpha^2 = 1/2$.

It can be seen that the form of the curve plotted in Figure 2.22 is altered significantly from that which was found when only the $J_0$ term was retained. In particular, there is a singularity in $J_d^r$, and hence in $mc^2 + J_d^r$, at a positive value of $c$. Presumably, this is related to the singularity, attributable to a Tollmien-Schlichting wave, that would be expected if viscosity was fully accounted for. By again considering intersections between the curve and horizontal lines, it may be concluded that for small enough mean-flow speeds there are three, rather than two, possible values of

the phase velocity. In addition to the upstream and downstream solutions found before, there is solution with a relatively small positive phase velocity. As will be demonstrated later, this solution can be identified as the inviscid counterpart of a Tollmien-Schlichting wave. When the mean-flow speed is increased, the phase velocity of the faster downstream wave decreases until it can take the value $c = 1$. Travelling wave flutter may then set in, just as before. However, the upstream wave can no longer change its direction of propagation. The phase velocity can only vanish in the limit where the effective wall stiffness also vanishes. This would correspond to an infinite mean-flow speed. Thus, there would not appear to be any possibility of divergence instability. (It should be noted that there is no physical interpretation for the parts of the plotted curve which lie below the $x$-axis, since the wall stiffness cannot be negative.) It can be seen that flutter instability is also excluded. Instead, the solution that corresponds to travelling wave flutter coalesces with the additional solution that we have attributed, provisionally, to the Tollmien-Schlichting mode of disturbance. The occurrence of such modal coalescence can be traced, once more, by interpreting the minimum in the plotted curve.

The account given immediately above may be brought into question. It could be considered inconsistent to neglect the effect of the critical layer when our stated aim is to examine the full consequences of taking the rational approximation $J = J_d$. If $J$ is replaced by $J_d$, rather than the real-valued function $J_d^r$, then there is no longer any singularity for a real value of the phase velocity. However, a residue of the singular behaviour can be traced in extremely rapid variations that are displayed by both the real and the imaginary parts of $J_d$. These occur over a very small range of phase velocities, centred around the phase velocity at which $J_d^r$ was found to be singular. Rather than attempting to provide a more formal justification for the graphical analysis which employed the quantity $J_d^r$, we will simply check that such an analysis does, in fact, predict the correct behaviour for solutions of the inviscid dispersion relation in the case where the unamended rational approximation $J = J_d$

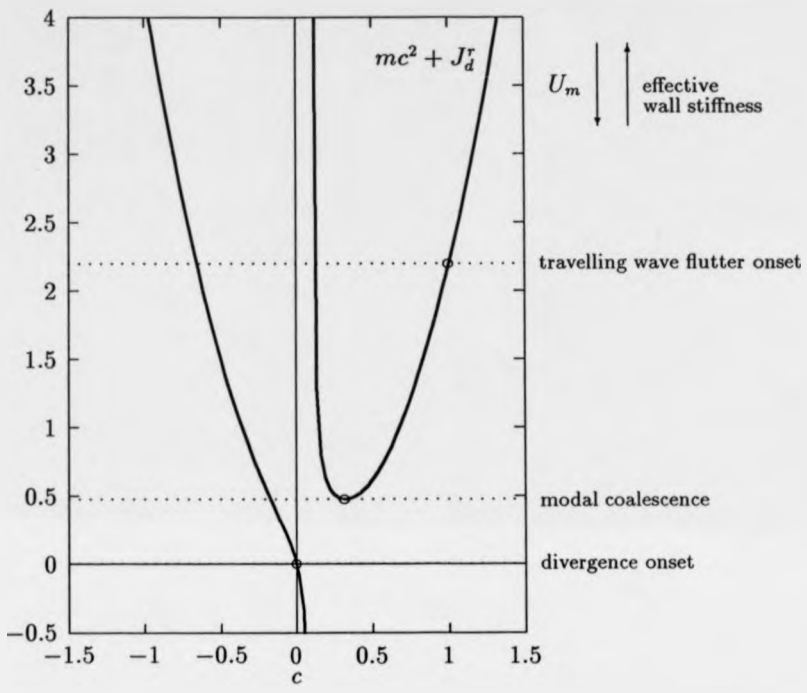


Figure 2.22: Variation of the quantity $mc^2+J_d^r(\alpha, c)$ when the wavenumber is specified by $\alpha^2 = 0.5$. The compliant wall mass is again taken to be $m = 2$. With the exception of divergence, the labelled onset points are now only pertinent to the single chosen value of the wavenumber.

is applied. In turn, it will be shown that the inviscid solutions, when so determined, can be used to anticipate the behaviour of numerical solutions obtained directly from the Orr-Sommerfeld equation.

Figure 2.23 displays solutions, for the complex phase velocity, derived from the inviscid dispersion relation using the approximation $J = J_d$. The wavenumber was fixed at the critical value $\alpha_c$. In order to facilitate comparisons with solutions computed from the Orr-Sommerfeld equation, the variation is shown with respect to the Reynolds number $R$, rather than the mean-flow speed $U_m$. (It should be remembered

that in the context of the wholly inviscid theory, the Reynolds number is just another measure of the mean-flow speed.) Plots are also given for solutions that were obtained using the lowest-order approximation $J = J_0$.

As expected, there are three distinct solution branches when $J_d$ is substituted for $J$. The solution with the largest positive phase velocity corresponds to travelling wave flutter. It can be seen that for sufficiently large Reynolds numbers, this solution is highly unstable. By contrast, the other solution representing a wave with a downstream phase velocity is subject to strong stabilisation. From a comparison with the results obtained using the lowest-order approximation, it becomes apparent that the merger that would have led to flutter instability has been supplanted. However, it would perhaps be more accurate to attribute the altered form of behaviour to an intense modal interaction rather than a modal coalescence. Finally, it may be noted that when the approximation $J = J_d$ is applied, there is a solution that always represents an upstream travelling wave. It no longer appears to be possible to obtain any reversal in the direction of wave propagation that would signal the onset of divergence instability. When taken together, the above observations provide a vindication for the results that were obtained, more simply, using the graphical analysis.

Figure 2.24 displays numerical solutions of the Orr-Sommerfeld equation for the same values of the wall parameters and the wavenumber as were considered in the previous figure. For ease of comparison, there is also a replot of the solutions that were obtained from the inviscid shear layer theory by substituting $J_d$ for $J$. (In order to avoid any need to use the Gaster transformation [45] to convert between spatial and temporal growth rates, the Orr-Sommerfeld equation was solved in a temporal formulation. This was achieved by a simple amendment of the solution procedure developed for spatial eigenvalues, to allow for the possibility of complex-valued temporal frequencies. An iterative adjustment of the complex frequency could then be employed so as to obtain any specified real-valued wavenumber as the spatial eigenvalue.) It can be seen that the more sophisticated version of the inviscid dispersion relation gives

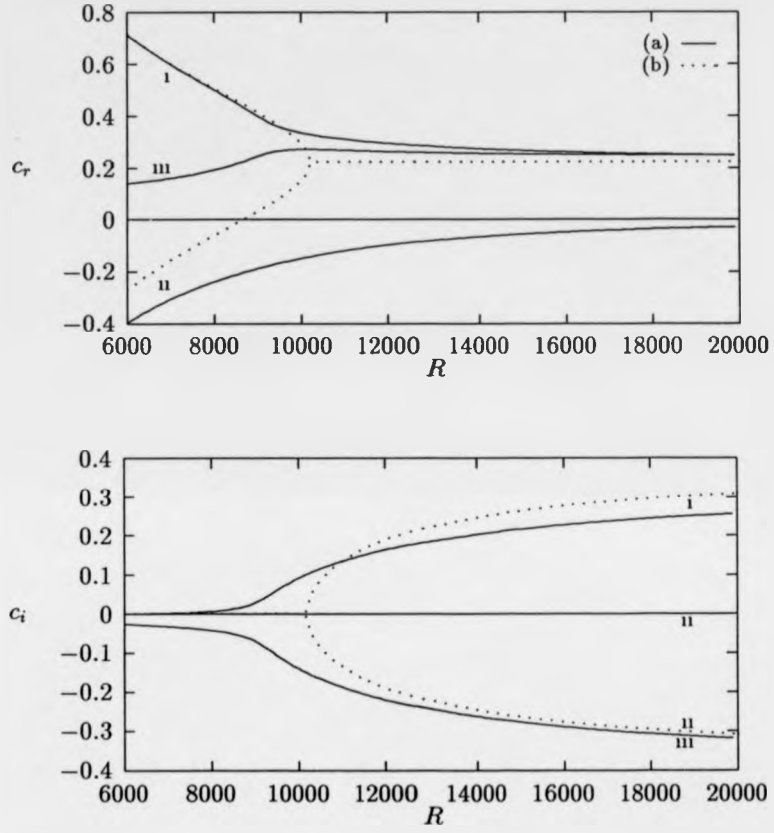


Figure 2.23: Real and imaginary parts of the phase velocity, as obtained from the inviscid dispersion relation using the approximations (a) $J = J_d$, (b) $J = J_0$. The non-dimensional wall parameters are $m = 2$, $B = 4 \times 10^7$, $K = 1 \times 10^7$. The wavenumber is held constant at the critical value $\alpha = \alpha_c$, where $\alpha_c = (K/B)^{\frac{1}{4}} = 1/\sqrt{2}$. The labels (i), (ii) distinguish the two solution branches that are related to the free waves that would propagate in opposite directions along the compliant wall in the absence of the fluid. The solution marked as (iii) can be associated with the Tollmien-Schlichting mode of instability. (In case (a), the imaginary part of the phase velocity is identically zero for the branch of solutions that represents an upstream travelling wave.)

a fairly reliable guide to the behaviour discovered by solving the Orr-Sommerfeld equation directly. In particular, the inviscid theory anticipates, correctly, the existence of an additional branch of solutions with a downstream phase velocity. It is a straightforward matter to verify that such solutions represent Tollmien-Schlichting waves when they are obtained directly from the Orr-Sommerfeld equation.

The inviscid theory also predicts the interaction between travelling wave flutter and what we have now identified as the Tollmien-Schlichting mode of disturbance. As a consequence of this interaction, travelling wave flutter becomes very strongly unstable. Simultaneously, the Tollmien-Schlichting mode is subjected to a stabilisation which, though not so strong as the destabilisation suffered by travelling wave flutter, is still considerable. Thus, the interaction retains the hallmarks of a Class A / Class B modal coalescence. The Class C character of the subsequent instability is confirmed by the fact that the temporal growth rates are little affected by the introduction of moderate levels of damping into the compliant wall model. As might have been expected, the inviscid shear layer theory gives quite poor quantitative predictions for the real and imaginary parts of the phase velocity along the solution branch that is associated with the Tollmien-Schlichting waves. A more accurate treatment would require a careful account of the balance between the viscous effects attributable to the critical layer and those which arise from the viscous wall layer. However, it can be seen that such a treatment is not necessary if we are only interested in locating the onset of the strong instability that arises when the Tollmien-Schlichting mode of disturbance interacts with travelling wave flutter. In fact, if we return to the graphical analysis that was presented earlier, which involved the neglect of all critical layer effects, then it may be conjectured that viscosity is inessential to the instability mechanism, except in so far as there would appear to be a need for a shear in the mean flow.

We will now turn to the branch of solutions that in the inviscid theory, subject to the approximation $J = J_d$, was always found to represent an upstream travelling

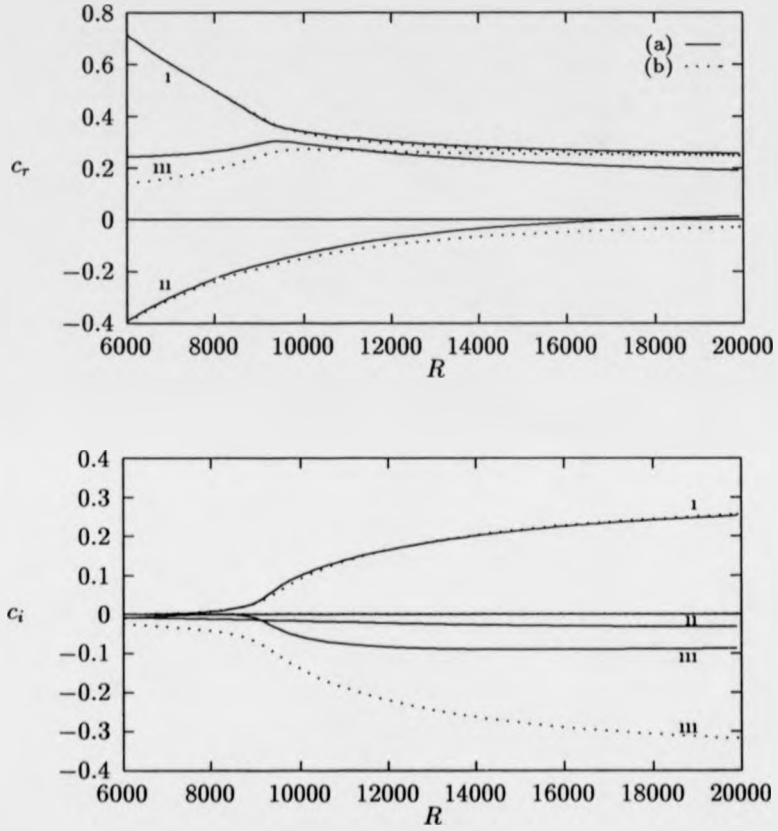


Figure 2.24: Real and imaginary parts of the phase velocity, as obtained from (a) direct numerical solution of the Orr-Sommerfeld equation, (b) the inviscid dispersion relation using the approximation $J = J_d$. The non-dimensional wall parameters and the fixed wavenumber are the same as in the previous figure.

wave. For the corresponding solutions obtained from the Orr-Sommerfeld equation, there is a reversal in the direction of wave propagation for high enough Reynolds numbers. The Reynolds number at which there is a wave with a vanishing phase speed is about twice the critical Reynolds number predicted for the onset of divergence instability on the basis of the lowest-order inviscid approximation $J = J_0$. This can be verified by referring back to Figure 2.23. Further investigation of numerical solutions to the Orr-Sommerfeld equation revealed that even when the phase velocity does become orientated downstream, the group velocity remains in the upstream direction until the Reynolds number is very much larger. Thus, there would seem to be little prospect of realising an absolute instability that could be described as divergence. Moreover, it can be seen that the solutions derived from the Orr-Sommerfeld equation have an appreciable negative growth rate. Consequently, the introduction of fairly high levels of wall damping does not lead to any significant destabilisation.

It may be noted that although the inviscid theory, with the approximation $J = J_d$, fails to anticipate the reversal in phase velocity that was discovered from the solution of the Orr-Sommerfeld equation, the predictions for the behaviour of the upstream travelling waves are still considerably better than those that were obtained using the lowest-order inviscid approximation $J = J_0$. A further improvement can be made if a viscous wall layer correction is included in the manner[16] that was described in Section 2.3.4. In particular, it is possible to obtain some measure of agreement for the growth rates of the upstream waves. As a consequence, it would seem plausible to attribute the stability that was noted in the solutions of the Orr-Sommerfeld equation to the effect of the viscous wall layer. When the real part of the phase velocity is negative, there is no critical layer, so the uncorrected inviscid theory can only predict

[16]There is the complication that, for negative phase velocities, an appropriate branch of the square root needs to be taken for the quantity $J_\nu$ defined in (2.97). The choice needs to made so as to ensure that the viscous component that is included in the composite solution for the streamfunction does in fact decay, rather than grow, beyond the viscous wall layer.

neutral stability. The incorporation of a viscous wall layer correction also leads to a slight improvement in the values predicted for the real parts of the phase velocities. However, it is still not possible to locate the appearance of a wave with a vanishing phase speed. In the present study there will be no attempt to pursue such matters in any further detail. Instead, we will have to be content with making a few general observations and some conjectures.

It may have been noted, already, that the apparent exclusion of divergence instability is somewhat at odds with results that were presented in the previous section. For the case of a compliant wall modelled as a tensioned membrane, solution of the Orr-Sommerfeld equation revealed the onset of divergence instability at the critical Reynolds number $R_d$ that was derived using the inviscid dispersion relation in conjunction with the approximation $J = J_0$. The instability was found to set in at zero wavenumber, precisely as could be anticipated by perturbing the approximated inviscid dispersion relation so as to include a representation of the balance between the destabilisation arising from wall damping and the stabilising effect due to the critical layer. An explanation for the success of the lowest-order predictions, in this particular case, may lie in the fact that there is no specific lengthscale associated with the motion of a tensioned membrane. The effective wall stiffness is independent of the wavenumber. Consequently, the stiffness remains finite even in the limit where the wavenumber approaches zero. (A discussion of the behaviour of the function $J_d$ in the same limit is included in a note at the end of the current section.) By contrast, for Kramer-type compliant surfaces there will always be a critical wavenumber at which the wall stiffness is minimised. In the analysis that was presented immediately above, we assumed, implicitly, that the critical wavenumber was comparable to wavenumbers that could be used to characterise the Tollmien-Schlichting instability. It might be expected that such an assumption of similar lengthscales would be necessary in order to obtain optimised stability effects for Tollmien-Schlichting waves. If, on the other hand, we had chosen to conduct an analysis for a compliant wall with a critical

wavenumber that was very much smaller than the wavenumbers at which there could be unstable Tollmien-Schlichting waves, then we might have discovered only limited departures from the simple form of behaviour that was documented earlier for inviscid solutions obtained by setting $J = J_0$. The presence of the Tollmien-Schlichting mode of disturbance would no longer be expected to affect the character of the flow-induced surface waves. (At the critical wavenumber, any singularity in the ratio of the wall pressure to the wall displacement attributable to a Tollmien-Schlichting wave would have to be located at a complex value of the phase velocity with a relatively large negative imaginary part. Thus, it can be conjectured that the singularity would have only a minimal effect on the form of the inviscid dispersion relation for the near real values of the phase velocity that we should expect to find associated with flow-induced surface waves.) Clearly, there is a need for a more detailed investigation, irrespective of the merits of the particular speculations that have just been entertained.

It should be remarked that though the results concerning the onset of divergence instability remain somewhat incomplete, they may represent some form of progress over previous studies that have been conducted for the case of Blasius flow. Such studies have achieved very limited success in linking analytic results derived for divergence with numerical solutions of the Orr-Sommerfeld equation. (For a recent example, reference should be to Figure 17 in the study reported by Carpenter & Morris [14].) It is possible that the difficulties that have been encountered in the case of Blasius flow may be traced to the same source as for the channel flow. For Blasius flow, we should again expect to find singularities in the function defining the ratio of the wall pressure to the wall displacement. These would be attributable to Tollmien-Schlichting waves that can propagate along a Blasius boundary layer adjacent to a rigid wall. Thus, for Blasius flow as well as for plane channel flow, it may not always be feasible to give an account of flow-induced surface waves without also treating Tollmien-Schlichting waves, or their inviscid counterparts, within the same analytic framework.

We will conclude this section by noting that the interaction (or more loosely speaking, the merger) between the Tollmien-Schlichting mode of disturbance and travelling wave flutter was replicated in numerical results that were obtained for other sets of compliant wall parameters that could be used to model Kramer-type surfaces. Similarly, it was found that the features suggesting an avoidance of divergence instability could be reproduced. In all such cases, the wall properties were chosen so as to yield a critical wavenumber that was broadly comparable with the wavenumbers characteristic of unstable Tollmien-Schlichting waves. Later on, when selecting compliant wall parameters for use in numerical simulations of Tollmien-Schlichting waves propagating over rigid/compliant wall joins, we will often make reference to the critical Reynolds number for the onset of divergence, as if this presented no further difficulty. What will nearly always be meant, when making such a reference, will be the nominal value $R_d$ that can be computed using the results of the inviscid shear layer theory with the approximation $J = J_0$. Thus, the restrictions that will be placed on the wall parameters, with the intention of ruling out any possibility of divergence instability at a given value of the Reynolds number, will usually be somewhat stronger than is strictly necessary.

**A note on the behaviour of the function $J_d$ in the limit where both the wavenumber and the phase velocity vanish**

The behaviour displayed by the approximating function $J_d(\alpha, c)$ when $(\alpha, c) \rightarrow (0, 0)$ is pertinent to the onset of divergence instability in the case where the compliant wall is modelled as a tensioned membrane. Solution of the Orr-Sommerfeld equation indicates that instability sets in when both the wavenumber and the phase velocity vanish. Behaviour in the same limit would be expected to be of much less significance for the case of a Kramer-type compliant surface, unless the wall parameters happened to be chosen so as to yield a very small value for the critical wavenumber, *i.e.* the wavenumber at which the effective wall stiffness is minimised.

If we consider the definition of $J_d$ given by (2.110), then we can obtain the result

$$\lim_{\alpha \to 0} J_d(\alpha, c) = J_0(c) \tag{2.115}$$

for non-vanishing values of the phase velocity. Proceeding to take the limit as the phase velocity tends to zero, it may be seen that

$$\lim_{c \to 0} \left( \lim_{\alpha \to 0} J_d(\alpha, c) \right) = J_0(0) = \frac{8}{15} . \tag{2.116}$$

By contrast, if we first allow the phase velocity to approach zero, and then consider the limit of a vanishing wavenumber, we obtain (compare equation (2.111))

$$\lim_{\alpha \to 0} \left( \lim_{c \to 0} J_d(\alpha, c) \right) = 0 . \tag{2.117}$$

Thus the function $J_d$ displays a discontinuity at the point $(\alpha, c) = (0, 0)$. Without embarking upon a more elaborate investigation, it would be impossible to determine the appropriate form of limiting behaviour. However, since for the case of a tensioned membrane a perturbation analysis based upon the approximation $J = J_0$ was found to yield the correct prediction for the onset of divergence instability, it would appear that (2.116), rather than (2.117), should be employed.

# Chapter 3

# Methods for simulating the coupled fluid and wall motion

In the previous chapter we gave an account of the instabilities that could arise for a plane channel flow when the channel walls were taken to be compliant throughout. We now turn to the case where only one section of the channel is comprised of compliant walls, the remainder being rigid. Our main interest will be in the behaviour exhibited by Tollmien-Schlichting waves when they propagate over joins between the two distinct types of wall. For the most part, this behaviour will be investigated by means of a direct numerical simulation of the physical situation concerned. Consequently, we will begin by giving an account of earlier simulation work that has been undertaken with the aim of studying the spatial evolution of Tollmien-Schlichting waves under similar circumstances. Following this introductory survey, we will formulate a mathematical description of the model problem that provides the focus of the present work. We can then proceed to discuss the numerical discretisation of the system of equations that is obtained. Particular attention will be paid to the aspects of the developed numerical scheme that ensured there was a numerically stable coupling between the fluid motion and that of the compliant walls.

## 3.1 Numerical Simulation of Transition

The study of boundary layer transition by direct numerical solution of the Navier-Stokes equations has progressed considerably since the first investigations carried out by Fasel [53] almost two decades ago. Limitations in available computing power restricted the scope of the earliest studies to the simulation of the initial development of small amplitude two-dimensional disturbances. Owing to rapid progress in computer technology and improvements in numerical solution procedures, it is now possible to simulate the process of transition all the way to fully developed three-dimensional turbulence, at least for some highly idealised cases with particularly simple geometry. The review by Kleiser & Zang [54], and the related survey articles by Herbert [55] and Biringen & Laurien [56], describe the impressive achievements of recent numerical simulation.

For present purposes, much of the sophistication required in state of the art simulations is unnecessary. Initially at least, we are only interested in two-dimensional disturbances with amplitudes sufficiently small for linearised theory to hold. The physical set-up which is to be investigated is designed to delay the progression to nonlinear stages of disturbance development in the transition to turbulence. Since the detailed study of these stages is precisely what motivates most numerical simulations of transition, there is a sense in which our studies end at a point where others have begun. However, the current problem has an added complication arising from the need to simulate the interactive coupling between the fluid and the compliant walls.

The difficulties arising from incorporating fluid-solid coupling were successfully overcome in the simulations conducted by Metcalfe and his co-workers. These are described in [57] and [58]. In the latter of these two works, both three-dimensional disturbances and nonlinear developments were simulated (and results obtained which suggest that the beneficial effect of compliant walls in postponing transition to tur-

bulence can be sustained well into the nonlinear regime). Thus, it might at first seem that the problem that was depicted in Figure 1.2, namely the propagation of a Tollmien-Schlichting wave down a plane channel bounded first by rigid walls then by compliant walls, could be tackled using a variation of the methods developed by Metcalfe *et al.* In fact, the present problem would appear to be much simpler, since attention is restricted to two dimensions and linearised disturbances. This appearance is deceptive, for reasons which are now described.

As in many other transition simulations, the work of Metcalfe *et al* makes an assumption of streamwise periodicity. In what has become known as temporal simulation, the fluid is allowed to evolve aperiodically in time but not in space. The imposition of such a restriction allows the use of pseudo-spectral numerical methods, based on Fourier expansions of the disturbances fields in the streamwise direction. (Often combined with a Chebyshev expansion in the wall-normal direction and a further Fourier expansion to resolve the spanwise variation.) In this way a high resolution simulation can be performed using relatively few independent modes in the numerical discretisation. This allows both computer memory and run time requirements to be kept within fairly reasonable—though still large— bounds. In effect, all the available computing resources can be concentrated on a single Tollmien-Schlichting wavelength, rather than spread over the many wavelengths which would be needed to simulate directly the details of the spatial evolution to transition found in physical experiments.

The assumption of streamwise periodicity means that temporal simulation results need to be carefully interpreted when they are checked against observations from experiments. In controlled experiments, the fluid flow fields are often expected to show a time-periodic response to the forcing imposed by a vibrating ribbon. The transition to turbulence occurs non-periodically in space at locations downstream of the ribbon. Thus comparisons between temporal simulations and experiment can only be achieved by drawing an analogy between spatially periodic and time periodic

behaviour. The success of this analogy relies in part on the spatial homogeneity of the conditions imposed on the fluid; the temporal behaviour at different downstream locations in the experiment needs to be matched in an appropriate fashion to the spatial behaviour at different times in the numerical simulation. Within the framework of a spatially periodic simulation, making allowance for the abrupt spatial inhomogeneity due to a rigid/compliant wall join would appear to necessitate a change in the nature of the wall boundary conditions for the whole computational domain at some chosen instant in the time evolution. It is difficult to see how this could be done in a manner that would give rise to physically meaningful results. Consequently, we prefer to avoid any assumptions about spatial periodicity; the streamwise development of Tollmien-Schlichting waves in the situation depicted by Figure 1.2 is to be studied explicitly. Unfortunately, this means that the numerical methods developed by Metcalfe *et al* cannot be amended for use on the current problem. Instead we will develop a scheme which builds on the work begun much earlier by Fasel [53].

The numerical studies of boundary layer transition undertaken by Fasel and his collaborators aim to resolve the whole of the streamwise development to turbulence, without resort to any convenient assumptions about analogies between spatial and temporal evolution. Recent examples of this work are described in references [59], [60] and [61]. Such studies have become known as spatial simulations, in order to draw out the contrast with the more restricted situation that is investigated in temporal simulation. Spatial simulations necessitate the use of a computational domain which has sufficient streamwise extent to contain the successive downstream developments that lead to turbulent flow. The computer storage requirements are thus much larger than what would be required in corresponding temporal simulations. Furthermore, spectral methods cannot be immediately applied to the discretisation of the streamwise variation of the flow. Less computationally efficient finite-difference schemes become a more natural choice[1]. A further difficulty with spatial simulations

[1]Some recent spatial simulations have managed to employ spectral methods for discretising the

stems from the need to determine appropriate downstream boundary conditions. The spatially elliptic character of the Navier-Stokes equations leads to the mathematical necessity of imposing such conditions. Unlike the conditions which hold at the other computational boundaries, there is no obvious physical basis for their selection. This matter is discussed in more detail later on. It will be seen that the formulation of the downstream boundary condition causes no great obstacle to progress for the problem of current interest, because only two-dimensional disturbances in the linear regime of transition are to be simulated.

Before describing the mathematical formulation and the chosen numerical discretisation of the problem that was depicted in Figure 1.2, we first mention an alternative approach to boundary layer stability and transition simulation which has recently been introduced by Herbert and Bertolotti [63], [62]. This approach draws on the fact that experimental and numerical studies of boundary layer transition suggest that there is little upstream propagation of information about the downstream development of disturbances. At a given streamwise location, the behaviour found depends strongly on phenomena occuring at positions upstream of the given location, but is affected only weakly by what occurs downstream. Although the Navier-Stokes equations are formally elliptic in each direction of space, the physically selected solutions are seen to display the kind of behaviour that would arise from equations which were parabolic in the streamwise spatial direction. By making plausible assumptions about the behaviour of spatially evolving, time periodic disturbances, Herbert was able to derive a parabolic approximation to the governing equations. The parabolic stability equation thus obtained works directly with locally defined disturbance wavenumbers and corresponding disturbance profiles. The spatial evolution of a disturbance is determined by computing the streamwise variation of these quantities.

The parabolic stability equation has been used to study the spatial evolution of

---

streamwise operators. See for example the work of Spalart reported in [62].

Tollmien-Schlichting waves in a growing boundary layer [62]. The results obtained were found to be in excellent agreement with those determined by direct numerical solution of the Navier-Stokes equations. This agreement persisted well into the nonlinear regime of transition. Compared with spatial simulation, the computational requirements for solving the parabolic stability equation are very low. In view of this, it might be expected that the parabolic stability equation could be fruitfully used to tackle the problem of a Tollmien-Schlichting wave propagating over a rigid/compliant wall join. In fact, the formulation of the parabolic stability equation would seem to be particularly well suited to such a problem, since it works directly with locally defined wavenumbers, the imaginary parts of which describe the spatial growth and decay of disturbance waves. Unfortunately, the behaviour of a Tollmien-Schlichting wave as it adapts to the presence of a compliant wall turns out to violate a key assumption needed to derive the parabolic stability equation. This is the assumption that the locally defined wavenumber and profile change slowly in the streamwise direction. As will be seen in the simulation results presented later, both the profile and wavenumber can vary rapidly in the vicinity of a rigid/compliant wall join.

Rather than applying the parabolic stability equation, a less restrictive approach would be to simplify the fluid governing equations in the manner described in an earlier work by Murdock [64]. Investigating nonlinear effects on boundary layer stability, Murdock found that a parabolised form of the vorticity transport equation yielded numerical results that were in good agreement with those obtained by solving the full Navier-Stokes equations. The formulation that he employed can be thought of as providing an intermediate approximation between the parabolic stability equation and the full Navier-Stokes equations. If the same formulation could be adopted in the present work, there would still be a substantial reduction in computational costs[2].

For disturbances propagating along a boundary layer bounded by a compliant

[2]Murdock remarks that a one-twentieth reduction in computing time can be obtained through the use of a parabolised vorticity equation.

wall, the possibility of significant upstream influence cannot be discounted, at least not without further study. It is plausible to suppose that information could be carried from downstream locations by flow-induced surface waves travelling in an upstream direction. Thus, for the type of problem that is of current interest, the validity of even the relatively mild form of parabolisation used by Murdock may turn out to be doubtful. It would seem prudent to retain the full ellipticity of the fluid governing equations, despite the fact that this may increase, considerably, the computational expense involved in obtaining numerical solutions. The need for such a cautious approach is confirmed by the simulation results that were actually obtained using the unreduced Navier-Stokes equations, as will be reported in more detail later. There is evidence that, in certain circumstances, upstream travelling waves do in fact play an important role in determining the adaptive behaviour of a Tollmien-Schlichting wave as it propagates over a rigid-compliant wall.

## 3.2 Problem Formulation

This section outlines the mathematical formulation and consequent numerical discretisation of the problem that was indicated by Figure 1.2, *i.e.* a Tollmien-Schlichting wave propagating down a plane channel bounded first by rigid walls then by compliant walls. The same approach can be used to tackle variations on the same theme, for example a channel which has compliant walls throughout or which contains finite length compliant panels embedded in otherwise rigid walls.

### 3.2.1 Mathematical model of the fluid

The fluid motion is governed by the linearised two-dimensional Navier-Stokes equations for incompressible flow. These are taken in a vorticity-velocity form. Fasel [65] discusses the merits of using such an approach in the context of hydrodynamic stability and spatial simulations of transition to turbulence. A more general review of

the advantages and disadvantages of the vorticity-velocity formulation is given by Gatski [66].

The fluid governing equations are applied in a rectangular domain $0 \leq x \leq l$, $-1 \leq y \leq 1$ where $x$ is the direction parallel to the channel walls and $y$ is the wall-normal direction. All distances are non-dimensionalised using the channel half-width. The streamwise length $l$ of the channel needs to be chosen so that a sufficient number of Tollmien-Schlichting wavelengths can be resolved within the computational domain. Attention is confined to fluid disturbances for which the normal velocity component is symmetric about the channel centre. This choice, along with the restriction to two dimensions, stems from the fact that such disturbances determine the linear stability of the flow for the case of rigid walls [36]. (For compliant walls of infinite streamwise extent, an extension of Squire's theorem can be made for channel flow, as has previously been discussed in Sections 2.1 and 2.2.2. This provides further justification for studying only two-dimensional disturbances.)

Letting $u$, $v$ be the streamwise and wall-normal velocity perturbations, and $\omega$ the vorticity perturbation, we can write the fluid equations in the form

$$\frac{\partial \omega}{\partial t} + U\frac{\partial \omega}{\partial x} + U''v = \frac{1}{R}\nabla^2\omega \tag{3.1}$$

$$u = \int_0^y \omega \, dy + \frac{\partial}{\partial x}\int_0^y v \, dy \tag{3.2}$$

$$\nabla^2 v = -\frac{\partial \omega}{\partial x}\,, \tag{3.3}$$

where the mean flow is given by $U = 1 - y^2$ and $R$ is the Reynolds number based on the centre-line velocity and channel half-width. Equation (3.1) is the linearised vorticity transport equation. The usual Poisson equation for $u$

$$\nabla^2 u = \frac{\partial \omega}{\partial y} \tag{3.4}$$

has been replaced with an equation obtained by integrating the definition of vorticity

$$\omega = \frac{\partial u}{\partial y} - \frac{\partial v}{\partial x} \tag{3.5}$$

indefinitely across the channel. For the strictly parallel mean flow $U$, the equation for $u$ is decoupled from those for $v$ and $\omega$, apart from the imposition of the boundary condition for $u$ which is discussed below. Hence $u$ can be determined after $v$ and $\omega$ have already been found.

The physical boundary conditions on the fluid at the upper channel wall can written in the general form

$$u_w = \bar{u}(x,t) \tag{3.6}$$

$$v_w = \bar{v}(x,t) \tag{3.7}$$

where the suffix $w$ denotes evaluation at $y = 1$ and the functions $\bar{u}$, $\bar{v}$ are determined by the wall motion in a manner to be described later. For the rigid-walled section of the channel, both of these functions vanish identically. It should be noted that there is no need to impose boundary conditions at the lower channel wall since we will work implicitly with disturbance fields for which $v$ is symmetric about the channel centre. Consistent with this, $\omega$ is also taken to be symmetric, whilst $u$ must be antisymmetric. (The consequent condition that $u$ should vanish at the channel centre $y = 0$ is already subsumed in equation (3.2).)

In order to obtain a well-posed mathematical problem, in which all of the physical boundary conditions are utilised in a convenient manner, we need to derive a constraint to be applied to the vorticity. This is found by applying the boundary condition on $u$ in equation (3.2) to give

$$\int_0^1 \omega \, dy = \bar{u} - \frac{\partial}{\partial x} \int_0^1 v \, dy \, . \tag{3.8}$$

Later on, it will be shown how such a condition may be used in conjunction with the vorticity transport equation to develop a numerical scheme for computing the time evolution of the vorticity. In many studies employing the vorticity-velocity formulation, the corresponding constraint is taken in the form of a boundary condition on the vorticity at the location of the wall(s). For instance, Fasel [53] uses the

condition

$$\frac{\partial \omega_w}{\partial x} = -\frac{\partial^2 v_w}{\partial y^2} \tag{3.9}$$

for a rigid wall. This is derived from the Poisson equation for $v$ and the rigid wall boundary condition $v_w = 0$. When the wall is compliant, a further term $-\partial^2 v/\partial x^2$ needs to be added to the right-hand side of (3.9), in order to account for the possibility of wall motion. In either case, no use is made of the boundary condition on the $u$-component of the fluid velocity. But as previously remarked, for the present problem the $u$-component does not appear in the vorticity transport equation. It follows that if the condition (3.9) were used, the problem would be physically under-determined. The evolution of the vorticity would not be constrained, directly or indirectly, by any boundary condition on $u$. In contrast, when the integral constraint (3.8) is used, the condition on $u$ is implicitly imposed on the vorticity. (For studies which include nonlinearity or a non-parallel mean flow, the same difficulties in using wall vorticity boundary conditions do not arise. There are additional terms in the vorticity transport equation that involve $u$ explicitly. The evolution of $\omega$ can then be seen to be directly coupled to the values of $u$ at all spatial locations.)

A further reason for using the integral constraint on the vorticity is that, taken together with the Poisson equation for $v$, it ensures incompressibility holds at the walls. The same does not follow from conditions such as (3.9). This difference is significant because of a general difficulty with the vorticity-velocity formulation in its usual differential form, *i.e.* the vorticity transport equation in conjunction with the two Poisson equations (3.4) and (3.3). The Poisson equations only imply that

$$\nabla^2 \mathcal{D} = 0 \ \text{ where } \ \mathcal{D} = \frac{\partial u}{\partial x} + \frac{\partial v}{\partial y} \, . \tag{3.10}$$

From the maximal principle for harmonic functions, it follows that if the incompressibility condition $\mathcal{D} = 0$ is satisfied on the boundaries, then it holds everywhere. Consequently, (see for example [65]) Fasel chose to use a discretised version of this condition, applied at the wall locations, in determining a finite-difference represen-

tation for the wall normal second derivative that appears in his vorticity boundary condition. It is not clear that such a strategy can be formally justified, though it does give acceptable numerical results in practice. Mathematically, the present approach would seem to be more satisfactory.

The discussion given above illustrates that the imposition of boundary conditions within the vorticity-velocity formulation is not a trivial matter. Quartapelle and Valz-Gris [67] have shown that integral rather than local conditions may need to be imposed on the vorticity when it is used in non-primitive variable formulations of the Navier-Stokes equations. (A review of boundary conditions requirements and related issues for the various possible formulations of the Navier-Stokes equations is given by Quartapelle in [68].) Such integral conditions ensure that the system which is then obtained is fully equivalent to the primitive variables form of the Navier-Stokes equations with the usual no-slip boundary conditions on the velocity components. The need to make use of integral conditions on the vorticity appears somewhat at variance with conventional pictures of vorticity generation at solid boundaries, which might be thought to suggest that local conditions such as Fasel's would be more appropriate.

With the usual Poisson equation for $u$ replaced by (3.2), it is straightforward to show using the Poisson equation for $v$ that incompressibility is in fact satisfied at all locations. Consequently, it can be shown that equations (3.1), (3.3), (3.2) with conditions (3.7), (3.8) are fully equivalent to the linearised Navier-Stokes equations in primitive variables with imposed boundary conditions (3.6), (3.7). (Further details are given in an appendix.) These remarks assume that the disturbance fields have the symmetries described previously.

We now discuss the imposition of the boundary conditions associated with the finite streamwise extent of the computational domain. At the upstream boundary at

$x = 0$ the disturbances are prescribed in the form

$$v = \Re\left(v_{os}(y)\, e^{-i\beta t}\right) \tag{3.11}$$

$$\omega = \Re\left(\omega_{os}(y)\, e^{-i\beta t}\right) , \tag{3.12}$$

where $v_{os}$ and $\omega_{os}$ are complex eigenfunction profiles found from the solution of the (rigid-walled) Orr-Sommerfeld equation for spatially evolving waves with temporal frequency $\beta$. The numerical methods described in Section 2.2 can be used to yield a streamfunction profile $\phi(y)$ and complex spatial wavenumber $\alpha$, whence we can take

$$v_{os} = -i\alpha\phi \ , \ \omega_{os} = \left(D^2 - \alpha^2\right)\phi \, , \tag{3.13}$$

where $D = d/dy$. There is no necessity to prescribe $u$ at the upstream computational boundary in order to determine the behaviour of $v$ and $\omega$. This is a consequence of the absence of $u$ from the vorticity transport equation. Alternatively, the prescription of $\omega$ can be viewed, via equation (3.2), as a means of ensuring that

$$u = \Re\left(u_{os}(y)\, e^{-i\beta t}\right) \ \text{ where } \ u_{os} = D\phi \tag{3.14}$$

at the upstream boundary. This assumes that the disturbances are spatially periodic close the boundary, so that it is permissible to replace $\partial/\partial x$ with multiplication by $i\alpha$.

The time-periodic forcing of the fluid at $x = 0$ models the situation found in vibrating ribbon experiments for streamwise locations sufficiently distanced from the ribbon [42]. A more general means of obtaining waves within the computational domain would be to generate them using blowing and suction strips at the walls, as discussed by Fasel [59]. There would then be no need to specify detailed forms for inflowing disturbances; we could simply set $v = \omega = 0$ at the upstream boundary. For investigations into the behaviour of spatially and temporally localised waves, or for studies of nonlinear developments, there would be advantages to generating disturbances in such a fashion. However, the need to use a longer domain in order

to allow for the decay of transients away from the vicinity of the wave generators adds to the computational expense of the problem. Consequently, in the present study we will always prescribe the inflow disturbances at the upstream boundary using (3.11), (3.12).

As was mentioned in the previous section, the choice of boundary conditions at the downstream end of the computational domain is difficult in general. For the case of three-dimensional nonlinear disturbances propagating in a transitional flow, the selection of appropriate conditions is still a matter of active research. An up-to-date discussion is given in [61]. Broadly, the aim is to find 'soft' conditions which allow disturbances to propagate out of the domain without distorting the upstream flow through the introduction of unphysical reflections at the boundary.

If the disturbances could be described exactly as two-dimensional waves with a complex streamfunction of the form

$$\psi(x,y,t) = A(y,t)e^{i\alpha x} \tag{3.15}$$

then it would follow that

$$\frac{\partial^2\psi}{\partial x^2} = -\alpha^2\psi\,. \tag{3.16}$$

at all times and spatial locations. This can be reversed, *i.e.* if $\psi$ satisfies (3.16) then it must be of the same form as (3.15), (though possibly with the replacement $\alpha \to -\alpha$). For the associated real-valued flow fields we would have

$$\frac{\partial^2 v}{\partial x^2} + 2\alpha_i\frac{\partial v}{\partial x} + |\alpha|^2 v = 0 \tag{3.17}$$

$$\frac{\partial^2 \omega}{\partial x^2} + 2\alpha_i\frac{\partial \omega}{\partial x} + |\alpha|^2 \omega = 0 \tag{3.18}$$

and similarly for $u$. Thus if we imposed conditions of this form at points on the downstream boundary, then disturbances which are locally well described in the manner of (3.15) could be expected to pass through the boundary without distortion. The boundary conditions would be compatible with the type of the disturbance. For Tollmien-Schlichting waves, which are known to show only weak growth or decay, we

can assume that $|\alpha_i| \ll 1$ and so neglect the term involving the first derivative which appears in each of (3.17), (3.18). Similarly, we could replace $|\alpha|^2$ by $\alpha_r^2$ and so take conditions of the more simple form

$$\frac{\partial^2 v}{\partial x^2} + \alpha_r^2 v = 0 \tag{3.19}$$

$$\frac{\partial^2 \omega}{\partial x^2} + \alpha_r^2 \omega = 0\,. \tag{3.20}$$

In numerical simulations, Fasel [53] found that downstream boundary conditions of the type described above would allow two-dimensional small amplitude Tollmien-Schlichting waves to pass smoothly out of the computational domain, even when the value of $\alpha_r$ was poorly selected. Taking the crude approximation $\alpha_r = 0$ only degraded the results for about one and a half wavelengths upstream of the outflow boundary, provided the total streamwise extent of the computational domain was sufficiently large. When the disturbance amplitude is larger, and rapid nonlinear growth ensues, the use of such conditions is less satisfactory. Strong distortions may arise in the flowfield no matter how well $\alpha_r$ is chosen. See, for example, the reports of numerical simulations conducted by Fasel *et al* in [60]. For the problem under current consideration, such difficulties should not arise since the governing equations are always linearised. Furthermore, if a Tollmien-Schlichting wave, after propagating over a rigid/compliant wall join, has fully adapted to the presence of wall compliance before it passes out of the computational domain, then we may know in advance the value of $\alpha_r$ that ought to be used in the outflow boundary conditions. This can be computed directly from the Orr-Sommerfeld equation with an appropriate choice of wall parameters. In practice the value of $\alpha_r$ corresponding to rigid walls could be taken instead. (This value is already required in the specification of the upstream disturbance profiles.) The introduction of wall compliance should not cause any drastic change in $\alpha_r$ from its rigid wall value, and on the basis of Fasel's earlier work, it might be expected that the simulation results would not be very sensitive to the precise value of $\alpha_r$ selected for the boundary condition, at least for disturbances in

the linear regime. That this is in fact the case can be confirmed by examining the results obtained from numerical simulations conducted using various values of $\alpha_r$ in the outflow conditions. Similarly, we can numerically check the self-consistency of assumptions about the streamwise extent of the computational domain that is required to capture the spatial adaptation of the Tollmien-Schlichting waves.

Before leaving the subject of downstream boundary conditions, we make two further comments. Firstly, it may have been noted that no condition was written down for $u$. There is no need to specify, explicitly, any constraint on $u$ at the downstream boundary, for the same reason that prescription of $u$ is not necessary at the upstream boundary. Secondly, if the disturbance waves have large enough growth rates, for instance if travelling wave flutter is excited over particularly soft compliant walls, then the approximation given by ignoring the $\alpha_i$ terms in the conditions (3.17) and (3.18) may not be appropriate. It might be necessary to use these conditions exactly as they stand. (In fact the fuller form of the downstream boundary conditions turns out to be to be useful in other ways. It helps to minimise the upstream influence of the boundary and hence allows the use of computational domains of relatively short streamwise extent for code validation purposes.)

The physical boundary conditions imposed on the fluid at the channel walls have not yet been given a specific form. This is remedied in the next section when the motion of the compliant walls is addressed. In order to compute the wall motion, we first need to know the fluid perturbation pressure at the walls. Thus we now describe the calculation of the fluid perturbation pressure, which we denote by $p$. If the values of $v$ and $\omega$ are already known, $p$ can be found using the expression

$$p = -\int_0^y \left( \frac{\partial v}{\partial t} + U\frac{\partial v}{\partial x} + \frac{1}{R}\frac{\partial \omega}{\partial x} \right) dy \, . \tag{3.21}$$

This is obtained by integrating the $y$-momentum equation across the channel, observing that we can take $p = 0$ at the channel centre for disturbances with the chosen symmetry, and then using (3.3). In practice, the term involving the factor $1/R$ turns

out to be negligible, but for completeness we retain it here. An alternative expression for the pressure can be derived in a similar manner using the $x$-momentum equation, but it is less convenient for numerical computation since it involves streamwise integration. The fluid pressure at the upper wall of the channel can be found simply by setting $y = 1$ as the upper limit in the integral that appears in (3.21). For future reference, we write this result down separately as

$$p_w = -\int_0^1 \left( \frac{\partial v}{\partial t} + U\frac{\partial v}{\partial x} + \frac{1}{R}\frac{\partial \omega}{\partial x} \right) dy \tag{3.22}$$

where the suffix $w$ labels the upper wall. (The sign of the pressure is reversed at the lower wall.)

The need to determine the wall pressure accurately provides part of the motivation for using a vorticity-velocity formulation rather than a vorticity-streamfunction formulation for the fluid governing equations. If a streamfunction $\psi$ were used, $v$ would need to be replaced by the derivative $-\partial\psi/\partial x$ in computing the wall pressure via (3.22). A corresponding complication would also occur in implementing the boundary conditions on the fluid at the channel walls. A further disadvantage of the vorticity-streamfunction formulation appears in the implementation of downstream boundary conditions. To avoid an increase in the order of numerically computed derivatives, the condition (3.19) on $v$ would have to be replaced by a condition of exactly the same form applied to $\psi$. As discussed by Fasel in [65], such a constraint on $\psi$ would be physically more restrictive and consequently more prone to set up spurious reflections at the outflow boundary when used in numerical simulations.

If the wall pressure is computed using the expression (3.22), then it is possible to show that the following identity must hold

$$\frac{\partial p_w}{\partial x} = \frac{1}{R}\frac{\partial \omega_w}{\partial y} - \left( \frac{\partial u_w}{\partial t} + U'_w v_w \right) . \tag{3.23}$$

This can be derived as a formal consequence of the vorticity transport equation, the vorticity definition and the Poisson equation for $v$. It can also be obtained more

directly from the $x$-momentum equation and the Poisson equation for $u$. For the types of compliant wall that are considered below, the quantity contained within the brackets on the righthand side of (3.23) vanishes when the wall and fluid motion are matched to each other. (See the boundary conditions (3.27), (3.28).) We then have simply

$$\frac{\partial p_w}{\partial x} = \frac{1}{R}\frac{\partial \omega_w}{\partial y} \,. \tag{3.24}$$

This equality can be tested out for numerically determined flow-fields. Given simulation data for $v$ and $\omega$, the wall pressure can be computed using the integral expression (3.22), and its streamwise derivative taken. The result thus obtained may then be compared with the value expected from a calculation of the wall-normal derivative of the vorticity. Alternatively equation (3.24) could be verified in its streamwise integrated form

$$p_w = (p_w)_0 + \frac{1}{R}\int_0^x \frac{\partial \omega_w}{\partial y}\, dx \,, \tag{3.25}$$

where $(p_w)_0$ is the wall pressure at the upstream boundary. Either approach provides a stringent consistency check on the numerical scheme used to solve the fluid equations.

### 3.2.2 Wall motion

The compliant sections of the channel walls are modelled in a simple fashion as spring-backed plates. The use of this model for the case of a channel with constant wall properties has been described in some detail previously. For present purposes, we recall a few salient features. The equation governing the motion of the upper wall can be written as

$$m\frac{\partial^2 \eta}{\partial t^2} + \frac{d}{R}\frac{\partial \eta}{\partial t} + \frac{1}{R^2}\left(B\frac{\partial^4}{\partial x^4} - T\frac{\partial^2}{\partial x^2} + K\right)\eta = p_w \tag{3.26}$$

where $\eta$ is the vertical displacement of the wall from its equilibrium position at $y = 1$. The various wall parameters are defined as follows: $m$ is the plate mass per unit area, $d$ the wall damping coefficient, $B$ the flexural rigidity, $T$ the tension per

unit width and $K$ the spring constant. These parameters are all non-dimensionalised in such a way that the corresponding dimensional quantities remain fixed when the Reynolds number $R$ is varied by changing the centre-line velocity of the mean flow. The wall motion is driven solely by the perturbation fluid pressure $p_w$ acting at the wall; viscous stresses are neglected in the fluid forcing term on the right-hand side of (3.26). Furthermore, the wall model precludes any possibility of horizontal motion.

The wall motion is matched to that of the fluid via the linearised conditions

$$u_w = -U'_w \eta \tag{3.27}$$

$$v_w = \frac{\partial \eta}{\partial t} . \tag{3.28}$$

As before, the suffix $w$ indicates evaluation at $y = 1$, *i.e.* the unperturbed location of the upper wall. The right-hand sides of these equations give specific forms to the functions $\bar{u}$, $\bar{v}$ considered in the preceding section. In this way the fluid/compliant wall coupling is made explicit. The fluid pressure $p_w$ determines the time dependence of the wall displacement $\eta$ via equation (3.26), but $\eta$ in turn constrains the motion of the fluid by appearing in the boundary conditions (3.27), (3.28).

At the join between the rigid and compliant walls the boundary conditions for the wall motion are taken to be those for a hinge

$$\eta = \frac{\partial^2 \eta}{\partial x^2} = 0 . \tag{3.29}$$

There is no difficulty in implementing other forms for these conditions, e.g. for a compliant wall which is clamped at the join. At the downstream end of the computational domain, the boundary conditions on the wall follow from compatibility requirements with the constraints imposed on the fluid. They can be derived most simply if we suppose that

$$\frac{\partial^2 u}{\partial x^2} + 2\alpha_i \frac{\partial u}{\partial x} + |\alpha|^2 u = 0 \tag{3.30}$$

on the outflow boundary[3]. In particular, we assume this holds at the corner of the

[3]Instead of the same condition applied to $v$.

computational domain located at $x = l$, $y = 1$. Matching the fluid and wall motion by substituting for $u_w$ using the condition (3.27) then yields

$$\frac{\partial^2 \eta}{\partial x^2} + 2\alpha_i \frac{\partial \eta}{\partial x} + |\alpha|^2 \eta = 0 \,. \tag{3.31}$$

as the first constraint on the wall motion at the downstream boundary. Taking the $y$ derivative of the outflow condition (3.18) on the vorticity, and then using the fact that $\partial\omega/\partial y = \nabla^2 u$ we obtain

$$\nabla^2 \left( \frac{\partial^2 u}{\partial x^2} + 2\alpha_i \frac{\partial u}{\partial x} + |\alpha|^2 u \right) = 0 \tag{3.32}$$

which reduces to

$$\frac{\partial^2}{\partial x^2} \left( \frac{\partial^2 u}{\partial x^2} + 2\alpha_i \frac{\partial u}{\partial x} + |\alpha|^2 u \right) = 0 \tag{3.33}$$

on presumption that (3.30) holds at all $y$-locations on the downstream boundary. Thus, again using the relation (3.27), we can obtain

$$\frac{\partial^2}{\partial x^2} \left( \frac{\partial^2 \eta}{\partial x^2} + 2\alpha_i \frac{\partial \eta}{\partial x} + |\alpha|^2 \eta \right) = 0 \tag{3.34}$$

as the second condition to be applied to the wall at the end of the computational domain. As was the case with the conditions on the fluid, the derivatives multiplied by $\alpha_i$ may be neglected and $|\alpha|$ replaced by $\alpha_r$, provided the growth or decay rate is small. Finally, we note that for a finite-length compliant panel embedded within an otherwise rigid channel wall, there are no conditions to be applied on the wall at the outflow boundary. Instead we just need to apply the conditions for a rigid/compliant wall join at a second $x$-location within the computational domain.

## 3.3 Numerical Methods

Having detailed the mathematical formulation of our problem, we now turn to a discussion of its numerical discretisation, which will be arranged as follows. The methods used to discretise the governing equations for the fluid, and the procedures

employed to solve the resulting large system of equations, will be treated first. At this stage, the coupling between the fluid and the compliant-walls will only be specified in the most general terms. We will then go on to describe how the wall motion is discretised, and at the same time discuss the detailed arrangements required in order to match the wall and fluid motion.

### 3.3.1 Numerical discretisation of the fluid equations

The discretisation of the fluid equations is achieved using second-order finite-differences in time and the streamwise spatial direction, and a Chebyshev expansion across the channel. We begin with an account of the Chebyshev discretisation.

#### Chebyshev discretisation

The expansions for $\omega$, $v$ are restricted to even Chebyshev polynomials, in order to impose the required symmetry about the channel centre. Thus we write

$$\omega(x,y,t) = \frac{1}{2}\omega_1(x,t) + \sum_{k=2}^{N} \omega_k(x,t)\, T_{2(k-1)}(y) \tag{3.35}$$

$$v(x,y,t) = \frac{1}{2}v_1(x,t) + \sum_{k-2}^{N} v_k(x,t)\, T_{2(k-1)}(y) \tag{3.36}$$

where $T_n$ is the $n$-th Chebyshev polynomial, which may be defined via the relationship

$$T_n(\cos\theta) = \cos n\theta \; . \tag{3.37}$$

The expansion for $u$ would consist of odd Chebyshevs, but as noted previously, there is no need to solve directly for this component — it can be recovered from $\omega$, $v$ using (3.2).

The use of Chebyshev expansions in the $y$-direction facilitates the accurate resolution of disturbance profiles. The general advantages of using such spectral expansions in computational fluid dynamics are described by Canuto *et al* in [43]. For the particular problem under current consideration, it turns out to be possible to use the

Chebyshev expansions to derive a numerical discretisation which in some key respects takes the same form as the discretisation that would follow from using second-order finite-differences throughout. Thus, it will be seen that we may obtain the benefits of spectral accuracy without significantly increasing the computational costs. Furthermore, the use of Chebyshev expansions allows a precise evaluation of the integral across the channel that appears in the expression (3.22) for the fluid pressure at the wall. This gives a significant additional advantage, since the forcing of the wall motion by the fluid pressure is a crucial aspect of the problem that is being investigated numerically.

Before discretisation, the governing equations (3.1), (3.3) are first integrated twice, indefinitely, across the channel. The vorticity transport equation then becomes

$$\frac{\partial}{\partial t}\iint \omega + \frac{\partial}{\partial x}\iint U\omega + \iint U''v = \frac{1}{R}\left(\omega + \frac{\partial^2}{\partial x^2}\iint \omega\right) + c \tag{3.38}$$

whilst the Poisson equation for $v$ yields

$$v + \frac{\partial^2}{\partial x^2}\iint v = -\frac{\partial}{\partial x}\iint \omega + d \tag{3.39}$$

where $\iint f$ is shorthand for $\int_0^y \int_0^{y'} f(y'')\,dy''\,dy'$ and the functions $c = c(x,t)$, $d = d(x,t)$ are integration functions. (The occurrence of only a single integration function in each equation stems from the fact that we have $\partial\omega/\partial y = \partial v/\partial y = 0$ at the channel centre for disturbances with the selected symmetry.) As in the numerical discretisation of the Orr-Sommerfeld equation described earlier, such a procedure is adopted because the integral operators take a more convenient form than the corresponding differential operators, when they are applied to the Chebyshev expansions. It was noted in Section 2.2.3 that the second integral operator

$$f \to \iint f \tag{3.40}$$

takes the tridiagonal form

$$f_k \to \frac{1}{8}\left(\frac{f_{k-1}}{(k-1)(2k-3)} - \frac{4f_k}{(2k-3)(2k-1)} + \frac{f_{k+1}}{(k-1)(2k-1)}\right) \tag{3.41}$$

for $k \geq 2$, when it acts on Chebyshev coefficients[4]. If centred second-order finite differences had been used to discretise the $y$-derivatives which occur in the unmodified governing equations, then the differential operator $f \rightarrow \partial^2 f/\partial y^2$ that appears in place of (3.40) would also have taken a (much simpler) tridiagonal form, when represented in terms of nodal values. Because of this common tridiagonal structure, it is possible to solve the algebraic equations that arise from our mixed spectral/finite-difference approach using a procedure akin to the one which was successfully applied by Fasel [53] in his finite-difference scheme.

The operator $f \rightarrow Uf$ can be specified as

$$f_1 \rightarrow \frac{f_1 - f_2}{2} \ , \ f_k \rightarrow \frac{f_k}{2} - \left( \frac{f_{k+1} - f_{k-1}}{4} \right) \ \text{for } k \geq 2 \tag{3.42}$$

using the fact that the parabolic mean flow may be written in the form $U = (T_0 - T_2)/2$ and then applying the relationship

$$T_m T_n = \frac{1}{2} \left( T_{m+n} + T_{|m-n|} \right) \tag{3.43}$$

for the product of Chebyshev polynomials. Composing this mean flow multiplication with the second integral operator, we can then determine the action of

$$f \rightarrow \iint Uf \tag{3.44}$$

on the Chebyshev coefficients. This completes the description, in a Chebyshev representation, of all the operators that appear in the integrated form of the governing equations . (Note that $U'' = -2$, so no further work is required to specify the operator involving $U''$ which appears in the vorticity transport equation.)

Substituting the Chebyshev expansions for $\omega$ and $v$ into the the integrated vorticity transport equation (3.38) generates a new series of Chebyshev polynomials on each side of the equation. Matching the coefficients of these polynomials on both sides of the equation then gives a set of conditions on the expansion coefficients $\omega_k$,

[4]It will be seen that there is no necessity to specify the effect of this operator for $k = 1$.

$v_k$. This procedure can be repeated for the integrated Poisson equation (3.39) to obtain a further set of conditions. In this way, it is possible to derive two systems of equations which can be written as

$$\sum_{k=1}^{N} \left\{ I_{jk} \left( \frac{\partial \omega_k}{\partial t} - 2v_k - \frac{1}{R} \frac{\partial^2 \omega_k}{\partial x^2} \right) - \frac{1}{R} \omega_j + IU_{jk} \frac{\partial \omega_k}{\partial x} \right\} = 0 \qquad (3.45)$$

$$\sum_{k=1}^{N} \left\{ v_j + I_{jk} \left( \frac{\partial^2 v_k}{\partial x^2} + \frac{\partial \omega_k}{\partial x} \right) \right\} = 0 \qquad (3.46)$$

for $j = 2, \ldots, N$. The second integral operator (3.40) appears in the form of the tridiagonal matrix $(I_{jk})$, which is defined by (3.41). The matrix $(IU_{jk})$ represents the composite operator given by (3.44). (It can be seen via (3.42) that the parabolic profile of the mean flow leads $(IU_{jk})$ to take pentadiagonal form.) The $j$-th equation in each of (3.45), (3.46) arises from considering coefficients of $T_{2(j-1)}$. The $j = 1$ equations which could have been obtained by matching the coefficients of $T_0$ have been deliberately omitted[5]. This is because they involve the unknown integration constants $c$ and $d$. Instead, two further equations will be derived from the boundary conditions imposed on the fluid. In this way a system of $2N$ equations for the $2N$ expansion coefficients $\omega_k$, $v_k$ is obtained.

The action of the operators in the governing equations on the Chebyshev expansions for $\omega$, $v$ also generates the higher-order polynomials $T_{2N}$, $T_{2(N+1)}$. The coefficients of these polynomials are not matched together in any way; to do so would lead to an over-constrained system of equations. The residuals of these higher-order terms—defined by the difference between their respective coefficients on the left and right hand sides of the governing equations—may be used to measure the extent to which the finite-order approximations for $\omega$, $v$ fail to satisfy the governing equations exactly. Thus the numerical procedure adopted is a tau-method. The use of this method to discretise the Orr-Sommerfeld equation was described earlier in Section 2.2.3. It can be seen that the Chebyshev discretisation of the vorticity-velocity

[5]Hence there is no need to specify how the second integral operator acts on the lowest expansion coefficient.

equations is achieved in a very similar fashion. The main difference is that two second-order governing equations have replaced a single fourth-order equation.

It remains to describe the further constraints on the Chebyshev coefficients that replace the two equations that would have arisen from setting $j = 1$ in (3.45), (3.46). These constraints are derived from the integral and boundary conditions (3.8), (3.7) that need to be applied to $\omega$ and $v$ respectively. Substituting the Chebyshev expansions into these conditions yields

$$\sum_{k=1}^{N} q_k \left( \omega_k + \frac{\partial v_k}{\partial x} \right) = \bar{u} \tag{3.47}$$

$$\sum_{k=1}^{N} r_k v_k = \bar{v} \tag{3.48}$$

where $\bar{u}$, $\bar{v}$ are determined by the wall motion. The constants $q_k$, $r_k$ arise from considering integrals across the channel and values at the upper channel wall. They are defined as follows:

$$\begin{aligned} q_1 &= r_1 = \frac{1}{2} \\ q_{k+1} &= \int_0^1 T_{2k}(y)dy = -\frac{1}{4k^2 - 1} \\ r_{k+1} &= T_{2k}(1) = 1 \end{aligned} \tag{3.49}$$

The constraint on the vorticity, cast in the form of (3.47), can be used in conjunction with the set of equations (3.45) derived from the vorticity transport equation to find the expansion coefficients $\omega_k$, provided the values of $v_k$ are already given. Similarly, the boundary condition on $v$ specified via (3.48) may be applied, together with the set of equations (3.46) derived from the Poisson equation for $v$, to find the values of $v_k$ using known values of $\omega_k$. The determination of $\omega_k$, $v_k$ could thus be achieved using a process of iteration. Alternatively, the solution of the coupled system of equations could be attempted by a direct method, yielding both $\omega_k$, $v_k$ in a single computation. The latter approach is not taken. It will be seen that an iterative calculation of $\omega_k$, $v_k$ may be included within a marching procedure that is used to

obtain the streamwise variation. At this juncture it should be remembered that the Chebyshev coefficients are functions of both $x$ and $t$. We now address the streamwise and temporal aspects of the discretisation.

### Temporal and streamwise discretisation

Second-order finite-differences are used to approximate the $t$-derivative and the $x$-derivatives that appear in the governing equations. A fully implicit three-point backward difference scheme is applied to the time derivative, whilst all of the $x$-derivatives are discretised using centred differences. Implicit time discretisation is necessary in order to obtain numerical stability when resolving unsteady disturbances in a viscous fluid at high Reynolds numbers. (See for example the discussion given by Fasel [69], [65] which is directly concerned with the present problem situation. A broader treatment of implicit methods may be found in texts such as those of Canuto *et al* [43] and Fletcher [70].) The use of an implicit time discretisation may also be mandatory when the motion of the fluid is coupled, interactively, to the motion of a compliant wall. The computation of the coupled fluid/wall motion can be expected to be particularly prone to numerical instability.

If we introduce the notation

$$f^l_{,n}(y) = f(x_n, y, t_l) \tag{3.50}$$

where $f$ is a flow-field variable, then the finite-difference approximations can be defined as

$$\frac{\partial f^l}{\partial t}_{,n} = \frac{1}{2\Delta t}\left(3f^l_{,n} - 4f^{l-1}_{,n} + f^{l-2}_{,n}\right) \tag{3.51}$$

$$\frac{\partial f^l}{\partial x}_{,n} = \frac{1}{2\Delta x}\left(f^l_{,n+1} - f^l_{,n-1}\right) \tag{3.52}$$

$$\frac{\partial^2 f^l}{\partial x^2}_{,n} = \frac{1}{(\Delta x)^2}\left(f^l_{,n+1} - 2f^l_{,n} + f^l_{,n-1}\right) . \tag{3.53}$$

The space and time intervals $\Delta x$, $\Delta t$ are taken to be constant. In addition we will

write

$$f^l_{k,n} = f_k(x_n, t_l) \tag{3.54}$$

where $f_k$ is the $k$-th coefficient in the Chebyshev expansion of $f$.

Using the finite-difference approximations for the $x$ and $t$ derivatives, the system of equations obtained previously for the expansion coefficients $\omega_k$, $v_k$ can now be fully discretised. This yields, after some rearrangement,

$$\begin{aligned} \left\{ I_{jk}\left(3 + \frac{4\Delta t}{R(\Delta x)^2}\right) - 2\delta_{jk}\frac{\Delta t}{R} \right\} \omega^l_{k,n} + IU_{jk}\frac{\Delta t}{\Delta x}\left(\omega^l_{k,n+1} - \omega^l_{k,n-1}\right) & \\ -I_{jk}\left(4\,\omega^{l-1}_{k,n} - \omega^{l-2}_{k,n} + 4\Delta t\, v^l_{k,n} + \frac{2\Delta t}{R(\Delta x)^2}\left(\omega^l_{k,n+1} + \omega^l_{k,n-1}\right)\right) &= 0 \end{aligned} \tag{3.55}$$

$$\begin{aligned} \left(2I_{jk} - (\Delta x)^2\delta_{jk}\right) v^l_{k,n} & \\ -I_{jk}\left(v^l_{k,n+1} + v^l_{k,n-1} - \frac{\Delta x}{2}\left(\omega^l_{k,n+1} - \omega^1_{k,n-1}\right)\right) &= 0 \end{aligned} \tag{3.56}$$

$$q_k\left(\omega^l_{k,n} + \frac{1}{2\Delta x}\left(v^l_{k,n+1} - v^l_{k,n-1}\right)\right) = \bar{u}^l_n \tag{3.57}$$

$$r_k\, v^l_{k,n} = \bar{v}^l_n\,. \tag{3.58}$$

These four sets of equations are the discretisations of the vorticity transport equation, the Poisson equation for $v$, the vorticity integral constraint and the wall boundary condition on $v$, respectively. The summation convention is adopted for the repeated $k$-indices, *i.e.* there is an implied sum over the range $k = 1, \ldots N$. In (3.55), (3.56) the equation for $j = 1$ is omitted, just as before. The wall motion functions $\bar{u}$, $\bar{v}$ are discretised at the same $x$, $t$ values as the fluid.

It is convenient to define the vector of Chebyshev coefficients $\boldsymbol{\omega}^l_n = (\omega^l_{1,n}, \ldots, \omega^l_{N,n})^T$ and similarly for $\boldsymbol{v}^l_n$. For given values of $l$ and $n$, *i.e.* at a particular time instant and a chosen streamwise location, these vectors contain all the information necessary for specifying the disturbance profiles across the width of the channel. The discretised vorticity transport equation and vorticity integral constraint may be combined

together and re-written in terms of $\boldsymbol{\omega}_n^l$, $\boldsymbol{v}_n^l$ as

$$\mathbf{S}\boldsymbol{\omega}_n^l = \mathbf{L}\left(\boldsymbol{v}_n^l, \boldsymbol{\omega}_{n+1}^l, \boldsymbol{\omega}_{n-1}^l, \boldsymbol{\omega}_n^{l-1}, \boldsymbol{\omega}_n^{l-2}; \bar{u}_n^l, \boldsymbol{v}_{n+1}^l, \boldsymbol{v}_{n-1}^l\right) \tag{3.59}$$

where $\mathbf{S} = (S_{jk})$ is the matrix defined by

$$\begin{aligned} S_{1k} &= q_k \\ S_{jk} &= I_{jk}\left(3 + \frac{4\Delta t}{R(\Delta x)^2}\right) - 2\delta_{jk}\frac{\Delta t}{R}\ , \ \text{for } j \geq 2\,. \end{aligned} \tag{3.60}$$

The detailed structure of the vector-valued operator $\mathbf{L}$ can be obtained by inspection from (3.55), (3.57). The three quantities that follow the semi-colon in its list of arguments are needed for the imposition of the vorticity integral constraint. They only affect the value of the first component of $\mathbf{L}$. In a similar fashion, the discrete versions of the Poisson equation and boundary condition for $v$ can be re-written as

$$\mathbf{T}\boldsymbol{v}_n^l = \mathbf{M}\left(\boldsymbol{v}_{n+1}^l, \boldsymbol{v}_{n-1}^l, \boldsymbol{\omega}_{n+1}^l, \boldsymbol{\omega}_{n-1}^l; \bar{v}_n^l\right) \tag{3.61}$$

where in this case

$$\begin{aligned} T_{1k} &= r_k \\ T_{jk} &= 2I_{jk} - (\Delta x)^2\delta_{jk}\ , \ \text{for } j \geq 2. \end{aligned} \tag{3.62}$$

The operator $\mathbf{M}$ may be explicitly defined by examining the details of equations (3.56), (3.58). Its dependence on the function $\bar{v}$ is due to the inclusion of the wall boundary condition.

Both of the matrices $\mathbf{S}$, $\mathbf{T}$ are tridiagonal except for their first rows. This follows from the tridiagonal nature of $(I_{jk})$. Thus it is possible to invert equations (3.59), (3.61) to obtain the vectors $\boldsymbol{\omega}_n^l$, $\boldsymbol{v}_n^l$ using a slightly modified version of the Thomas algorithm. (Further details are given later.) This inversion, of course, assumes that the right-hand sides of the equations are already known, which is not in fact the case. However, such a procedure may still be utilised to provide the basis for

an iterative method. Introducing the notation $\omega_n^{l,i}$ *etc.* to indicate values obtained at the $i$-th iteration, we can cast equations (3.59), (3.61) in the form

$$\mathbf{T}\boldsymbol{v}_n^{l,i} = \mathbf{M}\left(\boldsymbol{v}_{n+1}^{l,i-1}, \boldsymbol{v}_{n-1}^{l,i}, \boldsymbol{\omega}_{n+1}^{l,i-1}, \boldsymbol{\omega}_{n-1}^{l,i}; \bar{v}_n^{l,i-1}\right) \tag{3.63}$$

$$\mathbf{S}\boldsymbol{\omega}_n^{l,i} = \mathbf{L}\left(\boldsymbol{v}_n^{l,i}, \boldsymbol{\omega}_{n+1}^{l,i-1}, \boldsymbol{\omega}_{n-1}^{l,i}, \boldsymbol{\omega}_n^{l-1}, \boldsymbol{\omega}_n^{l-2}; \bar{u}_n^{l,i-1}, \boldsymbol{v}_{n+1}^{l,i-1}, \boldsymbol{v}_{n-1}^{l,i}\right) . \tag{3.64}$$

The equation used to determine $\boldsymbol{v}_n^{l,i}$ precedes that for $\boldsymbol{\omega}_n^{l,i}$ since the first of these quantities is needed in the calculation of the latter, but not vice versa. The values of the functions $\bar{u}$, $\bar{v}$ are supplied from the solution of the wall motion equation at the previous level of iteration. (The wall motion calculation is described in the next section.)

The relations given in (3.63), (3.64) define a line iteration. For incremented values of the grid parameter $n$, *i.e.* at successively downstream locations, the variation of the flow fields across the channel is updated by re-calculating the Chebyshev vectors. The updated values determined at each streamwise position are immediately utilised in the calculation at the next streamwise position. When the Chebyshev vectors have been re-calculated at all positions down to the outflow boundary, the whole process is repeated, beginning again at the inflow. This streamwise marching procedure is very similar to the one successfully used by Fasel [53] in his finite-difference scheme. The main changes in the present case are that nonlinear terms have been neglected and the wall boundary conditions applied in a different fashion. (Nonlinearity could be included if so desired, but this would necessitate the calculation of products of Chebyshev series, and the consequent introduction of fast Fourier transforms for computational efficiency [43]. Otherwise, the approach taken would be same as that of Fasel; at each update the nonlinear terms would be calculated using values obtained from the previous iteration.)

As has previously been mentioned, the chosen method of Chebyshev discretisation retains the tridiagonality of Fasel's scheme, even though the detailed form of the matrices involved is more complicated. This means that the solution of the sets

of implicit equations defined at each streamwise location can still be achieved with limited computational expense. For Blasius flow, the use of Chebyshev polynomials would have to be preceded by a domain mapping to replace the semi-infinite range of the $y$-variable. This would destroy the tridiagonal nature of the system of equations obtained in the subsequent discretisation, and hence give rise to a less economic numerical scheme.

It remains to describe the numerical imposition of the inflow and outflow boundary conditions. At the inflow boundary located at $n = 0$ we simply take

$$\boldsymbol{v}_0^l = \Re\left(\boldsymbol{v}_{os} e^{-i\beta l \Delta t}\right) \tag{3.65}$$

$$\boldsymbol{\omega}_0^l = \Re\left(\boldsymbol{\omega}_{os} e^{-i\beta l \Delta t}\right) \tag{3.66}$$

where the constant vectors of Chebyshev coefficients $\boldsymbol{v}_{os}$, $\boldsymbol{\omega}_{os}$ define the profiles of the input disturbances. These are obtained from numerical solutions of the Orr-Sommerfeld equation via the relationships given in (3.13). As before, $\beta$ is the temporal frequency with which the fluid is forced. For the outflow boundary at $n = n_e$, we can discretise the conditions (3.19), (3.20) to obtain

$$\boldsymbol{v}_{n_e+1}^l - \left(2 - \alpha_r^2 (\Delta x)^2\right) \boldsymbol{v}_{n_e}^l + \boldsymbol{v}_{n_e-1}^l = 0 \tag{3.67}$$

$$\boldsymbol{\omega}_{n_e+1}^l - \left(2 - \alpha_r^2 (\Delta x)^2\right) \boldsymbol{\omega}_{n_e}^l + \boldsymbol{\omega}_{n_e-1}^l = 0\,. \tag{3.68}$$

Although these conditions are imposed at $n = n_e$, we view them as a means of determining values at the point $n = n_e + 1$, which strictly speaking lies outside the computational domain. A more usual procedure would be eliminate all references to such 'dummy' grid points by simultaneously applying the boundary conditions and the governing equations at the boundary location. The set of equations to be solved at the boundary would then have a different structure to the one applying in the interior of the domain. In the present problem, adopting such an approach would bring undue complication to the numerical scheme. Instead, we will update the values at $n = n_e$ in exactly the same fashion as for interior points, *i.e.* by solving

equations (3.63), (3.64), then afterwards update the values at the additional point $n = n_e + 1$ using the boundary conditions in the form

$$v^{l,i}_{n_e+1} = \left(2 - \alpha_r^2(\Delta x)^2\right) v^{l,i}_{n_e} - v^{l,i}_{n_e-1} \tag{3.69}$$

$$\omega^{l,i}_{n_e+1} = \left(2 - \alpha_r^2(\Delta x)^2\right) \omega^{l,i}_{n_e} - \omega^{l,i}_{n_e-1} \,. \tag{3.70}$$

If in practice this gives convergent behaviour, it should yield the same numerical results as a procedure which makes no use of spurious grid points.

### Line iteration solution algorithm

We complete the description of the numerical scheme for the fluid with an account of the modified Thomas algorithm used to solve the implicit sets of equations that occur at each streamwise location. Both of the matrix equations (3.63), (3.64) are tridiagonal except for the first row. They can be written in the general form

$$\begin{bmatrix} d_1 & d_2 & d_3 & \cdot & d_k & \cdot & d_{N-1} & d_N \\ a_2 & b_2 & c_2 & & & & & \\ & a_3 & b_3 & c_3 & & & & \\ & & \cdot & \cdot & \cdot & & & \\ & & & a_k & b_k & c_k & & \\ & & & & \cdot & \cdot & \cdot & \\ & & & & & a_{N-1} & b_{N-1} & c_{N-1} \\ & & & & & & a_N & b_N \end{bmatrix} \begin{bmatrix} w_1 \\ w_2 \\ w_3 \\ \cdot \\ w_k \\ \cdot \\ w_{N-1} \\ w_N \end{bmatrix} = \begin{bmatrix} e \\ f_2 \\ f_3 \\ \cdot \\ f_k \\ \cdot \\ f_{N-1} \\ f_N \end{bmatrix} \tag{3.71}$$

where $\mathbf{w} = (w_1, w_2, \ldots, w_N)^T$ is the unknown vector of Chebyshev coefficients. The constants $a_k$, $b_k$, $c_k$, $d_k$ are fixed in advance by the discretisation parameters and the selected Reynolds number $R$. For the equation used to update the normal velocity component, the constants depend only on the value of $\Delta x$. For the equation applied in updating the vorticity, they are also functions of $\Delta t$ and $R$. The quantities $e$, $f_k$ on the righthand side of (3.71) represent the components of one or the other of the

vector-valued operators **L**, **M**. They need to be calculated afresh on each occasion that a solution for **w** is sought.

Using the $N$-th equation contained in (3.71), we can eliminate $w_N$ from the $(N-1)$-th equation. The modified equation thus derived can then be used to remove $w_{N-1}$ from the $(N-2)$-th equation, and so on until $w_3$ is removed from second equation. In this fashion we can obtain

$$\begin{bmatrix} d_1 & d_2 & d_3 & \cdot & d_k & \cdot & & d_{N-1} & d_N \\ a_2 & \beta_2 & & & & & & & \\ & a_3 & \beta_3 & & & & & & \\ & & \cdot & \cdot & & & & & \\ & & & a_k & \beta_k & & & & \\ & & & & \cdot & \cdot & & & \\ & & & & & & a_{N-1} & \beta_{N-1} & \\ & & & & & & & a_N & \beta_N \end{bmatrix} \begin{bmatrix} w_1 \\ w_2 \\ w_3 \\ \cdot \\ w_k \\ \cdot \\ w_{N-1} \\ w_N \end{bmatrix} = \begin{bmatrix} e \\ \gamma_2 \\ \gamma_3 \\ \cdot \\ \gamma_k \\ \cdot \\ \gamma_{N-1} \\ \gamma_N \end{bmatrix} \tag{3.72}$$

where $\beta_k$, $\gamma_k$ are defined by

$$\begin{aligned} \beta_N &= b_N \ , \ \gamma_N = f_N \\ \beta_k &= b_k - \frac{c_k}{\beta_{k+1}} a_{k+1} \ , \ \gamma_k = f_k - \frac{c_k}{\beta_{k+1}} \gamma_{k+1} \ , \ \text{for } k = N-1, \ldots, 2. \end{aligned} \tag{3.73}$$

During this backward sweep we can also successively eliminate the terms in the first equation

$$d_1 w_1 + d_2 w_2 + \ldots + d_{N-1} w_{N-1} + d_N w_N = e$$

to obtain, after $N-k$ steps

$$d_1 w_1 + d_2 w_2 + \ldots + d_{k-1} w_{k-1} + \delta_k w_k = \epsilon_k$$

where

$$\begin{aligned} \delta_N &= d_N \ , \ \epsilon_N = e \\ \delta_k &= d_k - \frac{\delta_{k+1}}{\beta_{k+1}} a_{k+1} \ , \ \epsilon_k = \epsilon_{k+1} - \frac{\delta_{k+1}}{\beta_{k+1}} \gamma_{k+1} \ , \ \text{for } k = N-1, \ldots, 1. \end{aligned} \tag{3.74}$$

Thus we can manipulate equation (3.71) into the form

$$\begin{bmatrix} \delta_1 & & & & & & \\ a_2 & \beta_2 & & & & & \\ & a_3 & \beta_3 & & & & \\ & & \cdot & \cdot & & & \\ & & & a_k & \beta_k & & \\ & & & & \cdot & \cdot & \\ & & & & a_{N-1} & \beta_{N-1} & \\ & & & & & a_N & \beta_N \end{bmatrix} \begin{bmatrix} w_1 \\ w_2 \\ w_3 \\ \cdot \\ w_k \\ \cdot \\ w_{N-1} \\ w_N \end{bmatrix} = \begin{bmatrix} \epsilon_1 \\ \gamma_2 \\ \gamma_3 \\ \cdot \\ \gamma_k \\ \cdot \\ \gamma_{N-1} \\ \gamma_N \end{bmatrix} . \tag{3.75}$$

This is then readily solved using the forward sweep

$$w_1 = \frac{\epsilon_1}{\delta_1} \ , \ w_k = \frac{(\gamma_k - a_k w_{k-1})}{\beta_k} \ , \ \text{for } k = 2, \ldots, N. \tag{3.76}$$

Since the matrix elements $a_k$, $b_k$, $c_k$, $d_k$ are fixed for a given discretisation of the governing equations and value of the Reynolds number, so are $\beta_k$, $\delta_k$. All of these quantities are independent of the streamwise position and do not vary in time. Once they have been calculated and stored, along with various of their ratios, they can then be used again and again without alteration. Thus the repeated solution of the implicit equations (3.63), (3.64) to update the velocity and vorticity fields may be achieved in a computationally efficient manner. Finally, we note that the elimination scheme described above has always proved to be numerically stable when applied in the present context. If we had $d_k = 0$ for $k \geq 3$, *i.e.* if the first row in (3.71) was also of tridiagonal form, then the scheme would reduce to the usual Thomas algorithm, which is stable for a diagonally dominant matrix. Inspection of the detailed structure of the particular matrices $(S_{jk})$, $(T_{jk})$ used in the current application reveals that they are diagonally dominant after the first row.

Before turning to the numerical discretisation of the wall motion equation, we describe the calculation of the fluid pressure at the wall. Substituting the Chebyshev

expansions for $v$, $\omega$ into the expression (3.22) gives

$$p_w = -\sum_{k=1}^{N} \left\{ q_k \left( \frac{\partial v_k}{\partial t} + \frac{1}{R} \frac{\partial \omega_k}{\partial x} \right) + s_k \frac{\partial v_k}{\partial x} \right\} \tag{3.77}$$

where the constants $s_k$ are given by

$$s_1 = \frac{1}{3} \ , \ \ s_{k+1} = \int_0^1 U(y) T_{2k}(y)\, dy = \frac{6}{(4k^2-9)(4k^2-1)} \ . \tag{3.78}$$

The constants $q_k$ have already been defined in (3.49). The $x$ and $t$ derivatives appearing in (3.77) can be discretised in the same manner as before.

### 3.3.2 Discretisation of the wall motion equation

The matching of the wall and fluid motion via the relations (3.27), (3.28) requires that we define

$$\bar{u} = -U_w' \eta \tag{3.79}$$

$$\bar{v} = \frac{\partial \eta}{\partial t} \tag{3.80}$$

as the functions appearing in the integral constraint on the vorticity and the normal velocity component boundary condition. Values for these functions must be supplied if the matrix equations (3.63), (3.64) are to be used to update the fluid velocity and vorticity at successive streamwise locations. From the updated values for the flow fields, the fluid pressure at the wall can be recalculated using (3.77). In turn, this updated wall pressure may be used in a discrete version of the wall motion equation to obtain revised values for the wall displacements and velocities. Using these to re-specify $\bar{u}$, $\bar{v}$, the whole procedure can then be repeated. Unfortunately, attempts to implement such a scheme using a straightforward discretisation of the wall motion equation were found to lead to numerical instability. The iterative loop used to couple the fluid and wall motion failed to converge. As will be described shortly, this difficulty was initially overcome using an assumption of time periodicity to modify the formulation of the equation governing the wall motion.

For the situation of prime interest in the present work, involving, as it does, the *spatial* adaptation of a Tollmien-Schlichting wave, assumptions concerning time periodicity would not appear to be over restrictive. In general, for a convective instability, it should be possible to analyse any disturbance displaying complicated temporal behaviour into a superposition of time-periodic modes, each defined by a particular temporal frequency. Provided the disturbance remains in the linear regime, no interaction between modes with differing frequencies can occur, so it becomes acceptable to treat them independently. Such an approach is implicit in seeking solutions to the Orr-Sommerfeld equation in the form of spatially growing or decaying normal modes. However, if absolute instabilities are also possible, assumptions about time periodicity need to be treated with caution. For instance, we would not necessarily expect to find time-periodic disturbances propagating over compliant walls where the wall parameters and Reynolds number are such that a merger of the Tollmien-Schlichting mode of instability with travelling wave flutter is anticipated. The same reservations would apply when divergence is predicted. Such remarks notwithstanding, the time-periodic case remains central to the problem addressed in the present studies. We are interested in studying situations where the compliant-wall stiffness and inertia parameters are chosen to yield a stabilising effect on Tollmien-Schlichting waves, but the walls are not made so soft that flow-induced surface instabilities are introduced. Thus, we aim to explore regions of parameter space where time-aperiodic motion can plausibly be excluded. (The selection of appropriate wall properties may be made under the guidance of the linear stability analysis which was described earlier.)

**Restriction to time-periodic wall motion**

The considerations outlined immediately above suggested a preliminary restriction in the scope of the simulations to cases where the compliant walls were expected to have a time-periodic response to a time-periodic forcing imposed on the fluid at the inflow. This limitation facilitated the development of a numerically stable scheme

which successfully incorporated the interactive coupling between the fluid and wall motion; the iterative loop used to implement the coupling could be made to converge. In the first instance, an assumed periodic feature of the wall motion was used to derive a restrictive form for the wall equation. Building on results obtained in such fashion, it then proved possible to devise a numerical method which avoided any need to limit, artificially, the possible behaviour of the wall. Thus, although the technical difficulties that motivated the use of a modified form for the wall motion equation were eventually resolved, an account of the numerical scheme developed from this more limited basis will be given first. Such an account provides a good starting point for describing how the general case was tackled.

If we assume that the wall displacement satisfies the condition $\partial^2\eta/\partial t^2 = -\beta^2\eta$, where $\beta$ is the frequency of the disturbances entering the fluid at the upstream boundary, then the wall motion equation may be cast in the form

$$-m\beta^2\eta + \frac{d}{R}\frac{\partial\eta}{\partial t} + \frac{1}{R^2}\left(B\frac{\partial^4}{\partial x^4} - T\frac{\partial^2}{\partial x^2} + K\right)\eta = p_w \qquad (3.81)$$

$$\frac{\partial}{\partial t}\left(\frac{\partial\eta}{\partial t}\right) = -\beta^2\eta\,. \qquad (3.82)$$

These two equations can be viewed as determining the evolution of the wall displacements and velocities respectively. This interpretation may be made more explicit if we replace $\partial\eta/\partial t$ by a new dependent variable $\xi$ and then restate the equations as

$$-m\beta^2\eta + \frac{d}{R}\xi + \frac{1}{R^2}\left(B\frac{\partial^4}{\partial x^4} - T\frac{\partial^2}{\partial x^2} + K\right)\eta = p_w \qquad (3.83)$$

$$\frac{\partial\xi}{\partial t} = -\beta^2\eta\,. \qquad (3.84)$$

We will treat the equations in this latter form as governing equations for the quantities $\eta, \xi$. They may be used in conjunction with the definitions

$$\bar{u} = -U'_w\eta \qquad (3.85)$$

$$\bar{v} = \xi \qquad (3.86)$$

to give an alternative specification of the coupling between the fluid and the wall motion. This way of formulating the coupling avoids any direct reference to the wall velocity $\partial\eta/\partial t$. However, the numerical results obtained from such an approach will only be physically meaningful if in practice the wall velocity may be identified with the quantity $\xi$.

Because of the time periodicity assumption used in their derivation, equations (3.83), (3.84) are not fully equivalent to the original form of the wall motion governing equation. Although they certainly imply that

$$m\frac{\partial\xi}{\partial t} + +\frac{d}{R}\xi + \frac{1}{R^2}\left(B\frac{\partial^4}{\partial x^4} - T\frac{\partial^2}{\partial x^4} + K\right)\eta = p_w \tag{3.87}$$

the equality of $\xi$ and $\partial\eta/\partial t$ cannot always be inferred. In fact, for the case of an undamped wall, if $\tilde{\eta}(x,t)$, $\tilde{\xi}(x,t)$ are solutions of equations (3.83), (3.84) then so are $\tilde{\eta}(x,t)$, $\tilde{\xi}(x,t) + f(x)$ where $f$ is an arbitrary function of the streamwise position. Thus we may find solutions that only satisfy a relation of the form

$$\xi = \frac{\partial\eta}{\partial t} + f\ . \tag{3.88}$$

Such solutions will be of little physical significance unless measures can be taken to ensure that $f$ vanishes. In practice this turns out to be possible. If the solution obtained for $\xi$ settles down to time-periodic behaviour, in the sense that it eventually obeys the condition $\partial^2\xi/\partial t^2 = -\beta^2\xi$, then it follows directly from (3.84) that we must have $\xi = \partial\eta/\partial t$. Furthermore $\eta$ will also be time-periodic with the same temporal frequency. The behaviour that precedes the attainment of time periodicity in $\eta$, $\xi$ will not be physically realistic. It may be viewed as a form of numerical transience, introduced through the use of amended governing equations for the wall motion.

Having given some account of the limitations that their usage entails, we now describe how the equations which determine the evolution of $\eta$, $\xi$ are discretised. As with the fluid governing equations, second-order finite-differences are employed. These are centred for the streamwise derivatives and implicit for the time evolution.

To simplify the notation, no explicit reference will be made to the iteration that is used to incorporate the interactive coupling between the fluid and wall motion. Thus, it should be remembered that the wall motion equations will need to be solved on each occasion that updated values for the wall pressure are supplied. The values of $\eta$, $\xi$ that are then calculated will in turn have to be passed back to the routine used to determine the fluid flow-fields.

In order to discretise the governing equation for $\eta$ it is convenient to first define the two-component quantities

$$\boldsymbol{\eta} = \begin{bmatrix} \eta \\ \frac{\partial^2 \eta}{\partial x^2} \end{bmatrix} \quad , \quad \mathbf{p} = \begin{bmatrix} 0 \\ p_w - \frac{d}{R}\xi \end{bmatrix} \tag{3.89}$$

Equation (3.83) can then be written in the form

$$\frac{1}{R^2}\left(B\frac{\partial^2}{\partial x^2} + \mathbf{A}\right)\boldsymbol{\eta} = \mathbf{p} \tag{3.90}$$

where

$$\mathbf{A} = \begin{bmatrix} 0 & -B \\ K - m\beta^2 R^2 & -T \end{bmatrix} .$$

At the location of a hinged join between rigid and compliant sections of the channel walls, the boundary conditions (3.29) imposed on the wall motion can be stated in the form

$$\boldsymbol{\eta} = 0 \, . \tag{3.91}$$

The conditions (3.31), (3.34) applied at the downstream boundary may be rewritten as

$$\left(\frac{\partial^2}{\partial x^2} + \alpha_r^2\right)\boldsymbol{\eta} = 0 \tag{3.92}$$

where terms that involve the growth rate $\alpha_i$ have been neglected. Substituting (3.92) into the recast form of the governing equation (3.90) yields the relation

$$\frac{1}{R^2}\left(-B\alpha_r^2\,\mathbf{I} + \mathbf{A}\right)\boldsymbol{\eta} = \mathbf{p} \, , \tag{3.93}$$

where $\mathbf{I}$ is the $2 \times 2$ identity matrix. This implicitly determines $\boldsymbol{\eta}$ at the location of the downstream boundary. It may be inverted to give

$$\boldsymbol{\eta} = \mathbf{C}\,\mathbf{p} \tag{3.94}$$

with

$$\mathbf{C} = \left(\frac{1}{R^2}\left(B\alpha_r^4 + T\alpha_r^2 + K\right) - m\beta^2\right)^{-1} \begin{bmatrix} 0 & 1 \\ 0 & -\alpha_r^2 \end{bmatrix}$$

(The fact that the first entry in $\mathbf{p}$ is always zero means that we can choose to put zeros in the first column of the matrix $\mathbf{C}$.)

Now that the governing equation for $\eta$ and its associated boundary conditions have been written in terms of $\boldsymbol{\eta}$, it is a simple matter to obtain a discretisation. Taking the second-order centred approximation[6]

$$\left(\frac{\partial^2 \boldsymbol{\eta}}{\partial x^2}\right)_n = \frac{1}{(\Delta x)^2}\left(\boldsymbol{\eta}_{n+1} - 2\boldsymbol{\eta}_n + \boldsymbol{\eta}_{n-1}\right)\,, \tag{3.95}$$

with the suffixes labelling the streamwise position, the wall motion equation for $\boldsymbol{\eta}$ becomes

$$\frac{1}{R^2}\left(\frac{B}{\Delta x^2}\mathbf{I}\left(\boldsymbol{\eta}_{n+1} + \boldsymbol{\eta}_{n-1}\right) + \left(\mathbf{A} - \frac{2B}{\Delta x^2}\mathbf{I}\right)\boldsymbol{\eta}_n\right) = \mathrm{p}_n\,. \tag{3.96}$$

Incorporating the boundary conditions at each end of the wall, we can then obtain

[6]This is fully equivalent to using the second-order approximations

$$\left(\frac{\partial^2 \eta}{\partial x^2}\right)_n = \frac{1}{(\Delta x)^2}\left(\eta_{n+1} - 2\eta_n + \eta_{n-1}\right)$$
$$\left(\frac{\partial^4 \eta}{\partial x^4}\right)_n = \frac{1}{(\Delta x)^4}\left(\eta_{n+2} - 4\eta_{n+1} + 6\eta_n - 4\eta_{n-1} + \eta_{n-2}\right)\,.$$

the system of equations

$$\begin{bmatrix} \left(\frac{(\Delta x)^2}{B}\mathbf{A} - 2\mathbf{I}\right) & \mathbf{I} & & & & & \\ \mathbf{I} & \left(\frac{(\Delta x)^2}{B}\mathbf{A} - 2\mathbf{I}\right) & \mathbf{I} & & & & \\ & \ddots & \ddots & & & & \\ & & \ddots & \ddots & & & \\ & & & \mathbf{I} & \left(\frac{(\Delta x)^2}{B}\mathbf{A} - 2\mathbf{I}\right) & \mathbf{I} & \\ & & & & \mathbf{I} & \left(\frac{(\Delta x)^2}{B}\mathbf{A} - 2\mathbf{I}\right) \end{bmatrix}$$

$$\times \begin{bmatrix} \boldsymbol{\eta}_{n_j+1} \\ \boldsymbol{\eta}_{n_j+2} \\ \cdot \\ \cdot \\ \boldsymbol{\eta}_{n_e-2} \\ \boldsymbol{\eta}_{n_e-1} \end{bmatrix} = \frac{R^2(\Delta x)^2}{B} \begin{bmatrix} \mathbf{p}_{n_j+1} \\ \mathbf{p}_{n_j+2} \\ \cdot \\ \cdot \\ \mathbf{p}_{n_e-2} \\ \mathbf{p}_{n_e-1} \end{bmatrix} - \begin{bmatrix} 0 \\ 0 \\ \cdot \\ \cdot \\ 0 \\ \mathbf{C}\,\mathbf{p}_{n_e} \end{bmatrix} . \quad (3.97)$$

The positions denoted by $n_j$, $n_e$ correspond to the wall join and downstream boundary, respectively. All quantities are evaluated at the same point in time, since there is no time derivative to be considered.

The block-tridiagonal character of the system of equations (3.97) means that it can be efficiently solved using a version of the Thomas algorithm. The only change from the usual procedure is that the forward and backward elimination sweeps now involve $2 \times 2$ matrices and two-component vectors instead of scalar quantities. Because there is no time dependence in the entries of the block-tridiagonal matrix, the various multipliers that are utilised in the algorithm need only be calculated on a single occasion. The repeated solution of (3.97) can then be achieved with minimal computational cost[7].

[7]It is interesting to note that the use of the fourth-order compact approximation

$$\left(\frac{\partial^2 \boldsymbol{\eta}}{\partial x^2}\right)_{n+1} + 10\left(\frac{\partial^2 \boldsymbol{\eta}}{\partial x^2}\right)_{n} + \left(\frac{\partial^2 \boldsymbol{\eta}}{\partial x^2}\right)_{n-1} = \frac{12}{(\Delta x)^2}\left(\boldsymbol{\eta}_{n+1} - 2\boldsymbol{\eta}_n + \boldsymbol{\eta}_{n-1}\right)$$

would involve only a very slight modification of the solution procedure developed for the second-order

The numerical solution of the equation (3.84) used to determine the time evolution of $\xi$ is extremely simple. Applying the same three-point backward difference approximation as was used to discretise the time derivative in the fluid governing equations, we obtain

$$\xi^l = \frac{1}{3}\left(4\xi^{l-1} - \xi^{l-2}\right) - \frac{2\Delta t\beta^2}{3}\eta^l \tag{3.98}$$

where the superscripts label the time variation and all quantities are evaluated at the same streamwise position. Thus $\xi$ can be found once the value of $\eta$ has been determined. However, it may be noted that the governing equation used to obtain $\eta$ includes a wall damping term that depends upon $\xi$. The weak coupling that this term induces can be accounted for by substituting the value of $\xi$ calculated at the previous iteration level.

At this point it is useful to review the overall structure of the numerical solution scheme which has now been described. The evolution of the coupled flow-wall system is computed using an implicit time discretisation, which necessitates the application of an iterative procedure at every time step. Iteration is utilised for two distinct purposes. Firstly, to solve the very large system of equations that arises from discretising the fluid governing equations. Secondly, to match the solution thus obtained to the pressure driven motion of the wall. Both of these tasks are achieved within a single iteration loop. In the first stage, the fluid flow-fields $\omega$, $v$ are updated through a streamwise marching process. Values for the wall displacements $\eta$ and velocities $\xi$ taken from the previous iteration are employed in the integral/boundary conditions imposed on the fluid. The structure of the sets of equations to be solved at each streamwise position is summarised in the relations (3.63), (3.64). When $\omega$, $v$ have been updated at all locations, the fluid pressure $p_w$ at the wall is re-calculated via

scheme. The block-tridiagonal character of the discretisation can be retained, so the computational demands are not significantly altered. In practice, apart from some possible improvement in robustness, there is little to be gained from using a fourth-order approximation for the wall motion equation, unless the fluid pressure that acts on the wall is calculated to the same degree of accuracy.

the fully discretised version of (3.77). The updated wall pressure can then be used (in conjunction with values of $\xi$ from the previous iteration for the case of non-zero wall damping) to obtain revised values for the wall displacements. This requires the solution of the set of equations defined by (3.97). The updated values for $\eta$ can in turn be used to re-calculate the values of $\xi$ via the relation (3.98). The revised values of $\eta$, $\xi$ are then passed back to the fluid update routine, and the whole process repeated until a converged solution is found. The same iterative procedure needs to be applied all over again at the next time step.

### Formulation for general wall motion

It should be recalled that the compliant wall model used in the numerical scheme described above has an in-built presumption that the wall motion is eventually time-periodic. As previously remarked, until or unless the wall displays such behaviour, the numerically computed evolution for the coupled wall and fluid will not necessarily be physically meaningful. In practice, it was often found that the wall motion became periodic within a computationally acceptable time-scale. The simulations were routinely initiated using null values for the fluid perturbation fields and undisturbed compliant walls. When the fluid was subsequently subjected to time-periodic forcing across the upstream boundary, time-periodic behaviour was typically observed throughout the whole computational domain once the leading front of the fluid disturbance had propagated down the streamwise length of the domain and out through the downstream boundary. Only from such times onward would the computed behaviour be expected to be of physical significance. Unfortunately, for some compliant wall parameters of interest, the time elapsed before periodic behaviour was attained could become much longer. Because of this, and for further reasons which will be indicated later, it was decided to develop a numerical scheme which avoided the need to build restrictive assumptions into the wall model. We now give an account of this more general scheme.

If we substitute the boundary condition (3.28) on the normal velocity component of the fluid into the unmodified form of the governing equation for the wall motion (3.26), and then utilise the expression (3.22) for the fluid pressure at the location of the wall, we can obtain the following relationship

$$\frac{\partial}{\partial t}\left(mv_w + \int_0^1 v\,dy\right) + \frac{d}{R}v_w + \frac{1}{R^2}\left(B\frac{\partial^4}{\partial x^4} - T\frac{\partial^2}{\partial x^2} + K\right)\eta = -\frac{\partial}{\partial x}\int_0^1 \left(Uv + \frac{1}{R}\omega\right)\,dy\,. \tag{3.99}$$

This may be interpreted as an evolution equation for the total momentum of the channel in the wall-normal direction,

$$\mu = mv_w + \int_0^1 v\,dy\,, \tag{3.100}$$

*i.e.* for the sum of the wall and the fluid momenta (more strictly speaking for each half-width of the channel). Such an interpretation is instructive when considering the numerical stability requirements for coupling together the fluid and wall motion. Earlier studies for the case a compliant wall interacting with an inviscid flow (see, for example, Lucey [71] and Lucey & Carpenter [46]) have highlighted the need to combine terms representing wall inertia and hydrodynamic inertia, in order to achieve convergence in numerical solution procedures. Roughly speaking, if wall and fluid inertia terms are separated so that they lie on opposite sides of any equation employed in an iterative method, then it is possible that the dominance of one over the other will cause a failure of the iteration to converge.

In the light of the comments above, one possible approach would be to treat $\mu$ as a new dependent variable governed by

$$\frac{\partial \mu}{\partial t} = -\left\{\frac{d}{R}v_w + \frac{1}{R^2}\left(B\frac{\partial^4}{\partial x^4} + T\frac{\partial^2}{\partial x^2} + K\right)\eta + \frac{\partial}{\partial x}\int_0^1 \left(Uv + \frac{1}{R}\omega\right)\,dy\right\}\,. \tag{3.101}$$

Consequently, we could view the relation

$$\frac{\partial \eta}{\partial t} = v_w \tag{3.102}$$

as an evolution equation for $\eta$, rather than taking it as the boundary condition on $v$. It then becomes necessary to find an alternative condition to be imposed on the normal velocity component. This is obtained simply by using (3.100) as a constraint on the normal velocity, instead of viewing it as definition. The integral constraint on the vorticity may be applied as before, except that the values of $\eta$ required for its implementation are now determined via (3.102). In such a manner, it is possible to give an alternative specification of the coupling between the wall and fluid motion. It is straightforward to show that this is fully equivalent to the coupling specified in the original formulation of the problem (without any assumptions of time periodicity). In a sense, all that is involved is a rearrangement and reinterpretation of the wall motion governing equation and fluid boundary conditions.

Attempts were made to develop a numerical scheme that coupled the wall and fluid together in the fashion indicated above. Though not entirely unsuccessful, they yielded unsatisfactory results, particularly when non-negligible values of the wall bending stiffness $B$ were employed. However, experimentation along the same lines eventually led to the development of a reliable scheme. Rather than retrace all the details of the path that led to its introduction, we will define the scheme in its final form and comment upon various of its features. The subscripts and superscripts used to denote different aspects of the discretisation remain as before. (In the interests of brevity, we will omit labels which take same the value for all the terms in a given equation.)

If the previously defined three-point backward finite-difference scheme is used to discretise the time derivatives in each of (3.101) and (3.102), then we obtain the relations

$$\mu^l = \frac{1}{3}\left(4\mu^{l-1} - \mu^{l-2}\right) - \frac{2\Delta t}{3}\left\{\frac{d}{R}v_w^l + \mathcal{K}\eta^l + \frac{\partial}{\partial x}\int_0^1 \left(Uv^l + \frac{1}{R}\omega^l\right) dy\right\} \tag{3.103}$$

$$\eta^l = \frac{1}{3}\left(4\eta^{l-1} - \eta^{l-2}\right) + \frac{2\Delta t}{3}v_w^l \tag{3.104}$$

where $\mathcal{K}$ is shorthand for the wall stiffness operator

$$\mathcal{K} = \frac{1}{R^2}\left(B\frac{\partial^4}{\partial x^4} - T\frac{\partial^2}{\partial x^2} + K\right) . \tag{3.105}$$

Eliminating $\eta^l$ from the first relation by substituting the second, we can derive the equality

$$\begin{aligned}\mu^l + \left(\frac{2d\Delta t}{3R} + \frac{4(\Delta t)^2}{9}\mathcal{K}\right)v_w^l &= \frac{1}{3}\left(4\mu^{l-1} - \mu^{l-2}\right) - \frac{2\Delta t}{9}\left(4\mathcal{K}\eta^{l-1} - \mathcal{K}\eta^{l-2}\right) \\ &- \frac{2\Delta t}{3}\frac{\partial}{\partial x}\int_0^1 \left(Uv^l + \frac{1}{R}\omega^l\right) dy . \end{aligned} \tag{3.106}$$

This equation will subsequently be used to impose the wall boundary condition required for the normal velocity component of the fluid. It explicitly accounts for an indirect dependence between the values taken by $v^l$ and the values of the wall stiffness term, $\mathcal{K}\eta^l$. By assembling the term involving $\mathcal{K}v_w^l$ alongside the term associated with the combined wall and fluid inertia, it proves possible to obtain convergence in the iteration used to match the wall and fluid motion.

Using centred second-order finite-differences, the streamwise derivatives in the wall stiffness operator $\mathcal{K}$ can be discretised to give

$$(\mathcal{K}f)_n = K_0 f_n - K_1\left(f_{n+1} + f_{n-1}\right) + K_2\left(f_{n+2} + f_{n-2}\right) \tag{3.107}$$

where the function $f$ denotes either $\eta$ or $v_w$, and the three constants $K_{i=0,1,2}$ take the form

$$\begin{aligned} K_0 &= \frac{1}{R^2}\left(\frac{6B}{(\Delta x)^4} + \frac{2T}{(\Delta x)^2} + K\right) \\ K_1 &= \frac{1}{R^2}\left(\frac{4B}{(\Delta x)^4} + \frac{T}{(\Delta x)^2}\right) \\ K_2 &= \frac{1}{R^2}\frac{B}{(\Delta x)^4} . \end{aligned}$$

The boundary conditions $\eta = \partial^2\eta/\partial x^2 = 0$ for a hinged rigid/compliant wall join located at $n = n_j$ may be directly incorporated into this discrete version of $\mathcal{K}$. We just need to make the replacements

$$f_{n_j} \rightarrow 0 \ , \ f_{n_j-1} \rightarrow -f_{n_j+1} \tag{3.108}$$

when determining the action of the operator at the first two streamwise positions beyond the join, *i.e.* in evaluating $(\mathcal{K}f)_{n_j+1}$, $(\mathcal{K}f)_{n_j+2}$. (The evaluation of $(\mathcal{K})_{n_j}$ is not necessary.) There is a subtlety here, since the values of $v_w$ are well defined—in fact they should be equal to zero—at rigid-wall locations upstream of the join. The need to replace $(v_w)_{n_j-1}$ by $-(v_w)_{n_j+1}$, when calculating the $\mathcal{K}v_w$ term appearing in (3.106), stems from the fact that this term only arises because the relation (3.104) has been substituted. Thus we must ensure that the discretised $\mathcal{K}$ operator is applied to $v_w$ in a manner consistent with its action on $\eta$. At the downstream boundary, or at a compliant/rigid wall join, similar considerations apply. Replacements analogous to (3.108) need to be made.

Making use of (3.107), the relation (3.106) can be further discretised to yield

$$\begin{aligned}
\mu_n^l + \left(\frac{2d\Delta t}{3R} + \frac{4(\Delta t)^2}{9}K_0\right)(v_w)_n^l = \\
\frac{1}{3}\left(4\mu_n^{l-1} - \mu_n^{l-2}\right) - \frac{2\Delta t}{9}\left(4(\mathcal{K}\eta)_n^{l-1} - (\mathcal{K}\eta)_n^{l-2}\right) \\
-\frac{\Delta t}{3\Delta x}\int_0^1 \left(U\left(v_{n+1}^l - v_{n-1}^l\right) + \frac{1}{R}\left(\omega_{n+1}^l - \omega_{n-1}^l\right)\right) dy \\
+\frac{4(\Delta t)^2}{9}\left(K_1\left((v_w)_{n+1}^l + (v_w)_{n-1}^l\right) - K_2\left((v_w)_{n+2}^l + (v_w)_{n-2}^l\right)\right) \qquad (3.109)
\end{aligned}$$

(The terms on the final line will need to be appropriately amended near the upstream and downstream extremities of the compliant wall.)

We may now eliminate any direct reference to $\mu$ as a dependent variable, by substituting its definition as the combined normal momentum of the wall and fluid. As previously remarked, it is possible to view this definition, when used in conjunction with an evolution equation for $\mu$, as a constraint to be applied to the normal velocity component of the fluid. Thus from (3.109) we can derive the relation

$$\begin{aligned}
\left(m + \frac{2d\Delta t}{3R} + \frac{4(\Delta t)^2}{9}K_0\right)(v_w)_n^l + \int_0^1 v_n^l\, dy = \\
\frac{1}{3}\left(m\left(4(v_w)_n^{l-1} - (v_w)_n^{l-2}\right) + \int_0^1 \left(4v_n^{l-1} - v_n^{l-2}\right) dy\right) - \frac{2\Delta t}{9}\left(4(\mathcal{K}\eta)_n^{l-1} - (\mathcal{K}\eta)_n^{l-2}\right) \\
-\frac{\Delta t}{3\Delta x}\int_0^1 \left(U\left(v_{n+1}^l - v_{n-1}^l\right) + \frac{1}{R}\left(\omega_{n+1}^l - \omega_{n-1}^l\right)\right) dy
\end{aligned}$$

$$+\frac{4(\Delta t)^2}{9}\left(K_1\left((v_w)^l_{n+1}+(v_w)^l_{n-1}\right)-K_2\left((v_w)^l_{n+2}+(v_w)^l_{n-2}\right)\right) \tag{3.110}$$

which will be interpreted as a 'boundary condition' to be imposed on $v$. It may be observed that, even though the dependent variable $\mu$ is no longer explicitly referred to, the insight that the wall and fluid inertia terms should be treated together is reflected in the way that the condition has been arranged. It should also be noted that the condition does not directly involve the values taken by the wall displacement at the current time level $l$. Both of these features help to ensure that numerical stability is achieved when the condition is used within an iterative procedure.

If we substitute the Chebyshev expansions for $v$ and $\omega$ into the condition (3.110) we can obtain the constraint

$$\begin{aligned}
&\left\{\left(m+\frac{2d\Delta t}{3R}+\frac{4(\Delta t)^2}{9}K_0\right)r_k+q_k\right\}v^l_{k,n}= \\
&\frac{1}{3}(mr_k+q_k)\left(4v^{l-1}_{k,n}-v^{l-2}_{k,n}\right)-\frac{2\Delta t}{9}\left(4(\mathcal{K}\eta)^{l-1}_n-(\mathcal{K}\eta)^{l-2}_n\right) \\
&\quad-\frac{\Delta t}{3\Delta x}\left(s_k\left(v^l_{k,n+1}-v^l_{k,n-1}\right)+\frac{1}{R}q_k\left(\omega^l_{n+1}-\omega^l_{n-1}\right)\right) \\
&+\frac{4(\Delta t)^2}{9}r_k\left(K_1\left(v^l_{k,n+1}+v^l_{k,n-1}\right)-K_2\left(v^l_{k,n+2}+v^l_{k,n-2}\right)\right)
\end{aligned} \tag{3.111}$$

where the summation convention applies to the repeated $k$-suffix associated with the Chebyshev discretisation. The constants $q_k$,$r_k$,$s_k$, have been defined previously in equations (3.49), (3.78). They arise from the evaluation of wall values and integrals across the channel.

The structure of (3.111) should be compared with that of (3.58), which is the relation obtained from the Chebyshev discretisation of the boundary condition $v_w = \bar{v}$. It may be seen that, despite the somewhat convoluted appearance of (3.111), the same general form has been retained. More specifically, we can abbreviate the new condition as

$$r^{\mu}_k\, v_k = \bar{v} \tag{3.112}$$

where

$$r_k^{\mu} = \left( m + \frac{2d\Delta t}{3R} + \frac{4(\Delta t)^2}{9} K_0 \right) r_k + q_k \tag{3.113}$$

and the function $\bar{v}$ collects together all the terms on the right-hand side of (3.111). Labels corresponding to the streamwise position and time level have been dropped. (The superscript in the constants $r_k^{\mu}$ is not a grid label; it merely references the fact that the constants arose through considering the total wall-normal momentum $\mu$ of the channel.) It follows that the boundary condition now to be imposed on $v$ may be incorporated into a streamwise marching procedure in very nearly the same manner as was described before. We just need to replace the constants $r_k$ by the new constants $r_k^{\mu}$, and supply values for $\bar{v}$ instead of for $\bar{v}$.

In the numerical scheme defined previously, it was supposed that values for the wall motion function[8] $\bar{v} = \partial\eta/\partial t$ could be determined before the beginning of each streamwise march. These values were not then revised until the fluid flow-fields had been updated at all locations. In contrast, the values of $\bar{v}$ at successive streamwise positions need to be recalculated using the latest available estimates for $v$ and $\omega$. We thus take

$$\bar{v}_n^{l,i-1} = \bar{v}\left( \boldsymbol{v}_n^{l-1}, \boldsymbol{v}_n^{l-2}, \mathcal{K}\eta_n^{l-1}, \mathcal{K}\eta_n^{l-2}, \boldsymbol{v}_{n-1}^{l,i}, \boldsymbol{v}_{n+1}^{l,i-1}, \boldsymbol{\omega}_{n-1}^{l,i}, \boldsymbol{\omega}_{n+1}^{l,i-1} \right) . \tag{3.114}$$

As before, the terms in bold-face denote vectors of Chebyshev coefficients, with $i$ labelling the iteration level. The details of the functional dependencies can be obtained by inspecting the right-hand side of the condition (3.111).

Using the value of $\bar{v}_n^{l,i-1}$ determined in the manner suggested, the updated vector $\boldsymbol{v}_n^{l,i}$ can be calculated by solving an amended form of the line iteration equation (3.63). The necessary amendments are limited to redefining the first row of the matrix $\mathbf{T}$, by taking $r_k^{\mu}$ in place of $r_k$, and using a different calculation, specified via (3.114), to obtain the first entry of the vector $\mathbf{M}$. The imposition of rigid-wall boundary

[8]For the case where the wall motion is presumed time-periodic, $\xi$ is used instead of $\partial\eta/\partial t$

conditions may be achieved within the same framework. All that is required is that we take

$$\tilde{v}_n^{l,i-1} = \int_0^1 v_n^{l,i-1}\, dy = q_k v_{k,n}^{l,i-1} \,. \tag{3.115}$$

In conjunction with (3.112), this ensures that the condition $v_w = 0$ holds when the iteration converges. By imposing the condition in this manner, we avoid the need to make any further changes to the line iteration matrix $\mathbf{T}$ when dealing with rigid-walled sections of the channel.

The previously defined line iteration for the vorticity, summarised in the relation (3.64), may be employed without alteration. By applying the coupling relation $\bar{u} = -U_w \eta$, values computed for $\eta$ can be used to implement the integral constraint on the vorticity in the manner described in Section 3.3.1. It remains to consider how the wall displacement may be determined.

Returning to equation (3.104), which is the time discretised version of the 'wall motion' equation (3.102), it might be thought that a method for determining the evolution of $\eta$ has already been presented. In fact, the calculation of $\eta$ by such means may be shown to be sufficient, from a formal point of view, for completing the specification of the coupling between the wall and fluid motion. Unfortunately, the numerical results obtained by evolving the wall displacement according to equation (3.104) turned out to be unreliable. A more successful method was developed as follows, by amending the approach taken for the restricted case of time-periodic wall motion.

Equation (3.99) may be rewritten as

$$\frac{1}{R^2}\left(B\frac{\partial^4}{\partial x^4} - T\frac{\partial^2}{\partial x^2} + K\right)\eta = p_w^{\mu} - \frac{d}{R}v_w \tag{3.116}$$

where the quantity

$$p_w^{\mu} = -\left\{\frac{\partial}{\partial t}\left(m v_w + \int_0^1 v\, dy\right) + \frac{\partial}{\partial x}\int_0^1 \left(Uv + \frac{1}{R}\omega\right)\right\} \tag{3.117}$$

is obtained by modifying the fluid pressure at the wall so that it includes the wall inertia term. Using the two-component vector $\boldsymbol{\eta}$, defined as before, equation (3.116)

can be cast in form

$$\frac{1}{R^2}\left(B\frac{\partial^2}{\partial x^2}+\mathbf{A}^{\mu}\right)\boldsymbol{\eta}=\mathbf{p}^{\mu} \tag{3.118}$$

where

$$\mathbf{A}^{\mu}=\begin{bmatrix} 0 & -B \\ K & -T \end{bmatrix}$$

and

$$\mathbf{p}^{\mu}=\begin{bmatrix} 0 \\ p_w^{\mu}-\frac{d}{R}v_w \end{bmatrix}.$$

This has the same structure as equation (3.90), which was used to determine $\eta$ when the wall motion was presumed time-periodic. The discretisation and subsequent implementation of an efficient numerical solution procedure are entirely analogous to the case already treated, so there is no need to repeat the details here. For present purposes, we just note that the wall displacements may be readily calculated, simultaneously at all streamwise locations, once estimates for the fluid flow-fields—and hence for the quantities $p_w^{\mu}$ and $v_w$—have been supplied. Values for $\eta$, thus determined, can be applied in the line iteration used to update the fluid, and the whole procedure then repeated.

We have now delineated a numerical scheme that can be employed to study the evolution of the coupled compliant-wall/fluid system, without resort to any assumptions about time periodicity. By way of a summary, it may be useful to highlight differences from the restricted scheme described previously. It can be seen that the solution procedure adopted for determining the fluid flow-fields is changed only slightly when the presumption of time-periodic wall motion is dropped. In particular, line iteration can be applied in the same manner as before, except that some minor alterations need to made in one of the matrices involved. These are necessary in order to incorporate a reformulation of the boundary condition imposed on the normal velocity component. (The new form of the condition is stated in equation (3.110).) The implementation of the integral constraint on the vorticity is unaffected. As before,

the wall and fluid motion are matched together within the iteration which is applied to solve the very large set of equations derived from discretising the fluid. For the time-periodic case, the values of the wall motion coupling functions $\bar{u}$, $\bar{v}$ could be revised after the fluid flow-fields had been updated at all spatial locations. For the more general case, whilst $\bar{u}$ may be determined in essentially the same fashion, the function $\bar{v}$, which replaces $\bar{v}$, must be recalculated inside the streamwise marching procedure used to update the fluid.

## 3.4 Code validation

The code obtained by implementing the numerical schemes outlined above has been tested for various problems for which solutions are known in advance by other means. These included the cases of channels with walls which are either rigid for the entire computational domain or else compliant for the whole domain. The first case enables the code for the fluid to be tested without the complications of fluid-wall interaction, whilst the second checks the validity of the code when the wall and fluid interact fully, but there is no streamwise variation due to the presence of a wall join. In both of these cases, a Tollmien-Schlichting wave introduced at the upstream boundary should propagate down the channel with the constant wavenumber and growth rate predicted from linear stability theory. Furthermore, the wave profile should retain the form specified at the upstream boundary, *i.e.* the eigenfunction profile determined from the solution of the Orr-Sommerfeld equation, should be presented at all streamwise locations.

Figures 3.1(a),(b),(c) display numerical simulation results obtained for the case of a rigid-walled channel. They plot the streamwise variation of square-integral magnitudes defined for the $u$, $v$ and $\omega$ flow-fields. The temporal frequency of the disturbances is chosen so that the spatial growth rate is close to the maximum attainable at the given Reynolds number. All three figures correspond to the same instant of

time. The simulation was conducted by using null values to initialise the perturbation flow-fields, and then introducing a time-periodic forcing at the upstream boundary. The depicted magnitudes are for a time after the leading front of the generated disturbances has propagated out through the downstream boundary. The flow-fields have by then become time-periodic throughout the whole of the computational domain. (Alternatively, the eigenfunction profiles obtained from linear stability theory could be used to specify initial values for the flow at all streamwise locations. In this case, the flow-fields should become time-periodic straight away. Such behaviour was confirmed in the results of appropriately conducted simulations.) It may be observed that there are no reflections of the disturbances at the outflow. Experimentation using different values for the wavenumber implemented in the downstream boundary conditions, showed that there is a fair degree of insensitivity to the exact value of $\alpha_r$ selected, as expected from previous studies by Fasel. Figures displaying the profile of the disturbances across the width of the channel, as well as their streamwise variation, will be given later. For the present, we just remark that the profiles were found to take the form anticipated from linear stability theory.

The dotted lines drawn in each of Figures 3.1(a),(b),(c) show the amplitude envelopes predicted from linear stability theory. It can be seen that there is good agreement with the simulation results. A more stringent check can be conducted by calculating spatial growth rates, together with wavenumbers, at every streamwise location. The details of the calculations involved will be given in a note at the end of the present section. For the time being, we will take it for granted that it is possible to define local values of $\alpha_r$, $\alpha_i$ using numerically determined flow data. Figures 3.2(a),(b) plot the streamwise variation of the wavenumbers and growth rates, computed using the same data for the vorticity flow-field that was presented in Figure 3.1(c) in the form of square integral magnitudes. It can be seen that there is very good quantitative agreement between the values of $\alpha_r$, $\alpha_i$ determined from the simulation and the constant values expected from linear stability theory. In fact,

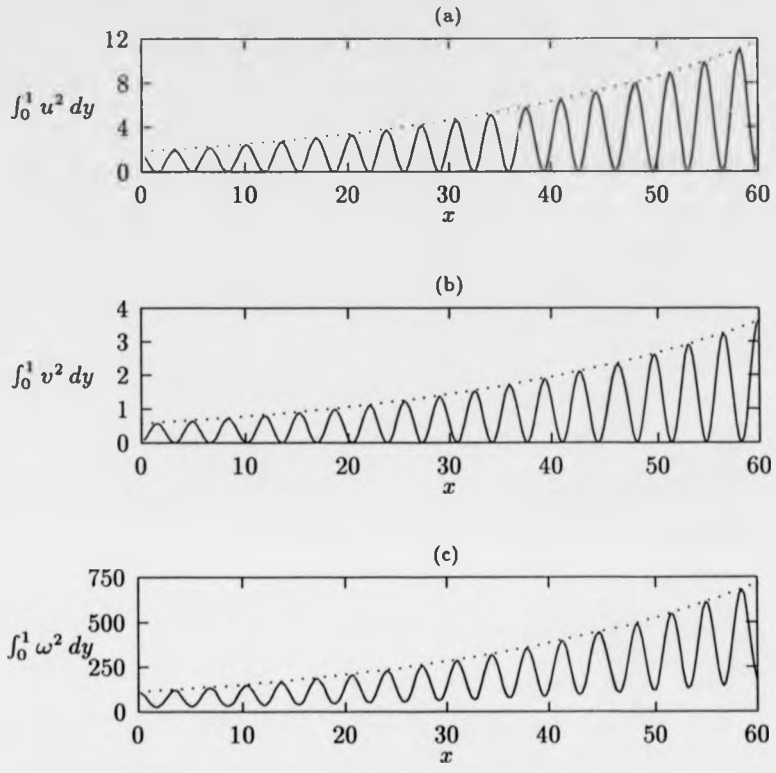


Figure 3.1: Streamwise development of Tollmien-Schlichting wave propagating in a rigid-walled channel. The Reynolds number is $R = 12000$ and the temporal frequency $\beta = 0.2$. See main text for explanation of dotted lines. (Data is displayed for the whole length of the computational domain used in the simulation.)

the lack of any streamwise variation is quite striking, apart from in the immediate vicinity of the upstream and downstream computational boundaries. (In order to minimise errors in the growth rates calculated near the downstream boundary, the results displayed in Figures 3.2(a),(b) are taken from a simulation in which the 'exact'

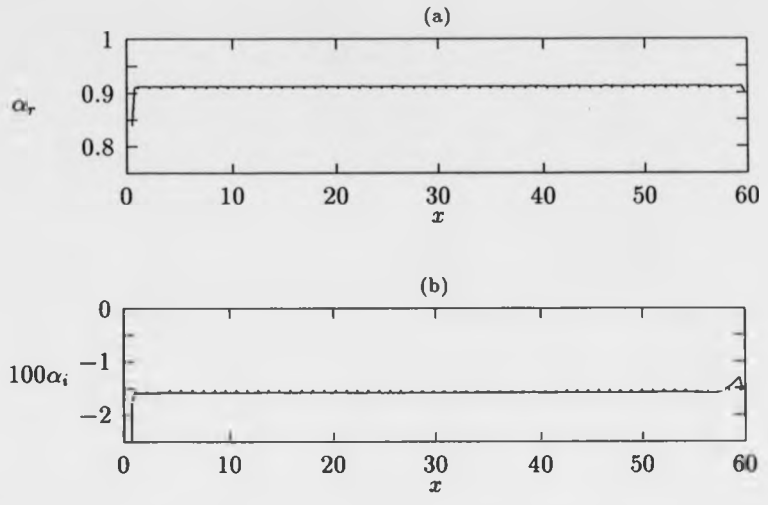


Figure 3.2: Streamwise variation of locally-defined wavenumbers and growth rates for the Tollmien-Schlichting disturbances depicted in the previous figures. The solid lines were obtained by applying the expressions (3.126), (3.128) to simulation data for the quantity $a = \int_0^1 \omega \, dy$. The dotted lines represent the constant values expected from a solution of the Orr-Sommerfeld equation.

outflow conditions (3.17), (3.18) have been applied.)

Once the fluid simulation code had been validated for an entirely rigid-walled channel, more demanding cases involving wall motion could be attempted. A number of artificially constructed problems were tested out first. These involved wall motion that was externally prescribed, rather than driven by the fluid pressure. In particular, the wall motion could be assigned so as to mimic the behaviour that would be expected if compliant walls were present.

For all cases involving wall motion throughout the streamwise extent of the channel, it is necessary to impose the wall motion as well as the fluid motion at the upstream computational boundary. To simulate the propagation of a Tollmien-

Schlichting wave into an entirely compliant-walled channel, the upstream forcing of both the wall and fluid must be derived from a solution of the Orr-Sommerfeld equation. The conditions on the fluid take the same form as for the rigid-walled case, *i.e.* they are specified by (3.11), (3.12) in conjunction with (3.13). The only change is that the streamfunction profile $\phi(y)$ used to define the profiles of $v$, $\omega$ is now obtained by solving the Orr-Sommerfeld equation with compliant-wall boundary conditions. The upstream wall motion is matched to that of the fluid by setting

$$\eta = \Re\left(\eta_{os} e^{-i\beta t}\right) \tag{3.119}$$

where the displacement amplitude is defined by

$$\eta_{os} = -\frac{D\phi_w}{U'_w} \,. \tag{3.120}$$

As usual, the subscript $w$ denotes evaluation at the wall location $y = 1$, and $\beta$ is the temporal frequency of the forcing. The relation (3.120) follows from the linearised boundary condition (3.27). It is already utilised in solving the Orr-Sommerfeld equation for a compliant-walled channel, as was described in Section 2.2.

The wall motion required to imitate the response of compliant walls at other streamwise locations can be obtained in a simple manner from (3.119). We just need to shift the phase and prescribe a spatial growth or decay in the amplitude. More specifically, the required wall displacement takes the form

$$\eta = \Re\left(\eta_{os} e^{i(\alpha x - \beta t)}\right) \,, \tag{3.121}$$

where $x = 0$ is the position of the upstream boundary. The complex wavenumber $\alpha$ is determined from the Orr-Sommerfeld equation for the chosen wall compliance parameters. The prescription of the wall velocity $\partial\eta/\partial t$ is similar—we just need to premultiply by $-i\beta$ before taking the real part. Using these specifications of the wall displacement and velocity, the fluid is in effect time-periodically forced at all wall locations as well as at the upstream boundary. The fluid-flow fields obtained from

a simulation conducted with such boundary conditions should be the same as they would have been if 'genuine' compliant walls were present, *i.e.* if the wall motion had been determined by the fluid pressure. Hence we would expect the growth rates, wavenumbers and profiles found for the fluid to be exactly as expected from linear stability theory for a compliant-walled channel. This was verified to be the case.

Having tested the fluid code for the case of prescribed motion at the channel walls, it was possible to proceed to the case where the fluid motion and wall motion are interactively coupled together[9]. In order to determine the wall motion when the walls are compliant throughout the whole of the channel, it is necessary to supplement the upstream wall forcing given by (3.119) with a second condition. This takes the form

$$\frac{\partial^2 \eta}{\partial x^2} = -\Re\left(\alpha^2 \eta_{os} e^{-i\beta t}\right) . \tag{3.122}$$

We thus have the two-component condition

$$\boldsymbol{\eta} = \Re\left\{ \begin{bmatrix} 1 \\ -\alpha^2 \end{bmatrix} \eta_{os} e^{-i\beta t} \right\} , \tag{3.123}$$

in the notation defined previously. The implementation (3.123) in the discretisation is a simple matter. It replaces the boundary condition $\boldsymbol{\eta} = 0$ that would apply at the location of a rigid/compliant wall join.

Validations were conducted for each of the two numerical schemes developed to incorporate the fluid/compliant-wall coupling. The earliest simulations were carried out using the restricted scheme obtained by building an assumption of time-periodicity into the equation governing the wall motion. These gave satisfactory results, except that for some selected compliant-wall parameters, the computational time elapsed before time-periodic behaviour was observed could become excessively long. As previously remarked, until time-periodicity is attained, the physical significance of any

[9] As a further check on the code—for a situation intermediate between those where the wall motion is imposed or computed interactively—the wall velocity could be prescribed, but the wall displacement calculated using the fluid pressure. Consistent results were obtained.

numerical results obtained using the restricted scheme cannot be assured. Consequently, we will confine our detailed reports to the results of simulations conducted using the more general scheme developed to overcome such shortcomings. It should be noted, though, that this development was only achieved after the restricted scheme had been extensively tested. In fact, since time-periodic motion is of sole concern in the present context, numerical results obtained using the restricted and general schemes should agree, provided the simulations involving the restricted scheme are allowed to evolve for a sufficient length of time. This was found to be the case.

The numerical results obtained in simulations for which the channel walls were taken to be compliant throughout the whole computational domain showed the same level of consistency with the linear stability theory predictions as had been found for the rigid-walled case. The computed streamwise variation of the integral magnitudes for the disturbances remained analogous to that shown in Figures 3.1(a),(b),(c). A significant difference, of course, was that the wall parameters could be chosen so as to reduce the spatial growth rates, or even to cause a decay of waves that would otherwise have grown over rigid walls. The locally computed growth rates and wavenumbers were again in good agreement with values determined from the Orr-Sommerfeld equation. Furthermore, the wave profiles appeared just as expected. The eigenfunction imposed at the upstream boundary—which incorporated the inclusion of wall motion—was replicated in the form taken by the profile as the disturbances propagated downstream.

For the compliant-walled channel, we do not display any plots corresponding to those given for the rigid-walled case. This is to avoid a repetition of results which will be presented later. It turns out that the behaviour expected in an entirely compliant-walled channel may be discerned in simulations of Tollmien-Schlichting waves propagating in a channel which contains rigid/compliant or compliant/rigid wall joins. In the compliant-walled sections of such a channel, away from the immediate vicinity of any wall joins, the waves can take the same detailed character as

they would have had if no joins were present, *i.e.* they are just as predicted from linear stability theory for a channel which has compliant walls throughout. The fact that such a coincidence of behaviour can occur provides further verification for the computer code used in the simulations.

**Note on the calculation of local growth rates and wavenumbers**

Suppose $a$ is some fluid flow-variable which takes the form

$$a(x,y,t) = \Re\left(A(y,t)e^{i\alpha x}\right) \tag{3.124}$$

where the complex wavenumber $\alpha = \alpha_r + i\alpha_i$ is constant. Then it is straightforward to show that

$$\frac{\partial^2 a}{\partial x^2} + 2\alpha_i \frac{\partial a}{\partial x} + |\alpha|^2 a = 0\,. \tag{3.125}$$

In fact, relations of exactly the same form have already been used to determine the outflow boundary conditions on the fluid. If we divide throughout by $a$, and then differentiate with respect to $x$, we obtain the expression

$$2\alpha_i = -\frac{\frac{\partial}{\partial x}\left(\frac{1}{a}\frac{\partial^2 a}{\partial x^2}\right)}{\frac{\partial}{\partial x}\left(\frac{1}{a}\frac{\partial a}{\partial x}\right)}\,. \tag{3.126}$$

This can be employed to calculate spatial growth rates $\alpha_i$ from the flow-fields determined in numerical simulations. If the simulation results were in exact agreement with the predictions of linear stability theory, then a discretised version of the function defined by the right-hand side of (3.126) would take the same constant value whichever flow-field—for instance either of $u$ or $v$—is substituted for $a$. In practice, using numerically determined flow-field data, we would expect to find some streamwise variations, as well as a dependence on which fluid-variable is selected. Thus we can interpret (3.126) as defining the local growth rates associated with a given flow-field variable $a$. Using second-order finite-differences, we can discretise the streamwise derivatives to obtain

$$(\alpha_i)_n = -\frac{1}{\Delta x}\left(\frac{a_{n+2}a_{n-1} - a_{n-2}a_{n+1} - a_n(a_{n+1} - a_{n-1})}{a_{n+2}a_{n-1} + a_{n-2}a_{n+1} - a_n(a_{n+1} + a_{n-1})}\right) \tag{3.127}$$

where the subscripts label the streamwise location. Local wavenumbers may be determined in a similar fashion. The relation (3.125) can be rearranged in the form

$$\alpha_r^2 = -\left(\frac{1}{a}\frac{\partial^2 a}{\partial x^2} + 2\alpha_i \frac{1}{a}\frac{\partial a}{\partial x} + \alpha_i^2\right) \tag{3.128}$$

which then yields the discretised expression

$$(\alpha_r)_n = \left[-\left(\frac{1}{a_n}\frac{(a_{n+1} - 2a_n + a_{n-1})}{(\Delta x)^2} + \frac{(\alpha_i)_n}{a_n}\frac{(a_{n+1} - a_{n-1})}{\Delta x} + (\alpha_i)_n^2\right)\right]^{\frac{1}{2}} . \tag{3.129}$$

It should be emphasised that both of the numerical expressions (3.127), (3.129) were obtained on the assumption that the spatial growth rate and wavenumber—which they purport to locally define—are in fact constant. To be used in a consistent fashion, they need to yield nearly constant values when a particular flow-field variable $a$ is substituted. Thus, they have limited significance in situations where constant growth rates and wavenumbers are not anticipated, for instance for the flow-fields found in the proximity of a rigid/compliant wall join.

As an alternative to computing values of $\alpha_r$ and $\alpha_i$ at every grid-point within the computational domain, we could first take averages across the channel. For instance, we could set $a$ equal to $\int_0^1 v\,dy$ or $\int_0^1 \omega\,dy$. There is no need to amend the derivations given above—the expressions used to compute $(\alpha_r)_n$, $(\alpha_i)_n$ remain the same irrespective of whether any $y$-dependence is included or removed through averaging. Similarly, calculations can be performed by taking $a$ to represent such quantities as the wall displacement or velocity. The adequacy of simulation results can be tested by checking the agreement between values of the growth rate and wavenumbers computed in such various ways.

# Chapter 4

# Simulation results for the spatial adaptation of Tollmien-Schlichting waves

Having dealt with issues of code validation, we can now present numerical results for the problem of prime interest in the current work, namely the spatial adaptation of a Tollmien-Schlichting wave as it propagates over a rigid/compliant wall join. For the situation that was shown schematically in Figure 1.2, *i.e.* a Tollmien-Schlichting wave propagating in a plane channel flow that is bounded first by rigid walls and then by compliant walls, initial simulations suggested that the adjustment of the wave to the presence of compliant-wall boundary conditions could occur on a relatively small lengthscale. At a short distance beyond the rigid/compliant wall join, the profile, wavenumber and spatial growth rate of the disturbances were all indistinguishable from what would have been expected had the channel walls been compliant throughout. Consequently, the streamwise extent of the computational domain required for resolving the adaptation could be kept to just a few Tollmien-Schlichting wavelengths. This made it feasible to tackle the more ambitious problem depicted in Figure 4.1 without generating excessive demands on the available computational

resources[1]. Thus, in the simulations reported below, the adaptation of a Tollmien-Schlichting wave over a rigid/compliant wall join is considered in a setting where the join defines the upstream boundary of a finite-length compliant panel embedded within otherwise rigid channel walls. Amending the problem situation in such a way allows us to contrast the effects of a rigid/compliant wall join with those of a compliant/rigid wall join. Moreover, it gives a direct means of addressing the question: How long does a compliant wall have to be in order to have a significant stabilising influence on a Tollmien-Schlichting wave?


Figure 4.1: Tollmien-Schlichting wave propagating in a channel with a compliant-walled section.

Discussion of the simulation results will proceed as follows. We will begin with some comments about the selection of physically interesting wall compliance parameters. After these preliminaries, there will be a detailed discussion of the fluid flowfields and wall motion variables obtained from a particular numerical simulation. The results considered are chosen to exemplify what appears to be typical behaviour when Tollmien-Schlichting waves propagate in a channel that contains rigid/compliant or compliant/rigid wall joins. Following on from this, we will present an energy balance analysis which accounts for the various physical mechanisms that determine the

[1]The simulations were conducted on a Sun SS10 workstation with 48 mbytes of internal memory. The required computer run times varied from a few minutes, in the case of problems defined for code validation purposes, to several hours, for most of the studies reported immediately below. In some of the more demanding studies completed to date, for instance those presented in Section 4.6, the run times could exceed twenty four hours.

spatial growth and decay of the waves. We will then describe a very simple analytic procedure that can be employed to calculate the spatial scale over which the compliant wall motion is excited in the vicinity of a join. This development was motivated, in part, by an examination of the numerical simulation results. Finally, there will be an extensive examination of numerical simulation results wherein the excitation of flow-induced surface waves can be discerned.

## 4.1 Selection of compliant-wall parameters

Our concern with channel flow arises mainly from the fact that it provides a simplified problem situation. By investigating what can happen in a channel, we aim to bring to light behaviour that could occur in more technologically significant boundary layer flows. Bearing this in mind, we might hope to select the non-dimensional wall compliance parameters so that they correspond with parameters previously found to be of interest in the case of Blasius flow. However, it is not clear how such a correspondence should be accomplished, since the non-dimensionalisation of the wall properties in the Blasius case usually takes a different form to that which has been applied for the channel flow. For Blasius flow, the wall properties are non-dimensionalised to ensure that their dimensional counterparts remain fixed when the Reynolds number is interpreted as varying solely through changes in the streamwise position. In contrast, for the case of a channel, it is more natural to vary the Reynolds number through changes in the maximum velocity of the mean flow[2]. Thus, any desired matching between the non-dimensional wall properties may only be achieved at a single Reynolds number.

Aside from differences in non-dimensionalisation procedures, there is the further complication that the critical Reynolds number at which the Tollmien-Schlichting instability sets in for a rigid-walled channel flow is considerably larger than the cor-

[2]See Section 2.2.2 for a fuller discussion.

responding Reynolds number, based on displacement thickness, for the Blasius case. Moreover, the unstable disturbance wavelengths and frequencies lie in ranges which are specific to each flow. The details of these ranges need to be considered when determining the relative importance of the inertia and stiffness terms which appear in the equation governing the motion of the walls. For instance, the effect of the bending stiffness on the wall motion is proportional to the fourth power of the wavenumber $\alpha$. In a channel, unstable Tollmien-Schlichting waves are typically found with $\alpha \sim 1$, so $\alpha^4$ may be of order unity. By contrast, for the Blasius case, we would usually have $\alpha \sim 0.25$, and thus find $\alpha^4$ to be of much smaller order in magnitude[3].

In view of such considerations, we will not attempt any precise co-ordination of the wall properties used in the present studies with those relevant to obtaining transition delay for Blasius flow. We will, however, aim to choose our non-dimensional wall parameters so that they at least meet the following criteria:

1. The non-dimensional wall parameters can be realised for compliant wall materials that have previously been found to be of physical interest (for drag reduction purposes) in the Blasius case.

2. This realisation can occur when the fluid is taken to be water at temperatures typical in marine applications. Moreover, it should be possible to select the dimensional half-width of the channel so that it lies within the range of values

[3]The disparity could be much reduced if we chose to use the channel flow displacement thickness $\delta^* = h/3$, instead of the half-width $h$, as the lengthscale for the non-dimensionalisation. The non-dimensional wavenumbers and temporal frequencies characterising the Tollmien-Schlichting instability for the channel flow would then be quite similar to those that arise for the Blasius flow. However, we would still have to contend with the fact that the Reynolds number based on the displacement thickness would be of the order $R_{\delta^*} \sim 2000$ for the onset of the Tollmien-Schlichting instability. This is still significantly larger than the corresponding critical Reynolds number that is found in the case of the Blasius flow.

found for the laminar boundary layer thickness in such applications[4].

Subject to these rather loose constraints, the wall parameters need to be picked so that a significant stabilising effect is obtained for Tollmien-Schlichting waves. For given wall parameters, the extent of any such stabilisation can be gauged by examining appropriate solutions of the Orr-Sommerfeld equation. However, improvements in the stability of Tollmien-Schlichting waves must be achieved without the introduction of flow-induced surface instabilities. Otherwise, we would defeat our purpose of studying a situation that is pertinent to transition delay. In practice, these further considerations lead to the most stringent restrictions on the values taken by the wall compliancy parameters.

We can aim to exclude the occurrence of additional instability modes by applying the analytic theory for flow-induced surface instabilities which was presented earlier. For ease of reference, we restate here the results for the onset of divergence and travelling wave flutter instability that were derived in Section 2.3. When originally presented, these results took the form of expressions defining dimensional critical velocities for the mean fluid flow. As has already been remarked[5], there is no difficulty in translating such expressions into non-dimensional terms, owing to the fact that the Reynolds number varies only through changes in the mean flow centre-line velocity. We then obtain the following critical Reynolds numbers for the divergence and travelling wave flutter instabilities:

$$R_d = \left(\frac{15}{8}\right)^{\frac{1}{2}} R_0 \quad , \quad R_t = \left(\frac{1}{m+\frac{1}{5}}\right)^{\frac{1}{2}} R_0 \tag{4.1}$$

where the quantity

$$R_0 = \left(2\sqrt{BK} + T\right)^{\frac{1}{2}}$$

[4]For instance, in the case of Blasius flow with a free stream speed of $5\,\mathrm{ms}^{-1}$, the boundary layer displacement thickness would be of order 1 mm or less at locations upstream of the transition point.

[5]See also Section 2.3.5

is the non-dimensional analogue of the velocity $U_0$ that was previously used to characterise an effective stiffness for the compliant walls. Thus, it is a straightforward matter to ensure that the wall parameters are chosen so as to yield values for the critical Reynolds numbers which are greater than any given value of the Reynolds number that may be employed in a flow simulation. However, since there are only two constraints on the four wall parameters $m$, $B$, $K$, and $T$, there is still considerable freedom in their selection. This latitude can be reduced if we always take the wall tension $T$ to be negligible, as was done in the studies by Carpenter & Garrad [6] for Blasius flow over Kramer-type compliant surfaces.

In the case of Blasius flow, it makes sense to choose the wall properties so that, according to results obtained from inviscid theory, both divergence and travelling wave flutter are marginally stable at a given flow speed. This choice may be utilised in optimising the stabilising effect achievable for Tollmien-Schlichting waves [16]. In fact, it is the very possibility of such an optimisation that motivates much of the present study[6]. If the same method for selecting the wall properties is adopted in the case of channel flow, it always yields the condition that $m = 1/3$, as can be seen directly by equating the expressions for $R_d$ and $R_t$ defined in (4.1). The simplicity of this condition arises from the fact that, for the channel flow, the critical Reynolds numbers (or corresponding dimensional velocities) for the onset of divergence and travelling wave flutter instability are determined by the wall properties in a very similar fashion. The only point of difference is that there is a dependence on the wall mass in the case

[6]We recap the argument here. For Blasius flow, it turns out that the best results, in terms of transition delay, may be obtained if the dimensional wall properties are allowed to depend on the streamwise position. This suggests the practical use of a series of compliant panels, each with a locally optimal character. For design purposes, it is necessary to determine how short such panels may be made whilst still retaining a significant effect on the stability of Tollmien-Schlichting waves. Thus, it is important to assess how long it takes for a Tollmien-Schlichting wave to adapt to the presence of wall compliance, which leads us to the problem situation of current concern.

of the latter instability but not in the former. Such functional similarity between the expressions used to predict the onset of divergence and travelling wave flutter does not hold for Blasius flow[7]. The condition that appears instead of $m = 1/3$ is more involved. Certainly, it does not just select a particular value for the non-dimensional wall mass. Thus for the channel flow, demanding marginal stability for both divergence and travelling wave flutter could be over restrictive. It pushes one analogy with the Blasius case at the possible expense of limiting the scope for drawing others. Conceivably, it may be more appropriate to retain some freedom in choosing the wall mass. Nonetheless, in the interests of simplicity, we have set $m = 1/3$ in the numerical simulations reported below. (To provide some assurance that the results obtained for $m = 1/3$ do not take an exceptional form, a few additional simulations were conducted using other values of the wall mass.)

If the wall tension is set to be zero, then to yield marginal stability for divergence and travelling wave flutter at a given Reynolds number $R$, the bending stiffness and spring stiffness must take the general form

$$K = \frac{4}{15}\alpha_c^2 R^2 \quad , \quad B = \frac{4}{15}\alpha_c^{-2} R^2 \, . \tag{4.2}$$

This can be seen directly from the expressions (4.1) for the critical Reynolds numbers $R_d$, $R_t$. The quantity $\alpha_c = (K/B)^{\frac{1}{4}}$ is the critical wavenumber for the onset of both the divergence and travelling wave flutter flow-induced surface instabilities. In the present context, $\alpha_c$ can be employed to define a one parameter family of non-dimensional properties for the compliant walls.

Before turning to describe the results of particular numerical simulations, we

[7]For Blasius flow, taking an untensioned spring-backed plate model of the compliant wall, the critical velocities are of the form

$$U_d = 2\left(\frac{B^*(K^*)^3}{27\rho^4}\right)^{\frac{1}{6}} \quad , \quad U_t = \left(\frac{2\sqrt{B^*K^*}}{m^*}\right)^{\frac{1}{2}} \, ,$$

where the asterixes denote the use of dimensional wall properties and $\rho$ is the fluid density [7].

conclude our discussion of the choice of wall compliance parameters with some general remarks about the specification of the critical wavenumber $\alpha_c$. This wavenumber can be applied to define a lengthscale for the compliant wall motion. Consequently, it may be anticipated that the influence of the wall compliance on Tollmien-Schlichting waves will be strongest when the value of $\alpha_c$ is chosen so as to be comparable with values of the wavenumber that characterise the Tollmien-Schlichting instability. A heuristic argument in support of this conjecture can be provided as follows. For disturbances with wavenumber $\alpha$ and frequency $\beta$, we can define a wall stiffness coefficient $S$ as the ratio of the perturbation fluid pressure $p_w$ at the wall to the wall displacement $\eta$. From the equation governing the compliant wall motion we have

$$S = \frac{p_w}{\eta} = \frac{1}{R^2}\left(B\alpha^4 + K\right) - m\beta^2 , \tag{4.3}$$

where, as immediately before, the wall tension $T$ has been set equal to zero and the wall damping term ignored. In general, we might expect to obtain the largest stability effect on a Tollmien-Schlichting wave, with a given wavenumber $\alpha$, when the magnitude of $S$ is close to being minimised. Of course, such minimisation must be achieved subject to the requirement that no flow-induced surface instabilities are introduced. (It may be noted that, for present purposes, we do not need to account for the shift in the wavenumber $\alpha$ from its value for a rigid-walled channel. We only make the implicit assumption that there is no drastic, *i.e.* order of magnitude, change in $\alpha$.)

If the wall properties are restricted to the set for which $R_d = R_t = R$, then it is straightforward to show that

$$S = \alpha^2 \left( \frac{4}{15}\left( \left(\frac{\alpha}{\alpha_c}\right)^2 + \left(\frac{\alpha_c}{\alpha}\right)^2 \right) - \frac{1}{3}c^2 \right) \tag{4.4}$$

where $c = \beta/\alpha$ is the phase velocity. As a first approximation, we may suppose that both $\alpha$ and $c$ are real. We can then use the inequality

$$\left(\frac{\alpha}{\alpha_c}\right)^2 + \left(\frac{\alpha_c}{\alpha}\right)^2 \geq 2 , \tag{4.5}$$

together with the fact that $c < 1$ for Tollmien-Schlichting waves, to conclude that the inertia term in (4.4), (*i.e.* the term which involves $c^2$), will be smaller than the sum of the other terms. Thus, we have

$$S \geq \alpha^2 \left( \frac{8}{15} - \frac{1}{3} c^2 \right) > 0 , \tag{4.6}$$

with an equality only when $\alpha_c = \alpha$. Furthermore, if $\alpha_c$ is not of the same order of magnitude as $\alpha$, then the value of $S$ will be very much larger than its allowable minimum. Taken together, these observations suggest that the most significant effects on Tollmien-Schlichting waves should be obtained when $\alpha_c$ lies in, or near, the range of wavenumbers associated with the Tollmien-Schlichting instability[8]. Confirmatory evidence that this is in fact the case can be provided by considering numerical solutions of the Orr-Sommerfeld equation.

## 4.2 Results for a selected case

We now give a detailed account of a particular simulation involving the propagation of Tollmien-Schlichting waves in a channel flow which is bounded above and below by solid surfaces comprised of compliant panels fixed in otherwise rigid walls. The joins at both ends of each panel are taken to be hinged. The value of the Reynolds number is set at $R = 12000$, which is slightly greater than twice the critical Reynolds number for the onset of Tollmien-Schlichting instability in a rigid-walled channel. In accordance with the criteria given at the end of the previous section, the non-dimensional compliant wall parameters are selected as

$$m = 1/3 , \; T = 0 , \; d = 0 , \; B = 1.92 \times 10^7 , \; K = 4B = 7.68 \times 10^7 .$$

These yield $R_d = R_t = 12000$ with $\alpha_c^2 = 2$. Such a set of non-dimensional wall parameters can be realised for water flow in a channel using Kramer-type surfaces

[8]It is possible to generalise the argument. Rather than taking $R_d = R_t = R$, all that needs to be assumed is that the wall properties are such that $R_d \geq R$ and $R_t \geq R$.

similar to those discussed by Carpenter & Garrad [6][9].

The periodic forcing of the fluid at the upstream boundary is imposed so as to introduce a Tollmien-Schlichting wave with a temporal frequency of $\beta = 0.24$. In a rigid-walled channel the corresponding spatial wavenumber, obtained by numerical solution of the Orr-Sommerfeld equation, takes the complex value $\alpha = 1.03 - i\,0.93 \times 10^{-2}$ . The spatial growth rate of such a wave is about 60% of the maximum attainable at the selected Reynolds number. If the channel were to have compliant walls throughout, with wall parameters as specified above, then a wave with the same temporal frequency would have its spatial wavenumber shifted to $\alpha = 0.940 + i\,1.09 \times 10^{-2}$ . Thus, in the presence of the compliant walls, the Tollmien-Schlichting wave should decay at a rate comparable to the rate at which it would grow over rigid walls.

At the given Reynolds number, it is certainly not the case that Tollmien-Schlichting waves of all temporal frequencies can be stabilised by introducing compliant walls with the selected parameters. This may be seen from the appropriate neutral stability curve displayed in Figure 4.2. The compliant walls have had to be kept sufficiently stiff to ensure that flow-induced surface instabilities are avoided. This requirement would seem, in practice, to preclude the total elimination of Tollmien-Schlichting instability. (The theoretical possibility of achieving complete stabilisation of the Tollmien-Schlichting mode may be inferred from an inspection of the neutral stabil-

[9]For example, if the channel half-width was taken to be 1.5 mm, then, assuming that the wall materials have a density near equal to that of water, the plate used to form the upper part of the compliant surface would need to be 0.5 mm thick and have an elastic modulus of approximately $E = 4 \times 10^6\,\mathrm{Nm}^{-2}$. This plate could be supported by stubs of height 1 mm made from a material with an elastic modulus slightly less than one twentieth of that of the plate. (See the cited reference for further details and an illustration of the geometry involved.) Such a choice of stub characteristics presumes that the ratio of the area directly bolstered by the stubs to the overall surface area of the plate is the same as that used in the original Kramer constructions.

For a channel half-width of 1.5 mm, the Reynolds number of $R = 12000$ could be obtained for water flow (sea water at 10 °C) with a centre-line velocity close to $11\,\mathrm{ms}^{-1}$.

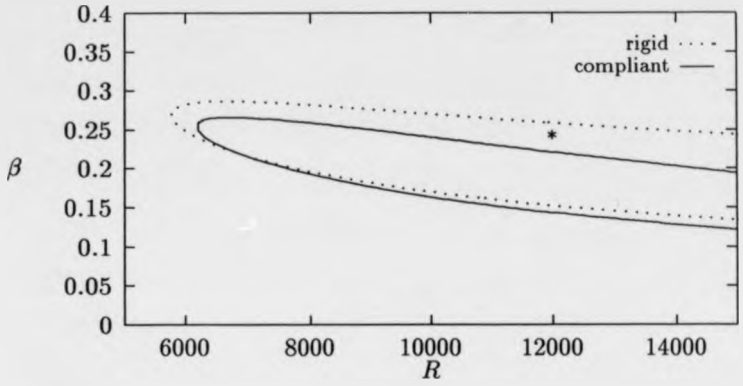


Figure 4.2: Neutral stability curves for Tollmien-Schlichting waves. The compliant wall parameters are $m = 1/3$, $K = 7.68 \times 10^7$, $T = 0$, $B = 1.92 \times 10^7$, $d = 0$. The asterisk labels the Reynolds number and frequency used in the reported numerical simulation.

ity curves presented in Section 2.2.4, in particular those given in Figure 2.1.) For instance, at the temporal frequency associated with the most unstable wave found over rigid walls, the presence of compliant walls with the designated properties only causes a reduction in the spatial growth rate to about half of its rigid-walled value. Consequently, it might be thought more appropriate to conduct numerical simulations at temporal frequencies for which Tollmien-Schlichting waves remain unstable. Our excuse for concentrating, initially, on a situation involving the complete stabilisation of a Tollmien-Schlichting wave is that it affords a clearer illustration of the adaptative behaviour that occurs as the wave passes into, and out of, the compliant-walled section of the channel. Results will be displayed later to show that very similar behaviour can be discerned for the case of waves which are only partially stabilised.

Having given some account for our particular choice of wall and flow properties, we can finally turn to present the numerical simulation results. Figure 4.3 contains

plots for the streamwise variation of integral magnitudes defined by the $u$, $v$ and $\omega$ disturbance fields. The information contained in the first two of these plots is combined together in an additional plot that shows the integrated disturbance energy $E = \int_0^1 (u^2 + v^2)/2\, dy$. The compliant-walled section of the channel is positioned between the streamwise locations denoted by $x = 12$ and $x = 60$. All the plots included in the figure correspond to the same instant of time. They depict the time-periodic flow-fields which are found after the Tollmien-Schlichting wave introduced at the inflow has propagated down the streamwise length of the computational domain and passed through the downstream boundary.

The presence of the compliant/rigid and rigid/compliant wall joins is readily discerned in the form taken by the disturbance fields. For the $u$-component, there is a pronounced increase in the integral magnitude as the wave propagates over the rigid/compliant wall join. This is followed by a decrease near the location of the compliant/rigid wall join. It would seem that the behaviour which occurs in the immediate vicinity of each of the joins is, in some sense, the reverse of that found at the other. The symmetry becomes more apparent if account is taken of the decay in the disturbance amplitude that occurs over the full length of the compliant-walled section of the channel. Similar features are found in the plot of the integral magnitude for the vorticity, except that there is now a decrease over the rigid/compliant join, succeeded by an increase near the compliant/rigid join. The wall joins cause much smaller modifications in the magnitude of $v$-component; such slight changes as do occur seem to be oriented in the same manner as for the $u$-component.

We will return later to provide a more detailed examination of the behaviour that is exhibited by the Tollmien-Schlichting wave as it enters and leaves the compliant-walled section of the channel. Prior to this, we can still address the question of how long it takes for the spatial growth rate to approach the value that would have been expected had the channel walls been compliant throughout. Included in each of the plots displayed in Figure 4.3, there are two dotted lines that define amplitude

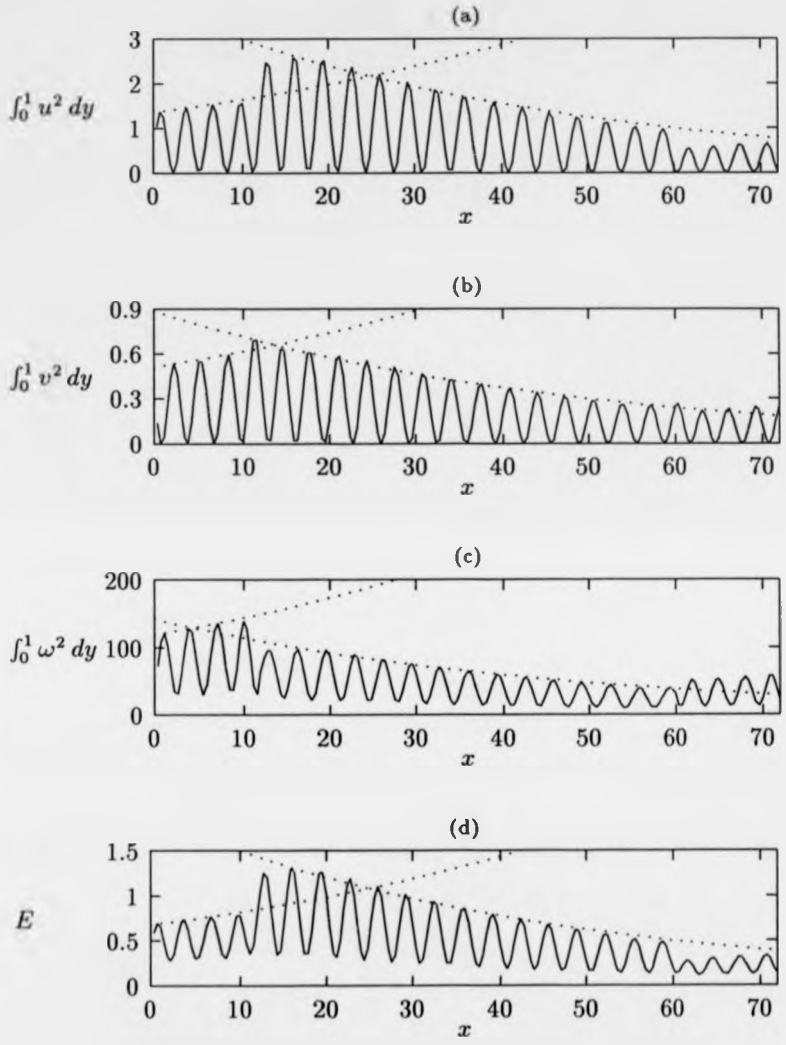


Figure 4.3: Streamwise development of Tollmien-Schlichting wave propagating in a channel containing a compliant-walled section. The Reynolds number is $R = 12000$ and the temporal frequency $\beta = 0.24$. The dotted lines give the amplitude envelopes predicted using linear stability theory.

envelopes. The first of these lines gives the growth predicted from linear stability theory for a Tollmien-Schlichting wave in a rigid-walled channel. It may be seen that, upstream of the rigid/compliant wall join located at $x = 12$, the wave behaves as if the channel were entirely rigid. The same kind of behaviour can be observed downstream of the compliant/rigid join at $x = 60$, though in the interests of clarity the associated amplitude envelopes have been omitted. The second member of each pair of dotted lines depicts the decay caused by the presence of compliant walls. Starting from a value for the disturbance amplitude at a streamwise position near to the centre of the compliant-walled section, the amplitudes at other locations have been projected using the spatial decay rate obtained from linear stability theory for a channel with the appropriate wall compliance parameters. It can be seen that for most of the compliant-walled section, the Tollmien-Schlichting wave is stabilised in exactly the manner that would have been anticipated had there been no joins or rigid walls. The only discrepancies occur at the joins, and even there are confined within a distance that is comparable to a single Tollmien-Schlichting wavelength. (There is a possible source of confusion in Figure 4.3. The square-integral magnitudes display a spatial periodicity over each *half* wavelength of the disturbance.) It would seem that the spatial adaptation of the Tollmien-Schlichting wave to the presence of wall compliance, and the re-adaptation to its absence, both take place on a relatively short lengthscale.

Figure 4.4 contains instantaneous plots of the wall displacement, wall velocity and fluid perturbation pressure at the wall. They are taken at the same moment of time as for the previous plots. It can be seen that the wall motion is smoothly excited. The effects caused by the presence of the hinged wall joins seem to be quite limited. At short distances away from the joins, the wall displacement and velocity display the kind of sinusoidal behaviour that would be predicted for compliant walls of unbounded streamwise extent. Furthermore, in the plot of the wall pressure, the presence of the wall joins can barely be discerned. The pressure wave appears remarkably uniform.

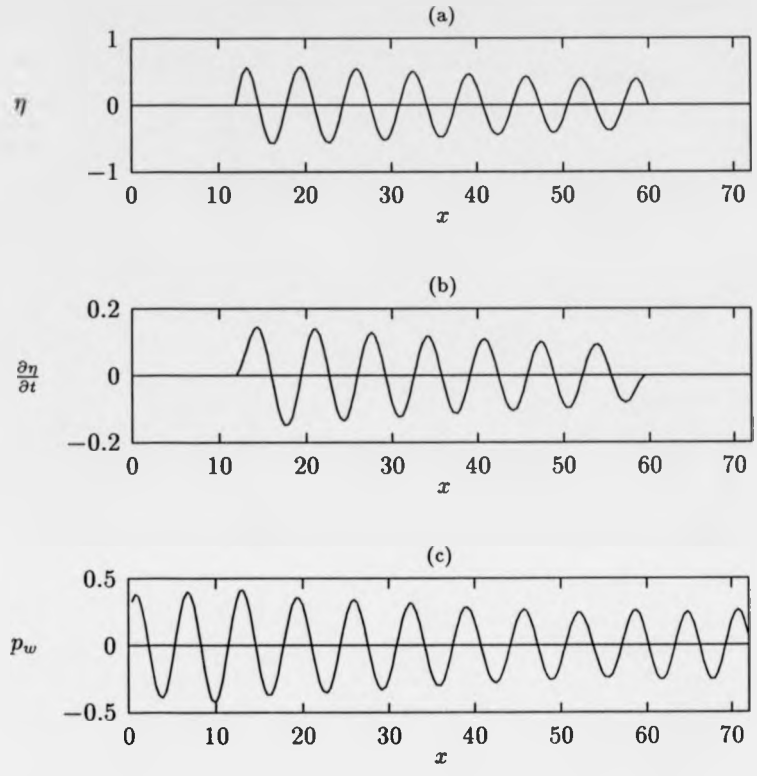


Figure 4.4: Streamwise variation of wall displacement, velocity and fluid perturbation pressure for the Tollmien-Schlichting wave depicted in the previous figure.

This observation will later be utilised to derive a specific lengthscale for the spatial excitation of the wall motion, and thus to render in a more precise fashion some of the comments made immediately above.

Figures 4.5, 4.6, 4.7, 4.8 give visualisations for the velocity, pressure and vorticity disturbance flow-fields at the instant of time considered in the previous figures. They show both the streamwise and wall-normal variation of the disturbances. At

streamwise locations away from the vicinity of the wall joins, the profiles across the half-width of the channel take the form predicted by linear stability theory. Upstream of the rigid/compliant wall join, as well as at locations downstream of the compliant/rigid join, the profiles are just as they would be for an entirely rigid-walled channel. In most of the compliant-walled section of the channel, the profiles take on the character that would have been expected in the absence of accompanying rigid-walls. It may be discerned that the alteration of the profiles as the wave passes over the wall joins takes place in a very smooth fashion. The streamwise development of the the fluid motion, as it matches the motion of the walls, shows no sign of discontinuity. In particular, the wall joins do not appear to generate any detrimental effects akin to those that can occur in the presence of wall roughness elements.

The localised rapid rise and fall noted previously in the plots of square integral magnitudes can be traced to adaptations in the profiles of the disturbances. It can be seen from Figure 4.5 that there is a marked increase in the maximum value of the $u$-component profile as the wave propagates over the rigid/compliant wall join. This alone would be expected to cause an increase in the the size of the computed integral. But more significantly, the decline in $u$ from its maximum value, as the wall location is approached, becomes less pronounced where the wall is in motion. Another way of putting this is to say that effect of the no-slip boundary condition is mitigated when compliant walls are present. As a consequence, when the wave passes over the rigid/compliant wall join, there is an appreciable increase in the value obtained for the square integral of $u$; beyond the join there are additional contributions arising from the motion of the fluid at and near the location of the wall. A similar pattern of behaviour occurs at the location of the compliant/rigid wall join, except that the streamwise sequence is reversed, so there is a fall rather than a rise in the integral magnitude of $u$. The adaptation of the $v$-component profile to the presence of compliant walls leads to a much smaller change in the associated integral magnitude. Figure 4.6 illustrates the fact that the maximum value of $v$ occurs

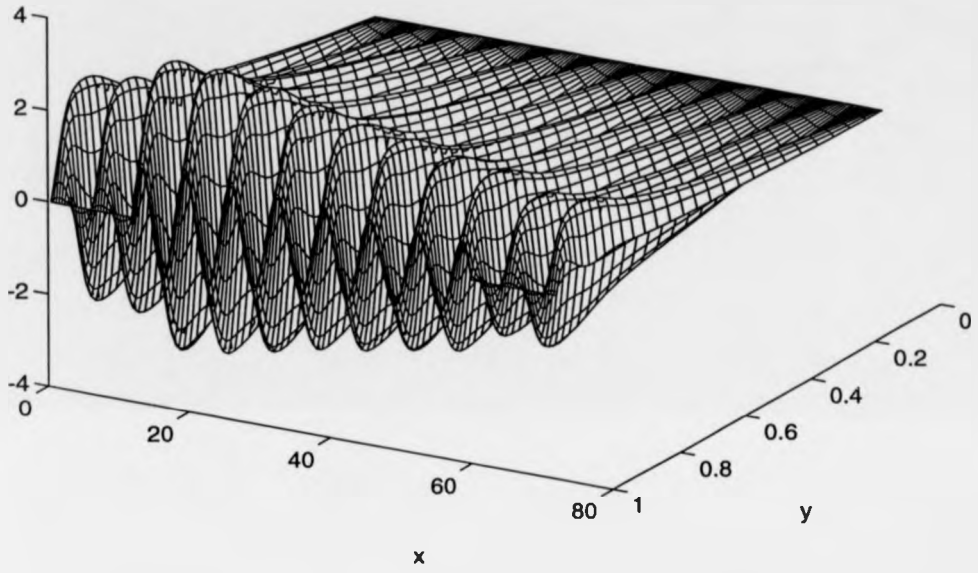


Figure 4.5: $u$-component of the fluid perturbation velocity, for the Tollmien-Schlichting wave considered in the previous two figures. (The grid-lines of constant $x$ correspond to the points used for the finite-difference discretisation along the streamwise direction. The grid-lines of constant $y$ arise from evaluating the Chebyshev expansions for the flow-field variables at the Gauss-Lobatto points $y_k = \cos(\pi(k-1)/2(N-1))$ for $k = 1, \ldots N$. The spatial resolution was defined by $dx = 0.4$, $N = 32$.)

at the channel centre. Contributions from the vicinity of this maximum would be expected to dominate the square integral of $v$ across the half-width of the channel, even when the effects of wall motion are brought into consideration. (Putting the above remarks together, it could be claimed that, in some sense, the fluid disturbance energy associated with a Tollmien-Schlichting wave propagating over a compliant wall

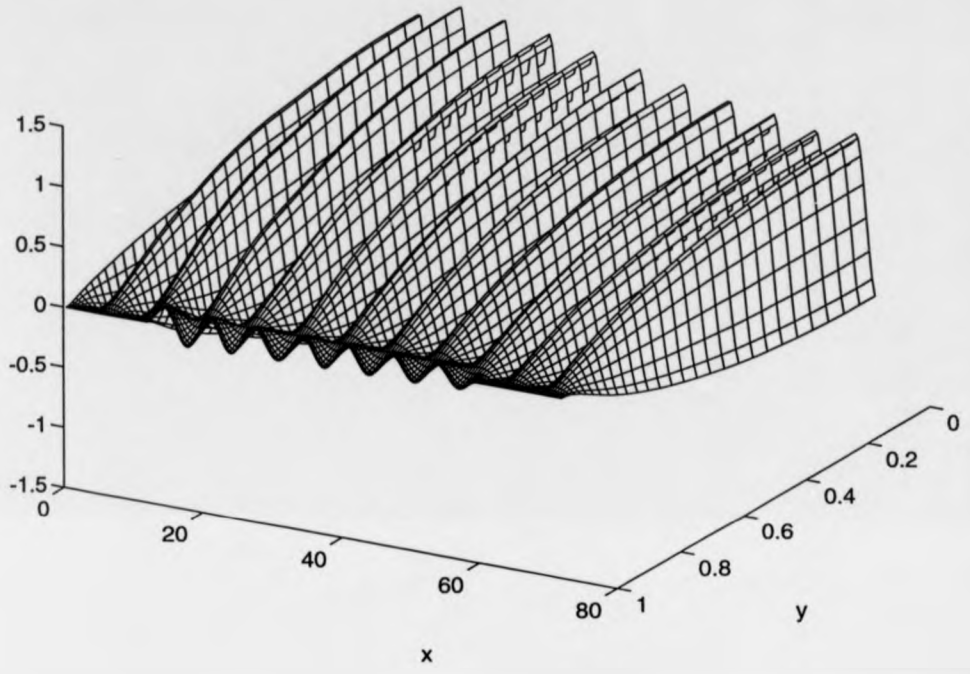


Figure 4.6: $v$-component of fluid perturbation velocity.

is inherently larger than that associated with a 'corresponding' wave over rigid walls. In the compliant-walled case, the fluid needs to remain in motion right up to the walls.)

The alteration in the $u$-component profile that leads to an increase in the disturbance energy, as the wave propagates into the compliant-walled section of the channel, can also be held responsible for the noted decrease in the integral magnitude of the vorticity. From Figure 4.7 it may be seen that the largest values of the vorticity are to be found in close proximity to the wall. Elsewhere, the vorticity is much smaller. The distribution of the vorticity reflects the appearance of steep gradients in the wall-normal variation of the $u$-component. These gradients, in turn,

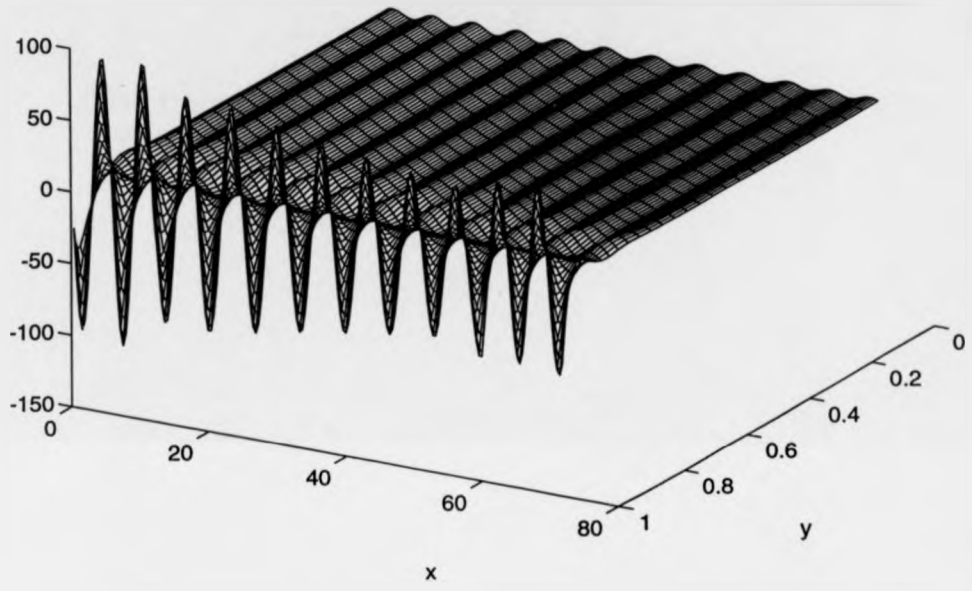


Figure 4.7: Fluid perturbation vorticity.

can be attributed to the need to satisfy the no-slip boundary condition at the wall. Thus, when the severity of the no-slip condition is diminished because there is the possibility of wall motion, it might be expected that the vorticity would be reduced. That this is in fact the case may be confirmed directly from the visualisation of the vorticity disturbance field given in Figure 4.7. The decrease in the square integral of the vorticity is an immediate consequence; the value taken by the integral is dictated by the vorticity field adjacent to the wall.

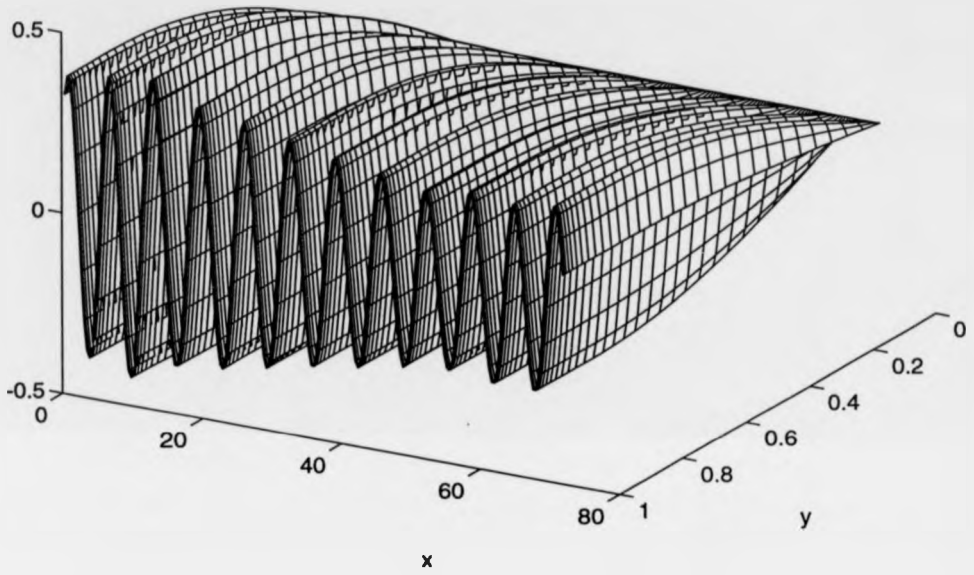


Figure 4.8: Fluid perturbation pressure.

## 4.3 Energy balance

We will now describe an energy balance equation that may be used to measure the relative importance of the various physical processes involved in the spatial growth and decay of the fluid disturbances. For two-dimensional linearised disturbances from the parallel mean flow $U$, the following relationship obtains

$$\left(\frac{\partial}{\partial t}+U\frac{\partial}{\partial x}\right)\left[\frac{1}{2}(u^2+v^2)\right]+uvU'+\frac{\partial(up)}{\partial x}+\frac{\partial(vp)}{\partial y}=\frac{1}{R}\left(\frac{\partial(u\omega)}{\partial y}-\frac{\partial(v\omega)}{\partial x}-\omega^2\right). \tag{4.7}$$

This can be derived by multiplying the $u$-momentum equation by $u$, the $v$-momentum equation by $v$, adding the resulting equations, and then employing the incompressibil-

ity condition together with the relation that defines the vorticity $\omega$. For time-periodic disturbance fields, we can eliminate the time derivative appearing in (4.7) by taking averages over a single time period. We will signify such averaging by placing a bar over the quantity concerned. If, in addition, an integration is performed across the half-width of the channel, then we can obtain the energy balance equation

$$\frac{d}{dx}\Big[\overbrace{\int_0^1 \frac{1}{2}U(\overline{u^2}+\overline{v^2})\,dy}^{\text{(I)}} + \overbrace{\int_0^1 \overline{up}\,dy}^{\text{(II)}} + \overbrace{\frac{1}{R}\int_0^1 \overline{v\omega}\,dy}^{\text{(III)}}\Big] = \underbrace{\int_0^1 (-\overline{uv})U'\,dy}_{\text{(i)}} \underbrace{-\frac{1}{R}\int_0^1 \overline{\omega^2}\,dy}_{\text{(ii)}} \underbrace{-\overline{v_w p_w}}_{\text{(iii)}} \underbrace{+\frac{1}{R}\overline{u_w \omega_w}}_{\text{(iv)}} . \tag{4.8}$$

As before, the subscript $w$ is used to denote evaluation at the unperturbed wall location $y = 1$. The significance of each of the separately labelled quantities will be discussed shortly. (Because of the assumed symmetries of the disturbance profiles about the channel centre, terms evaluated at $y = 0$ have been set equal to zero.)

Equation (4.8) provides a means of analysing the spatial growth or decay of the disturbances. Usually, it is more tractable to consider temporal rather than spatial growth, so averages would be taken over space instead of time. As has been mentioned previously, the temporal approach is not appropriate in the present context, since there is no obvious means of drawing an analogy between temporal and spatial evolution when the spatial homogeneity (in the streamwise direction) is broken by the inclusion of wall joins. Another change from accustomed energy balance formulations lies in the use of quantities which are defined in such a way that their dependence upon the vorticity flow-field is made explicit. The role played by the vorticity can then be discussed more readily. The chosen formulation also has some minor computational advantages when applications are made to numerical flow-field data. Further detailed comments are given in the appendix.

We will now interpret the various terms appearing in equation (4.8). The term labelled as (I) defines the average disturbance energy that is being convected past a given streamwise location by the mean flow. The term denoted by (II) can be thought

of as measuring the work done by the fluid disturbances against the perturbation pressure, across an imagined boundary drawn through the fluid at the appropriate streamwise position. In a study of the spatial instability of jets, Morris [72] treated the two terms (I), (II) together, calling their sum the integrated mechanical energy flux. The final term on the left-hand side of (4.8) can be related to the work done by the fluid disturbances against the viscous stresses they generate, over the same internal boundary considered for the pressure work. In practice, (III) is always negligible[10], so we will not dwell any further on its interpretation.

It may be argued that it is misleading to call (4.8) an energy balance equation. The left-hand side consists of the streamwise derivative of a quantity that is more properly identified as an energy flux. Nevertheless, in interpreting the terms on the right-hand side, we will persist with a nomenclature that, strictly, is only appropriate when temporal rather than spatial growth is under consideration. The term labelled as (i) is just the usual Reynolds stress production term, except for the change from spatial to temporal averaging. It represents the transfer of energy from the mean flow to the disturbances. The term marked with the label (ii) can be viewed as defining the viscous dissipation. For the case of rigid walls and temporal growth, we would have the identity

$$\frac{1}{R}\int_0^1 \overline{\omega^2}\, dy = \int_0^1 \overline{\sigma_{ij}\frac{\partial u_i}{\partial x_j}}\, dy \tag{4.9}$$

where $\sigma_{ij}$, $i,j = 1,2$ are the perturbation viscous stresses and, in this instance, the overlines denote averages along a disturbance wavelength. If time averaging replaces spatial averaging, or there is possible wall motion, the two expressions can no longer be equated. However, the discrepancy involved is usually slight, at least in the problem situation of current concern. (Further technical details are relegated to the appendix.)

For the case of rigid walls, the two terms (i), (ii) give the balance between energy

[10] An explanation of this fact is given in the appendix

production and removal. The destabilisation of Tollmien-Schlichting disturbances occurs when an indirect viscous mechanism leads to the generation of a positive Reynolds stress. This can establish sufficient production of energy to overcome the viscous dissipation. The additional terms on the right-hand side of equation (4.8) arise because there is the possibility of wall motion. The term labelled (iii) represents an energy transfer to the wall. It gives the work done by the perturbation fluid pressure on the upper wall of the channel. (The fact that the upper channel wall is being considered accounts for a change in sign from that which appears in studies of Blasius flow; see for example [14]. A positive value for $\overline{v_w p_w}$ indicates a positive transfer of energy from the fluid to the wall.) The interpretation of the final term in the energy balance equation is less straightforward. No term corresponding to (iv) appears in the energy equation that can be obtained for the motion of the wall. This means that we cannot attribute (iv) to any process that transfers energy between the wall and fluid. In studies conducted by Carpenter *et al* [14], [73], a term which can be shown to be closely approximated by (iv) was taken to represent an energy transfer from the disturbance to the mean flow. More specifically, it was argued that such a term arose from an interaction between the displaced mean flow and the perturbation viscous shear stress acting at the wall. This interpretation may be challenged[11]. It may be more appropriate to attribute (iv) to an additional form of viscous dissipation that can occur when the wall bounding the mean fluid flow is no longer kept at a fixed position. Whatever the character of the physical mechanism that (iv) is presumed to reflect, it would seem, both from previous studies and from the investigations reported herein, that for a Tollmien-Schlichting wave propagating over a compliant wall, the sign of (iv) is typically such that a stabilising effect is obtained.

Figure 4.9 displays computed results for the streamwise development of the various terms in the energy balance equation. These were obtained from the same numer-

[11] Private communication, P.W. Carpenter.

ical simulation that was considered in the previous section. Figure 4.9(a) contains plots of the two quantities (I), (II) that appear on the left-hand side of the energy balance equation. (No plot is given for the quantity (III), since it is negligible everywhere.) It can be seen that they undergo a pronounced growth in the vicinity of the rigid/compliant wall join. Shortly beyond the join, both quantities become subject to a constant decay. Thus, the spatial development noted previously for the disturbance energy $E$ is replicated in the behaviour of the two quantities (I), (II), which together make up the time-averaged mechanical energy flux. It can be inferred, once more, that the Tollmien-Schlichting wave adapts to the presence of the compliant walls over a distance comparable to its wavelength. Similar remarks may be made concerning the behaviour at the compliant/rigid wall join, except that the streamwise sequence is inverted.

Figure 4.9(b) shows how the Reynolds stress production term varies as the wave passes into and out of the compliant-walled section of channel. It can be seen that in the immediate vicinities of the wall joins, the magnitude of the production term is much larger than at other streamwise locations. Near the rigid/compliant wall join, where fluid adjacent to the wall is being brought into motion, there is a strong peak in positive energy production. By contrast, when the compliant/rigid wall join is approached, the fluid in contact with the wall must adjust to a state of rest. This is reflected in the fact that the production term becomes markedly negative. Away from the joins, the Reynolds stress energy production is positive in the parts of the channel where the wave propagates over rigid walls. In the compliant-walled section, it may be inferred that the Reynolds stress distribution has been substantially modified, since there is energy removal instead of production. (It should be noted that a change in the sign of the energy production term is not a prerequisite for the stabilisation of Tollmien-Schlichting waves by compliant walls. In simulations conducted for other choices of wall compliance parameters, or for the same wall parameters with a wave at a different temporal frequency, it was found that the Reynolds stress production

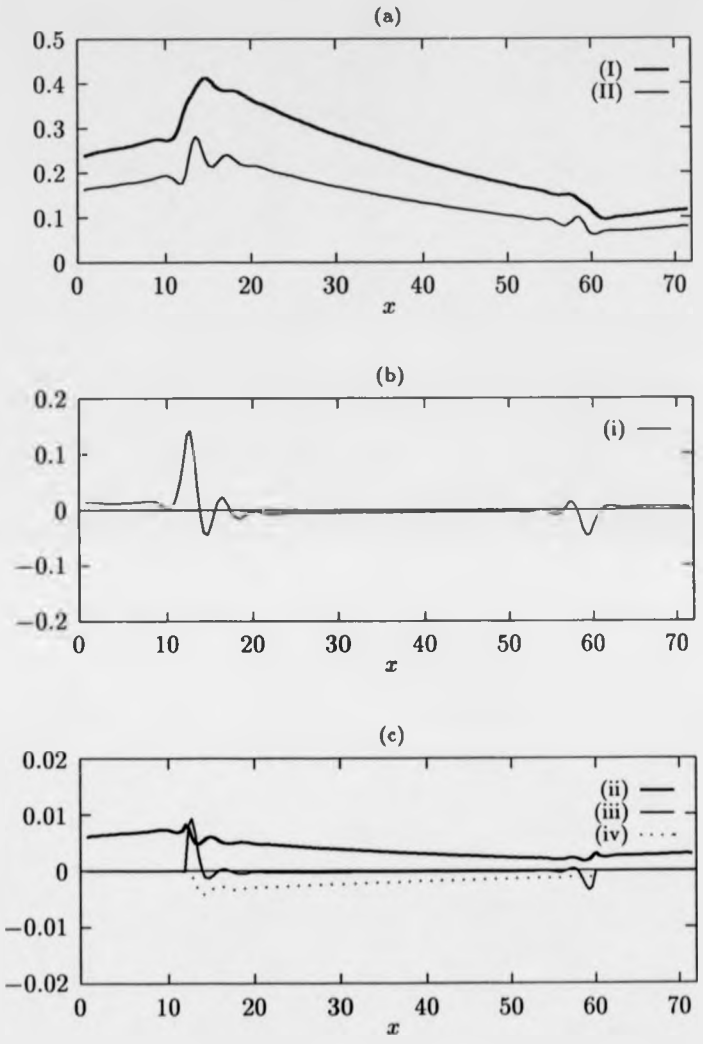


Figure 4.9: Streamwise variation of the terms from the energy balance equation (4.8). As before, $R = 12000$ and $\beta = 0.24$. For the compliant-walled section of the channel, which extends from $x = 12$ to $x = 60$, the wall parameters are $m = 1/3$, $K = 7.68 \times 10^7$, $T = 0$, $B = 1.92 \times 10^7$, $d = 0$.

term could only be reduced in magnitude, rather than reversed in sign. In such cases it was still possible to obtain a stabilised Tollmien-Schlichting wave.)

Figure 4.9(c) displays the remaining terms from the right-hand side of the energy balance equation. Note the change in scale from that which was used in plotting the Reynolds stress production term. In the vicinity of the wall joins, the production term reaches values that are an order of magnitude larger than any of the values taken by the other three terms. Away from the joins there is no such disparity. At locations within the rigid-walled parts of the channel, the Reynolds stress energy production term is very nearly balanced by the term (ii) which represents the viscous dissipation. This is only to be expected, since the difference between these two terms determines the weak spatial growth of the Tollmien-Schlichting wave in the absence of wall motion.

The presence of the wall joins is marked clearly in the behaviour of the dissipation term. There is a decrease in the value of (ii) over the rigid/compliant join, followed by an increase at the compliant/rigid join. In fact, there is nothing new to report here; the viscous dissipation term is obtained by time-averaging and scaling the vorticity integral magnitude that was considered earlier. The term (iii), which represents the work done by the fluid perturbation pressure on the compliant wall, is negligible except in the immediate neighbourhood of each wall join. At locations slightly downstream of the rigid/compliant join, the transfer of energy to the wall becomes comparable to the viscous dissipation. Upstream of the compliant/rigid wall join, there is a reversed energy transfer from the wall to the fluid, mirroring the behaviour at the first join. Over the rest of the length of the compliant-walled section, the very small values taken by (iii) are negative. Later on, the detailed streamwise variation of (iii) will be compared with predictions obtained from a simple analytic model. It will be seen that the features noted at the wall joins can be explained by examining the spatial excitation of the wall motion.

We have still to consider the term that was labelled as (iv) in the energy balance

equation. This term can be interpreted as representing an additional form of viscous dissipation. Be that as it may, it is apparent from Figure 4.9(c) that the sign of (iv) is such that a stabilising effect is obtained throughout the whole of the compliant-walled section of the channel. In fact, the magnitude of (iv) is of the same order as that of the conventional dissipation term (iii). This comparability may be anticipated from the following somewhat unsophisticated argument. As has been remarked previously, the vorticity distribution is concentrated close to the channel walls, where it reflects the presence of steep gradients in the profile of the $u$-component of the velocity. These gradients arise from the need to satisfy the no-slip boundary condition. For the case of a rigid-walled channel, the $u$-component is brought to zero over a lengthscale of the order $O(R^{-\frac{1}{2}})$ that characterises the viscous wall layer. Thus, we can suppose that the gradients in the $u$-component, and hence the values of the vorticity, are of order $O(R^{\frac{1}{2}})$ for points located up to a distance of order $O(R^{-\frac{1}{2}})$ away from the wall. From this, we can estimate that the square integral of the vorticity, along with its time-average, will be of order $O(R^{\frac{1}{2}})$. Hence, it is plausible to conclude that the viscous dissipation term (ii) should be of order $O(R^{-\frac{1}{2}})$. (Note that in making reference to various orders of magnitude, we have presupposed that the disturbance amplitudes are normalised to be of order unity in some appropriately chosen norm. For present purposes, such a norm could be defined by taking the maximum value of $u$ across the channel half-width.) If a compliant wall replaced the rigid wall, we would expect that the same estimate could still be made for (ii), provided the influence of the wall compliance does not lead to drastic reductions in the gradients found in the $u$-component profile close to the wall. More specifically, we will assume that these gradients retain their magnitude even when the wall is made so compliant that the value taken by $u$ at the wall is comparable to its maximum value elsewhere. (To gain some appreciation of the situation that is being considered, it may be helpful to refer back to the visualisation of the $u$-component given in Figure 4.5.) If this is the case, then we can infer that the product $u_w\omega_w$ will be of order $O(R^{\frac{1}{2}})$. We would

not expect time-averaging to yield a quantity with a different order of magnitude, unless it turned out that $u$ and $\omega$ were very near to being 90° out of phase at the wall location. It is simple to see that such a possibility does not arise. We have presumed that the vorticity close to the wall is determined largely by the wall-normal gradient of the $u$-component, so $u$ and $\omega$ should be either nearly in phase, or nearly in anti-phase at the wall. As a consequence, we can anticipate that the term (iv) will be of order $O(R^{-\frac{1}{2}})$, *i.e.* of the same order that was estimated for the viscous dissipation term (ii). Furthermore, if the effect of the wall compliance on the $u$-profile is to reduce the drop between the maximum value of $u$ and the value taken at the wall, whilst ensuring that $u$ and its wall-normal derivative remain of opposite sign right up to the location of the wall, then, to a good approximation, $u$ and $\omega$ will be in anti-phase at the wall. In such circumstances, the sign of the term (iv) will negative, and the contribution made to the energy balance will be stabilising. (Again, the details of the situation involved may become clearer if reference is made to Figure 4.5.)

## 4.4 Results for a partially stabilised wave

For the numerical simulation that has thus far been examined in detail, the temporal frequency $\beta$ of the Tollmien Schlichting wave was chosen in order that the spatial growth found over rigid channel walls would give way to spatial decay in the presence of compliant walls. In such circumstances, the adaptive behaviour of the wave could be distinguished in a particularly clear manner. However, it may be recalled that for the same selection of wall parameters and Reynolds number, the effect of the wall compliance on waves at other frequencies is insufficient to replace growth with decay.

So far as applications to transition delay are concerned, the behaviour of partially stabilised waves is likely to be of greater interest than that of completely stabilised waves. When the compliant walls are kept stiff enough to avoid the introduction of flow-induced instabilities, it does not appear to be possible, in situations of practical

concern, to eliminate the Tollmien-Schlichting instability for all temporal frequencies. Thus we will now present, in a briefer fashion than before, some numerical simulation results for a case where the presence of compliant walls only leads to a reduction in the spatial growth rate of the Tollmien-Schlichting wave. It will be seen that much the same form of behaviour is found as before, except that the effect of the wall compliance is less dramatic.

For the Reynolds number $R = 12000$ and the same wall compliance properties that were considered previously, Tollmien-Schlichting waves with a temporal frequency of $\beta = 0.2$ are expected to remain unstable. This may be confirmed from inspection of the neutral stability curves plotted in Figure 4.2. Solution of the Orr-Sommerfeld equation gives the complex spatial wavenumber for the case of rigid channel walls as $\alpha = 0.909 - i1.54 \times 10^{-2}$. When the walls are made compliant, the wavenumber is modified to $\alpha = 0.837 - i7.05 \times 10^{-3}$, so the spatial growth rate is approximately halved. For the rigid-walled channel, the growth rate predicted for $\beta = 0.2$ is close to the maximum attainable at the given Reynolds number. This remains the case when the channel walls are compliant, *i.e.* the growth rate stays near to the maximum that is possible for the selected compliant wall parameters.

Figure 4.10 contains plots for the computed streamwise development of the Tollmien-Schlichting wave with $\beta = 0.2$, as it enters and leaves the compliant-walled channel section. Apart from the changed temporal frequency, all parameters, including the computational domain size and the locations of the compliant panels, are the same as for the simulation reported in detail in Section 4.2. Thus, the results shown should be compared with those given previously in Figures 4.3 and 4.4. Dotted lines are again used to depict the amplitude envelopes that are consistent with linear stability theory. It can be seen that the behaviour near the locations of the rigid/compliant and compliant/rigid wall joins is very similar to that which was documented before. In particular, there is the same short lengthscale adaptation of the growth rate to the presence or absence of compliant walls. The abrupt changes in the disturbance

energy and square integral vorticity are also replicated. They occur with the same orientation as was discussed earlier.

Figure 4.11 displays the computed variation of the terms in the energy balance equation (4.8). A direct comparison should be made with Figure 4.10. It can be seen that the qualitative features that were previously noted have been retained, apart from the obvious alterations due to the fact that the Tollmien-Schlichting wave is no longer completely stabilised in the compliant-walled channel section. For instance, relatively large positive values of the Reynolds stress energy production term are again found in the vicinity of the rigid/compliant wall join. These are mirrored at the compliant/rigid wall join, where the energy production term now reaches negative values that are of even larger magnitude. The short streamwise lengthscale for the adaptation and re-adaptation of the wave, as it propagates through the compliant-walled section of the channel, can be discerned from the plots of the quantities (I), (II) that together make up the integrated mechanical energy flux. In order to emphasise the sharpness of the adaptive behaviour, additional lines have been included which show, for the convected disturbance energy (I), the distinct spatial growths expected from linear stability theory.

## 4.5 Wall excitation

For the type of problem that is investigated in the numerical simulations reported above, it is fairly straightforward to obtain an estimate for the lengthscale involved in the spatial excitation of the wall motion. This is achieved by considering time-periodic homogeneous solutions to the equation that governs the behaviour of the compliant walls. In principle, these solutions can be combined with a particular solution that represents the wall response to the forcing provided by the fluid pressure. In practice, the fluid forcing cannot be prescribed in advance of the wall motion, so the procedure adopted is only formally valid. For a finite length compliant wall, it

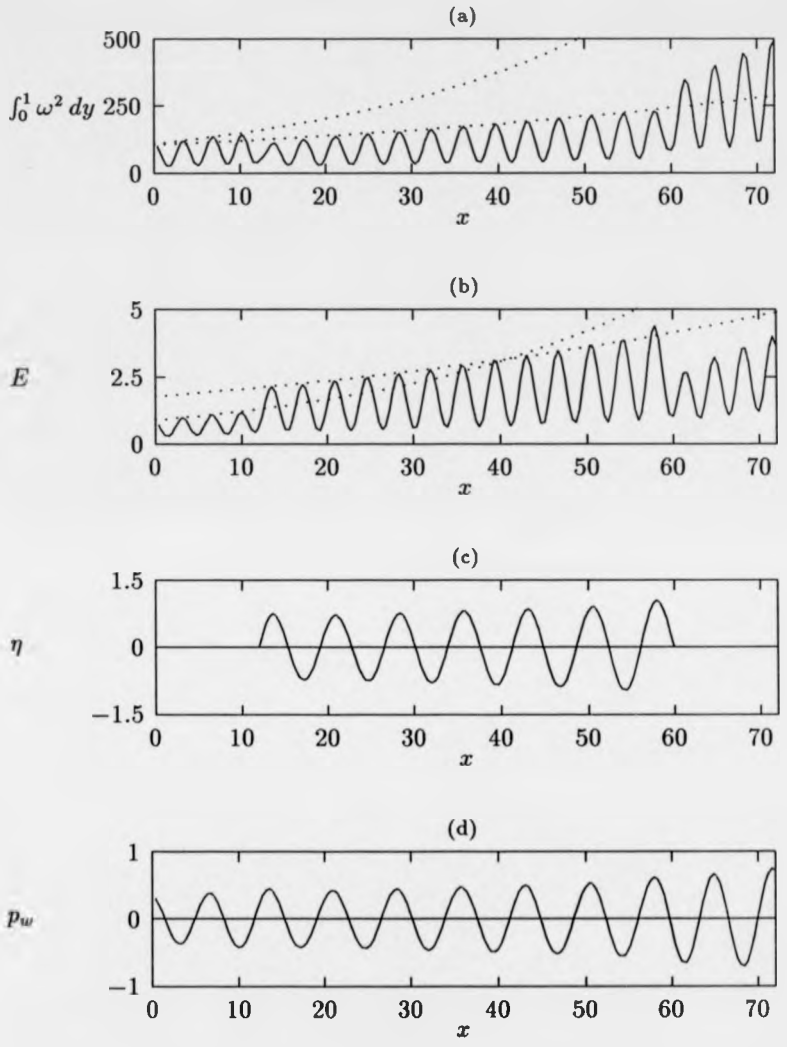


Figure 4.10: Streamwise development of Tollmien-Schlichting wave. The Reynolds number is $R = 12000$ and the temporal frequency $\beta = 0.2$. As before, the compliant wall parameters are $m = 1/3$, $K = 7.68 \times 10^7$, $T = 0$, $B = 1.92 \times 10^7$, $d = 0$.

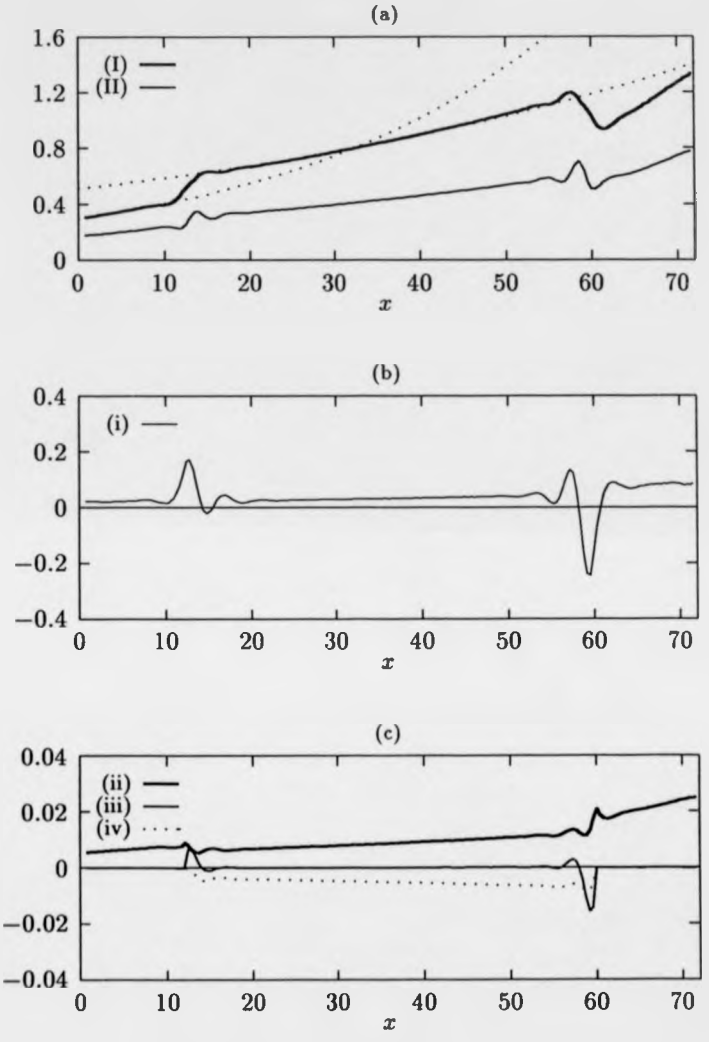


Figure 4.11: Streamwise variation of the terms from the energy balance equation (4.8). As in the previous figure, $R = 12000$ and $\beta = 0.2$. The wall parameters are also unchanged. The dotted lines in (a) show the projected spatial growth obtained from solutions of the Orr-Sommerfeld equation.

will be shown that the homogeneous solutions may be employed to ensure that the appropriate boundary conditions are met at each end of the wall. As a consequence, the homogeneous solutions can be taken to characterise the influence of the wall joins.

### 4.5.1 Time-periodic homogeneous solutions for the wall motion

For time-periodic wall motion with a frequency $\beta$, we can assume that the wall displacement takes the form

$$\eta(x,t) = \Re\left(\hat{\eta}(x)e^{-i\beta t}\right) . \tag{4.10}$$

Moreover, if we suppose that the fluid pressure at the wall can be written in the same manner as

$$p_w(x,t) = \Re\left(\hat{p}_w(x)e^{-i\beta t}\right) \tag{4.11}$$

then the governing equation for the compliant wall motion yields

$$-m\beta^2\hat{\eta} - i\beta\frac{d}{R}\hat{\eta} + \frac{1}{R^2}\left(B\frac{d^4}{dx^4} - T\frac{d^2}{dx^2} + K\right)\hat{\eta} = \hat{p}_w . \tag{4.12}$$

If $\hat{p}_w$ is given, this a fourth-order ordinary differential equation for the quantity $\hat{\eta}$. In order to avoid unnecessary complication, the wall damping term will be neglected. For the present investigation, we shall also set the tension $T$ equal to zero. Thus, we will consider solutions to

$$\left(\frac{B}{R^2}\frac{d^4}{dx^4} + \frac{K}{R^2} - m\beta^2\right)\hat{\eta} = \hat{p}_w . \tag{4.13}$$

Homogeneous solutions of the form

$$\hat{\eta}(x) = e^{\lambda x} \tag{4.14}$$

can be obtained for

$$\lambda^4 = -\frac{K - m\beta^2R^2}{B} . \tag{4.15}$$

There are two distinct cases to be considered:

1. $K > m\beta^2 R^2$.

   We then have

$$\lambda = \pm(1 \pm i)\gamma \tag{4.16}$$

   where

$$\gamma = \left(\frac{K - m\beta^2 R^2}{4B}\right)^{\frac{1}{4}} . \tag{4.17}$$

   The four linearly independent homogeneous solutions can be taken as

$$\bar{\eta} = e^{\pm\gamma x}\cos\gamma x \ , \ e^{\pm\gamma x}\sin\gamma x \ . \tag{4.18}$$

2. $K < m\beta^2 R^2$.

   For this case we have

$$\lambda = \pm\delta \ , \ \pm i\delta \tag{4.19}$$

   where

$$\delta = \left(\frac{m\beta^2 R^2 - K}{B}\right)^{\frac{1}{4}} . \tag{4.20}$$

   The homogeneous solutions are then

$$\bar{\eta} = e^{\pm\delta x} \ , \ \cos\delta x \ , \ \sin\delta x \ . \tag{4.21}$$

It can be seen that in the case considered first, there are two solutions which grow exponentially with increasing $x$, and two solutions which decay. The lengthscale for the growth/decay is defined by $\gamma^{-1}$. For a compliant wall of finite streamwise extent, *i.e.* a compliant panel, it will be shown that the two decaying solutions may be associated with the enforcement of the boundary conditions at the upstream end of the wall. Their contribution to the total wall motion is diminished exponentially at other locations. Similar remarks apply for the two growing homogeneous solutions. These turn out to be important close to the downstream end of a compliant panel, but play a negligible role elsewhere.

For the second case, where $K < m\beta^2 R^2$, we can again extract a spatial lengthscale from the homogeneous solutions. This is given by $\delta^{-1}$. There is now only one

solution that grows exponentially, together with a single decaying solution. The other two solutions are purely oscillatory. As in the previous case, the homogeneous solutions may be combined with a particular solution in order to satisfy the boundary conditions at the ends of a compliant panel. However, the contributions made by the homogeneous solutions to the overall wall response are no longer localised to the vicinity of the panel ends.

To illustrate the significance of the homogeneous solutions in a more concrete fashion, it is necessary to specify the streamwise variation of the fluid perturbation pressure that forces the wall motion. In general, the forcing provided by the fluid cannot be known in advance. The compliant wall and the fluid must be treated as interactively coupled. In fact, the precise computation of this interaction provides much of the challenge for the problems tackled in the present work. Nevertheless, some insight, as well as some testable predictions, can be obtained by overlooking the full effect of the wall motion on the fluid pressure. Thus, for simplicity, we will consider the case where the fluid forcing is prescribed as

$$p_w(x,t) = \Re\left(Ae^{i(\alpha x - \beta t)}\right) \tag{4.22}$$

in which case we have

$$\hat{p}_w = Ae^{\imath\alpha x}\,. \tag{4.23}$$

If the compliant wall were of unbounded extent in both the upstream and downstream directions, such a form forcing could be associated, legitimately, with a Tollmien-Schlichting wave propagating in the fluid. (Alternatively, it could be associated with a flow-induced surface instability, but this possibility is not immediately relevant for present purposes.) For a finite-length compliant wall, we might expect that the prescribed fluid forcing would only be realised, if it all, in an approximate manner.

It is straightforward to see that a particular solution to (4.13) with $\hat{p}_w$ specified by (4.23) may be given as

$$\hat{\eta}_p = Ce^{\imath\alpha x} \tag{4.24}$$

where

$$C = \frac{A}{\frac{1}{R^2}(B\alpha^4 + K) - m\beta^2} .$$

The general solution can then be expressed in the form

$$\hat{\eta} = Ce^{i\alpha x} + \sum_{j=1}^{4} D_j e^{\lambda_j x} \tag{4.25}$$

where the four roots $\lambda_j$ define the homogeneous solutions. The constants $D_j$ need to be determined by applying appropriate boundary conditions. For a compliant panel, we can impose conditions for a hinged join

$$\hat{\eta} = \frac{d^2\hat{\eta}}{dx^2} = 0 \tag{4.26}$$

at the locations $x = x_u$, $x_d$ of the upstream and downstream wall ends.

If the wall parameters satisfy the relation $K > m\beta^2 R^2$, then the solution that meets the hinged join boundary conditions may be obtained as

$$\hat{\eta} = C\left(e^{i\alpha x} + e^{i\alpha x_u} g(x - x_u) + e^{i\alpha x_d} g(x_d - x)\right) \tag{4.27}$$

where the function $g$ is defined by

$$g(x) = -e^{-\gamma x}\left(\cos\gamma x + \frac{\alpha^2}{2\gamma^2}\sin\gamma x\right) . \tag{4.28}$$

We have assumed that the spatial lengthscale associated with the homogeneous solutions $\gamma^{-1}$ is smaller than the length of the compliant panel, $l = x_d - x_u$, so that terms involving the factor $e^{-\gamma l}$ can be neglected. Furthermore, the spatial growth/decay that is prescribed for the fluid forcing is presumed to be much weaker than that defined by the homogeneous solutions. In other words, we suppose that $\alpha_i \ll \gamma$. Some indication of the physical import, and reasonableness, of these assumptions may be obtained as follows. When the compliant wall parameters are selected to yield $R_d = R_t = R$, it can be shown that

$$\gamma = \frac{\alpha_c}{\sqrt{2}}\left(1 - \frac{5}{4}\left(\frac{\beta}{\alpha_c}\right)^2\right)^{\frac{1}{4}} , \tag{4.29}$$

where $\alpha_c$ is the critical wavenumber for the flow-induced surface instabilities. Usually, the wall properties will also be chosen so that $\alpha_c \sim \alpha$. Such a choice is required in order to optimise the effect of the wall compliance on the stability of the Tollmien-Schlichting wave, with wavenumber $\alpha$, that provides the forcing of the wall motion. In these circumstances we will have $\beta/\alpha_c \sim$ *phase speed of the Tollmien-Schlichting wave* $\sim 0.25$, and hence $\gamma \sim \alpha/\sqrt{2}$. This means that the lengthscale defined by $\gamma^{-1}$ will be of the same order as the wavelength of the Tollmien-Schlichting wave. The neglect of terms involving $e^{-\gamma l}$ is then acceptable on condition that the panel length $l$ is sufficiently large compared with the Tollmien-Schlichting wavelength. Since we expect to have $\alpha_i \ll \alpha_r$, it can be seen that there is no difficulty in making the further supposition that $\alpha_i \ll \gamma$.

Detailed inspection of (4.27) reveals that the complete solution is constructed in the manner that was anticipated earlier. The inclusion of a linear combination of the two decaying homogeneous solutions, in the guise of the function $g(x - x_u)$, ensures that the two boundary conditions at the upstream wall end are satisfied. The two growing homogeneous solutions, which are combined together in $g(x_d - x)$, can be seen to play an analogous role at the downstream end of the wall. Away from the ends of the compliant panel, the contribution of the homogeneous part to the total solution for the wall motion is insignificant. Thus, it is possible to interpret the homogeneous solutions as defining the spatial excitation, and de-excitation, of the compliant wall motion. They determine the extent of the constraining influence that is exerted by the wall joins.

When $K < m\beta^2 R^2$, the complete solution for the wall motion which meets the boundary conditions may be constructed in the form

$$\hat{\eta} = C\left(e^{i\alpha x} + e^{i\alpha x_u}\, h(x - x_u) + e^{i\alpha x_d}\, h(x_d - x)\right) \tag{4.30}$$

where the function $h$ is given as

$$h(x) = \frac{1}{2}\left(\left(\frac{\alpha^2}{\delta^2} - 1\right) e^{-\delta x} + \left(\frac{\alpha^2}{\delta^2} + 1\right) \frac{\sin \delta(x - l)}{\sin \delta l}\right) \tag{4.31}$$

with $\delta$ defined as in (4.20). In the same manner as for the previous case, it has been assumed that the quantity $e^{-\delta l}$ may be ignored in obtaining the coefficients for the homogeneous part of the solution. The presence of a constant amplitude sinusoidal component in the function $h$ implies that the wall joins extend an influence over the whole length of the panel. Thus, if the solution given by (4.30) proved to be physically realisable, it would no longer be appropriate to view the wall motion as only being excited, and then de-excited, near the localities of the upstream and downstream wall ends. However, it should be recalled that the interactive coupling between the fluid and wall motion has been deliberately oversimplified. In order to appear in practice, the sinusoidal wall motion associated with the homogeneous part of the solution would need to be matched in the motion of the fluid. The fluid would have to support, over the full streamwise extent of the compliant panel, neutrally stable disturbances with the spatial wavenumber $\delta$. More particularly, it would be necessary for the fluid to sustain the linear combination of upstream and downstream propagating waves[12] that is stipulated in (4.30). By contrast, the requirements for the case where $K > m\beta^2 R^2$ can be seen to be far less stringent. For the solution defined by (4.27) to be realised, the motion of the fluid that matches the homogeneous part of the wall motion would only have to be maintained at locations close to the wall ends.

Although the fluid cannot be expected to support arbitrary forms of wall motion over indefinite streamwise distances, it may be possible, depending on the wall compliance parameters and the temporal frequency involved, to sustain motions that are associated with flow-induced surface modes of disturbance. In the present context, these would be represented by non-homogeneous solutions to the wall motion equation. We might conjecture that when $K < m\beta^2 R^2$, such non-homogeneous solutions could, in practice, take over the role that was attributed to the two sinusoidal homogeneous solutions. Clearly though, no further progress can be made using the

[12]The purely sinusoidal component of the homogeneous part of the total solution for $\eta$ can also be written in the form $ae^{i\delta x} + be^{-i\delta x}$, where, in general, neither of the complex constants $a$, $b$ vanish.

simplistic form of analysis presented above. The presence of flow-induced surface waves would have to be reflected in a modified form for the fluid perturbation pressure used to force the wall motion; a straightforward prescription of the pressure, as in (4.23), would no longer be acceptable.

In summary, the analysis of the homogeneous solutions for the wall motion suggests that two distinct types of behaviour may occur as a Tollmien-Schlichting wave propagates over a finite-length compliant panel. For behaviour of the first type, the effects of the wall joins are highly localised. Away from the immediate vicinity of the joins, it may be possible for the wave to take the form that would have been anticipated for compliant walls of unbounded streamwise extent. The second class of behaviour is characterised by longer range effects from the wall joins. However, since the predicted form of wall motion is unlikely to be sustainable, there is the prospect that the Tollmien-Schlichting wave may become superposed with flow-induced surface waves, in order to meet the boundary conditions applying at the ends of the panel.

Later on, we will examine, in the light of the above discussion, results obtained from direct numerical simulations. But before doing this, we note that homogeneous solutions to the wall motion equation have also been considered, albeit from a different point of view, by Carpenter & Morris [14]. These authors used a global eigenvalue scheme to determine solutions of the Orr-Sommerfeld equation for Blasius flow over a compliant wall. They found a particular eigenvalue which, according to conventional interpretation, implied the existence of a powerful spatially growing instability. It turned out to be possible to identify this anomalous eigenvalue with one of four spatially developing free wave modes in the compliant wall. These modes are just the homogeneous solutions, differently described. The associated complex spatial eigenvalues are given by

$$\alpha = -i\lambda \tag{4.32}$$

where the possible values of $\lambda$ are as indicated previously. (The anomalous eigenvalue determined from the Orr-Sommerfeld equation by Carpenter & Morris can be related to the homogeneous solution with $\lambda = (1+i)\gamma$, for which $\alpha = (1-i)\gamma$.)

Carpenter, Joslin & Morris [74] have offered a physical interpretation for such eigenvalues, by considering an appropriate initial-value problem. They were able to argue that, so far as the free wave modes are concerned, the occurrence of a complex spatial eigenvalue with a positive real part and negative imaginary part need not be indicative of instability. The analysis of the homogeneous solutions, presented above, supports such a conclusion. In fact, it suggests that the spatially growing (and decaying) free wave modes may be most profitably interpreted in a context where the compliant wall is taken to be of finite, rather than infinite, streamwise extent.

### 4.5.2 Non-homogeneous solutions for the wall motion

The connection between free wave modes of the compliant wall and solutions of the Orr-Sommerfeld equation is not quite as simple as some of the preceding comments might suggest. When the fluid and wall motion are interactively coupled, the free waves become subject to modification. In the terminology used earlier, such modification coincides with a passage from homogeneous to non-homogeneous solutions of the wall motion equation. The latter type of solution has already been investigated in Section 2.3, using inviscid shear layer theory to derive an approximate expression for the perturbation fluid pressure at the wall. The results that were presented for the case of temporally growing waves may be extended to include the possibility of spatial growth. We will now digress to give a brief account of how this can be achieved.

It may be recalled that an approximate wave dispersion relation was derived, allowing the determination of the phase velocity $c$ for disturbances with wavenumber

$\alpha$. For convenience, we restate the dispersion relation here in the form

$$\frac{1}{R^2}\left(B\alpha^2 + \frac{K}{\alpha^2}\right) - mc^2 = J_0(c) \tag{4.33}$$

where the quadratic function

$$J_0(c) = c^2 - \frac{4}{3}c + \frac{8}{15}$$

gives a first approximation to the forcing provided by the fluid pressure. (At such a level of approximation, there is no account of any critical layer effects.) For simplicity, both the wall damping coefficient and the wall tension have again been set equal to zero. If we make the naïve replacement $c = \beta/\alpha$, where $\beta$ is taken to be the real temporal frequency, then we obtain

$$\frac{1}{R^2}\left(B\alpha^4 + K\right) - m\beta^2 = \beta^2 - \frac{4}{3}\beta\alpha + \frac{8}{15}\alpha^2 \,. \tag{4.34}$$

The complex values of $\alpha$ that correspond to spatially developing free wave modes can be found by neglecting the terms on the right-hand side. If these terms are retained, then, assuming that the frequency $\beta$ is prescribed, we have a quartic polynomial equation for $\alpha$, with real-valued coefficients. Without further analysis, all that can be said about the four roots of such an equation is that they will either be real or appear in complex conjugate pairs.

At this point, it is pertinent to reformulate the conditions $K > m\beta^2R^2$ and $K < m\beta^2R^2$ that were previously used in distinguishing the two possible forms of behaviour associated with the homogeneous solutions. If we define[13]

$$\beta_0 = \frac{1}{R}\left(\frac{K}{m}\right)^{\frac{1}{2}} \tag{4.35}$$

then the type of behaviour that is found will depend on whether the temporal frequency satisfies $\beta < \beta_0$ or $\beta > \beta_0$. From a conventional point of view, $\beta_0$ can be

[13]The appearance of the factor $1/R$ in the expression for $\beta_0$ is just a consequence of the adopted non-dimensionalisation procedure.

interpreted as defining a cut-off frequency for free waves propagating along the compliant wall. If complex values of the spatial wavenumber are excluded, then there are no free waves with temporal frequencies below $\beta_0$.

When the wall is coupled to the fluid, we might still expect to find a cut-off frequency for the appearance of waves with a real wavenumber. Detailed inspection reveals that this expectation cannot always be fulfilled. It may be shown that unless

$$\sqrt{KB} > \frac{4}{15}R^2 \tag{4.36}$$

there will be at least two, and possibly four, real values of $\alpha$ that satisfy equation (4.34), irrespective of the value chosen for the temporal frequency. This can be seen by rewriting the equation in the form

$$\alpha^2\left(\frac{8}{15} - \frac{B}{R^2}\alpha^2\right) = \left(\frac{K}{R^2} - (m+1)\beta^2\right) + \left(\frac{4\beta}{3}\right)\alpha\,, \tag{4.37}$$

and then considering the graphs of the two functions of $\alpha$ defined by the left-hand and right-hand sides. Other mentioned characteristics of the solutions for $\alpha$ can be discerned in the same fashion.

The relation specified in (4.36) coincides with the restriction on the wall compliance parameters that, according to the inviscid theory, is necessary for the avoidance of divergence instability. In other words, it is equivalent to the condition $R_d > R$, where $R_d$ is the critical Reynolds number defined by (4.1). (Note that we have set $T = 0$.) When this condition is satisfied, it may be demonstrated that there is, in fact, a value $\beta_1$ of the temporal frequency below which no real-valued solutions for $\alpha$ can be obtained. It may also be shown that the cut-off frequency vanishes in the limiting case where the compliant wall properties are chosen so as to yield marginal stability with respect to divergence, *i.e.* so that $R_d = R$. At frequencies just above $\beta_1$, there are two real solutions for $\alpha$, both of which, being negative, represent upstream travelling waves. Such a form of behaviour may be contrasted with that which is found for the case of free waves. If the fluid forcing is neglected, then for frequencies

larger than the cut-off $\beta_0$, the two real solutions obtained for $\alpha$ have equal magnitudes but opposite signs. They correspond to waves which propagate upstream and downstream with the same phase speed.

No matter how the wall parameters are selected, it can be shown that if the temporal frequency is greater than

$$\beta_2 = \frac{1}{R}\left(\frac{K}{m+1}\right)^{\frac{1}{2}} \tag{4.38}$$

then there are (at least) two real values of $\alpha$ that satisfy (4.34), one of which must be positive, the other negative. As in the free wave case, these two values correspond to a downstream and an upstream travelling wave, respectively, though the phase speeds need no longer be equal. (For large enough frequencies, there are no other real-valued solutions for $\alpha$; the remaining two solutions can only be complex.) From the foregoing discussion it should be clear that $\beta_2$ is not a cut-off frequency; $\beta \geq \beta_2$ is a sufficient, but not necessary, condition for obtaining waves with real wavenumbers. Thus, it is straightforward to show that we must have $\beta_2 > \beta_1$, in addition to the relation $\beta_2 < \beta_0$ which follows directly from the definitions.

As a final observation concerning the solutions of (4.34), we note that if all the wall compliance parameters are made sufficiently large[14], then the cut-off frequency $\beta_1$ approaches the value $\beta_0$ that would apply in the case of free waves. At each temporal frequency, the solutions obtained for $\alpha$, when the fluid forcing is included, can be shown to agree with the solutions that are found if the forcing is left out.

We have digressed from our simple analysis of the excitation and de-excitation of the wall motion at the wall joins. This was partly in order to give some indication of how the spatially developing free wave, or as we previously described them, homo-

[14]Strictly speaking, we need to consider wall parameters defined in the form

$$B = sB_c \ , \ K = sK_c \ , \ m = sm_c$$

for fixed values of $B_c$, $K_c$ and $m_c$, and then take the limit as the parameter $s$ tends to infinity.

geneous, solutions might need to be amended if the interactive coupling between the wall and the fluid were to be treated more thoroughly. In a sense, the analysis based on the homogeneous solutions marks out its own limitations, by identifying the possibility of non-localised effects from the wall joins when the condition $K > m\beta^2 R^2$, or $\beta < \beta_0$, is violated. For $\beta > \beta_0$, a more sophisticated treatment is required. It was suggested that this might involve the accommodation of additional modes of disturbance in the form of flow-induced surface waves. The inclusion of such waves would supply an alternative means of meeting the boundary conditions on the wall motion at the wall joins.

The observations that were made concerning the appearance, or non-appearance, of cut-off frequencies in the inviscid theory dispersion relation (4.34) only apply, from a strict point of view, to the case where the compliant wall is taken to be of infinite streamwise extent. However, the same observations can be expected to remain pertinent when a finite-length compliant panel is under consideration. In particular, it may be conjectured that even for $\beta < \beta_0$, flow-induced surface modes could play a significant role in determining the adaptive behaviour of a Tollmien-Schlichting wave, provided we still had $\beta > \beta_1$. Bearing this in mind, it should be recalled that $\beta_1$ vanishes when the wall parameters are chosen so that, according to the inviscid theory, divergence is marginally stable at the Reynolds number specified for the fluid flow. Such a choice of wall parameters has been made for all of the numerical simulations reported thus far.

At this point it needs to be emphasised that no attempt has been made to achieve a complete analysis of the excitation of the wall motion; the approach taken is far too rudimentary. All that is being sought is some guidance for interpreting the numerical simulation results. We will now return to the consideration of such results, to see to what extent the solutions that were constructed for the wall motion may be used to gain an understanding of the simulated behaviour.

### 4.5.3 Comparison with numerical simulation results

The relation $\beta < \beta_0$ (or $K > m\beta^2 R^2$) holds for the flow and wall parameters selected for the particular simulation that was discussed in detail in Section 4.2. It was noted there that the streamwise variation of the fluid perturbation pressure remained very smooth, and sinusoidal, as the Tollmien-Schlichting wave passed over the rigid/compliant and compliant/rigid wall joins. (In order to fix ideas, it may be useful to refer back to Figure 4.4.) Thus, it seems plausible to suppose that, over the length of the compliant-walled section of the channel, the variation of the wall pressure takes the simple form specified in (4.22), at least to a first approximation. If this supposition is valid, then it should be possible to obtain a good description of the wall motion using the solution for $\hat{\eta}$ defined by (4.27).

It may be recalled that $\hat{\eta}$ represents the complex amplitude corresponding to a time-periodic, real-valued wall displacement $\eta$. Taking time-averages we have

$$\overline{\eta^2} = \frac{1}{2}\,|\hat{\eta}|^2 \ . \tag{4.39}$$

Making use of this relationship, the streamwise variation of the averaged square wall displacement, as computed from the numerical simulation, can be compared directly with the variation predicted from the solution that was derived for $\hat{\eta}$. In a similar manner, the time-average of the pressure work done by the fluid on the wall may be anticipated using the relation

$$\overline{p_w v_w} = \frac{\beta}{2}\,\Im\,(\hat{\eta}\hat{p}_w^*) \ , \tag{4.40}$$

where $v_w = \partial\eta/\partial t$ is the normal component of fluid velocity at the location of the wall, and the complex-valued pressure amplitude $\hat{p}_w$ takes the form given in (4.23).

Figure 4.12 displays numerical simulation results for the time-averaged square wall displacement and pressure work, together with the distributions expected from the simplified analysis. It may be seen that there is good agreement. In particular, the streamwise distance over which the wall motion is excited is accurately predicted.

This implies that the influence exerted by the wall joins may be characterised using the lengthscale $\gamma^{-1}$ that defines the homogeneous solutions to the wall motion governing equation. So far as the pressure work is concerned, the predictions of the simple analytic theory are barely distinguishable from the results obtained in the full simulation. The pronounced transfers of energy between the fluid and the compliant wall, which are found in the immediate vicinities of the wall joins, may be attributed, almost entirely, to the homogeneous components of the wall motion. These produce localised phase shifts between the wall pressure and the wall velocity.

In prescribing the wall pressure amplitude $\hat{p}_w$, the value for the complex wavenumber $\alpha$ was taken to be that which would be appropriate for a channel with compliant walls throughout. This evidently leads to the correct prediction of the decay in $\overline{\eta^2}$ that is found over most of the length of the compliant wall, away from the immediate vicinities of wall joins. Thus, it would appear that $\gamma^{-1}$ is, in fact, the only significant lengthscale involved in the adaptation of the wave to the presence of the wall compliance. As soon as the wall motion is excited, the growth rate of the fluid disturbance takes on the value that would have been expected for an entirely compliant-walled channel. (It should be remarked that the analytic solution for $\hat{\eta}$ had to be normalised before comparisons could be made with the simulation results. The magnitude of $\hat{p}_w$ must be specified at a single streamwise position. In effect, this determines the magnitude of the constant $A$ in (4.23). An appropriate value was supplied from the numerical simulation, by taking the computed amplitude of the wall pressure wave at a location near the centre of the compliant panel. This procedure ensures that there is no free parameter which can be varied to improve the match between the results obtained from the simulation and those derived from the simple analytic theory.)

For the numerical simulation of a partially stabilised wave that was reported in Section 4.4, the relation $\beta < \beta_0$ still holds. Good agreement was again found between the wall motion computed in the simulation and that predicted using the analytic solution. Similar consistency was obtained with the results of some further

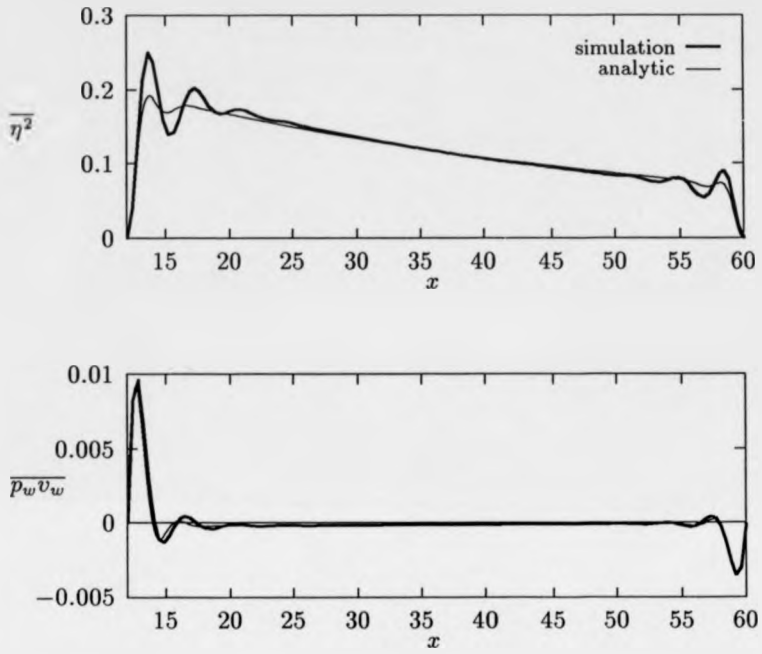


Figure 4.12: Streamwise distribution of time-averages for the squared wall-displacements and the pressure work. The Reynolds number is $R = 12000$ and the temporal frequency $\beta = 0.24$. The wall parameters are $m = 1/3$, $K = 7.68 \times 10^7$, $T = 0$, $B = 1.92 \times 10^7$, $d = 0$. (This choice of parameters yields $\gamma^{-1} = 1.01$. The wavelength of the Tollmien-Schlichting wave, as determined from the Orr-Sommerfeld equation for an entirely compliant walled channel, takes the value $\lambda = 6.68$.) The wall joins are at $x = 12$ and $x = 60$.

simulations. These were conducted for other choices of the wall parameters that gave a cut-off frequency $\beta_0$ exceeding that of the Tollmien-Schlichting wave.

When $\beta > \beta_0$, the analysis of the homogeneous solutions to the wall motion governing equation indicates that a different type of wall behaviour may occur, though,

as previously discussed, the exact form of the predicted motion is unlikely to be realised in practice. In any case, it would appear that, for channel flow, there is little physical interest in such a situation. Investigation of solutions to the Orr-Sommerfeld equation suggests that it is not possible to obtain a significant stability effect on Tollmien-Schlichting waves if, in addition to requiring that neither divergence or travelling wave flutter is destabilised, the wall parameters must be chosen so that $\beta_0$ does not exceed all relevant values of the temporal frequency, *i.e.* values which lie within a range characteristic of the Tollmien-Schlichting instability[15]. However, as has to some extent been anticipated in remarks made earlier, it turns out that even in cases where $\beta < \beta_0$, the behaviour found in the simulations can become much more complicated than that predicted on the basis of the homogeneous solutions. The effects of the wall joins may no longer take a localised form. We will now discuss several such cases.

---

[15]The outlines of an explanation can be given by developing the heuristic argument that was presented at the end of Section 4.1. It may be recalled that a measure of the wall stiffness, $S$, was found to be minimised for a Tollmien-Schlichting wave with wavenumber $\alpha$ when the wall properties were chosen so as to yield $\alpha_c = \alpha$. The minimisation was achieved subject to the requirement that $R_d \geq R$ and $R_t \geq R$. If the wall properties are selected so that, in fact, $R_d = R_t = R$, then as noted previously, we have $m = 1/3$ and $K = 4\alpha_c^2 R^2/15$. It follows from the definition (4.35) that the free wave cut-off frequency will be given by $\beta_0 = 2\alpha_c/\sqrt{5}$. So to obtain $\beta_0 < \beta$ for a temporal frequency $\beta$ that corresponds to a Tollmien-Schlichting wave, we will need to have $\alpha_c < \sqrt{5}\beta/2$ and hence $\alpha_c/\alpha < \sqrt{5}c/2$, where $c \sim 0.25$ is the phase velocity of the Tollmien-Schlichting wave. In these circumstances, it is straightforward to show that the value of the stiffness coefficient $S$ will be of order $1/c^2$ greater than its minimum allowed value. Consequently, any stabilising effects of the compliant wall motion can be expected to be relatively weak.

## 4.6 Results involving a superposition with flow-induced surface waves

In this section we will describe results from a number of simulations where a more complex form of behaviour occurs as a Tollmien-Schlichting wave propagates over a finite-length compliant wall. As for the simulations reported earlier, it will be seen that the Tollmien-Schlichting wave undergoes localised adaptation in the vicinities of the rigid/compliant and compliant/rigid wall joins. In particular, it will be argued that, once again, the lengthscale over which the spatial growth rate becomes adjusted to the presence or absence of wall compliance is relatively small. However, in contrast to the behaviour that was documented before, the passage of the Tollmien-Schlichting wave through the compliant-walled section of the channel will be seen to be accompanied by the excitation of flow-induced surface waves.

A careful analysis is required in order to disentangle any behaviour attributable to flow-induced surface waves from behaviour that may be taken as defining the adaptation of the Tollmien-Schlichting wave. For all the simulations that have, thus far, been subjected to a detailed examination, it has turned out to be possible to, in effect, subtract out any flow-induced surface wave components of the total disturbance. The fact that such a procedure is at all viable suggests that flow-induced surface waves play only a secondary role as the Tollmien-Schlichting wave adjusts itself to changes in the character of the channel walls. It would seem that the presence of flow-induced surface waves complicates, but does not fundamentally alter, the adaptive behaviour that was described earlier for cases where such waves were absent.

At this point it should be mentioned that the numerical iteration procedure used to couple the fluid flow and wall motion calculations was amended, slightly, for simulations involving a significant excitation of flow-induced surface waves. It was discovered that, for a given total number of iterations per time-step, the best rate of convergence could be obtained if the streamwise marching procedure used to update

the fluid flow-field variables was repeated several times before recalculating the values of the wall displacements. In fact, in some instances, convergent solutions could not be obtained without such a modification to the form of the iteration.

Generally speaking, it was found that the computational expense of the simulations increased when flow-induced surface waves made a sizable contribution to the fluid flow-fields. Part of this increased computing cost may have arisen because it was possible for flow-induced surface waves to propagate upstream. The downstream marching procedure used to update the estimates for the fluid flow-fields might be expected to perform less effectively in a situation where there is significant upstream transmission of information. Be that as it may, it should be noted that the application of any form of parabolisation to the equations governing the fluid would, most likely, have yielded very poor results. Parabolised equations can only be derived by assuming that the behaviour of the fluid at any given location does not depend strongly on what happens downstream of this location.

The excitation of flow-induced surface waves was found to be quite common amongst the simulations that have been completed to date. Such waves could be discerned in numerical results that were obtained over a range of wall and flow parameters. However, for the present, we shall restrict our reports to simulations that were conducted using the same Reynolds number $R = 12000$ and temporal frequency $\beta = 0.24$ that were considered earlier. Thus, the behaviour of the Tollmien-Schlichting waves in the rigid-walled parts of the channel should be unaltered. We will only change the wall compliance parameters, together with the streamwise extent of the compliant-walled section of the channel. The compliant panel lengths were increased so that some general features of the results could be exhibited in a clearer manner. For similar reasons, attention will again be concentrated upon cases where the presence of compliant walls leads the Tollmien-Schlichting wave to be completely, rather than only partially, stabilised.

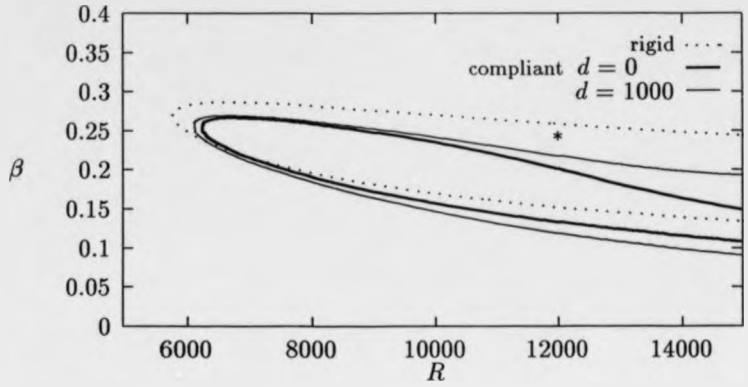


Figure 4.13: Neutral stability curves for Tollmien-Schlichting waves. The other compliant wall parameters are $m = 1/3$, $B = 7.68 \times 10^7$, $T = 0$, $K = 1.92 \times 10^7$. The asterisk labels the Reynolds number and frequency used in the reported numerical simulations.

### 4.6.1 Behaviour for undamped compliant walls

The wall parameters were selected in accordance with the guidelines described in Section 4.1. They were taken to be

$$m = 1/3\ ,\ T = 0\ ,\ d = 0\ ,\ B = 7.68 \times 10^7\ ,\ K = B/4 = 1.92 \times 10^7\ .$$

These yield $R_d = R_t = 12000$ with $\alpha_c^2 = 1/2$. (In the simulations reported earlier, the wall parameters were fixed by setting $\alpha_c^2 = 2$.) Figure 4.13 displays the corresponding neutral stability curve for the Tollmien-Schlichting instability, obtained from the numerical solution of the Orr-Sommerfeld equation. The figure also includes the neutral curve for rigid walls, as well a curve determined for a non-zero value of the wall damping coefficient $d$.

At a Reynolds number of $R = 12000$, the Tollmien-Schlichting wave with a temporal frequency of $\beta = 0.24$ has the complex wavenumber $\alpha = 1.03 - i0.93 \times 10^{-2}$, in

the case of a rigid-walled channel. (This was also noted in connection with the simulations described previously.) The wavenumber is shifted to $\alpha = 0.92 + i2.12 \times 10^{-2}$ when the channel walls are made compliant. Thus, we would expect the Tollmien-Schlichting wave with $\beta = 0.24$ to be subjected to a strong stabilisation upon entering a channel section bounded by compliant walls that have the specified set of compliancy properties. It can easily be verified that the temporal frequency $\beta = 0.24$ is less than the cut-off frequency $\beta_0$ for free waves propagating along the compliant walls. (In fact, over the range of Reynolds numbers for which the neutral curves are displayed in Figure 4.13, the frequencies of the unstable Tollmien-Schlichting waves—for either rigid or compliant channel walls—are always less than the cut-off frequency $\beta_0 = 1/R(K/m)^{\frac{1}{2}}$.) In view of this, we might have anticipated that the excitation and de-excitation of the wall motion, brought about by the passage of the Tollmien-Schlichting wave over the rigid/compliant and compliant/rigid wall joins, would have taken the same simple form as was documented for the earlier simulations.

Figure 4.14 displays numerical simulation results obtained for $R = 12000$ at a time when the Tollmien-Schlichting wave has propagated through the whole streamwise extent of the computational domain. The compliant-walled section of the channel lies between the locations labelled by $x = 20$ and $x = 120$. All the fluid flow-field and wall motion variables have become time-periodic with the frequency $\beta = 0.24$ that is imposed at the upstream boundary of the fluid, in order to generate the Tollmien-Schlichting wave. The first of the plots shows the streamwise variation of the disturbance energy $E = \int_0^1 (u^2 + v^2)/2\, dy$, whilst the second gives the corresponding variation of the integrated square of the vorticity $\omega$. Upstream of the rigid/compliant wall join, both the energy and the vorticity grow in the straightforward manner that would be expected from linear stability theory for an entirely rigid-walled channel. However, as the wave propagates into the compliant-walled section of the channel, the behaviour becomes considerably more complex. There is a sharp increase in the disturbance energy in the vicinity of the rigid/compliant wall

join. This is followed by what seems to be, on average, a decrease over much of the compliant-walled part of the channel. Beyond the rigid/compliant wall join it is difficult, using the energy variation alone, to distinguish any constant spatial wavelength that may be associated, unequivocally, with the Tollmien-Schlichting wave. As the compliant/rigid wall join is approached, the fluctuations in the disturbance energy begin to increase, before, very abruptly, appearing to vanish once the walls become rigid. Closer inspection, making use of a larger scale for the ordinate, reveals that there is a very small amplitude wave in the final rigid-walled part of the channel. This has the same regular characteristics as the much larger amplitude Tollmien-Schlichting wave that is found upstream of the compliant walls. Thus, the wave that propagates out through the downstream computational boundary may be identified as the remnant of the Tollmien-Schlichting wave that was introduced at the upstream boundary.

Turning now to the square integral of the vorticity, it can be seen that there is a localised drop in the disturbance amplitude near to the rigid/compliant wall join. Over the next Tollmien-Schlichting wavelength[16], there is an increase in the amplitude back to a value similar to that found just upstream of the join. This short lived increase is followed by rapid decay, up to a streamwise position that lies about halfway along the compliant-walled section of the channel. As the vorticity decays, it oscillates in a manner that suggests that the disturbance is dominated by a component with a well defined wavelength. It seems plausible to identify this dominant component as the stabilised Tollmien-Schlichting wave. Beyond the midpoint of the compliant-walled part of the channel, the vorticity ceases to decline. The amplitude of the fluctuations then remains relatively steady until the compliant/rigid wall join is approached. As soon as the channel walls become rigid, the vorticity drops to a level which is barely detectable on the scale used in the figure.

[16]The wavelength of the disturbance should be gauged by taking *twice* the distance between successive peaks of a squared flow-field variable.

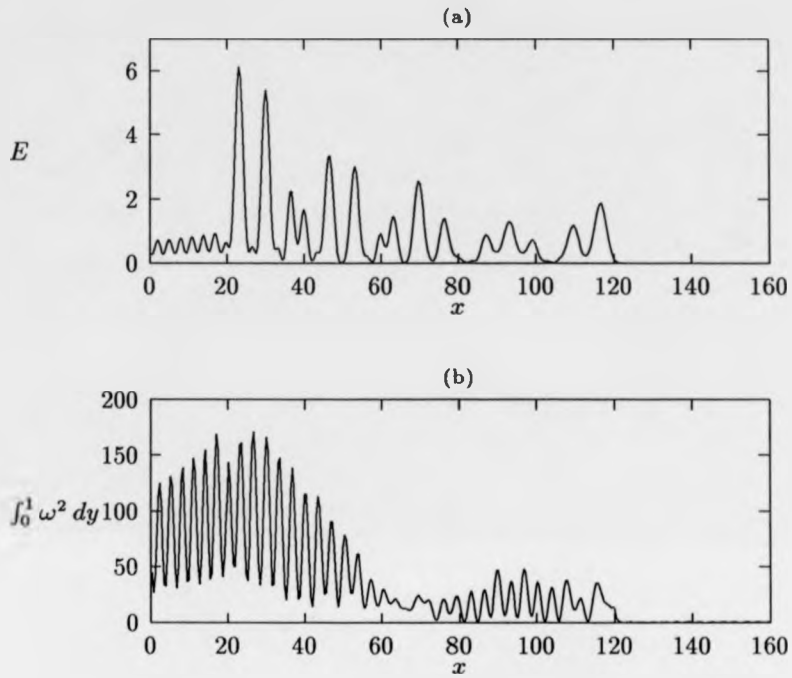


Figure 4.14: Instantaneous streamwise distribution of the fluid disturbance energy and integrated square vorticity, for a Tollmien-Schlichting wave with $\beta = 0.24$ at $R = 12000$. The wall joins are located at $x = 20$ and $x = 120$. The compliant wall parameters are $m = 1/3$, $B = 7.68 \times 10^7$, $T = 0$, $K = 1.92 \times 10^7$, $d = 0$.

Figure 4.15 displays plots of the wall displacement $\eta$ and wall velocity $\partial\eta/\partial t$, together with the fluid perturbation pressure $p_w$ and vorticity $\omega_w$ at the wall. These are taken for the same time instant as in the previous figure. Additionally, in Figure 4.16, there is a plot of the time-averaged square of the wall displacement. In each case, only the variation over the compliant-walled section of the channel is shown. On first inspection, it would seem that the instantaneous forms of the wall displacement and

wall velocity could be attributed to a superposition of two waves, one of which has a much longer wavelength than the other. In fact, as will be demonstrated later, there are three distinct wave components, two of which turn out to have very similar wavelengths. It will also be shown that the rather complicated spatial variation of the time-averaged square wall displacement may be readily accounted for if it is assumed that there are three, rather than two, wave components present. For the moment, though, we just note the contrast between the type of behaviour displayed in Figure 4.16 and the much simpler behaviour that was illustrated previously in Figure 4.12.

The wall pressure would appear to be in phase with the wall displacement, except in the immediate neighbourhood of the wall joins, where the wall motion is constrained to vanish. It may also be observed that the wall pressure has a weaker long wavelength component than that which is found for the wall displacement. The wall vorticity, to some extent, reflects the variation that was described earlier for the square integrated vorticity. However, the change in behaviour that occurs towards the centre of the compliant-walled section of the channel is not so easily distinguished in the plot of the wall vorticity.

Finally, we present a visualisation of the streamwise component $u$ of the perturbation fluid velocity. This is given in Figure 4.17, for same instant of time as was considered previously. The profile of a growing Tollmien-Schlichting wave can be distinguished in the upstream rigid-walled part of the channel. The flow-field takes the same form downstream of the compliant/rigid wall join, though the wave amplitude is very much reduced. There is a marked change in behaviour as the Tollmien-Schlichting wave passes into and out of the compliant-walled channel section. A particularly interesting feature is the sudden, and somewhat dramatic, reduction in the amplitude of the disturbances beyond the compliant/rigid wall join. The same feature has already been noted in discussing the disturbance energy and square integral vorticity. It would appear that, all the way up to the compliant/rigid wall

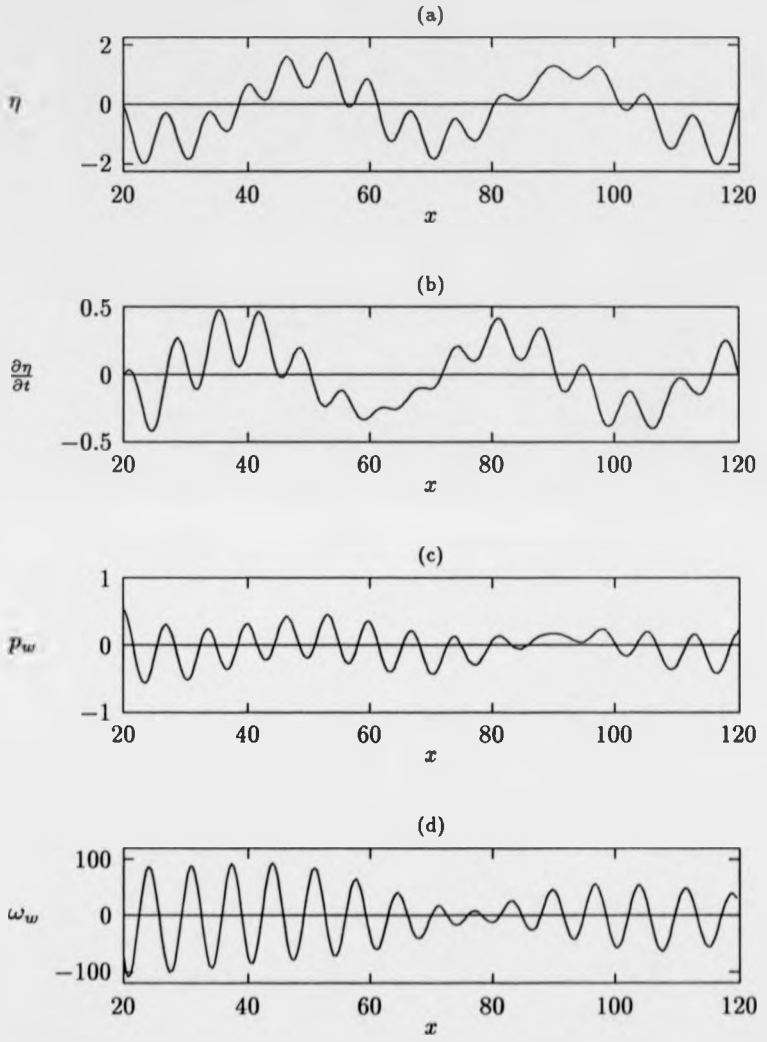


Figure 4.15: Wall motion variables, and flow-field variables at the wall, in the compliant-walled section of the channel. All four plots are for the same instant of time as in the previous figure.

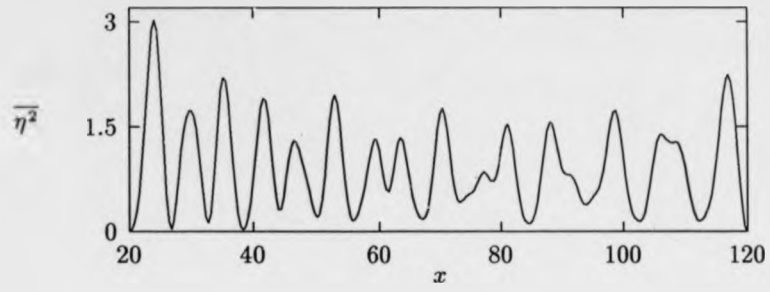


Figure 4.16: Time-averaged square of the wall displacement.

join, there is a significant component of the flow-field with a spatial periodicity akin to that displayed by the Tollmien-Schlichting wave in the rigid-walled parts of the channel. In fact, as will be verified later, beyond the mid-point of the compliant panels, the shorter lengthscale variation of the flow-field, is due, mainly, to an upstream propagating flow-induced surface wave. This just happens to have a similar wavelength to that of the Tollmien-Schlichting wave. Beyond the compliant/rigid wall join, flow-induced surface waves can no longer be maintained, so there is an abrupt drop in the disturbance amplitude.

Rather than embarking upon more elaborate descriptions of the behaviour that is found in the compliant-walled section of the channel, we will move on to demonstrate how the fluid and wall motion may be constructed from a superposition of the Tollmien-Schlichting wave with two flow-induced surface waves. Figure 4.18 shows power spectra obtained by considering the spatial variation of the disturbances. The first was calculated by taking the discrete Fourier transform of the wall displacement $\eta$ at single instant of time. The second was derived from the wall vorticity $\omega_w$ in a similar manner. In each case, only the data from the compliant-walled part of the channel has been utilised. It may be noted that the spectra have been normalised, separately,

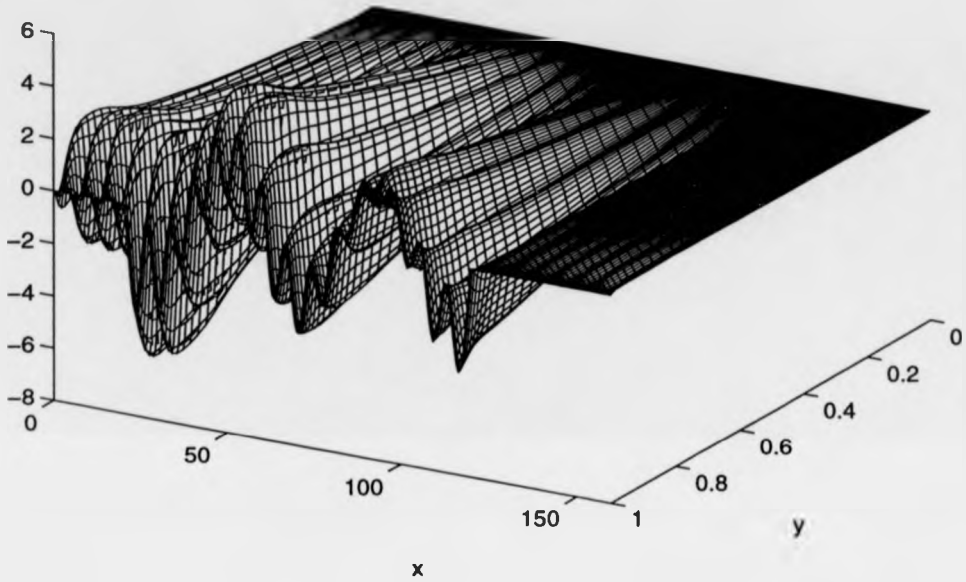


Figure 4.17: $u$-component of the fluid perturbation velocity, for the Tollmien-Schlichting wave considered in the previous two figures.

to give the same maximum value. The significance of the vertical dotted lines that are drawn in both of the plots will be explained shortly. The spectrum of the wall displacement indicates the presence of a strong component with a low wavenumber. Two other components at higher wavenumbers can also be distinguished. For the wall vorticity, the power spectrum is dominated by a component with a wavenumber that corresponds to one of the higher wavenumber components picked out in the displacement spectrum. Closer inspection suggests that the large peak in the vorticity spectrum may be masking the appearance of a second component at a neighbouring wavenumber. There may, in fact, be two distinct contributions to the wall vorticity

at higher wavenumbers, in accord with the features observed in the wall displacement spectrum. (In an additional numerical simulation that was conducted using the same wall and flow parameters, but with an extended compliant-walled channel section, the two higher wavenumber components could be resolved, sharply, in *both* spectra.) A low wavenumber component can also be discerned in the vorticity spectrum. The weak contribution made by this component towards the wall vorticity is in marked contrast to the contribution noted for the wall displacement.

On the basis of the power spectra, it would seem reasonable to conclude that there are three separate components involved in the wall and fluid motion. It will now be shown that such a conclusion is consistent with the results obtained from the Orr-Sommerfeld equation, for the case of an entirely compliant-walled channel. A global eigenvalue analysis, at the specified temporal frequency $\beta = 0.24$, reveals that there are two upstream travelling waves, in addition to the stabilised Tollmien-Schlichting wave. The three relevant eigenvalues are

$$\begin{aligned} \alpha_1 &= -0.15 \quad +i1.3 \times 10^{-4} \\ \alpha_2 &= -0.83 \quad -i1.4 \times 10^{-2} \\ \alpha_{ts} &= +0.92 \quad +i2.1 \times 10^{-2} \, . \end{aligned}$$

The first two eigenvalues $\alpha_1$, $\alpha_2$ may be interpreted as representing flow-induced surface waves. Such an interpretation follows from a comparison with the temporal eigenvalues found using the inviscid shear layer theory that was described in Section 2.3. Moreover, the occurrence of two distinct eigenvalues associated with upstream propagating flow-induced surface waves is in accord with the remarks that were made in Section 4.5, concerning possible solutions to the inviscid dispersion relation for the case where $R = R_d$. The third complex wavenumber $\alpha_{ts}$ corresponds to the Tollmien-Schlichting wave (as was noted earlier).

In the power spectra displayed in Figure 4.18, dotted vertical lines have been

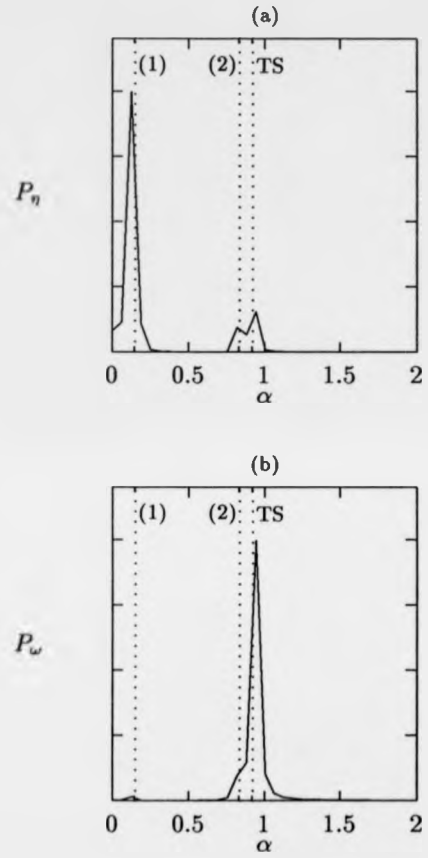


Figure 4.18: Power spectra obtained by analysing the instantaneous spatial distribution of the wall displacement and wall vorticity. The labels on the dotted vertical lines refer to wavenumbers determined from the solution of the Orr-Sommerfeld equation.

used to mark locations defined by the magnitudes[17] of the real parts of the three computed eigenvalues $\alpha_1$, $\alpha_2$, $\alpha_{ts}$. Bearing in mind the numerical resolution, which is limited by the number of grid points at which the wall displacement and wall vorticity are known, it can be seen that the peaks in the spectra are positioned in accord with the eigenvalues. Thus, the power spectra provide strong evidence that the wall and fluid motion in the compliant-walled section of the channel may be ascribed to a linear superposition of the stabilised Tollmien-Schlichting wave with two flow-induced surface waves.

Before proceeding any further with the analysis of the simulation data, we will make a few comments about the two eigenvalues that correspond to flow-induced surface waves. Since the temporal frequency $\beta$ has been taken to be positive, a negative real part for the wavenumber implies that the phase velocity is orientated upstream. Consequently, it might be thought that the flow-induced surface wave defined by $\alpha_1$ should be interpreted as being unstable in its direction of propagation. The small positive imaginary part of $\alpha_1$ is indicative of weak upstream growth. However, when examining the stability of a given disturbance mode, the group velocity, as well as the phase velocity, must be considered; in general, the behaviour of wave packets will be of greater physical interest than the behaviour of any individual harmonic component. It turns out that, in the case of the flow-induced surface wave with wavenumber $\alpha_1$, the group velocity is aligned downstream, *i.e.* in the opposite direction to the phase velocity. This may be shown through an analysis of the dispersion relation, describing the dependency between $\beta$ and $\alpha$, that was derived using the inviscid shear layer theory. (Alternatively, the group velocity can be calculated, more directly, by considering the appropriate numerical solution of the Orr-Sommerfeld equation.) Taking the orientation of the group velocity into account, the positive imaginary part of

[17]Power spectra determined from the instantaneous spatial variation of a real quantity do not distinguish between positive and negative wavenumbers.

$\alpha_1$ may be interpreted as a sign of stability rather than instability[18]. There are no such complications in deciding the stability of the flow-induced surface wave with wavenumber $\alpha_2$. Both the phase velocity and the group velocity are in the upstream direction, so the negative imaginary part of the wavenumber can be taken to indicate that the wave is stable. Incidentally, it may be noted that the stabilised Tollmien-Schlichting wave is expected to decay more rapidly than either of the flow-induced surface waves.

Having digressed in order to make some remarks concerning the stability, or otherwise, of the flow-induced surface waves, we will now return to the examination of the results of the numerical simulation. Power spectra have been seen to be useful for extracting the wavenumbers that define the various components of the total wall and fluid motion. We would also like to be able to determine, from the simulation data, the spatial growth or decay of each distinct component. Unfortunately, a conventional Fourier analysis cannot be used for such purposes. It would presume that every component of the motion is specified by a real wavenumber and constant amplitude. This limitation could, in principle, be overcome by windowing the data, *i.e.* by partitioning the total data set into a number of smaller sets. The growth or decay of different wavenumber components could then be traced by making comparisons between the power spectra obtained from successive windows of data. However, the viability of such an approach depends on how many wavelengths of the largest wave-

[18]Formulating the stability problem in terms of temporal growth, as opposed to spatial growth, does not lead to the same difficulty of interpretation. It can be anticipated that the temporal growth rate $\beta_i$ will be related, approximately, to the spatial growth rate $\alpha_i$ by the Gaster transformation [45]

$$\beta_i = -c_g \alpha_i$$

where $c_g$ is the group velocity. Thus, $\beta_i$ will be negative, indicating stability, when both $\alpha_i$ and $c_g$ are positive. This explains why the temporal analysis, as presented in Section 2.3, does not indicate any instability for the upstream travelling wave that, in the spatial formulation, is identified by the real temporal frequency $\beta$ and complex wavenumber $\alpha_1$.

length component are contained within the full set of data. In the present instance, the data provided by the simulation would be insufficient; the flow-induced surface wave with wavenumber $\alpha_1$ only appears for just over two full wavelengths.

### 4.6.2 Three wave fit to the simulation data

In view of the difficulties mentioned above, we will adopt a less direct method of examining the simulation data. We will begin by *assuming* that the wall and fluid motion in the compliant-walled section of the channel may be decomposed into a Tollmien-Schlichting wave and two flow-induced surface waves. The consequences of such an assumption will then be checked, in detail, against the actual simulation results. More particularly, we will investigate the extent to which it is possible to obtain, in a self-consistent manner, an accurate fit to the data supplied by the simulation.

If the wall motion can be treated as a superposition of different modes, in the manner just suggested, then along the compliant-walled part of the channel the wall pressure should take the form

$$p_w = \Re\left(\hat{p}e^{-i\beta(t-t_0)}\right) \tag{4.1}$$

where the complex amplitude $\hat{p}$ is given by

$$\hat{p} = A_{ts}e^{i\alpha_{ts}x} + A_1e^{i\alpha_1 x} + A_2e^{i\alpha_2 x}\,. \tag{4.2}$$

For expositional convenience, an arbitrary reference time $t_0$ has been included within the factor used to describe the periodic time dependence in (4.1). The complex constants $A_{ts}$, $A_1$, $A_2$ define the contributions to the wall pressure due to the Tollmien-Schlichting wave and the two flow-induced surface waves, respectively. When the wall pressure can be thus described, it follows from the governing equation for the compliant wall motion that the response of the wall will be of the form

$$\eta = \Re\left(\hat{\eta}e^{-i\beta(t-t_0)}\right) \tag{4.3}$$

where the complex amplitude $\hat{\eta}$ is specified as

$$\hat{\eta} = C_{t_s} e^{i\alpha_{t_s} x} + C_1 e^{i\alpha_1 x} + C_2 e^{i\alpha_2 x} + \sum_{j=1}^{4} D_j e^{\lambda_j x} \tag{4.4}$$

with

$$C_{t_s} = \frac{A_{t_s}}{\frac{1}{R^2}(B\alpha_{t_s}^4 + K) - m\beta^2} \;,\; C_s = \frac{A_s}{\frac{1}{R^2}(B\alpha_s^4 + K) - m\beta^2} \quad s = 1, 2\,. \tag{4.5}$$

The four additional constants $D_j$ define the homogeneous part of the wall-motion, which must be included in order that the boundary conditions at the wall joins may be satisfied. The exponents $\lambda_j$ take the form described in Section 4.5.1, for the case where $K > m\beta^2 R^2$, *i.e.* $\beta < \beta_0$.

Equation (4.3) yields the relationship

$$\hat{\eta} = \left(\eta + i\frac{1}{\beta}\frac{\partial \eta}{\partial t}\right)_{t_0} . \tag{4.6}$$

Thus, upon the assumption of time-periodicity, it is possible to determine a discrete approximation to the complex amplitude $\hat{\eta}$ using data for the wall displacement and wall velocity obtained from the numerical simulation at the single time instant $t_0$. Furthermore, if $\hat{\eta}$ takes the form specified in (4.4), then we should expect to have

$$\left(\eta_k + i\frac{1}{\beta}\frac{\partial \eta_k}{\partial t}\right)_{t_0} = C_{t_s} e^{i\alpha_{t_s} x_k} + C_1 e^{i\alpha_1 x_k} + C_2 e^{i\alpha_2 x_k} + \sum_{j=1}^{4} D_j e^{\lambda_j x_k} \tag{4.7}$$

for each streamwise location $x_k$ at which simulation data can be provided. The set of equations defined by (4.7) could, in principle, be used to determine values for the constants $C_{t_s}$, $C_1$, $C_2$ and $D_j$. However, the number of points for which data may be supplied far exceeds the number of unknown constants. (For the numerical simulation under consideration, the spatial resolution in the streamwise direction was defined by taking $dx = 0.4$, whilst the compliant panels were of length $l = 100$. Hence, there are $N_l = l/dx + 1 = 251$ grid-points to be accounted for.) This over-determination can be turned to advantage. We can check whether (4.4) gives a viable description by measuring the extent to which (4.7) may be satisfied, simultaneously, at all positions $x_k$ along the compliant-walled part of the channel.

It is a straightforward matter to obtain a least-squares solution to the system of equations defined by (4.7), *i.e.* to determine complex constants $C_{ts}$, $C_1$, $C_2$, $D_j$ which minimise the sum, over all grid-points, of the squares of the differences between the left and right-hand sides. (For each streamwise position $x_k$, the left-hand side needs to be evaluated using simulation data obtained for a particular instant of time. By definition, this time is taken to be $t = t_0$.) The values computed for the constants can then be used, reapplying the superposition assumed in (4.4), to construct a least-squares fit $\hat{\eta}^f$ to the complex wave amplitude. From this we can define, via the relation (4.6), the corresponding fits to the data for the wall displacement and wall velocity that was supplied from the numerical simulation.

On the scales that were used in Figure 4.15, it would be impossible to distinguish the fitted distributions for the wall displacement and the wall velocity from the original simulation data; the coincidence is too close. Figure 4.19 shows an enlargement, for a portion of the channel close to the centre of the compliant-walled section. The dots represent the simulation data, whilst the continuous lines plot the fits obtained in the manner described above. It can be seen that there is excellent agreement. This remains the case at other streamwise locations, including those near the wall joins, where the homogeneous solutions make a significant contribution. Figure 4.20 displays the separate components of the fit to the wall displacement. It can be seen that, in accord with the results of the spectral analysis discussed earlier, the largest contribution is made by the flow-induced surface wave with wavenumber $\alpha_1$. This wave is very close to being neutrally stable. By contrast, the Tollmien-Schlichting wave component decays along its downstream direction of propagation, whilst the flow-induced surface wave with wavenumber $\alpha_2$ decays upstream. In the first half of the compliant-walled channel section, the shorter lengthscale variation of the total wall displacement is dominated by the Tollmien-Schlichting wave, but further downstream, as the compliant/rigid wall join is approached, the flow-induced surface wave with wavenumber $\alpha_2$ takes over. Plausibly, this latter wave could be viewed as

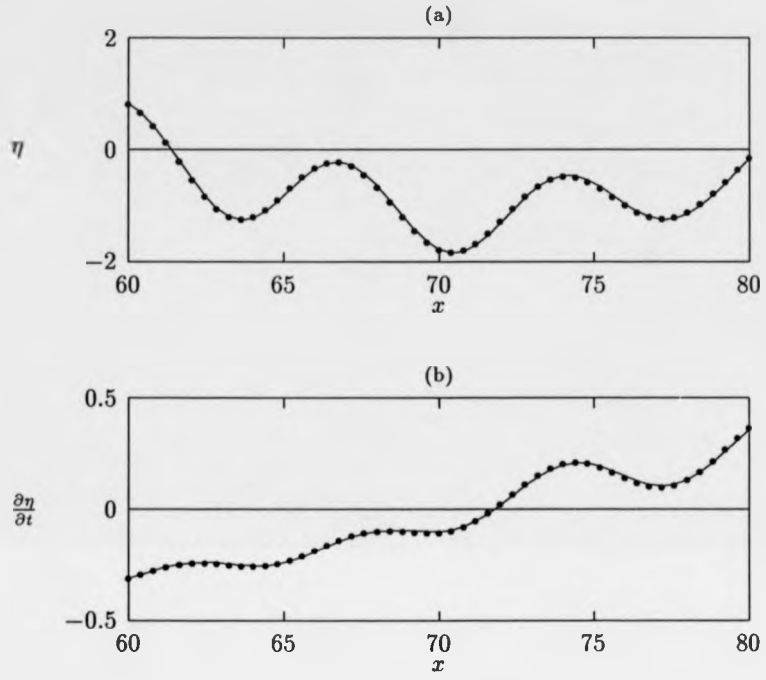


Figure 4.19: Fitted wall displacement and velocity distributions (solid lines), together with the discrete simulation data. Only the central portion of the compliant-walled section of the channel is shown. (The simulation data are a subset of that previously displayed in Figures 4.15(a),(b).)

being excited at the compliant/rigid wall join, from where it propagates upstream, decaying as it goes. In a similar manner, it may be possible to attribute the excitation of the flow-induced surface wave with wavenumber $\alpha_1$ to the effects of the rigid/compliant wall join. Some support for such a contention can be provided by recalling that the wave with wavenumber $\alpha_1$ decays, weakly, along the downstream direction in which its group velocity is orientated. Finally, it should be noted that the contribution made by the homogeneous solutions is confined to the immediate

vicinities of the wall joins, just as in the simulations reported previously, where there was no significant excitation of flow-induced surface waves.

The agreement between the fitted wall displacement and velocity distributions and the simulation data was found to be destroyed if either of the two flow-induced surface waves was not taken into consideration. Moreover, the degree of the fit proved to be quite sensitive to the actual values assigned for the three wavenumbers $\alpha_{ts}$, $\alpha_1$, $\alpha_2$. If the real part of any one of these wavenumbers was shifted by only a few percent from the value determined by solving the Orr-Sommerfeld equation, then the fit began to deteriorate markedly[19]. The dependency of the fit upon the values imposed for the imaginary parts of the wavenumbers was not so strong as it was for the real parts. This is only as would expected, since the spatial growth/decay of all three components can be seen to be fairly weak over distances comparable to their respective wavelengths.

Having determined a least-squares fit $\hat{\eta}^f$ to the complex wave amplitude for the wall motion, we can predict that the time-averaged squared wall displacement will be given by $|\hat{\eta}^f|^2/2$. Similarly, making use of the relations (4.5), in conjunction with (4.2), we can determine a consistent fit to the perturbation fluid pressure at the wall. In particular, it is possible to obtain a prediction for the form taken by the wall pressure at the selected time $t_0$. As with the wall displacements and wall velocities, the agreement between the fitted wall pressure and the simulation data proved to be very good. The same was true for the time-averaged squared wall displacement. Figure 4.21 illustrates the degree of conformity, for a portion of the channel around

[19]In fact, it was found that the best fit could be obtained if the real part of the wavenumber corresponding to the Tollmien-Schlichting wave was altered slightly from the value determined by solving the Orr-Sommerfeld equation. However, the extent of this alteration was consistent with the numerical resolution of the simulation; it was in accord with the accuracy to which the real part of the wavenumber could be computed in other simulations where there was no significant excitation of flow-induced surface waves.

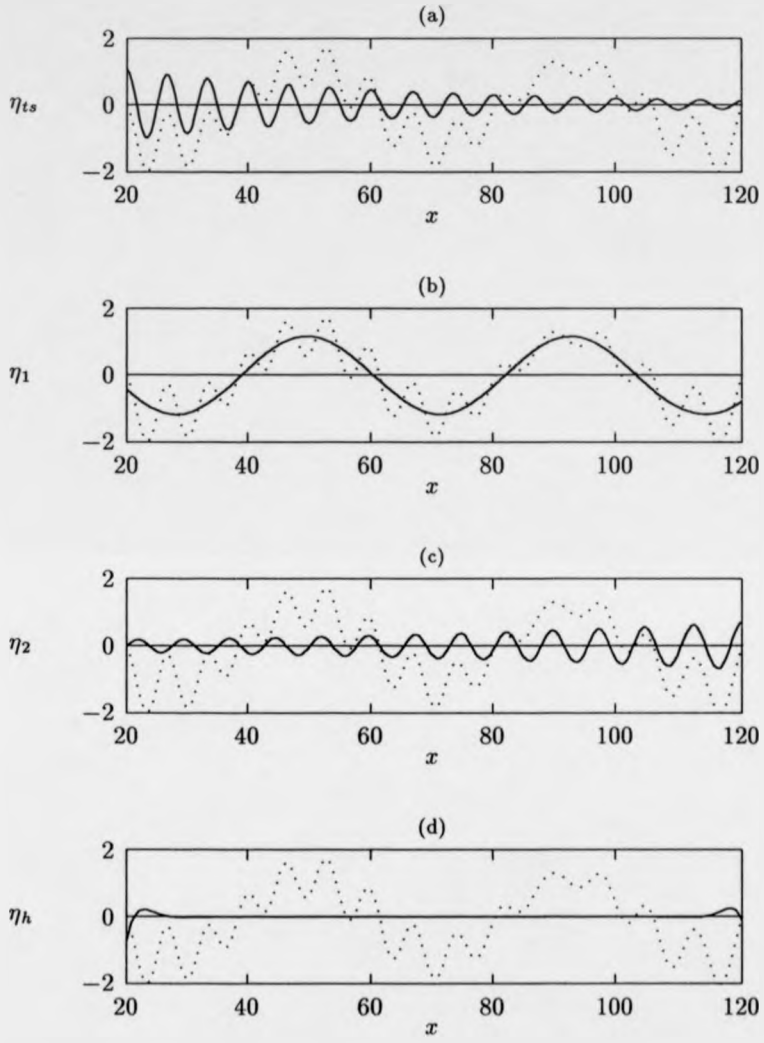


Figure 4.20: Components of the wall displacement. (a) Tollmien-Schlichting wave, (b) flow-induced surface wave with wavenumber $\alpha_1$, (c) flow-induced surface wave with wavenumber $\alpha_2$, (d) component contributed by the homogeneous solutions to the wall motion equation. In each plot the total wall displacement is reproduced using a dotted line.

the centre of the compliant-walled channel section. Once more, it would be impossible to distinguish the fitted distributions from the simulation data using the scales taken in the plots of the same variables that were presented earlier.

By way of a summary, it may be remarked that by choosing values for a small number of complex constants—$C_{ts}$, $C_1$, $C_2$, $D_j$—it was possible to fit, in a consistent manner, data provided from the numerical simulation for the wall displacement, velocity and perturbation fluid pressure, as well as for the time-averaged squared wall displacement. In total, there were over a thousand items of data to be considered. Away from the immediate vicinity of the wall joins, where the homogeneous part of the wall motion is negligible, the data was fitted, in effect, using just three constants $C_{ts}$, $C_1$, $C_2$. Thus, we have strong evidence in support of the contention that the wall and fluid motion in the compliant-walled section of the channel may be ascribed to a superposition of a stabilised Tollmien-Schlichting wave with two flow-induced surface waves. Further support can be provided by analysing the wall vorticity in a similar manner. We will omit the details of the analysis, except to remark that it proved necessary to exclude the data supplied by the simulation at streamwise positions very close to the rigid/compliant and compliant/rigid wall joins. In the vicinities of the joins, the variation of the wall vorticity could not be described solely in terms of a Tollmien-Schlichting wave superposed with flow-induced surface waves. The effects of the wall joins on the vorticity could not be neglected in the same manner as had been possible for the fluid perturbation pressure.

Figure 4.22 displays the instantaneous components of the wall vorticity, extracted using a least-squares fit to the data provided by the numerical simulation. Data for grid-points within a single Tollmien-Schlichting wavelength of the wall joins were discarded in obtaining the fit. Over the remaining portion of the compliant-walled channel section, the reconstructed wall vorticity was found to exhibit the same level of agreement with the simulation data as had been noted previously for the fits to the wall displacement and wall velocity. Returning to the figure, it may be observed that

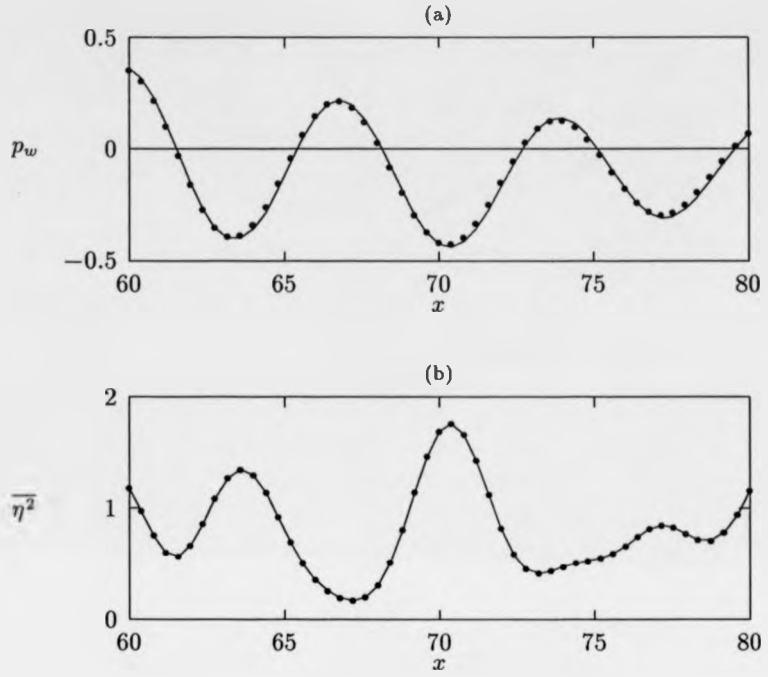


Figure 4.21: Fitted wall perturbation fluid pressure and time-averaged squared wall displacement (solid lines), together with the discrete simulation data. Only the central portion of the compliant-walled section of the channel is shown. The simulation data are a subset of that previously displayed in Figures 4.15(c), 4.16.

in conformity with the results of the spectral analysis presented earlier, the Tollmien-Schlichting wave makes the largest contribution to the total wall vorticity. The flow-induced surface wave with wavenumber $\alpha_1$ is associated with very little vorticity, in marked contrast to its role in determining the compliant wall motion. Over the latter part of the compliant-walled section of the channel, it can seen that the amplitude of the Tollmien-Schlichting wave decays to a level below that of the flow-induced surface

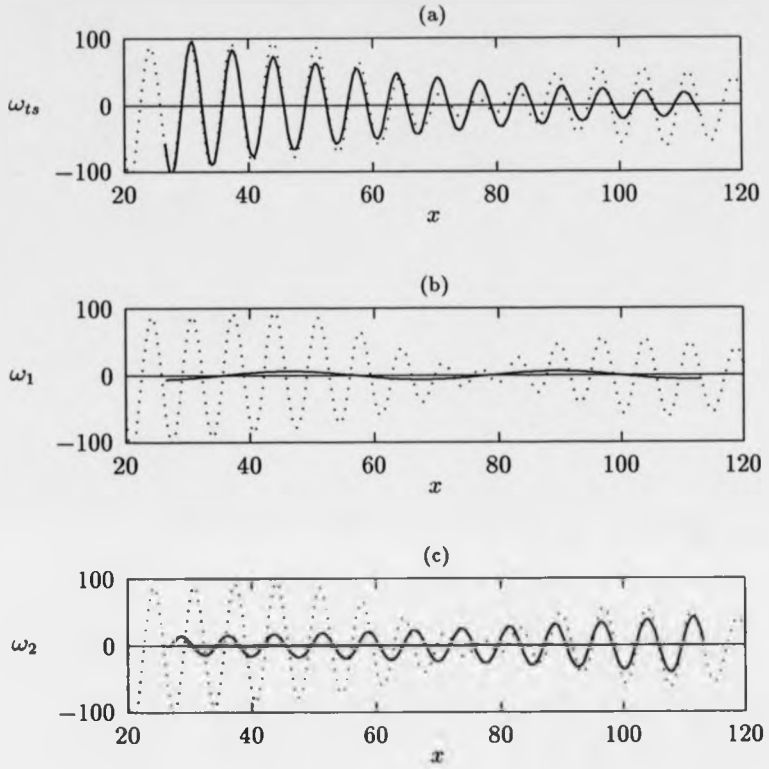


Figure 4.22: Components of the wall vorticity. (a) Tollmien-Schlichting wave, (b) flow-induced surface wave with wavenumber $\alpha_1$, (c) flow-induced surface wave with wavenumber $\alpha_2$. In each plot the total wall vorticity is reproduced using a dotted line. (Simulation data for grid points within a distance $\lambda_{ts} = 2\pi/\alpha_{ts}$ of the wall joins were not included when determining the components.)

wave with wavenumber $\alpha_2$. Thus, the second flow-induced surface wave comes to dominate the wall vorticity as the compliant/rigid wall join is approached.

### 4.6.3 Some additional remarks about cut-off frequencies

Before proceeding to consider the effect of including damping in the compliant wall model, we will digress to make a few observations concerning the difference in behaviour between the simulation that has just been documented and the simulations that were reported earlier, where no excitation of flow-induced surface waves could be traced. In the case of the numerical simulation described in Section 4.2, the Tollmien-Schlichting wave is less stable than any flow-induced surface wave that can be identified at the same temporal frequency. In fact, for the specified frequency, Reynolds number, and compliant wall parameters, a global eigenvalue analysis of the Orr-Sommerfeld equation brings to light no flow-induced surface waves with spatial growth/decay rates that are even broadly comparable to that determined for the Tollmien-Schlichting wave. It would appear that a cut-off frequency is in operation. This suspicion can be confirmed by a more extensive investigation of numerical solutions to the Orr-Sommerfeld equation, as will be described shortly. It should be noted, though, that the existence of a cut-off frequency is at variance with the predictions made in Section 4.5.2. When the compliant wall properties are chosen so as to yield $R_d = R$, the inviscid shear layer theory suggests that there will be two upstream travelling flow-induced surface waves, irrespective of the temporal frequency selected. The cut-off should be located at zero frequency. At least, such is the conclusion if only the first-order approximation to the inviscid dispersion relation is considered. To obtain more reliable results, a higher-order approximation must be utilised, but the advantages of simplicity are then lost.

Figure 4.23 shows the variation, with the temporal frequency $\beta$, of two complex spatial eigenvalues determined as numerical solutions to the Orr-Sommerfeld equation. The compliant wall properties and Reynolds number are the same as those defined for the simulation reported in Section 4.2. The figure also displays eigenvalues derived using the inviscid shear layer theory. These real-valued solutions were

obtained from a higher-order approximation to the inviscid dispersion relation. More specifically, the dispersion relation was taken in the form

$$\frac{1}{R^2}\left(B\alpha^2 + \frac{K}{\alpha^2}\right) - mc^2 = J_d(c) \tag{4.8}$$

where $\alpha$ is the wavenumber, $c = \beta/\alpha$ the phase velocity[20], and the function

$$J_d(c) = J_0(c) + \frac{\alpha^2 J_1(c)}{1 + \alpha^2 I_1(c)}$$

approximates the forcing provided by the fluid pressure. As has been noted previously, $J_0$ is a simple quadratic. Detailed definitions giving the more complicated functional forms of $J_1$, $I_1$ may be found in Section 2.3.6, which contains a discussion of the problems encountered in attempting to predict the onset of divergence instability. For present purposes, all that needs to be noted is that we have included a correction to the approximation applied in the earlier treatment of cut-off frequencies. In Section 4.5.2, only the $J_0$ term was retained in defining the fluid forcing.

Returning to Figure 4.23, it may be seen that the corrected inviscid dispersion relation (4.8) gives a good guide to the behaviour of the eigenvalues obtained by direct numerical solution of the Orr-Sommerfeld equation. In particular, it is possible to detect the presence of a cut-off frequency in the vicinity $\beta = 0.37$. (No attempt was made to continue the solutions determined from the corrected inviscid dispersion relation by considering complex-valued spatial wavenumbers for temporal frequencies below the cut-off.) This frequency lies well above the range of frequencies for which, at the given Reynolds number, Tollmien-Schlichting waves can become unstable, whether the channel walls are rigid, or compliant with the specified set of properties. Thus, for the numerical simulation originally reported in Section 4.2,

[20]Over most of the range of temporal frequencies displayed, the phase velocities are negative. Where the phase velocity becomes positive, it remains greater than unity. In either case, there is no critical layer to be accounted for. This means that both the temporal frequency and spatial wavenumber can be taken to be real.

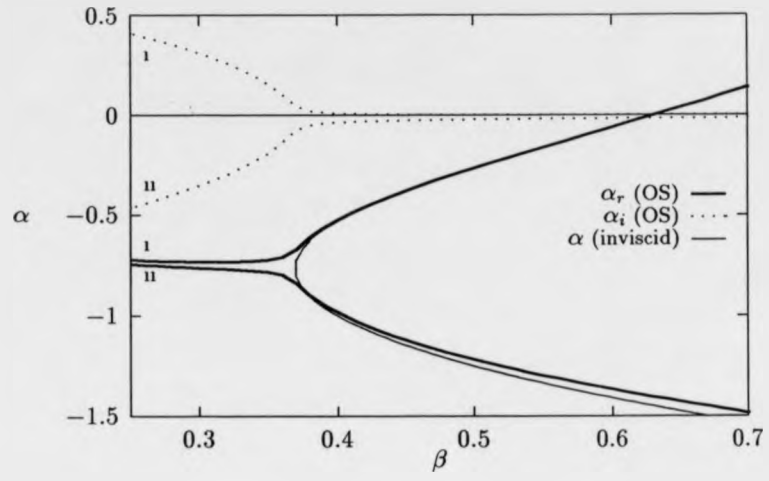


Figure 4.23: Variation with temporal frequency of spatial eigenvalues associated with flow-induced surface waves. The labels (i), (ii) reference the two distinct solutions obtained from the Orr-Sommerfeld equation. Only real-valued inviscid solutions are shown. The Reynolds number is fixed at $R = 12000$. The compliant wall parameters are $m = 1/3$, $K = 7.68 \times 10^7$, $T = 0$, $B = 1.92 \times 10^7$, $d = 0$. (In the case of a rigid-walled channel, unstable Tollmien-Schlichting waves are found within the frequency range $0.15 < \beta < 0.26$, for the selected Reynolds number. When the walls are made compliant, the unstable range is shifted to $0.14 < \beta < 0.22$. The cut-off frequency for *free* waves is given by $\beta_0 = 1/R\,(K/m)^{\frac{1}{4}} = 1.26$.)

it is perhaps not too surprising to find that the Tollmien-Schlichting wave provides the only significant component of the wall and fluid motion, aside from the highly localised contributions attributable to the homogeneous solutions of the compliant wall governing equation. There are no other sustainable forms of motion.

By contrast, for the simulation that was analysed in Sections 4.6.1, 4.6.2 immediately above, the passage of the Tollmien-Schlichting wave through the compliant-

walled portion of the channel leads to the excitation of flow-induced surface waves. These were seen to give a contribution to the total wall and fluid motion that is comparable to the contribution made directly by the Tollmien-Schlichting wave. As distinct from the earlier simulation, the occurrence of flow-induced surface waves can be shown to be compatible with the results that may be obtained from the inviscid shear layer theory. The situation is illustrated by Figure 4.24. This provides a counterpart to the previous figure, for the different set of compliant-wall properties. It can be seen that, once more, the corrected inviscid dispersion relation locates the appearance of a non-zero cut-off frequency. However, the cut-off now lies below, rather than above, the range of frequencies for which there are unstable Tollmien-Schlichting waves.

Rather than relying on a detailed inspection for each individual case, it would be helpful to have some simple general criteria for deciding when flow-induced surface waves may be triggered as a Tollmien-Schlichting wave passes into and out of a compliant-walled channel section. A systematic means of determining cut-off frequencies would provide a step towards achieving such a goal. It is unfortunate that the most straightforward approximation that can be obtained from the inviscid shear layer theory leads to inadequate results. Although the location of cut-off frequencies can be predicted more accurately by using the inviscid theory with a higher-order approximation, the application of such a procedure has not, as yet, provided much in the way of insight. Clearly, some further investigation is required.

The problems arising in the study of cut-off frequencies are bound up with the more general difficulty of predicting the onset of divergence instability. The continued appearance of a non-zero cut-off frequency when the wall properties are chosen so that $R_d = R$ can be interpreted as a sign that divergence is being avoided. (The terminology is perhaps a little confusing here. It should be remembered that $R_d$ is defined solely on the basis of the first-order approximation to the inviscid dispersion relation.) Divergence instability is expected to set in when a flow-induced surface wave can oc-

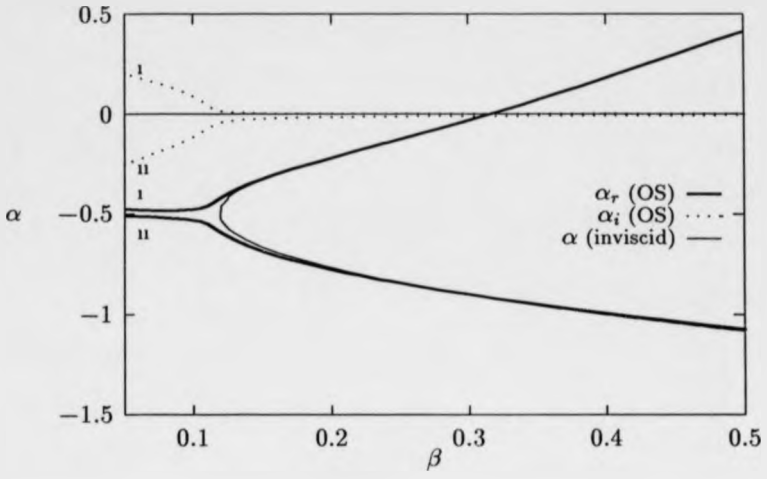


Figure 4.24: Variation with temporal frequency of spatial eigenvalues associated with flow-induced surface waves. As in the previous figure, the Reynolds number is fixed at $R = 12000$, but the compliant wall parameters are now $m = 1/3$, $K = 1.92 \times 10^7$, $T = 0$, $B = 7.68 \times 10^7$, $d = 0$. (For this set of wall compliance parameters, unstable Tollmien-Schlichting waves lie in the frequency range $0.13 < \beta < 0.20$. The cut-off frequency for free waves is at $\beta_0 = 0.63$.)

cur with a vanishing phase velocity. This would correspond to the cut-off frequency approaching zero. Thus, it may be surmised that if the wall parameters could, in fact, be selected so as to yield marginal stability with respect to divergence at the Reynolds number specified for the fluid flow, then there would be the definite possibility of flow-induced surface waves being excited whenever a Tollmien-Schlichting wave propagated over the wall joins. Flow-induced surface waves could always make an appearance, whatever the temporal frequency imposed by the Tollmien-Schlichting wave. Moreover, if the kind of behaviour illustrated in Figures 4.23, 4.24 were to be retained as the cut-off frequency reached zero, then at any non-zero frequency

there would be two possible flow-induced surface waves. One of these would have an upstream group velocity $c_g = d\beta/d\alpha$. The other would have its group velocity orientated downstream, which, for sufficiently low temporal frequencies, would be in opposite direction to the phase velocity.

### 4.6.4 Behaviour for damped compliant walls

From a practical point of view, questions concerning the appearance of flow-induced surface waves may not be of much importance, provided that, if such waves do occur, they remain stable and do not delay, or in any other way mitigate against, the adaptation of the Tollmien-Schlichting wave to the presence, or absence, of wall compliance. Certainly, the analysis presented in Section 4.6.2 is consistent with the conjecture that the Tollmien-Schlichting wave adjusts its spatial growth rate in the same rapid manner for the case where surface waves are excited as when they are not. Further evidence in support of such a claim was obtained by performing a similar analysis on the results of other numerical simulations, conducted for different temporal frequencies and Reynolds numbers, and various sets of compliant wall parameters. Thus, it would seem that the presence of stable flow-induced waves can be viewed as a benign complication in the adaptive behaviour of Tollmien-Schlichting waves. Be that as it may, we will conclude our simulation reports by illustrating how small levels of damping in the compliant walls can be used to diminish, even further, any role that could be played by flow-induced surface waves.

If the values prescribed in Section 4.6.1 are retained for the compliant wall mass $m$, bending stiffness $B$ and spring constant $K$, but the wall damping coefficient[21] is taken as $d = 1000$, then solution of the Orr-Sommerfeld equation for the temporal frequency $\beta = 0.24$, at $R = 12000$, yields the eigenvalues

$$\alpha_1 = -0.15 + i4.5 \times 10^{-2}$$

[21] It should be recalled that the effective non-dimensional damping is given by $d/R$.

$$\alpha_2 = -0.83 \quad -i3.1 \times 10^{-2}$$
$$\alpha_{ts} = +0.92 \quad +i1.5 \times 10^{-2} .$$

The real parts of these eigenvalues are only very slightly shifted from the values that were found in the absence of wall damping. However, it may be seen that the wall damping has had a strong stabilising effect on the two flow-induced surface waves. In particular, the first flow-induced surface wave, which in the absence of wall damping was close to being neutrally stable, is now the most stable of the three waves. As before, it is necessary to take account of the fact that, for the surface wave with wavenumber $\alpha_1$, the group velocity is orientated downstream, in opposition to the upstream phase velocity. The Tollmien-Schlichting wave, though still strongly stabilised by the wall compliance, is slightly less stable than before.

Figure 4.25 displays the disturbance energy and integrated square vorticity obtained from a numerical simulation in which the non-zero value of the compliant wall damping coefficient was applied. It can be seen that, once again, there are large peaks in the disturbance energy in the vicinity of the rigid/compliant wall join. There is then a general decline over the length of the compliant-walled section of the channel. The presence of the compliant/rigid wall join cannot be distinguished as sharply, from the variation of the disturbance energy, as it could be in the case where there was no wall damping. Turning now to the square integral of the vorticity, it may be observed that beyond the rigid/compliant wall join there is a steady decay, which continues until the compliant/rigid wall join is nearly reached. As the latter join is approached, there is a slight reversal in the decay of the vorticity, though this is barely detectable on the scale used in the figure.

Figure 4.26 shows, for the same instant of time as was considered in the previous figure, the wall displacement and wall velocity, as well as the perturbation fluid pressure and the vorticity at the wall. The variation of each of these quantities takes a far less complicated form than that which was displayed in Figure 4.15, for the

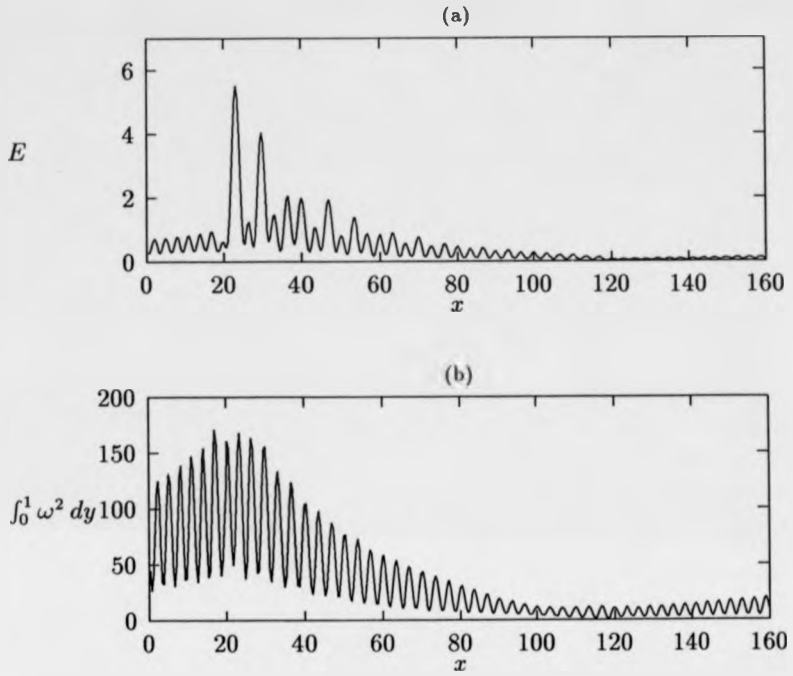


Figure 4.25: Instantaneous fluid disturbance energy and integrated square vorticity, as produced by a Tollmien-Schlichting wave with $\beta = 0.24$ at $R = 12000$. The wall joins are again located at $x = 20$ and $x = 120$. The compliant wall parameters are $m = 1/3$, $B = 7.68 \times 10^7$, $T = 0$, $K = 1.92 \times 10^7$, $d = 1000$.

case of undamped compliant walls. The presence of a longer wave component can be discerned in the wall displacement and velocity, at least at locations which are not too far removed from the rigid/compliant wall join. Such a component is more difficult to detect in the wall pressure, and cannot be distinguished at all in the wall vorticity. These observations are borne out by a spectral analysis, the results of which are presented in Figure 4.27. The spectrum for the wall displacement is dominated by a

component with a wavenumber corresponding to the stabilised Tollmien-Schlichting wave. There is a smaller, though still sizable, contribution due to the flow-induced surface wave with wavenumber $\alpha_1$. In contrast, the vorticity spectrum is very sharply peaked at the wavenumber of the Tollmien-Schlichting wave, with no other component discernible. Thus, the introduction of a relatively low level of compliant wall damping has had a dramatic effect in attenuating the excitation of flow-induced surface waves. It may be noted that, within the numerical resolution available, no contribution attributable to the flow-induced surface wave with wavenumber $\alpha_2$ can be detected in either of the spectra.

A more detailed investigation of the results of the numerical simulation can be conducted using the methods that were applied previously in the case where wall damping was absent. As before, the simulation data for the wall and fluid motion can be analysed by assuming a superposition of the stabilised Tollmien-Schlichting wave with the two possible flow-induced surface waves. Figure 4.28 shows the components of the wall displacement, extracted using a least-squares fit to both the wall displacement and wall velocity, for the instant of time considered in Figure 4.26. It can be seen that, over the whole length of compliant-walled section of the channel, the Tollmien-Schlichting wave provides the largest amplitude contribution. However, for a short distance beyond the rigid/compliant wall join, the long wavelength flow-induced surface wave has a comparable amplitude to that of the Tollmien-Schlichting wave. It would seem reasonable to assume that the excitation of the long wavelength surface wave is associated with the large peaks that were noted in the disturbance energy, at streamwise positions near to the wall join. These peaks are not sustained at locations further downstream, presumably owing to the fact the long wavelength component is subject to a far more rapid spatial decay than the Tollmien-Schlichting wave.

The decomposition of the wall motion derived using the least-squares fit indicates that, in addition to the component with wavenumber $\alpha_1$, there is a non-negligible

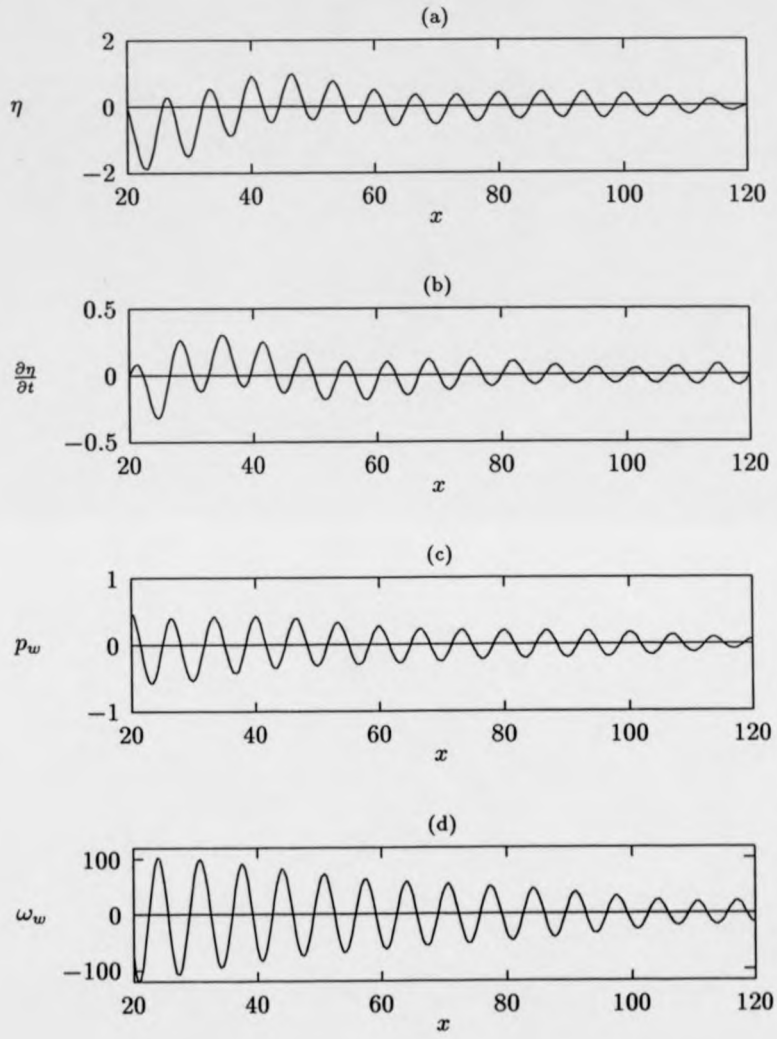


Figure 4.26: Wall velocity and displacement, and perturbation fluid pressure and vorticity at the wall, for the case of damped compliant wall motion. All four plots are for the same instant of time as in the previous figure.

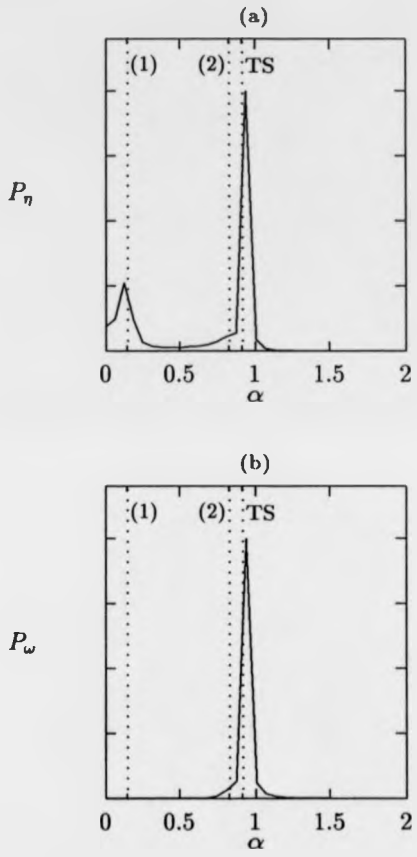


Figure 4.27: Power spectra obtained from the wall displacement and wall vorticity, for the case of damped compliant wall motion. The labels on the dotted vertical lines refer to the wavenumbers determined from the solution of the Orr-Sommerfeld equation.

contribution due to the flow-induced surface wave with wavenumber $\alpha_2$. As with the numerical simulation in which there was no wall damping, the second flow-induced surface wave appears to be excited as the compliant/rigid wall join is approached. However, as has already been remarked, the presence of such a wave can no longer be detected in the spectrum for the wall displacement. The contribution made to the wall motion, along the complete length of the compliant panel, is too small to be resolved. A least-squares fit to the wall vorticity can be applied to confirm that the flow-induced surface wave with wavenumber $\alpha_2$ does, in fact, make an appearance. It is likely that the excitation of this second flow-induced surface wave is responsible for the slight reversal in the decay of the square integral of the vorticity that was noted at locations just upstream of the compliant/rigid wall join. The existence of such a form of behaviour cannot be uncovered by inspecting the wall vorticity spectrum that was presented immediately above. The spectrum only reveals the presence of the stabilised Tollmien-Schlichting wave.

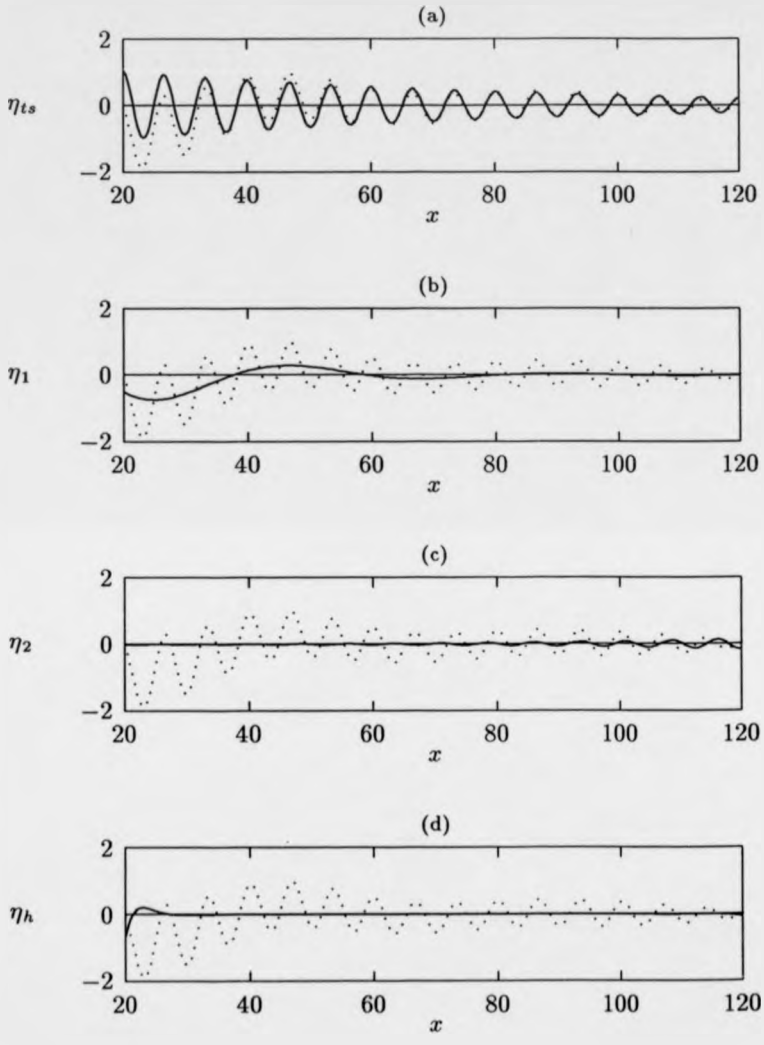


Figure 4.28: Instantaneous components of the wall displacement, for the case of non-zero wall damping. (a) Tollmien-Schlichting wave, (b) flow-induced surface wave with wavenumber $\alpha_1$, (c) flow-induced surface wave with wavenumber $\alpha_2$, (d) component contributed by the homogeneous solutions. The total wall displacement is shown using a dotted line.

# Chapter 5

# Conclusions and further work

We have investigated the behaviour of Tollmien-Schlichting waves when they propagate over the ends of finite-length compliant panels. The panels formed a compliant section in the walls bounding a plane channel fluid flow. A stable numerical scheme has been developed, based on a mixed finite-difference/spectral discretisation of the linearised two-dimensional Navier-Stokes equations. These were taken in a velocity-vorticity formulation. By considering the combined inertia of the compliant wall and the fluid, it proved possible to simulate the interactive coupling between the fluid and the wall motion, without any prior restriction on the form of the disturbances. However, in the present study we have only reported the results of simulations conducted for the case where there is a time-periodic forcing of the fluid. Such forcing was used to generate a spatially evolving Tollmien-Schlichting wave with a well defined temporal frequency. (The extension of the present results to the case where the fluid disturbances take the form of wave-packets, rather than single harmonic components, will be reported in a separate study.)

As a preliminary to the full numerical simulations, we investigated the linear stability of plane channel flow bounded by compliant walls throughout. In the case of the Tollmien-Schlichting instability this involved, for the most part, the determination of numerical solutions to the Orr-Sommerfeld equation. The flow-induced

surface instabilities could be studied more readily using an approximate analytic theory. Good agreement was found between the predictions of the analytic theory and numerical results derived directly from the Orr-Sommerfeld equation, particularly for the travelling wave flutter instability. Although a number of interesting results were obtained concerning the divergence instability, there is some need for further detailed examination of the circumstances under which divergence can arise.

The linear stability results for the wholly compliant-walled channel were used to assess the adaptative behaviour of Tollmien-Schlichting waves that was exhibited in the numerical simulations. It was discovered that, for compliant wall parameters chosen to be of interest for the purposes of transition delay, the spatial growth rates of Tollmien-Schlichting waves could become adjusted to changes between rigid and compliant walls over distances that were shorter than, but comparable to, the Tollmien-Schlichting wavelength. In some instances, such adjustment was accompanied by the excitation of stable flow-induced surface waves. However, the presence of flow-induced surface waves did not appear to have any detrimental effect on the short lengthscale adaptation of the Tollmien-Schlichting waves. In any case, the role played by the flow-induced surface waves could be very much diminished by introducing relatively low levels of damping into the model used to describe the compliant wall.

Although the current investigations have been limited to the case of plane channel flow, there are clear implications for flows that are of more obvious technological significance, such as Blasius flow. It may be recalled that much of the interest of the present work stems from the fact that the stability effects of compliant walls are highly Reynolds number dependent. For Blasius flow over a compliant wall with fixed dimensional properties, the extent to which Tollmien-Schlichting waves can be stabilised, subject to the constraint that no flow-induced surface instabilities are introduced, varies with the streamwise distance from the leading edge. This suggests the use of a series of compliant panels along the streamwise direction, each panel having

properties that are optimised for the local flow conditions. It then becomes necessary to assess how short such panels can be without compromising their capability to stabilise Tollmien-Schlichting waves. The results that we have reported indicate that panels as short as a few Tollmien-Schlichting wavelengths could be utilised. This is very promising from the point of view of practical applications. Typically, the section of the transition region over which Tollmien-Schlichting waves remain linear would be expected to contain something of the order of a hundred Tollmien-Schlichting wavelengths, and even more if transition was delayed. Thus, it should be possible to obtain a significant improvement on the transition delay that was computed by Carpenter [25] for Blasius flow in the case where there are only two distinct compliant panels. The use of ten or more panels, all with locally optimised wall compliance properties, would not appear to be unrealistic. (It is interesting to note that the present results can be used to justify an approximation that was made, implicitly, by Carpenter when selecting the optimal properties of his two-panel compliant wall. He assumed that the streamwise distance over which Tollmien-Schlichting waves would adapt to the change between the two compliant panels would be negligible in comparison with the total panel lengths.)

It may be observed that though the present studies were motivated by the consideration of boundary layer growth, there is no such growth in the genuinely parallel flow that has been simulated thus far. This is not such a shortcoming as it might first appear. The channel flow simulations demonstrate that the adaptation of Tollmien-Schlichting waves to changes in wall compliance can take place over distances that are shorter than the Tollmien-Schlichting wavelength, at least when the wall compliance parameters are chosen so as to lead to a significant stability effect. Thus, assuming that there is similar adaptive behaviour for the case of Blasius flow, it can be conjectured that boundary layer growth will not be important over the streamwise distances that we should expect to find involved.

Having dealt, to some extent, with one objection that could be made to drawing an

analogy between channel flow and Blasius flow, we will now mention another. It may be recalled that for the rigid-walled channel, the only unstable Tollmien-Schlichting waves are such that the normal velocity component $v$ satisfies $v(-y) = v(y)$, where $y = 0$ defines the channel centre-line. Accordingly, our studies have been limited to such a mode of symmetry. The possible influence of this symmetry on the adaptive behaviour of Tollmien-Schlichting waves is somewhat difficult to gauge. Without further study, it is not clear whether or not the imposed channel flow disturbance symmetry could lead to any distinctive behaviour that would not be replicated for Blasius flow. The issue needs to be settled by conducting numerical simulations for Blasius rather than channel flow. To this end, some preliminary investigations have already been undertaken. It appears to be possible to make a number of fairly simple modifications to the numerical scheme that was developed for the plane channel flow, so as to tackle the more demanding problem of Blasius flow. By choosing an appropriate mapping of the semi-infinite interval in the wall-normal direction that arises in the case of Blasius flow, a Chebyshev discretisation of the fluid governing equations can be obtained that retains the same general character as that which was successfully applied for the flow in the channel. In particular, when the streamwise and temporal variation is discretised using finite-differences, an efficient iterative streamwise marching solution procedure can still be employed. The main difference from the channel flow case is that the matrices that need to be inverted at each streamwise position take a block tridiagonal form; scalar entries are replaced by $2 \times 2$ matrices. At the time of writing the viability of amending the existing numerical scheme along the lines just mentioned remains a matter for active research.

In addition to the uncertainties about the generality of conclusions drawn from a study of plane channel flow, there is the question of whether it is acceptable to use a simple spring-backed plate model for the compliant panels. For practical applications we would most likely wish to employ a two-layer compliant wall, consisting of a relatively soft substrate covered by a thin layer of stiffer material. (See, for example,

the reports of the experimental investigations conducted for such walls by Gaster *et al* [8],[9].) Although the qualitative behaviour of two-layer walls, with compliancy properties of physical interest, may often be captured using a spring-backed plate model, a more sophisticated treatment is necessary in order to obtain reliable quantitative results. Werle *et al* [75] used the finite-element method to simulate the motion of a two-layer compliant panel. The substrate was modelled, in effect, by using a modified version of the Navier equations to describe the evolution of linear deformations. The equations were formulated so as to account for the near incompressibility of the substrate material. Thin-plate theory was applied to describe the upper wall layer. Perturbation fluid pressures supplied from a coupled potential fluid flow code were then used to drive the wall motion [71] [46].

Some simulations have recently been conducted in which the finite-element scheme developed by Werle for computing the motion of a two-layer compliant wall was used in conjunction with the numerical scheme for the channel flow that has been described in the present work. Initial studies indicate that the short lengthscale adaptive behaviour of Tollmien-Schlichting waves that was discovered previously, for the case of a spring-backed plate model of the compliant panel, is retained when the wall motion is determined in a more realistic manner. However, the computer code has not as yet been fully tested. It is interesting to note, though, that there seems to be much less difficulty in obtaining a numerically stable coupling between the wall and the fluid motion. Thus far, there has been no necessity to combine terms representing the compliant wall inertia and the fluid inertia when implementing the boundary conditions on the fluid. In the simulations for physically interesting sets of compliant wall parameters that have been completed to date, the inertia term associated with the fluid was no longer found to play a crucial role in determining the numerical stability of the fluid/wall motion coupling. Presumably, this is attributable to the fact that, in the case where the two-layer wall model is employed, the substrate provides an additional source of wall motion inertia.

Finally, we return to the question: How short can a compliant panel be made whilst retaining its capability to stabilise Tollmien-Schlichting waves? It has been shown that the effects of the ends of a compliant panel typically extend over a distance that is less than the Tollmien-Schlichting wavelength. Away from the immediate vicinities of the wall joins, the wave behaves as if it were propagating over a compliant wall of unbounded streamwise extent. In order to illustrate this in a particularly clear manner, we have confined our detailed simulation reports to cases where the wall joins were well separated. In Section 4.2, we considered the propagation of Tollmien-Schlichting waves over a compliant panel that was about seven wavelengths long. For the simulations described in Section 4.6 the panel length was doubled so that behaviour associated with the excitation of flow-induced surface waves could be more readily distinguished. Because the panel lengths used in the reported simulations were chosen, at least to some extent, for the sake of expositional convenience, it could be claimed that we have only given a partial answer to the question that was posed, once again, immediately above. To go some way towards rectifying this situation, we will end by giving a brief description of numerical results that were obtained from simulations conducted with compliant panels that extended to just two Tollmien-Schlichting wavelengths. Except for the panel lengths, the wall properties were taken to be the same as those that were employed in simulations that were reported earlier.

In Figure 5.1 we present two plots for the computed time-averaged convected disturbance energy. For the case shown in Figure 5.1(a) the wall parameters were chosen so that there could be no excitation of flow-induced surface waves. It can be seen that there is a section in the middle of the panel where, apart from a small amplitude fluctuation, the effects of the wall joins can be ignored and the wave decays as if the panel were of unbounded streamwise extent. The dotted lines indicate the spatial growth and decay consistent with the predictions of linear stability theory. For the wall parameters selected in the case that is illustrated in Figure 5.1(b), the presence of flow-induced surface waves was anticipated. The existence of such waves can

be detected from the very large increase in the convected disturbance energy at the rigid/compliant wall join, which is followed by a correspondingly large decrease at the compliant/rigid wall join. As a consequence, it is no longer possible to trace the decay of the Tollmien-Schlichting wave over the compliant panel in any straightforward manner. However, despite the complications that we have attributed to the excitation of flow-induced surface waves, it can still be argued that the Tollmien-Schlichting wave has been stabilised over much of the length of the compliant-panel. This can be seen from the reduction in the amplitude, at points beyond the downstream end of the panel, from the level that would have been attained had the channel walls been rigid throughout. In fact, by considering the ratio of disturbance amplitudes at two streamwise positions that are located either side of the compliant panel, it is possible to define an effective adaptation length for the Tollmien-Schlichting wave[1]. Such a length measures the difference from the overall growth/decay that would be obtained if the wave could adapt its behaviour instantaneously when it passes over the wall joins. For the case that involved the excitation of flow-induced surface waves, the calculated adaptation length, which can be viewed as incorporating the combined effect of both of the wall joins, was found to be only slightly smaller than the Tollmien-Schlichting wavelength. Thus, it could be claimed that little more than half of the panel length is effective in stabilising the wave. In the case where flow-induced surface waves were absent, the adaptation length was reduced to below one quarter of the Tollmien-Schlichting wavelength; the wave becomes stable over nearly all of the compliant panel. It may be shown that the variation in the adaptation lengths between the two cases is broadly in accord with the different wall excitation lengthscales that can be derived by considering homogeneous solutions to the wall motion governing

[1]The adaptation length does not depend on which particular definition of the wave amplitude is adopted. It should be the same whether, say, the disturbance energy or the squared vorticity is considered. This is provided that the two points taken in computing the amplitude ratio are sufficiently well removed from the wall joins.

equation.

A few simulations were also conducted for very short compliant panels that extended to only a single Tollmien-Schlichting wavelength, or less. In such circumstances it may be anticipated that the effects of the two wall joins will dominate over any stabilising effect that could be exhibited along a longer panel. Moreover, we would expect to find some kind of interference between the motions excited at each wall join. Interestingly, the simulations revealed that the adaptation length could become negative. In other words, it proved possible to obtain a reduction in the disturbance amplitude that was slightly larger than that which would have been found had the Tollmien-Schlichting wave adapted its spatial growth rate as soon as it propagated over each wall join. Clearly, the appearance of such an additional favourable stability effect merits further investigation.

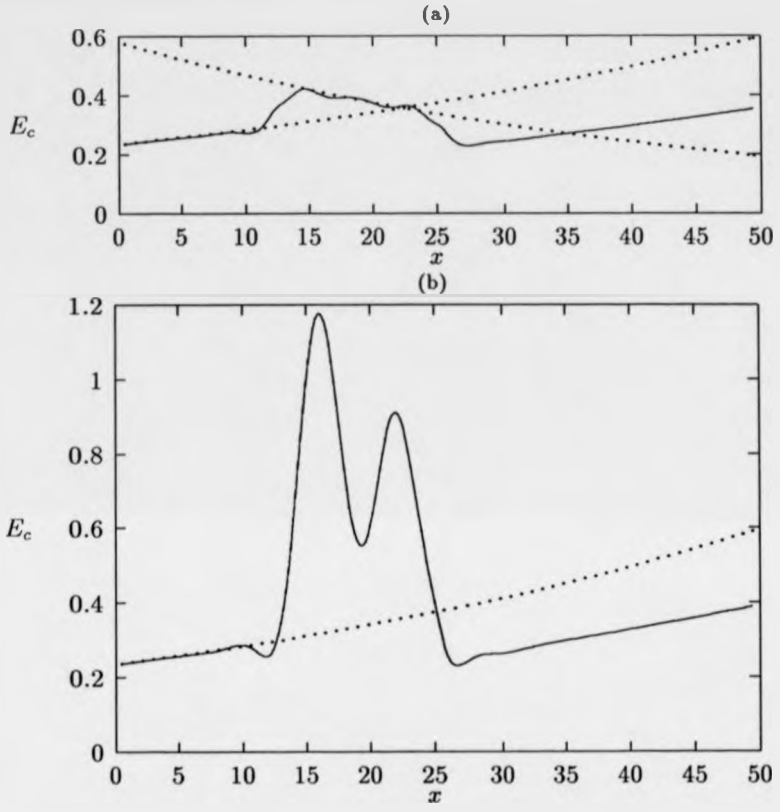


Figure 5.1: Streamwise distributions of the time-averaged convected disturbance energy $E_c = \int_0^1 U(\overline{u^2 + v^2})/2\,dy$ associated with the passage of a Tollmien-Schlichting wave over a short compliant panel. The temporal frequency is $\beta = 0.24$ and the Reynolds number is $R = 12000$. The panel ends are located at $x = 12$ and $x = 25.6$, giving a panel length of $l \approx 2 \times \lambda_{ts}$, where $\lambda_{ts}$ is the Tollmien-Schlichting wavelength. In each case $m = 1/3$, $T = 0$. The other wall parameters are given by (a) $K = 7.68 \times 10^7$, $B = 1.92 \times 10^7$, $d = 0$, (b) $K = 1.92 \times 10^7$, $B = 7.68 \times 10^7$, $d = 1000$. The lengthscale $\gamma^{-1}$ for the excitation of the wall motion, as defined by the homogeneous solutions considered in Section 4.5, can be computed to be (a) $\gamma^{-1} = 1.01$, (b) $\gamma^{-1} = 2.08$.

# Appendix A

# Equivalent formulations of the fluid governing equations

We wish to show that the linearised two-dimensional Navier-Stokes equations

$$\frac{\partial u}{\partial t} + U\frac{\partial u}{\partial x} + U'v = -\frac{\partial p}{\partial x} + \frac{1}{R}\nabla^2 u \tag{A.1}$$

$$\frac{\partial v}{\partial t} + U\frac{\partial v}{\partial x} = -\frac{\partial p}{\partial y} + \frac{1}{R}\nabla^2 v \tag{A.2}$$

$$\frac{\partial u}{\partial x} + \frac{\partial v}{\partial y} = 0 \tag{A.3}$$

together with the boundary conditions

$$u = \frac{\partial^2 u}{\partial y^2} = 0 \quad \text{at } y = 0 \tag{A.4}$$

$$u = \hat{u}\ ,\ v = \bar{v} \quad \text{at } y = 1 \tag{A.5}$$

can be recovered from the system of equations that was considered in the main text. (Note that we are excluding any consideration of the upstream and downstream boundary conditions. The two conditions imposed upon the $u$-component at the channel centre define the symmetry of the solutions.) In our amended vorticity-velocity formulation we took

$$\frac{\partial \omega}{\partial t} + U\frac{\partial \omega}{\partial x} + U''v = \frac{1}{R}\nabla^2 \omega \tag{A.6}$$

$$u = \int_0^y \omega \, dy + \frac{\partial}{\partial x} \int_0^y v \, dy \tag{A.7}$$

$$\nabla^2 v = -\frac{\partial \omega}{\partial x} \tag{A.8}$$

in conjunction with the boundary/integral conditions

$$\frac{\partial v}{\partial y} = \frac{\partial \omega}{\partial y} = 0 \quad \text{at } y = 0 \tag{A.9}$$

$$\int_0^1 \omega \, dy = \bar{u} - \frac{\partial}{\partial x} \int_0^1 v \, dy \tag{A.10}$$

$$v = \bar{v} \quad \text{at } y = 1. \tag{A.11}$$

If we simply define the vorticity as

$$\omega = \frac{\partial u}{\partial y} - \frac{\partial v}{\partial x} \tag{A.12}$$

then there is no great difficulty in establishing the implication from the equations and conditions given in the primitive variables formulation to the equations and conditions that were used in the vorticity/velocity formulation. Thus, we only need concern ourselves with the converse argument.

The boundary condition $u = 0$ at $y = 0$ follows directly from the expression (A.7) that defines the $u$-component in the vorticity/velocity formulation. Differentiating the expression for $u$ twice with respect to $y$, then utilising the boundary conditions applied to $v$ and $\omega$ at the channel centre, we can re-obtain the condition on the second derivative of $u$ that was taken to fix the symmetry of the flow-fields in the primitive variables formulation. Similarly, by using the definition of $u$ together with the integral constraint (A.10) that is applied to the vorticity, we can infer that $u = \bar{u}$ at $y = 1$. The boundary condition imposed on the normal component of the velocity at the wall location is exactly the same in each formulation. Thus, all the primitive variable boundary conditions can be derived from those that are specified within the vorticity-velocity formulation.

By differentiating (A.7) with respect to $y$ we may recover the definition of the vorticity that was given in (A.12). If, instead, the expression for $u$ is differentiated

with respect to $x$, then we can obtain

$$\frac{\partial u}{\partial x} = \int_0^y \left( \frac{\partial \omega}{\partial x} + \frac{\partial^2 v}{\partial x^2} \right) dy \,. \tag{A.13}$$

Substituting for the integrated terms using the Poisson equation (A.8) for $v$ yields

$$\frac{\partial u}{\partial x} = -\int_0^y \frac{\partial^2 v}{\partial y^2}\, dy = -\frac{\partial v}{\partial y} + \left( \frac{\partial v}{\partial y} \right)_{y=0} \,. \tag{A.14}$$

Since, by assumption, the derivative term evaluated at the channel centre vanishes, it follows that the continuity equation (A.3) is automatically satisfied.

We now define the two quantities

$$P_x = \frac{\partial u}{\partial t} + U\frac{\partial u}{\partial x} + U'v - \frac{1}{R}\nabla^2 u \tag{A.15}$$

$$P_y = \frac{\partial v}{\partial t} + U\frac{\partial v}{\partial x} - \frac{1}{R}\nabla^2 v \,. \tag{A.16}$$

It is straightforward matter to show, using the derived definition of the vorticity and the continuity equation, that we have

$$\frac{\partial P_x}{\partial y} - \frac{\partial P_y}{\partial x} = \frac{\partial \omega}{\partial t} + U\frac{\partial \omega}{\partial x} + U''v - \frac{1}{R}\nabla^2 \omega \,. \tag{A.17}$$

The expression on the right-hand side is just the difference between the terms that appear on the two sides of the vorticity transport equation (A.6). Thus, it must vanish identically. We then have

$$\frac{\partial P_x}{\partial y} = \frac{\partial P_y}{\partial x} \tag{A.18}$$

from which it follows, by an application of Green's theorem, ( *i.e.* Stokes' theorem restricted to two dimensions) that we can find a function $p$, defined uniquely up to an arbitrary constant, such that

$$P_x = -\frac{\partial p}{\partial x} \,, \; P_y = -\frac{\partial p}{\partial y} \,. \tag{A.19}$$

Referring back to the definitions of $P_x$, $P_y$, it can be seen that we have recovered the $x$- and $y$-momentum equations. This completes the demonstration of the equivalence between our vorticity-velocity system and that which holds in terms of the primitive variables.

# Appendix B

# Note on the formulation of the energy balance equation

The relation (4.7) contains no explicit reference to the viscous stresses $\sigma_{ij}$, $i,j = 1,2$. Instead, the viscous terms on the right-hand side have been defined using the vorticity $\omega$. If, as is more usual, the viscous stresses were retained, then the relation would be written as

$$\left(\frac{\partial}{\partial t} + U\frac{\partial}{\partial x}\right)\left[\frac{1}{2}(u^2+v^2)\right] + uvU' + \frac{\partial(up)}{\partial x} + \frac{\partial(vp)}{\partial y} = \frac{\partial}{\partial x_i}(u_j\sigma_{ij}) - \sigma_{ij}\frac{\partial u_j}{\partial x_i}\,. \quad \text{(B.1)}$$

Integrating this across the channel half-width and taking time averages (for the case of time-periodic behaviour) yields an energy balance equation in the form

$$\frac{d}{dx}\Big[\overbrace{\int_0^1 \frac{1}{2}U(\overline{u^2}+\overline{v^2})\,dy}^{\text{(I)}} + \overbrace{\int_0^1 \overline{up}\,dy}^{\text{(II)}} - \overbrace{\int_0^1 (\overline{u\sigma_{11}}+\overline{v\sigma_{22}})\,dy}^{\text{(III)}^*}\Big] =$$
$$\underbrace{\int_0^1 (-\overline{uv})U'\,dy}_{\text{(i)}} - \underbrace{\int_0^1 \overline{\sigma_{ij}\frac{\partial u_j}{\partial x_i}}\,dy}_{\text{(ii)}^*} - \underbrace{\overline{v_w p_w}}_{\text{(iii)}} + \underbrace{\overline{u_w(\sigma_{21})_w} + \overline{v_w(\sigma_{22})_w}}_{\text{(iv)}^*}\,. \quad \text{(B.2)}$$

The labelled terms in (B.2) should be compared with the corresponding terms in the alternative form of the energy balance equation (4.8) that was used to analyse the numerical simulation results. The addition of an asterisk to a label indicates that the quantity concerned has been redefined.

The relationship between the quantities that appear in the two versions of the energy balance may be assessed using the following identities:

$$\frac{\partial}{\partial x}\int_0^1 (u\sigma_{11} + v\sigma_{22})\, dy + \frac{1}{R}\frac{\partial}{\partial x}\int_0^1 v\omega\, dy = 2(f_1 + f_2) \qquad \text{(B.3)}$$

$$\int_0^1 \sigma ij \frac{\partial u_j}{\partial x_i}\, dy - \frac{1}{R}\int_0^1 \omega^2\, dy = 2(f_1 + 2f_2 + f_3) \qquad \text{(B.4)}$$

$$(u_w(\sigma_{21})_w + v_w(\sigma_{22})_w) - \frac{1}{R}u_w\omega_w = 2(f_2 + f_3) \qquad \text{(B.5)}$$

where

$$f_1 = \frac{1}{R}\frac{\partial^2}{\partial x^2}\int_0^1 u^2\, dy$$

$$f_2 = \frac{1}{R}\frac{\partial}{\partial x}(u_w v_w)$$

$$f_3 = -\frac{2}{R}v_w\frac{\partial u_w}{\partial x} = v_w(\sigma_{22})_w\ .$$

It will be argued below that the time-average of each of $f_1$, $f_2$, $f_3$ is negligible. As a consequence, the differently defined quantities which have been given matching labels in the two formulations of the energy balance equation may, in practice, be treated as equivalent. In other words, it makes little difference whether the quantities concerned are defined in terms of the vorticity, or, more cumbersomely, in terms of the viscous stresses. For instance, the term labelled as (ii) in the energy balance equation (4.8) can be identified with the 'conventional' viscous dissipation term (ii)* that appears in equation (B.2). Similar remarks apply for the quantities (iv) and (iv)*. In fact, since the part of (iv)* that involves the normal viscous stress $\sigma_{22}$ is itself negligible, it follows that (iv) gives a close approximation to the time-averaged product of the $u$-component and the perturbation shear stress at the wall location. This product was interpreted by Carpenter & Morris [14] as representing an irreversible energy transfer from the disturbance to the mean flow, due to an interaction between the displaced mean flow and the shear stress. (The interpretation of the quantities (III), (III)* that appear on the left-hand side of the energy balance is unimportant, since, as will be demonstrated shortly, both can be neglected.)

It remains to show that the time-averaged quantities $\overline{f}_1$, $\overline{f}_2$, $\overline{f}_3$ are negligible. If the spatial growth of the disturbances can be described using a locally defined growth rate $\alpha_i$, then $\overline{f}_1$ will be of order $O(\alpha_i^2/R)$, since it contains a second-order streamwise derivative. In contrast, the dominant terms in the energy balance equation should be at least of order $O(\alpha_i)$[1]. Thus, even when relatively large local growths rates are anticipated, the quantity $\overline{f}_1$ remains insignificant.

When the compliant wall is constrained to move only in the vertical direction, the boundary conditions

$$u_w = -U_w'\eta \ , \ v_w = \frac{\partial \eta}{\partial t} \tag{B.6}$$

used to match the wall and fluid motion imply that

$$\overline{u_w v_w} = -\frac{U_w'}{2}\frac{\partial \overline{\eta^2}}{\partial t} = 0 \ . \tag{B.7}$$

Hence, the time-average of $f_2$ vanishes identically. (If horizontal wall motion were allowed, we would expect $\overline{f}_2$ to be at most of order $O(\alpha_i/R)$, so it should still be negligible.) It also follows from the boundary conditions that

$$f_3 = \frac{2U_w'}{R}\frac{\partial \eta}{\partial t}\frac{\partial \eta}{\partial x} \tag{B.8}$$

so $\overline{f}_3$ may be estimated to be of order $O(1/R)$. For Tollmien-Schlichting waves, we would expect other terms in the energy balance equation to be of order $O(1/R^{\frac{1}{2}})$ (see, for instance, the heuristic argument at the end of Section 4.3), so it is admissible to neglect $\overline{f}_3$ by comparison.

Since $f_3$ can be written as the product of the wall velocity and the normal viscous stress at the wall, its time average ought to be associated with an energy transfer between the fluid and the compliant wall. In the formulation of the energy balance given by (B.2), the appropriate transfer term is contained within the quantity (iv)*.

[1]It is assumed that the disturbance amplitudes have been normalised using some appropriately defined norm. For example, we could specify that $1/2\int_0^1(\overline{u^2}+\overline{v^2})\,dy = 1$ at the upstream boundary of the computational domain

Previously, the normal viscous stress was omitted in specifying the fluid forcing of the wall motion. This means that any work done by the normal stress on the compliant wall has been implicitly ignored. Thus, if $\overline{f}_3$ turned out not to be negligible, there would be an inconsistency in the the treatment of the coupling between the wall and fluid motion. However, in the event of such inconsistency being reflected in the results obtained from a numerical simulation, it would be a straightforward matter to reformulate the fluid forcing of the wall motion so as to include the normal viscous stress.

It should be remarked that no approximations were made in deriving either of the two stated forms (4.8), (B.2) for the energy balance of the fluid disturbances, aside from the initial linearisation of the governing equations and the implicit neglect of a viscous energy transfer mechanism, as has just been described. Approximations only appear when, for the sake of convenience, we wish to identify quantities defined via the vorticity with quantities defined explicitly in terms of the viscous stresses.

Finally, we show that the quantity labelled as (III) on the left-hand side of the energy balance equation (4.8) is insignificant. It is simple to check that

$$\int_0^1 \overline{v\omega}\, dy = \frac{1}{2}\frac{d}{dx}\int_0^1 \left(\overline{u^2} - \overline{v^2}\right)\, dy \tag{B.9}$$

when the boundary conditions are such that $\overline{u_w v_w} = 0$. Using this, it can be seen that the term involving (III) makes a contribution of order $O(\alpha_i^2/R)$ in the energy balance, where, as before, $\alpha_i$ is the local spatial growth rate. Thus (III), and hence (III)*, can be ignored.

# Bibliography


[1] M. O. Kramer. Boundary–layer stabilization by distributed damping. *Journal of the Aeronautical Sciences*, 24:459, June 1957.

[2] M. O. Kramer. Boundary–layer stabilization by distributed damping. *Journal of the American Society of Naval Engineers*, 72:25–33, February 1960.

[3] J. Gray. Studies in animal locomotion. VI The propulsive powers of the dolphin. *Journal of Experimental Biology*, 13:192–199, 1936.

[4] T. B. Benjamin. Effects of a flexible surface on hydrodynamic stability. *Journal of Fluid Mechanics*, 9:513–532, 1960.

[5] M. T. Landahl. On the stability of a laminar incompressible boundary over a flexible surface. *Journal of Fluid Mechanics*, 13:609–632, 1962.

[6] P. W. Carpenter and A. D. Garrad. The hydrodynamic stability of flow over Kramer–type compliant surfaces. Part 1. Tollmien–Schlichting instabilities. *Journal of Fluid Mechanics*, 155:465–510, 1985.

[7] P. W. Carpenter and A. D. Garrad. The hydrodynamic stability of flow over Kramer–type compliant surfaces. Part 2. Flow–induced surface instabilities. *Journal of Fluid Mechanics*, 170:199–232, 1986.

[8] M. Gaster. Is the dolphin a red herring? In H. W. Liepmann and R. Narasimha, editors, *IUTAM Symposium on Turbulence Management and Relaminarisation*,

*Bangalore, India*, pages 285–304, New York, January 1987. Springer–Verlag.

[9] A. P. Daniel, M. Gaster, and G. J. K. Willis. Boundary layer stability on compliant surfaces. Final Report 35020, British Maritime Technology Ltd., Teddington, U.K., April 1987.

[10] G. J. K. Willis. *Hydrodynamic Stability of Boundary Layers over Compliant Surfaces.* PhD thesis, University of Exeter, U.K., 1986.

[11] P. K. Sen and D. S. Arora. On the stability of laminar boundary–layer flow over flat–plate with a compliant surface. *Journal of Fluid Mechanics*, 197:201–240, 1988.

[12] K. S. Yeo. The stability of boundary–layer flow over single– and multi–layer viscoelastic walls. *Journal of Fluid Mechanics*, 196:359–408, 1988.

[13] K. S. Yeo. The hydrodynamic stability of boundary–layer flow over a class of anisotropic compliant walls. *Journal of Fluid Mechanics*, 220:125–160, 1990.

[14] P.W. Carpenter and P.J. Morris. The effect of anisotropic wall compliance on boundary–layer stability and transition. *Journal of Fluid Mechanics*, 218:171–223, 1990.

[15] R.D. Joslin, P.J. Morris, and P.W. Carpenter. Role of three–dimensional instabilities in compliant wall boundary–layer transition. *AIAA Journal*, 29(10):1603–1610, October 1991.

[16] P. W. Carpenter. Status of transition delay using compliant walls. In D. M. Bushnell and J. N. Hefner, editors, *Viscous Drag Reduction*, pages 79–113. AIAA, 1990.

[17] J. J. Riley, M. Gad–el–Hak, and R. W. Metcalfe. Compliant coatings. *Annual Review of Fluid Mechanics*, 20:393–420, 1988.

[18] A.D. Lucey and P.W. Carpenter. An alternative route to transition in boundary layers over compliant walls: Comparison between theory and experiment. *Bulletin of the American Physical Society*, 35:2291, 1990.

[19] A.D. Lucey, P.W. Carpenter, and A.E. Dixon. The role of wall instabilities in boundary–layer transition over compliant walls. In *Proc. Boundary Layer Transition and Control Conference*, pages 35.1–35.10, Cambridge, U.K., April 1991. Royal Aeronautical Society.

[20] P. W. Carpenter. The optimization of compliant surfaces for transition delay. In H. W. Liepmann and R. Narasimha, editors, *IUTAM Symposium on Turbulent Management and Relaminarisation, Bangalore, India*, pages 305–313, New York, January 1987. Springer–Verlag.

[21] P.W. Carpenter, A.D. Lucey, and A.E. Dixon. The optimisation of compliant walls for drag reduction. In K.S. Choi, editor, *Recent Developments in Turbulence Management*, pages 195–221. Kluwer Academic Pub., 1991. (Proc. 5th European Drag Reduction Meeting).

[22] A.E. Dixon and A.D. Lucey. The application of parallel algorithms for the optimisation of single– and double–layer compliant walls for transition delay. In C. Taylor, J.H. Chin, and G.M. Homsy, editors, *Numerical Methods in Laminar and Turbulent Flow, Vol. VII, Part 2*, pages 1352–1362, Swansea, U.K., July 1991. Pineridge Press. Proc. of the Seventh International Conference held in Stanford, California.

[23] A.E. Dixon, A.D. Lucey, and P.W. Carpenter. The optimization of viscoelastic walls for transition delay. *AIAA Journal*, 32(2):256–267, 1994.

[24] P.W. Carpenter. The optimization of multiple–panel compliant walls for delay of laminar–turbulent transition. Paper 91–1772, AIAA, June 1991. presented at *AIAA 22nd Fluid Dynamics, Plasma Dynamics & Lasers Conference.*

[25] P.W. Carpenter. The optimization of multiple–panel compliant walls for delay of laminar–turbulent transition. *AIAA Journal*, 31(7):1187–1188, 1993.

[26] D. S. Weaver and M. P. Paidoussis. On collapse and flutter phenomena in thin tubes conveying fluid. *Journal of Sound and Vibration*, 50:117–132, 1977.

[27] J. B. Grotberg and E. L. Reiss. Subsonic flapping flutter. *Journal of Sound and Vibration*, 92:349–361, 1984.

[28] J. B. Grotberg and T. R. Shee. Compressible-flow channel flutter. *Journal of Fluid Mechanics*, 159:175–193, 1985.

[29] J. B. Grotberg. Pulmonary flow and transport phenomena. *Annual Review of Fluid Mechanics*, 26:529–571, 1994.

[30] F.D. Hains and J.F. Price. Effect of a flexible wall on the stability of Poiseuille flow. *Physics of Fluids*, 5:365, 1962.

[31] F. D. Hains. Comparison of the stability of Poiseuille flow and the Blasius profile for flexible walls. Technical Report D1-82-0264, Boeing scientific research laboratories, 1963.

[32] A.I. Korotkin. The stability of plane Poiseuille flow in the presence of elastic boundaries. *Prikl. Mat. Mekh.*, 29:1122–1127, 1965.

[33] O.Yu. Tsvelodub. Stability of plane Poiseuille flow in an elastic channel. *Zh. Prikl. Mekh. Tekh. Fiz.*, 5:75–80, 1977.

[34] C.H. Green and C.H. Ellen. The stability of plane Poiseuille flow between flexible walls. *Journal of Fluid Mechanics*, 51:403–416, 1972.

[35] R.F. Ganiev, L.E. Ukrainskii, and I.G. Ustenko. Stabilisation of small perturbations of Poiseuille flow in a channel with elastic walls. *Izvestiya Akademii Nauk SSSR, Mekhanika Zhidkosti i Gaza*, 23:378–382, 1988.

[36] P. G. Drazin and W. H. Reid. *Hydrodynamic Stability.* Cambridge University Press, U.K., 1981.

[37] J.M. Rotenberry and P.G. Saffman. Effect of compliant boundaries on weakly nonlinear shear waves in channel flow. *SIAM Journal of Applied Mathematics*, 50:361–394, 1990.

[38] M. Pierucci and P.G. Morales. Effect of finite thickness flexible boundary upon the stability of a Poiseuille flow. *ASME Journal of Applied Mechanics*, 57:1056–1060, 1990.

[39] J.M. Rotenberry. Finite amplitude shear waves in a channel with compliant boundaries. *Physics of Fluids A*, 4:270–276, 1992.

[40] M. Rossi. Nonlinear longwave shortwave coupling in flow over a compliant surface. *European Journal of Mechanics B Fluids*, 10:159–164, 1991.

[41] R. Pierce. The Ginzburg-Landau equation for interfacial instabilities. *Physics of Fluids A*, 4:2486–2494, 1992.

[42] M. Gaster. On the generation of spatially growing waves in a boundary layer. *Journal of Fluid Mechanics*, 22:433–441, 1965.

[43] C. Canuto, M.Y. Hussaini, A. Quarteroni, and T.A. Zang. *Spectral Methods in Fluid Dynamics.* Springer, Berlin, 1988.

[44] T. J. Bridges and P. J. Morris. Differential eigenvalue problems in which the parameter appears nonlinearly. *Journal of Computational Physics*, 55:437–460, 1984.

[45] M. Gaster. A note on the relation between temporally–increasing and spatially–increasing disturbances in hydrodynamic stability. *Journal of Fluid Mechanics*, 14:222–224, 1962.

[46] A.D. Lucey and P.W. Carpenter. A numerical simulation of the interaction of a compliant wall and inviscid flow. *Journal of Fluid Mechanics*, 234:121–146, 1992.

[47] A.D. Lucey and P.W. Carpenter. On the difference between the hydroelastic instability of infinite and very long compliant panels. *Journal of Sound and Vibration*, 163:176–181, 1993.

[48] W. Heisenberg. Über Stabilität und Turbulenz von Flussigkeitsströmen. *Ann. Physsik (4)*, 74:577–627, 1924.

[49] J. W. Miles. On the generation of surface waves by shear flows. *Journal of Fluid Mechanics*, 3:185–199, 1957.

[50] P. W. Carpenter and J. S. B. Gajjar. A general theory for two- and three–dimensional wall–mode instabilities in boundary layers over isotropic and anisotropic compliant walls. *Theoretical & Computational Fluid Dynamics*, 1:349–378, 1990.

[51] T. B. Benjamin. The threefold classification of unstable disturbances in flexible surface bounding inviscid flows. *Journal of Fluid Mechanics*, 16:436–450, 1963.

[52] R. J. Briggs. *Electron–Stream Interaction with Plasmas.* MIT Press, Cambridge, MA, 1964.

[53] H Fasel. Investigation of the stability of boundary layers by a finite difference model of the Navier-Stokes equations. *Journal of Fluid Mechanics*, 78:355–383, 1976.

[54] L. Kleiser and T.A. Zang. Numerical simulation of transition in wall-bounded shear flows. *Annual Review of Fluid Mechanics*, 23:495–537, 1991.

[55] Th. Herbert. Exploring transition by computer. *Applied Numerical Mathematics*, 7:3–25, 1991.

[56] S. Biringen and E. Laurien. Nonlinear structures of transition in wall bounded flows. *Applied Numerical Mathematics*, 7:129–150, 1991.

[57] J. A. Domaradski and R. W. Metcalfe. Stabilization of laminar boundary layers by compliant membranes. *Physics of Fluids*, 30:695–705, 1987.

[58] R. W. Metcalfe, F. Battistoni, J. Ekeroot, and S. A. Orszag. Evolution of boundary layer flow over a compliant wall during transition to turbulence. In *Boundary Layer Transition and Control, Cambridge U.K.*, pages 36.1–36.14, London, April 1991. Royal Aeronautical Society.

[59] H Fasel and U Konzelman. Non-parallel stability of a flat plate boundary layer using the complete Navier-Stokes equations. *Journal of Fluid Mechanics*, 221:311–347, 1990.

[60] H. Fasel, U. Rist, and U. Konzelmann. Numerical investigation of the three-dimensional development in boundary-layer transition. *AIAA Journal*, 28:29–37, 1990.

[61] M. Kloker, U. Konzelmann, and H. Fasel. Outflow boundary conditions for spatial Navier-Stokes simulations of transition boundary-layers. *AIAA Journal*, 31:620–628, 1993.

[62] F.P. Bertolotti, Th Herbert, and P.R. Spalart. Linear and nonlinear stability of the Blasius boundary layer. *Journal of Fluid Mechanics*, 242:441–474, 1992.

[63] Th. Herbert. Boundary–layer transition - analysis and prediction revisited. Paper 91–0737, AIAA, 1990.

[64] J. W. Murdock. A numerical study of nonlinear effects on boundary-layer stability. *AIAA Journal*, 15:1167–1173, 1977.

[65] H. Fasel. Recent developments in the numerical solution to the Navier-Stokes and hydrodynamic stability problems. In *Computational Fluid Dynamics*, pages 167–280. Hemisphere, 1980.

[66] T. B. Gatski. Review of incompressible fluid flow computations using the vorticity-velocity formulation. *Applied Numerical Mathematics*, 7:227–239, 1991.

[67] L. Quartapelle and F. Valz-Gris. Projection conditions on the vorticity in viscous incompressible flows. *International Journal of Numerical Methods in Fluids*, 1:129–144, 1981.

[68] L. Quartapelle. Solution of the time dependent incompressible Navier-Stokes equations by finite elements. In *Computational Fluid Dynamics.* von Karman Insititute, Belgium, 1992.

[69] H. Fasel. Numerical solution of the complete Navier-Stokes equations for the simulation unsteady flows. In *Lecture notes in mathematics 771*, pages 177–195. Springer, 1980.

[70] C.A.J Fletcher. *Computational Techniques for Fluid Dynamics*, volume 2. Springer, Berlin, 2 edition, 1991.

[71] A. D. Lucey. *Hydrodynamic Instability of Flexible Surfaces.* PhD thesis, University of Exeter, U.K., 1989.

[72] P. J. Morris. The spatial viscous instability of axisymmetric jets. *Journal of Fluid Mechanics*, 77:511–529, 1976.

[73] P. W. Carpenter, R. Joslin, and P.J. Morris. Energy exchange in flows over compliant walls. Tech. Note 92/3, University of Warwick, Mechanical Engineering, 1992.

[74] P. W. Carpenter, R. Joslin, and P.J. Morris. A note on the occurence of an apparently anomalous spatially growing eigenmode for the coupled-flow/compliant-wall eigen-problem. Tech. Note 92/2, University of Warwick, Mechanical Engineering, 1992.

[75] J. Werle, A. D. Lucey, and P. W. Carpenter. Hydroelastic stability of complex compliant-wall structures in fluid flow. In C. Taylor, editor, *Numerical Methods in Laminar and Turbulent Flow*, pages 1435–1446. Pineridge, Swansea, U.K., 1993.

[74] P. W. Carpenter, R. Joslin, and P.J. Morris. A note on the occurence of an apparently anomalous spatially growing eigenmode for the coupled-flow/compliant-wall eigen-problem. Tech. Note 92/2, University of Warwick, Mechanical Engineering, 1992.

[75] J. Werle, A. D. Lucey, and P. W. Carpenter. Hydroelastic stability of complex compliant-wall structures in fluid flow. In C. Taylor, editor, *Numerical Methods in Laminar and Turbulent Flow*, pages 1435–1446. Pineridge, Swansea, U.K., 1993.

7